学位論文

Quasi-free proton knockout reaction of ^{23,25}F

(^{23,25}F核の準弾性(p,2p)ノックアウト反応)

平成28年2月博士(理学) 申請

東京大学大学院理学系研究科

物理学専攻

鄧子良

Tang Tsz Leung

Quasi-free (p,2p) knockout reaction of ^{23,25}F

Tsz Leung TANG

Department pf Physics,

Graduate School of Science,

The University of Tokyo

A Dissertation Submitted in Partial Fulfillment of the Requirements for the Degree of Doctor of Philosophy

July, 2016, Tokyo

Acknowledgements

It is a pleasure to thank many people who made this thesis possible.

First and foremost, I offer my sincerest gratitude to my supervisor, Chief Scientist, Tomohiro Uesaka. I must thank for all the teaching, advices, encouragements, patential, cares, understanding, and everything that I learnt and received from him. "學而不思則罔，思而不學則殆。"

I would like to thanks for all collaborators of SHAQRA04 experiment: (according to alphabet of surname) D. Beaumel, M. Dozono, N. Fukuda, T. Fukunaga, T. Fujii, A. Galindo-Uribarri, S. H. Hwang, N. Inabe, D. Kameda, T. Kawahara, S. Kawase, W. Kim, K. Kisamori, M. Kobayashi, T. Kubo, Y. Kubota, K. Kusaka, C. S. Lee, Y. Maeda, H. Matsubara, S. Michimasa, H. Miyam, T. Noro, A. Obertelli, K. Ogata, S. Ota, E. Padilla-Rodal, S. Sakaguchi, M. Sasano, S. Shimoura, S. Stepanyan, H. Suzuki, M. Takaki, H. Takede, T. L. Tang, H. Tokieda, T. Uesaka, T. Wakasa, T. Wakui, K. Yako, Y. Yanagisawa, J. Yasuda, R. Yokoyama, and J. Zenihiro. I also thank the RIBF cyclotron crews and technical staffs for their support in providing a stable beam during the experiment. I have to personally thanks Daid Kahl for helping me went through the thesis submission procedure.

I would like to give a special thanks to Prof. Shinsuke Ota and Mr. Shinichiro Kawase for making the analysis code. I am very much appreciating their opinions, suggestions and comments. I also appreciate many helps from my colleagues, especially Dr. S.H. Haung, Dr. Kawahara Tomomi, Prof. S. Sakaguchi, and Prof. Takashi Wakui, their contributions to the spin-polarized proton target are very important and essential.

I like to thanks Prof. Susumu Shimoura, Prof. Atsushi Tamii, and Prof. Nori Aoi for teaching me nuclear physics and solidify my understanding. They also gave me a precious chance for staying in Japan after the scholarship.

I also have to thanks the chair of the thesis committee, Prof. N. Imai. He gave very helpful and clear instruction on improving the thesis. His encouragements and supports improved the quantities of this thesis significantly. Other committee members, Prof. K. Wimmer, Prof. T. Otsuka, T. Kawamoto, and J. Tanaka also have my thanks. Their opinions are very valuable and inspiring.

I also like to thanks Miss Lei Yu and Miss Sarah Malek for making this thesis to be reader friendly. I will never forget their unconditional support, and I will follow their example to help other unconditionally.

The nuclear physic community also has my thanks. The experiment number was NP1006-SHARAQ04. This work was supported by Center of Nuclear Study (University of Tokyo), RIKEN Nishina Center, Japanese Government (Monbukagakusho) Scholarship, and Research Center of Nuclear Physics, Osaka University. And many thanks give to some powerful software like AutoDesk Inventors, Mathematica, AnaPaw, ROOT by CERN, MS Words, Excel, PowerPoints, LINUX (Ubuntu), etc. Also Wikipedia, Physics Review, Google have credits.

Many thanks to my family and friends for all the supports they gave to me. First is to my parents and my two sisters. They always let me do whatever I want, support me unconditionally, and let me escape from family duty. There are so many people I like to thanks for their support too: Tim Tsang, YesTak Chan, Philip Yeung, Hui Ya Tsai, Alice Hollenstein, Connie Lam, Christine Hui, Dickson ma, Eveline Chan, Eunice Lee, GiGi Ho, Karin Tsai, Keita Kamakura, Kokchin Tok, Pheon Fung, P.Y. Chan, Sonia Chu, SQ Boey, and Wing Ho.

T.L. Tang

July, 2016, Tokyo

Contents

List of Figures

List of Tables

List of Symbols

General meaning of most symbols are listed in here. A symbol may represent different quantity, but it should be understandable within the context.

H	Nuclear Hamiltonian
S_n	Neutron separation energy deduced by experimental binding energy
S_p	Proton separation energy deduced by experimental binding energy
E_x	Excitation energy
$s_p(nlj)$	Proton separation energy from knockout of the nlj state
S_{nlj}	Spectroscopic factor of the nlj state
S_{exp}	Experimental spectroscopic factor
S_{th}	Theoretical spectroscopic factor, calculated using the shell model
σ	Reaction cross-section
σ_{DWIA}	Theoretical cross section from the DWIA calculation
R	Reduction factor of the spectroscopic factor when comparing to the shell limit
R_S	Reduction factor of the spectroscopic factor when comparing to S_{th}
$\mathbb{P}$	Relativistic four-momentum
$\vec{p}$	3-dimentional momentum vector
$\vec{k}$	3-dimentional momentum vector of residual nucleus
E	Relativistic total energy
T	Kinetic energy
A	Mass number
N	Neutron number
Z	Charge number

Quasi-free (p,2p) knockout reaction of ^{23,25}F

Tsz Leung TANG

Graduate School of Science, University of Tokyo

Abstract

The change of the neutron dripline from oxygen to fluorine indicates the $1d_{5/2}$ proton affects the neutron shell structure. We aim to know how the neutron sd-shell structure is changed by the $1d_{5/2}$ proton in neutron-rich ^{23}F and ^{25}F nucleus using proton spectroscopy. The spectroscopy is free from the effects of the proton shell structure, because the $1d_{5/2}$ proton in ^{23}F or ^{25}F is a single-particle state due to the $Z = 8$ magicity and even neutron number. If the neutron shell structure is not changed by the proton in ^{23,25}F, after the sudden removal of that proton, the spectroscopic factor of that proton should be unity and not fragmented. Therefore, the effect on the neutron-shell from the proton will be shown on the spectroscopy.

The quasi-free ^{23,25}F(p,2p) direct knockout reactions in inverse kinematics were performed in RIBF, RIKEN Nishina Center. Secondary beams of ^{23}F and ^{25}F were produced at ~280*A* MeV. The missing four-momentum of the residual oxygen (^{22}O or ^{24}O) was reconstructed using coincidence measurement of the incident nucleus and the two scattered protons. The excitation energy of the residue was then deduced.

From the experimental results, the occupation number of the $1d_{5/2}$ proton of ^{25}F was 0.1 ± 0.3 and the proton is indeed in single-particle state. Meanwhile, the spectroscopic strength of the $1d_{5/2}$ proton of ^{23}F or ^{25}F were fragmented. These pointed that the change of the sd-shell neutron structure due to the $1d_{5/2}$ proton is the reason of the fragmentation. The change of neutron shell suggests the disappearance of $N = 16$ magicity. The nuclear structures of the ^{25}F and ^{23}F demonstrated the Type-1 shell evolution. The comparison with the present shell model interactions (SFO, USDB, and SDPF-MU) indicated that the tensor force should be stronger. Also, the spectroscopic strength of the p-orbit was ~0.8 in ^{23,25}F, this shows that the short-range correlation in neutron-rich nuclei is as same as stable nuclei.

Chapter 0

Prologue

This chapter introduce the idea behind this study. We will briefly go through the background and then bring up the objective of this thesis. The detail will be presented in Chapter 1.

0.1 Background

One of the main objectives in nuclear physics is to understand the nuclear structure across the entire nuclide chart from the nucleon-nucleon interaction. The nucleon-nucleon interaction in free space is well known, but the medium modification and correlation effects are not trivial [1]. One of the interesting features is the shell evolution that the shell structure changes with number of protons and neutrons. It is a result of the interplay between different kinds of nuclear forces [2] [3]. With the access of radioactive nuclei, many new phenomena were discovered on the neutron rich region among the light nuclei (nuclear mass number $A < 40$) [4]. Figure 0-1 shows the region of where new features appear in the light nuclei region. For example: the neutron halo (yellow boxes) [5], the disappearance of the $N = 8$ shell closure [6] [7], the island of inversion [8] [9] [10], the intruder state [11], the disappearance of the magic number $N = 20$ [12], and the emergence of a new magic number $N = 16$ [13] [14] [15].

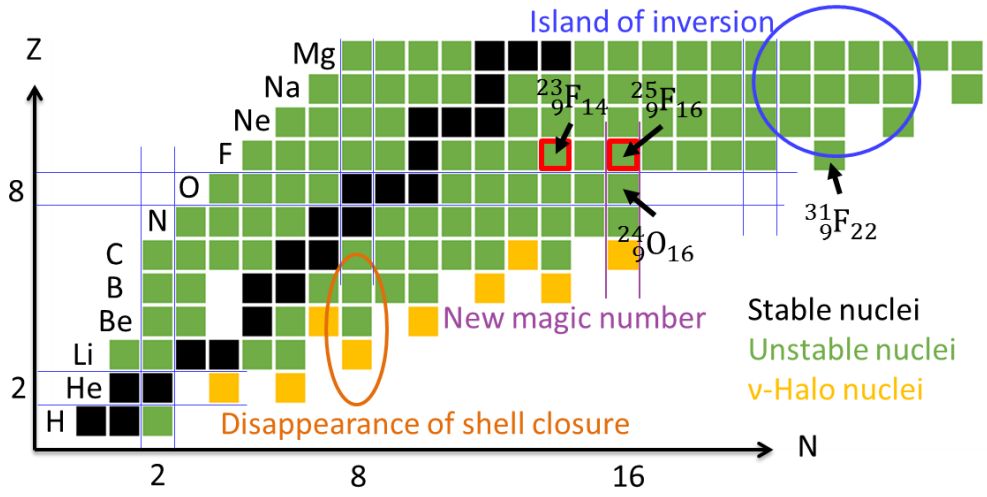

Figure 0-1 – New phenomena in the light nuclei region.
The x-axis is the neutron number. The y-axis is the proton number. The nuclide chart was remake from Reference [16].

We are curious and aim to study how the neutron sd-shell structure is changed by the $1d_{5/2}$ proton in neutron-rich ^{23,25}F nuclei using proton spectroscopy. The change of the neutron dripline from oxygen to fluorine draws or attention. The neutron dripline of oxygen is at ^{24}O, which is $N = 16$. The neutron dripline of fluorine extended from $N = 16$ to $N = 20$ by just a single $1d_{5/2}$ proton. Naively, this indicates the $1d_{5/2}$ proton in fluorine affects the neutron shell by lowering the $1d_{3/2}$ neutron orbit below the neutron threshold. The neutron dripline was studied by many theories [16] [17] [18]. The effects on the neutrons due to the excessive neutrons themselves were studies in many neutron-transfer or neutron-removal experiments [19].

The proton removal spectroscopy on neutron-rich fluorine isotopes are an ideal place to study the sd-shell structure and the proton-neutrons interaction. The $1d_{5/2}$ proton should be more sensitive to the neutron sd-shell structure than the structure of ^{16}O due to the double magic. The $1d_{5/2}$ proton is also in a single-particle state mainly because of the $Z = 8$ magicity. These makes the proton removal spectroscopy on fluorine free from the effect of the proton shell. When the single $1d_{5/2}$ proton is suddenly removed from fluorine nucleus, only neutrons are left on the sd-shell and the shell structure should be remained the same. If the fluorine nucleus is a simple system formed by adding a proton on top of an oxygen nucleus, so that the neutron-shell structure does not change, then the spectroscopic factor of the proton should be unity and not fragmented (see section 1.1.2 for spectroscopic factor). The result of the spectroscopic can be used to study the change of the neutron-shell structure, for example, the spin-orbit splitting of the 1d-shell could be reduced by the proton [20].

The $1d_{5/2}$ proton of ^{23}F or ^{25}F are in a single-particle state mainly due to $Z = 8$ magicity. The proton magicity $Z = 8$ is very robust because the shell gap between the $1d_{5/2}$ orbit and $1p_{1/2}$ orbits is roughly 10 MeV. The even number of neutrons and the weak proton-neutron correlation energy (0.7 MeV for ^{23}F and 0.07 MeV for ^{25}F, section 1.1.4) also support that the $1d_{5/2}$ proton is in a single-particle state. The valance proton in similar nuclei like ^{49}Sc or ^{209}Bi are in a single-particle state. The $1f_{7/2}$ proton of ^{49}Sc is surrounded by 8 neutrons in the $1f_{7/2}$ orbit. Using proton transfer reaction, the spectroscopic factor of the proton is 1 [21]. Another example is ^{209}Bi, the spectroscopic factor of the $1h_{9/2}$ proton is 0.95 using proton transfer reaction [22].

In addition to the sd-shell, there is almost no data for the states below Fermi surface (the p-orbit and 1s-orbit) for fluorine isotopes. There is one review journal shown the single-particle levels of the p-orbit [23], but it did not give any reference for that data. The extraction of the single-particle energy and spectroscopic factor, or the occupation number, could provide better understanding on the nucleon-nucleon interaction below the Fermi surface [24].

The (e,e´p) knockout reaction should be the most ideal method to study the proton spectroscopy. Because of the radial sensitivity and the rather simple reaction mechanism that only involves Coulomb force [1] [25]. However, in radioactive nuclei, an inverse kinematics must be used. And the beam intensity is small. A quasi-free proton knockout reaction is currently the most ideal and feasible method to study the proton spectroscopy of neutron rich nuclei [25] [26].

0.2 Thesis Objective

This study aims to probe the change of the neutron shell due to the $1d_{5/2}$ proton using proton knockout spectroscopy. The spectroscopic properties of the proton bound state of ^{23,25}F, such as single-particle energy, spectroscopic factor, or the occupation number (the sum rule of the spectroscopic factors), will be measured or extracted. Besides of the sd-shell, the p-shell can also be studied under the same reaction.

This study also aims to establish a method to probe the single-particle state of radioactive nuclei by (p,2p) knockout reaction using inverse kinematics and spin-polarized proton target. The experience gained from this study can shine a light on future experimental method and technique.

0.3 Thesis Organization

This thesis is arranged as follows: Chapter 0 provides a brief introduction and the motivation. Chapter 1 focuses on nuclear structure theory and the experimental method used in this work. Chapter 2 describes the experimental set-up, explaining the technical issues. The data analysis and results are described in Chapter 3. Here, we explain the methods used to extract the spectroscopic factor from the experimental data. We discuss the comparison of the results with present shell interactions in Chapter 4. This study is summarized in Chapter 5.

Following the main body of the text, we have included several appendices the reader may find useful. In Appendix A, we show some detailed calculations on the subjects. Appendix B focuses on the theory of proton polarization. Appendix C describes the solid spin-polarized proton target and Appendix D focuses on data analysis of proton-proton elastic scattering.

Chapter 1
Nuclear Shell Structure and Knockout Reaction

The present understandings of the nuclear structure will be described in the first half of this chapter. We are going to briefly explain the independent particle model, single-particle state, and spectroscopic factor. Then we describe three main components of the nuclear force and their effects. Following the discussion of the theory, we revisit the past experiments conducted on fluorine isotopes. In the second half of this chapter, we explain our experimental method including the kinematics of the knockout reaction and a brief explanation of the calculation of theoretical cross sections.

1.1 Nuclear Shell Structure

A nucleus is made of protons and neutrons. The nucleons are confined in a tiny volume by the nuclear potential that the energy levels of the nucleon orbits are quantized. From the nucleon separation energy and the first excitation energy, some stable nuclei with certain number of protons or neutrons are found to be more tightly bound than their neighbors. These numbers are 2, 8, 20, 28, 40, 50, 82, and 128, which are also called "magic numbers" [27]. These observations suggest the nuclear orbits are grouped in shells.

The bound nucleons are moving around their center of mass and carrying orbital angular momentum. Each of them has an intrinsic spin of 1/2. Therefore, one of the component of nuclear force is spin-orbit coupling. This force is more attractive when nucleon's spin is parallel to the angular orbital momentum. For example, the $1p_{3/2}$ orbit is more tightly bound than the $1p_{1/2}$ orbit [28].

The energy gap between the $j = l + s$ orbit and the $j = l - s$ orbit is called the spin-orbit splitting, where j is the total angular momentum, l is the orbital angular momentum, and s is the intrinsic spin. In the late 1940s, M. G. Mayer proposed a strong spin-orbit coupling on a spherical harmonic oscillator to model the potential well of the nucleus. Using this model, it is possible to reproduce the magic numbers up to 128 and correctly predicted the spin-parity of nuclei ground state [28] (Figure 1-1).

Nucleons fill the energy shells from the lowest level and obey Pauli's exclusion principle. The independent particle model (IPM) assumes each nucleon orbiting around a mean field and does not

interact with each other. This model well predicts the properties of nuclei with one plus (or minus) magic number. Interestingly, the strength of the spin-orbit splitting cannot be fully reproduced using nucleon-nucleon two-body spin-orbit (LS) coupling [29] [30] [31]. Later development on the meson-exchange theory explains the origin of the spin-orbit coupling (from the σ and ω mesons), but also introduced others contributions, for example, tensor force and spin-isospin interaction [32]. There is no full understanding of the splitting yet.

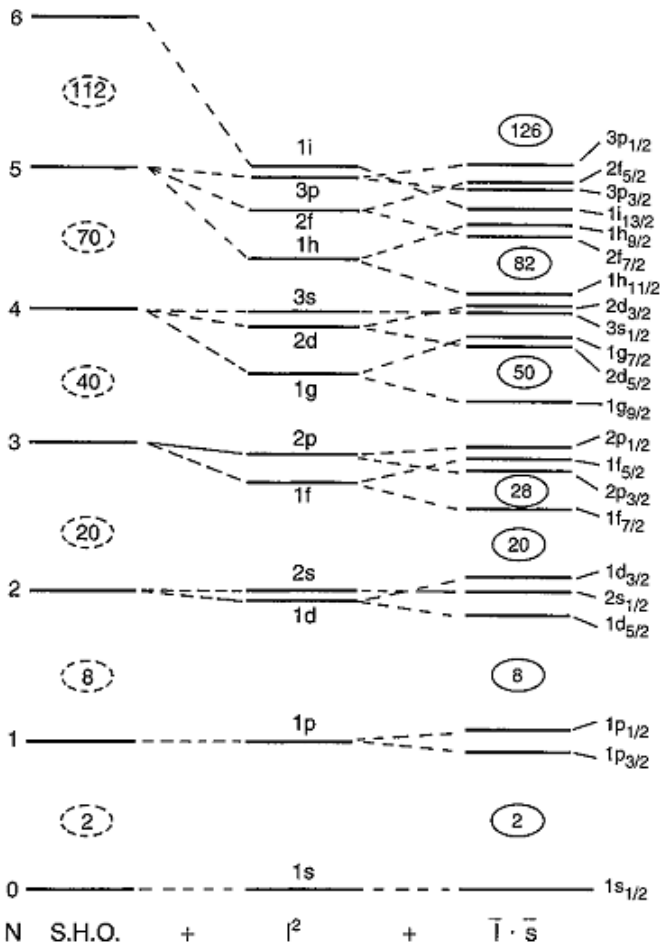

Figure 1-1 – Evolution of energy level by adding spin-orbital coupling [33].
The N is the number of simple harmonic oscillators (S.H.O.). The l^2 is the square of orbital angular momentum. The l·s is the spin-orbit coupling.

Before proceeding further, we feel it is necessary to define the bound, unbound, resonance, excited, valence, occupied, and unoccupied orbit. These terms are illustrated in Figure 1-2. Here, the bound orbits are below the particle threshold and the unbound orbits are above. The occupied orbits have at least one nucleon each. The valance orbit is the outermost occupied orbit according to the IPM. The excited orbits are higher energy than the valance orbit. When describing a single-particle orbit, "state" and "orbit" are having the same meaning.

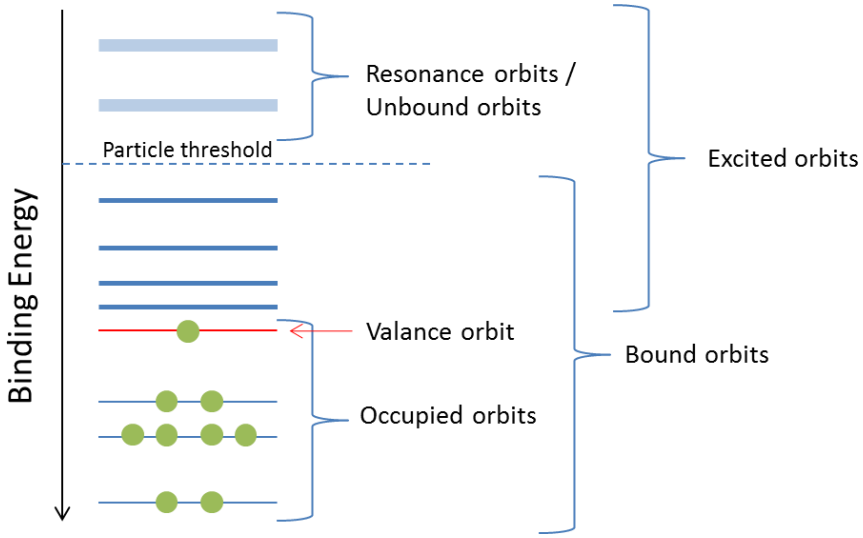

Figure 1-2 – Terminology of orbits.
The bound, unbound, resonance, excited, valance, occupied, and unoccupied orbits are shown in the figure. The valance orbit for fluorine nucleus is the $1d_{5/2}$ proton. The unoccupied states are the excited states and unbound states.

1.1.1 Nuclear Mean Field Shell Model and Single-Particle Energy

The mean field shell model (or mean field) is an effective theory and especially suitable for closed shell nuclei. It treats the interaction experienced by a nucleon as an average mean field created by others nucleons. The total Hamiltonian of a nucleus (up to two-body interaction) is

$$H = \sum_i \frac{P_i^2}{2m_i} + \sum_i \sum_{j<i} V_{ij}, \tag{1.1.1}$$

where the first term is the kinetic energy (where P_i is the momentum and m_i is the mass of the i-th nucleon) and the second term V_{ij} is the two-body interaction between nucleons, or the nucleon-nucleon interaction. The mean field U_i is added, so that

$$H = \sum_i \left(\frac{P_i^2}{2m_i} + U_i \right) + \sum_i \left(\sum_{j<i} V_{ij} - U_i \right) = \sum_i h_i + H_R = H_0 + H_R, \tag{1.1.2}$$

where h_i is the single-particle Hamiltonian and H_R is the residual interaction. The first term H_0 is also called the non-interacting potential that each nucleon is moving independently. When the residual term is very small and neglected, it is called the single-particle picture or the independent particle model (IPM). The simplest way of finding a self-consistent mean field from a given nuclear interaction is the Hartree method [34]. In order to minimize the total energy and preserve the anti-symmetry of the total wavefunction (this introduces an exchange term), the Hartree-Fock method of variation can be used. The mean field model can cope with paring (the Hartree-Fock-Bogoliubov method) and deformation. A common phenomenological mean field is the Woods-Saxon potential.

The IPM is a good approximation when the residual interaction H_R is negligible compared to the non-interacting term H_0. The IPM successfully explains the properties of nuclei with one nucleon added or removed on a magic nucleus. The spin-parity of the ground state and first few excited states of those nuclei can be well explained [35]. Nuclear deformation can be handled by changing the mean field to a non-spherical type. However, it is beyond the mean field model to study nucleon-nucleon correlation or configuration mixing.

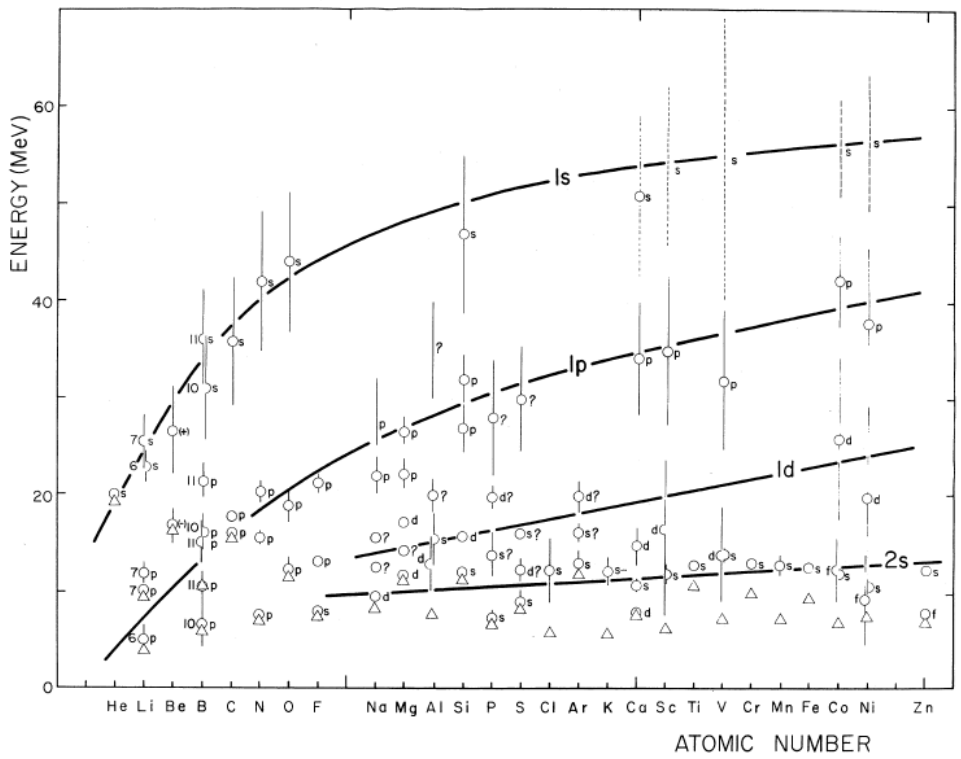

Figure 1-3 – Single-particle energy from quasi-free scatterings as a function of atomic number [23]. The solid line is only a guideline.

The single-particle energy ϵ is the eigen-energy of the single-particle Hamiltonian h, such that

$$h|\phi_i\rangle = \epsilon_i|\phi_i\rangle, \tag{1.1.3}$$

where ϕ_i is the wavefunction of i-th state for a single nucleon. The experimental separation energies of different orbits of different elements are shown in Figure 1-3. The single-particle energies for states near the Fermi surface of a closed-shell nucleus is related to the binding energy or the single-particle separation energy. The single-particle energies for protons are

$$\begin{aligned} \epsilon_p^{>}(Z,N) &= BE(Z,N) - BE(Z+1,N) = -S_p(Z+1,N), \\ \epsilon_p^{<}(Z,N) &= BE(Z-1,N) - BE(Z,N) = -S_p(Z,N), \end{aligned} \tag{1.1.4}$$

where $\epsilon_p^{>}$ is the single-particle energy for the proton on top of a nucleus with proton number Z and neutron number N and $\epsilon_p^{<}$ is the single-particle energy for the proton of the nucleus. The shell gap for a closed-shell nucleus is defined as $E_g = \epsilon_p^{<}(Z,N) - \epsilon_p^{>}(Z,N)$ [17].

The single-particle energies for states away from the Fermi surface can be obtained from knockout or transfer reactions. Figure 1-4 shows a comparison of the neutron single-particle energies of ^{16}O and ^{40}Ca between experimental data, SKX, and NL3 calculations. SKX is the skyrme potential with parameters fitted to the binding energies, root-mean-square charge radius, and single-particle energies of spherical nuclei [36]. NL3 is a parameter set for a relativistic mean-field calculation [37]. The NL3 calculation predicts the energy levels more accurately than SKX calculation. It is surprise that the relativistic calculation gives better prediction because the average nucleon kinematic energy is 35 MeV and much smaller than the nucleon mass of ~1 GeV/c^2. Figure 1-5 and Figure 1-6 show the proton single-particle energies of ^{23}F and ^{25}F calculated using WSPOT, SKX, and experimental binding energy respectively. WSPOT is a simple Woods-Saxon potential with spin-orbit coupling [38]. The parameters of WSPOT are listed in Table 1-1. The parameters of the diffuseness $a = 0.35$ fm and the reduced radius R_0 = 1.15 fm are fixed [39]. The depths of central potential and spin-orbit potential are fitted for single-particle energy of ^{23}F (^{25}F), ^{22}O (^{24}O) [40], and the root-mean-square charge radius of ^{23}F (^{25}F) [41].

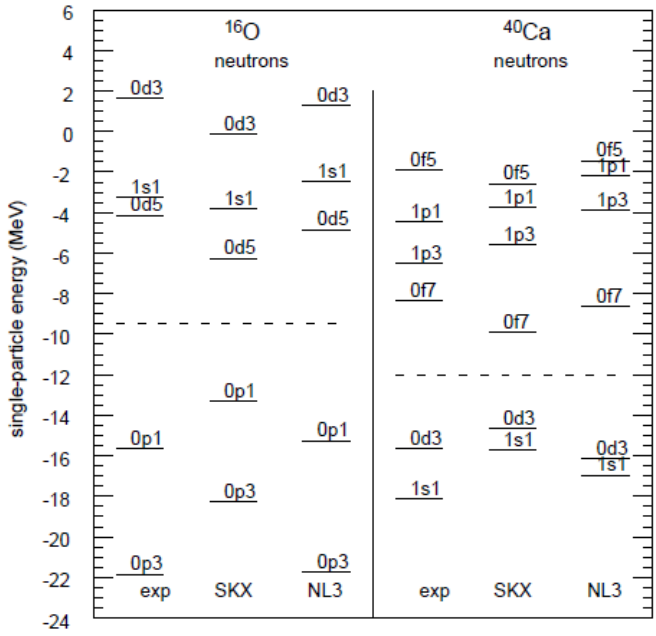

Figure 1-4 – The neutron single-particle energy of ^{16}O and ^{40}Ca.
The experimental values are compared SKX and NL3 potential in mean field calculation [38].

Table 1-1 – List of WSPOT parameters.

	V_0 [MeV]	V_{ls} [MeV]	R_0 [fm]	a [fm]
^{23}F	-67.855	18.04	1.15	0.35
^{25}F	-66.312	19.58		

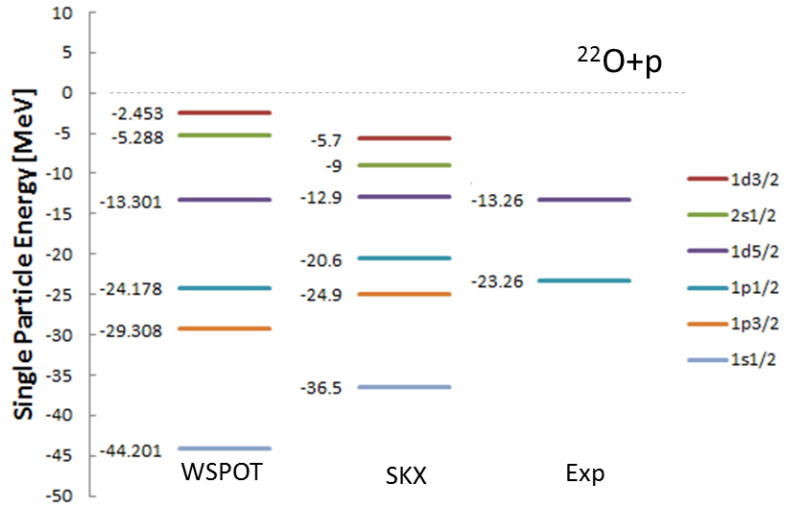

Figure 1-5 – The proton single-particle energies of ^{23}F.
They are calculated by WSPOT [38], SKX and experimental binding energy.

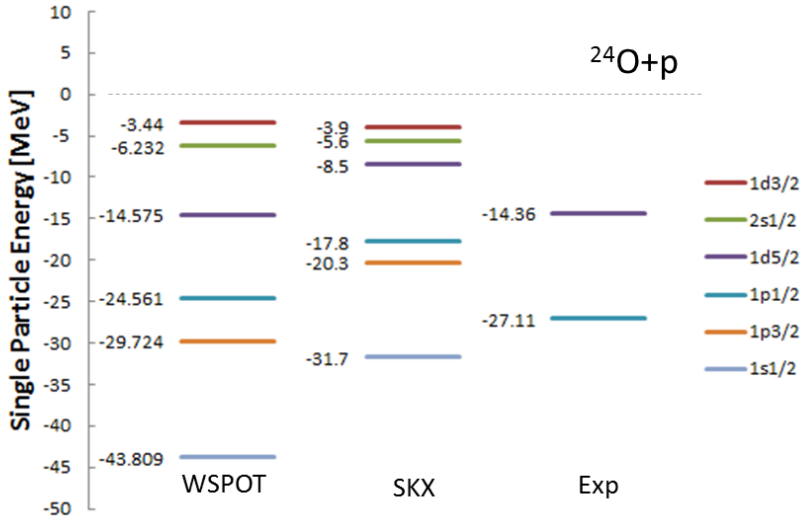

Figure 1-6 – The proton single-particle energies of ^{25}F.
They are calculated by WSPOT, SKX and experimental binding energy.

The shell model (or interactive shell model) calculation is based on the independent particle model to cope with the residual interaction. The off-diagonal terms are the reason for the nucleon-nucleon correlation and configuration mixing. The calculation diagonalizes the Hamiltonian within some major shells [42]. Due to the huge number of bases involved, it is more computationally suitable on light nuclei or within a truncated configuration space. The shell model cannot calculate the single-particle energies but uses them as one of the inputs; therefore, it is mainly used in calculating ground state and the excited states. The other input is the two-body matrix elements that bases on the nuclear interactions. The occupation number, which is the average number of particles in an orbit, can be calculated using the shell model calculation. The occupation number can be measured experimentally by the sum of the spectroscopic factors. It is worth to notice that because of the virtual excitation, there are ~30% highly excited component in the real wavefunction, which is neglected in the shell model calculation [38].

1.1.2 Spectroscopic Factor

The IPM assumed that nucleons are moving in a mean field independently, so that each nucleon is moving in a single-particle orbit. In this case, the spectroscopic factor equals 1. A correlated nucleon has a spectroscopic factor smaller than 1. There are two kinds of spectroscopic factors: theoretical and experimental. The theoretical spectroscopic factor only depends on the nuclear structure, while the experimental spectroscopic factor is more complicated that it depends on the nuclear structure and the reaction mechanics. These two kinds of spectroscopic factor should be the same in principle.

1.1.2.1 Theoretical Spectroscopic Factor

The definition of the theoretical spectroscopic factor can be found in References [38] [26] [43] [44] [45] [46] [47]. A brief definition borrowed from the References [26] [43] [44] is presented below.

In a nucleon knockout reaction, a nucleon is removed from a nucleus $|A\rangle$ to produce nucleus $|B\rangle$ in state J_B. The Hamiltonian H_A of the nucleus A can be expressed as

$$H_A = \sum_i h_i + \sum_{i\neq j} R_{ij} = h_1 + H_B + R_{1B}, \qquad R_{1B} = \sum_{i>1,j>1} \left(R_{ij} = V_{ij} - U_i\right) \tag{1.1.5}$$

where h_i is the single-particle Hamiltonian, R_{ij} is the two-body residual interaction, h_1 is the single-particle Hamiltonian of the interested nucleon, H_B is the Hamiltonian of the nucleus B, and R_{1B} is the total two-body residual interaction between the nucleon and the nucleus B. The wavefunctions of the single-particle orbit $|nlj\rangle$ (where n is the principle quantum number, l is the orbital angular momentum, and j is the total angular momentum of an orbit) came from the mean field calculation. The relation between them can be expressed as

$$\begin{aligned} |A\rangle_{J_A} = |B+1\rangle &= \sum_{B'}\sum_{nlj} \beta_{nlj}(A,B')\left[|nlj\rangle|B'\rangle_{J_{B'}}\right]_{J_A} \\ &= \sum_{B'}\sum_{nlj} \beta_{nlj}(A,B')\left[a^\dagger_{nlj}|B'\rangle_{J_{B'}}\right]_{J_A}, \end{aligned} \tag{1.1.6}$$

where B' represents the various states of nucleus $|B\rangle$ in state $J_{B'}$, $[\ \ ]_{J_A}$ is the antisymmetric operator and vector coupling to the total spin J_A, the coefficient β is the spectroscopic amplitude, and the $a^\dagger_{nlj}$ is the creation operator of the orbit $|nlj\rangle$. The isospin was dropped for simplicity.

By applying $\langle B|$ from the left side of the equation (1.1.6)

$$\langle B|A\rangle = \widehat{|nlj\rangle} = \sum_{nlj} \beta_{nlj}(A,B)|nlj\rangle\,, \tag{1.1.7}$$

and the spectroscopic factor is the square of coefficient β_{nlj}, such that

$$S_{nlj}(A,B) = \left|\beta_{nlj}(A,B)\right|^2, \tag{1.1.8}$$

where the quasi-particle state $|\widehat{nlj}\rangle$ (or called overlap orbit) is not necessary orthogonal with each other and not equal a pure single-particle state $|nlj\rangle$, unless the off-diagonal terms of the residual interaction are zero. Because the off-diagonal terms create configuration mixing when diagonalizing the total Hamiltonian [equation (1.1.5)], then the spectroscopic factors are fragmented. Since a wavefunction must be normalized, therefore $\sum\left|\beta_{nlj}\right|^2 = 1$ and $\left|\beta_{nlj}\right|^2 > 0$, thus the value of the spectroscopic factor lays between 0 and 1.

A bra $\langle A|$ can act from the left side of the equation (1.1.6)

$$\left\langle A\middle|a^\dagger_{nlj}\middle|B'\right\rangle = \beta_{nlj}(A,B'). \tag{1.1.9}$$

The spectroscopic factor is also related to the norm of the square of the overlap of the wavefunction of two nuclei by a creation operator $a^\dagger_{nlj}$

$$S_{nlj}(A,B) = \left|\left\langle A\middle|a^\dagger_{nlj}\middle|B\right\rangle\right|^2. \tag{1.1.10}$$

Therefore, the spectroscopic factor also reflects the overlap/likeliness of $|B\rangle$ nucleus pluses one nucleon with $|A\rangle$ nucleus.

1.1.2.2 Spectroscopic Strength and Occupation Number

The spectroscopic strength of an orbit is the sum of the spectroscopic factors of that orbit. The sum rule for the spectroscopic factors over all states of $|B\rangle$, in which a nucleon is knocked out from an orbit $|nlj\rangle$, is an average number of occupancy of the orbit $|nlj\rangle$

$$n_{sh}\sum_{J_B} S_{nlj}\left(A,B_{J_B}\right) = n_{sh}\sum_{J_B}\left|\beta_{nlj}\left(A,B_{J_B}\right)\right|^2 = n_{nlj}(A), \tag{1.1.11}$$

where n_{sh} is the shell limit (IPM limit) or the number of nucleon in the orbit $|nlj\rangle$ under IPM, $n_{nlj}(A)$ is called the occupation number. The shell limit is equal to $2j+1$ for a closed shell or equal to the maximum number of particles for an open shell. For example, the proton shell-limit of the $1d_{5/2}$ orbit in ^{23}F is 1 and that is 6 in ^{40}Ca. The fraction of occupancy is the ratio between the occupation number and the shell limit $n_{sh} \leq (2j+1)$. It is also as same as the spectroscopic strength. Note that equation (1.1.11) does not hold for transfer transition [43]. Figure 1-7 shows the occupation number calculated using the shell model calculation on the sd-shell [38]. Because of the nucleon-nucleon correlation, the occupancy of each sub-shell is not 100%, but the sum for all sub-shells is always equal to the shell limit.

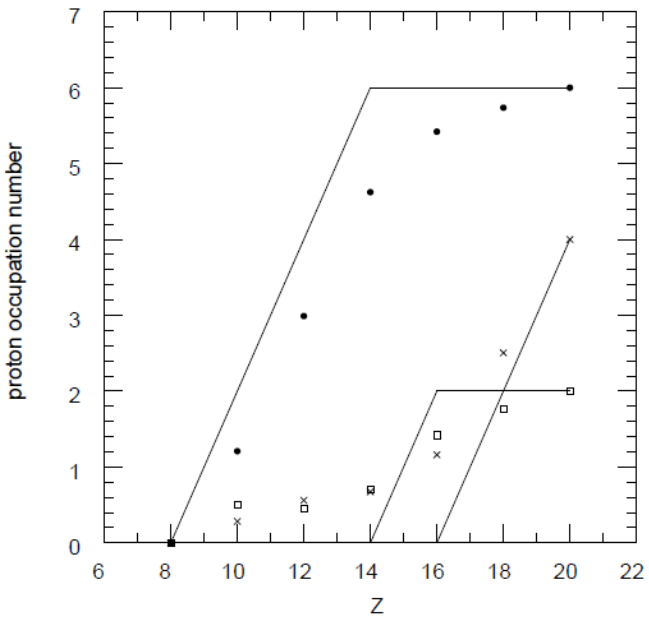

Figure 1-7 – The theoretical proton occupation number.
It was calculated for N=Z nuclei using the shell model. The filled circles are $1d_{5/2}$ orbit, the open squares are $2s_{1/2}$ orbit, and the crosses are $1d_{3/2}$ orbit. The lines show the shell limit. This figure is taken from Reference [38].

In statistical mechanics, the density of states of a non-interactive fermion system follows the Fermi-Dirac distribution. In the IPM model, each nucleon is moving under the mean field without nucleon-nucleon correlation. The fraction of occupancy in a function of kinetic energy should have a shape edge on the Fermi surface. Because of the nucleon-nucleon correlation (or more precisely, the long-range correlation [48]), the Fermi surface diffused. The short-range correlation due to the hard repulsive core reduces the fraction of occupancy below the Fermi surface and extends the high-energy tail. A typical shape of the distribution is shown in Figure 1-8 [49]. In the figure, the FG stands for the non-correlated Fermi-gas, which is the IPM model. The SRC and LRC stand for the short-range and long-range correlation respectively. The "corr. cont." stands for the correlated continuum. $n(E)$ is the fraction of occupancy in function of energy E. $n_c(E)$ is the fraction of occupancy in continuum. z is the quasi-particle strength of nuclear matter, which is similar to the fraction of occupancy. E_F is the energy of the Fermi surface. The blue data points are located at the single-particle energies of difference orbits of ^{208}Pb. The fractions of occupancy for ^{16}O, ^{40}Ca, ^{48}Ca, and ^{90}Zr also show similar distribution [24]. The SRC is supposed to be localized and independent of nuclear system. Therefore, we may expect a similar fraction of occupancy appears on radioactive nuclei.

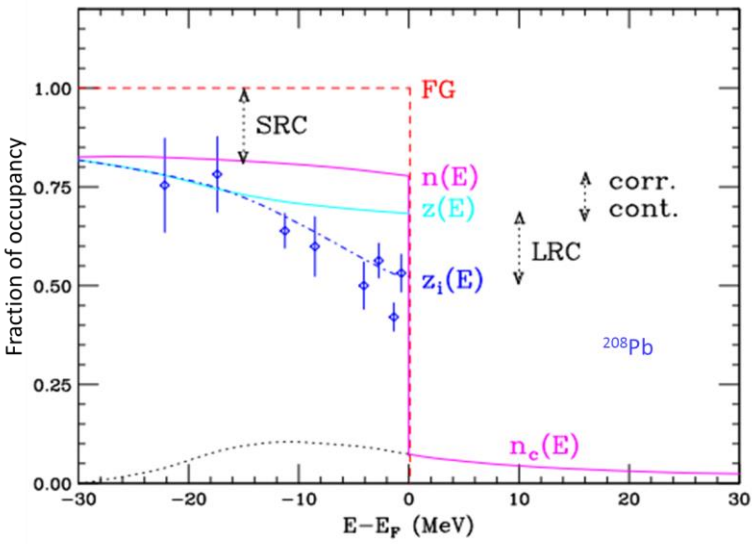

Figure 1-8 – The fraction of occupancy in a function of Fermi energy of ^{208}Pb [49]. See main text for detail.

1.1.2.3 Experimental Spectroscopic Factor

The experimental spectroscopic factor S_{exp} is deduced from dividing the (differential) cross section by a theoretical value, in which a unity spectroscopic factor (single-particle orbit) and proper treatment of the reaction mechanism are assumed, so that

$$\left(\frac{d\sigma}{d\Omega}\right)_{exp} = S_{exp} \times \left(\frac{d\sigma}{d\Omega}\right)_{DWIA}, \tag{1.1.12}$$

where $d\sigma/d\Omega$ is the differential cross section, DWIA is an aberration for the distorted wave impulse approximation [50]. The skeleton of the DWIA calculation will be shown in Section 1.2.4.

The correctness of the theoretical calculation relies on the assumed reaction mechanism. We used the DWIA reaction model for the reaction calculation [50]. This is a modification of a distorted wave Born approximation for a knockout reaction at medium and high incident energy. The impulse approximation was assumed that the major reaction channel is the quasi-free proton-proton elastic scattering and other reaction channels can be neglected [51].

1.1.2.4 Reduction Factors

The off-diagonal terms of the residual Hamiltonian lead to states mixing [1] [38] [48] [52]. The mixing spreads the spectroscopic factors of a state/nucleon to higher excitation energies, and then the sum of the spectroscopic factors up to the measurement limit could be smaller than the shell limit. The experimental sum of the spectroscopic factors can be compared with the shell limit, it tells us the deviation from the IPM and reveals the existence of the residual interaction. A comparison to the shell model calculation with certain interaction can help to study the detail of the nuclear force. The deviation

from unity implied an incomplete treatment on the shell model calculation [38] [53] or on the reaction models. Therefore, there are two kinds of reduction factors. One compares to the shell limit

$$R = \frac{S_{exp}}{n_{sh}}, \tag{1.1.13}$$

and the other one compares to theoretical spectroscopic factor [53]

$$R_S = \frac{\sigma_{exp}}{\sigma_{th} S_{th}} = \frac{S_{exp}}{S_{th}}, \tag{1.1.14}$$

where σ and S are the cross section and the spectroscopic factor respectively. The subscripts exp and th mean the experimental and the theoretical respectively.

The reduction factors R for the ground state orbit of ^{16}O, ^{40}Ca, and ^{208}Pb are between 0.6~0.9 [54] [55] [56] [57]. Figure 1-9 is taken from Reference [58], which compared reduction factors from (e,e′p) and (d,^{3}He) reactions for the ground state of ^{12}C, ^{16}O, ^{31}P, ^{40}Ca, ^{51}V, ^{90}Zr, ^{142}Nd, ^{206}Pb, and ^{208}Pb. The reduction is mainly due to the correlation that virtually excited nucleons into highly excited states [38].

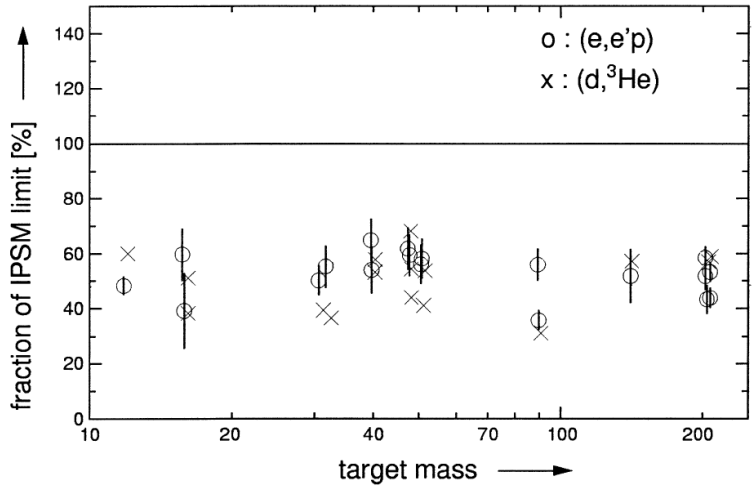

Figure 1-9 – The proton reduction factor R deduced from (e,e′p) and (d,^{3}He) reaction of difference nuclei [58].

Figure 1-10 shows another study by A. Gade *et al.* on the other reduction factor R_S. A relationship between R_S and a "boundedness" $\Delta S = \eta(S_n - S_p)$, where S_n and S_p are the separation energies of neutron and proton respectively, is found. Here, η is +1 for neutron removal and -1 for proton removal [59]. The study used the shell model calculation with difference interactions for the theoretical spectroscopic factor S_{th} and the Eikonal theory for the theoretical cross-section σ_{th}. The author stated that the relationship is originated from the nuclear structure that deeply bound states are more correlated with other nucleons, and then the spectroscopic factors reduced. The small reduction factor is interpreted as correlation effects that are beyond the effective interactions used in the shell model calculation. However, several experiments comparing the transfer and knockout reactions suggest the relationship is originated from reaction mechanism [60] [61].

By comparing Figure 1-9 and Figure 1-10, the results on the stable isotopes shows that the spectroscopic factors of shell model calculation are as same as that of the IPM. This is because the true wavefunction should include the highly virtual excited states ($> 10\hbar\omega$) due to the short-ranged interaction, but the shell model calculation ignored that and renormalized the wavefunction. Therefore, a quenching factor of ~0.7 should be multiplied on the spectroscopic factor of the shell model calculation.

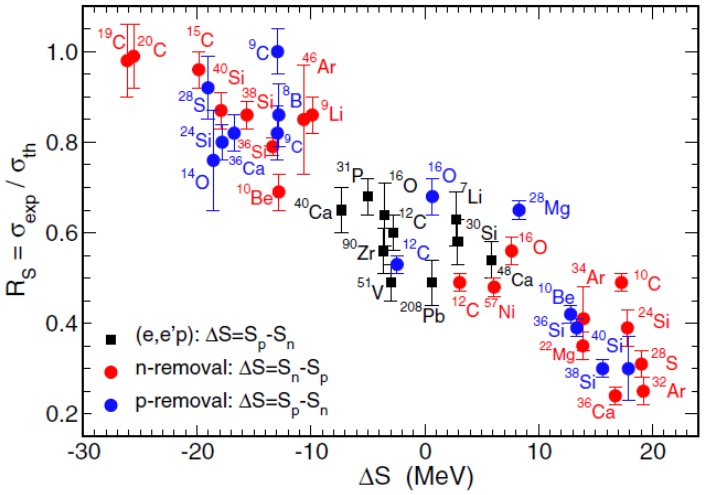

Figure 1-10 – The reduction faction R_S of different nuclei [59]. We call this figure as the Gade plot.

The reduction of the spectroscopic factors of oxygen isotopes was studied theoretically by included coupling-to-continuum degree of freedom [62]. The result is shown in Figure 1-11. The study stated that for the deeply bound protons near Fermi surface, the reduction is mainly due to many-body correlations arising from the coupling to the scattering continuum when the neutron scattering states are treated properly. The study also stated that the spectroscopic factors of the $1p_{1/2}$ proton of oxygen isotopes depend on the tail of neutron wavefunction.

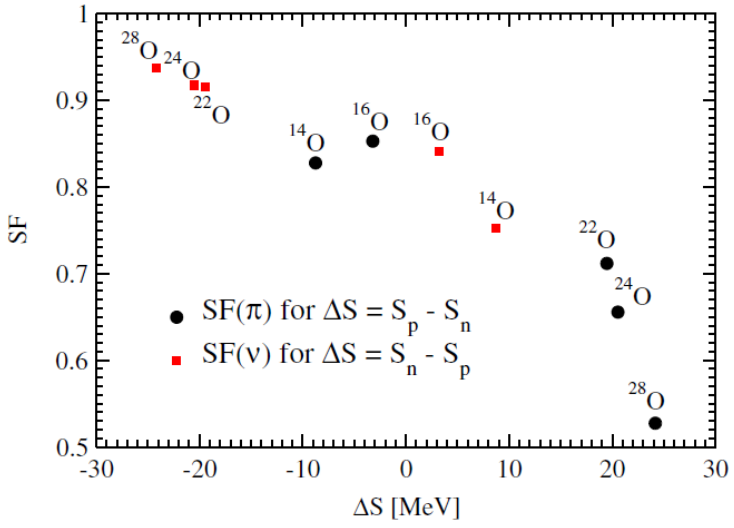

Figure 1-11 – The theoretical spectroscopic factors of valance nucleon of oxygen isotopes [62]. Note that the asymmetry energies were theoretical values.

A short summary, the reduction factors of nuclei near stable valley are approximately 0.7. The Gade plot (Figure 1-10) shows a relationship between reduction factors and ΔS [53] [59]. However, the plot did not agree with the results from some transfer reactions [61] [60]. Also the plot can be reproduced using different theoretical calculations by including more nucleon-nucleon correlation [62] or reconsidering the radial overlap of the wavefunctions [63]. Therefore, the origin of the relationship in the Gade plot is still unclear. It could be due to the nucleon-nucleon correlation (as the author's claim), the calculation of the theoretical reaction cross-section, or the treatment of the shell model calculation.

Although the reduction factors of ~0.7 are common for stable nuclei, the IPM is applied well on nuclei that are made of a doubly close shell core plus or minus one nucleon. Therefore, the spectroscopic factors for those nuclei are close to unity. An example of such nucleus with single-particle ground state neutron is ^{17}O ($S_{1d_{5/2}} = 0.8$) [64] ($S_{1d_{5/2}} = 1.0$) [65]. It consists of a double magic ^{16}O core plus a neutron on the $1d_{5/2}$ orbit. Also, the neutron is weakly bound so that the virtual excitation is small.

1.1.3 Nuclear Forces

In the beginning of section 1.1, we mentioned that the spin-orbital splitting plays an important role in determining the nuclear shell structure. The splitting can be approximated using an effective mean field spin-orbit coupling. The form of the mean field spin-orbit coupling can be understood relatively simply and classically. When a nucleon is moving near the center of a nucleus, it is surrounded by other nucleons in all direction and then not sensitive to the orbital angular momentum, as the nuclear force is almost isotropic. But a surface nucleon senses an uneven force that creates an orbital angular momentum. Thus, the mean field spin-orbit coupling is strong on the nuclear surface and weak at the interior. The effective mean field spin-orbit coupling V_{ls} is proportional to the derivative of mean field U of a nucleus. It takes the form

$$V_{ls} \propto \frac{dU(r)}{dr}(l \cdot s), \qquad l \cdot s = \begin{cases} \frac{l}{2}, & j = l + s \\ -\frac{l+1}{2}, & j = l - s \end{cases}. \tag{1.1.15}$$

Here, the small letter l and s are the orbital angular momentum and the intrinsic spin of a nucleon respectively. A Woods-Saxon potential is a good approximation of the effective mean field. The gradient of this potential is strong on the surface and weak in the interior. Neutron-rich nuclei have more diffusive surface because of excessive neutrons, and then the strength of the coupling is reduced [66] [67] [68].

The mean field spin-orbit coupling is originated from microscopic two-body or many-body forces. The primary contribution is the nucleon-nucleon spin-orbit coupling. This microscopic nucleon-nucleon

spin-orbit coupling involves only two nucleons and its strength has been measured from free nucleon-nucleon scattering. It is surprised that the nucleon-nucleon spin-orbit coupling only contributes approximately half of the total mean field spin-orbit coupling [31].

Another important component of the spin-orbit coupling is the tensor force. The tensor force is the main reason that the deuteron is more tightly bound than other proton-proton and neutron-neutron systems. Therefore, the tensor force is expected to play an important role in the nuclear structure. The microscopic origin of the tensor force is the spin-spin coupling as nucleon carries intrinsic spin. The tensor force is mediated by π or ρ meson [32], and it takes the form

$$V_T \propto \frac{1}{r^3}\left(\overrightarrow{\sigma_1}\cdot\overrightarrow{\sigma_2} - 3(\overrightarrow{\sigma_1}\cdot\hat{r})(\overrightarrow{\sigma_2}\cdot\hat{r})\right)(\overrightarrow{\tau_1}\cdot\overrightarrow{\tau_2}), \tag{1.1.16}$$

where the $\vec{\tau}$ is the isospin vector, $\vec{\sigma}$ is the spin vector, and $\hat{r}$ is the unit vector of relative position between two spins with length r. The effect of the tensor force is repulsive when two parallel spins aligned and attractive when they are anti-aligned. The situation analogy to two classical dipole magnets. The tensor force can be also expressed as [20]

$$V_T = f(r)([\overrightarrow{\sigma_1}\,\overrightarrow{\sigma_2}]^2\cdot Y^2)(\overrightarrow{\tau_1}\cdot\overrightarrow{\tau_2}), \tag{1.1.17}$$

where $f(r)$ is the radial component, Y^2 is a spherical harmonic of rank 2, and $[\overrightarrow{\sigma_1}\,\overrightarrow{\sigma_2}]^2$ represents the spins coupled to form a rank 2 tensor. Since a nucleon has intrinsic spin of 1/2, two nucleons can couple to spin-1 or spin-0 pair. Only the spin-1 pair is able to form a rank 2 tensor. Therefore, the two nucleons must have a parallel spin for the tensor force to act upon them. The mechanism of the tensor force is illustrated in Figure 1-12. A more detailed explanation can be found on Reference [16].

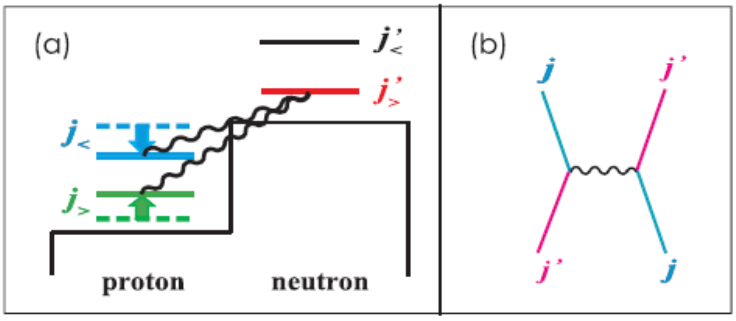

Figure 1-12 – Mechanism of the tensor force.
(a) The interaction between a proton in $j_{>,<} = l \pm 1/2$ and a neutron in $j'_> = l' + 1/2$ of the tensor force. (b) The exchange processes contributing to the monopole interaction of the tensor force [20].

Other component is the three-nucleon force. As the name suggests, this is a three-body force. It is different from the nucleon-nucleon spin-orbit coupling and the tensor force, which are two-body forces. Three nucleons involved as a nucleon excitation to Δ(1232) that connects others two nucleons when de-excited. The three-nucleon force was introduced from the analyzing power puzzle to explain the (N,d)

scattering data [42]. Analyzing power is the ability to produce left-right asymmetric differential cross section. The analyzing power was unable to be explained by the two-body forces and it is called the analyzing power puzzle.

The three-nucleon force could be the reason for the position of the neutron dripline of oxygen, in which the last bound isotope is at $N = 16$ [18]. There are others theoretical studies on the effect of the three-nucleon force [69] [70]. Figure 1-13 shows the ground state energies of nitrogen and fluorine isotopes using a mean field calculation with two-body and three-body interactions. The results of three-body interaction have better agreement with the experimental ground state energies.

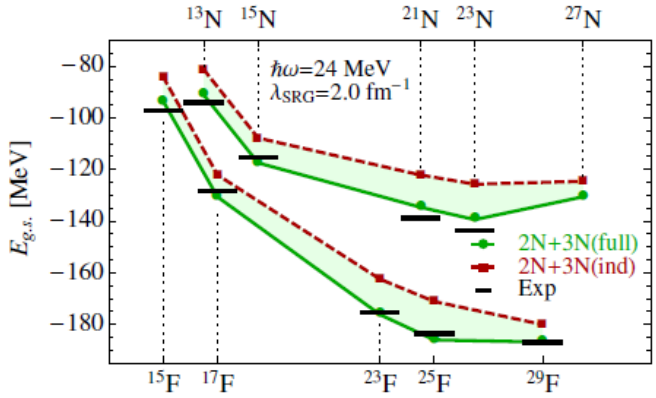

Figure 1-13 – The ground state energies of nitrogen and fluorine isotopes calculated using the three-body force [70].

In a short summary, we have briefly explained the effects and the roles of each component of the spin-orbit coupling: the nucleon-nucleon spin-orbit coupling, the tensor force, and the three-nucleon force. The first two components can be explained using one-meson exchange from chiral effect field theory [32]. This theory is derived from the quantum chromodynamics (QCD) for the low energy region. The spin-orbit coupling and the central force (a force only depends on the relative position) come from the σ and ω mesons. The spin-isospin interaction and the tensor force come from the π and ρ mesons. However, the contribution of each term to the mean field spin-orbit coupling is still unknown experimentally. Ando and Bando [30], Heghes and Couteur [29], and Pieper and Pandharipande [31] have estimated the contribution of each component theoretically. They all reached the similar conclusion that the nucleon-nucleon spin-orbit coupling contributes about 50%, the tensor force contributes about 25%, and the other component contributes the rest 25% (see Figure 1-14). Note that this partition is for the stable nuclei. Two questions naturally arise: 1) What is the exact partition? 2) Does this partition change toward the neutron dripline (as there are many extraordinary discoveries toward the neutron dripline)?

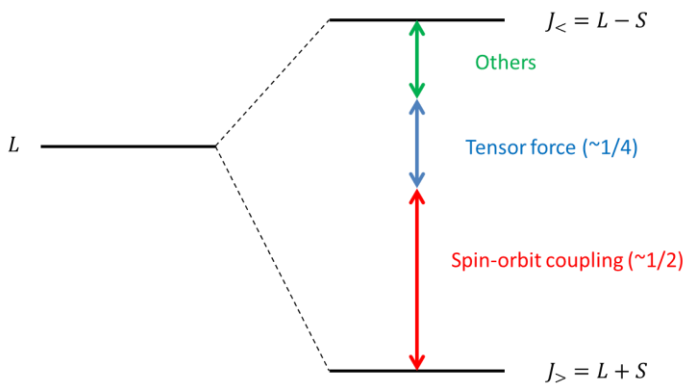

Figure 1-14 – Contribution to spin-orbit splitting from different component [29] [30] [31].

1.1.4 Proton Shell Structure of Fluorine Isotopes

Fluorine isotopes are interesting place to study for three primary reasons: 1) the sd-shell proton should be in a single-particle orbit because of the $Z = 8$ magicity, large shell gap between $1d_{5/2}$ and $1p_{1/2}$ orbits, and week proton-neutron correlation energy as we will see later, so that it serves as a simple probe of the excessive neutrons, 2) the isotopes chain span the new magic number $N = 16$ [13] [14] and the island of inversion, so that a lot of exotic phenomena can be studied, and 3) fluorine has a long extended neutron dripline $N = 22$ [71]. Fluorine isotopes can be thought as if a ^{16}O + $1d_{5/2}$ proton + sd-shell neutrons system, such that the ^{16}O serves as a non-interactive core because the double magicity of ^{16}O. It is amazing that a single proton on an sd-shell can hold twelve sd-shell and two pf-shell neutrons on top of a ^{16}O core!

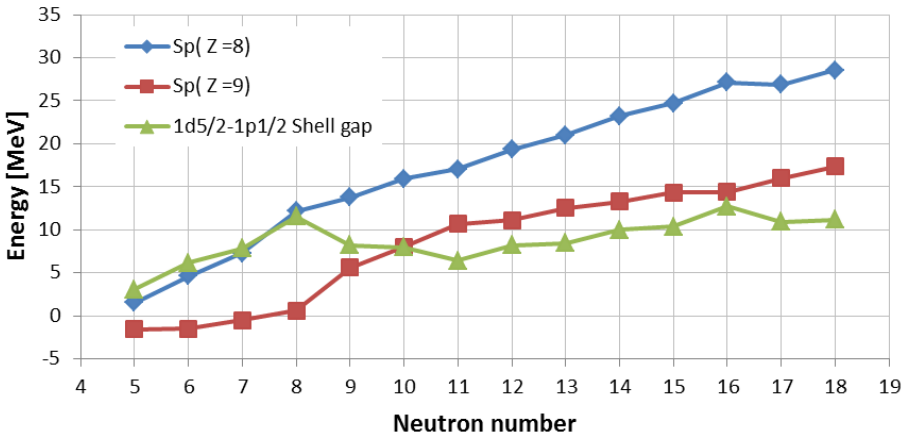

Figure 1-15 – The experimental data of proton separation energy of fluorine and oxygen isotopes [72]. The separation energy is same as the single-particle energy of oxygen isotopes near Fermi surface. The difference between the separation energy is the shell gap between $1p_{1/2}$ and $1d_{5/2}$ orbits.

The experimental shell gap between the $1p_{1/2}$ and $1d_{5/2}$ orbits is deduced from the binding energy [72] and is shown in Figure 1-15. The average shell gap is ~10 MeV. There are peaks at $N = 8$ and $N = 16$. The $N = 8$ peak is caused by the decrease of the proton separation energy of ^{17}F and the slightly increase of the proton separation energy of ^{16}O. This peak is expected as 8 is a magic number. The $1d_{5/2}$

proton in ^{18}F becomes more tightly bound by adding a $1d_{5/2}$ neutron. The separation energies of the $1p_{1/2}$ proton of oxygen almost increase linearly with neutron number. The peak at $N = 16$ is interesting as it provides supporting evidence for the new magic number [13] [14].

The nucleon-nucleon correlation energy can be extracted using the binding energy or separation energy

$$\Delta pn(Z,N) = S_p(Z,N) + S_n(Z,N) - S_{pn}(Z,N), \qquad (1.1.18)$$

where $S_{pn}(Z,N)$ is the separation energy of a proton and a neutron at the same time of a nucleus (Z,N) with Z protons and N neutrons. The equation can be understood by considering the Hamiltonians of three nuclei (Z,N), $(Z-1,N)$, and $(Z,N-1)$. The Hamiltonian of $(Z-1,N)$ nucleus is $H + h_n + V_n$, where H is the Hamiltonian of $(Z-1,N-1)$ nucleus, h_n is the neutron Hamiltonian and V_n is the residual interaction energy between the $(Z-1,N-1)$ nucleus and the neutron. Similarly, the Hamiltonian of the $(Z,N-1)$ nucleus is $H + h_p + V_p$, and that of the (Z,N) nucleus is $H + h_n + h_p + V_n + V_p + V_{np}$. Here, V_{np} is the residual interaction between the proton and neutron. The proton-neutron separation energy is the terms $h_n + h_p + V_n + V_p + V_{np}$. Therefore, the proton-neutron correlation energy is equation (1.1.18). The neutron-neutron correlation energy can be extracted by replacing proton with neutron in the above equation.

The correlation energy of fluorine isotopes is shown in Figure 1-16. Because fluorine has only one proton on the $1d_{5/2}$ orbit, the proton-proton correlation energy is not meaningful. The proton-neutron correlation energy with odd neutron numbers is always higher than those with even neutron numbers. It is interesting that with ~5 MeV extract correlation energy, ^{18}F is still not a stable isotope until one more neutron is added. The neutron-neutron correlation energies of odd neutron numbers are all negative, because removing two neutrons requires breaking a pair. It is also interesting that the neutron-neutron and proton-neutron correlation energies of even-neutron number suddenly drop at $N = 16$; this may be related to the new magic number $N = 16$.

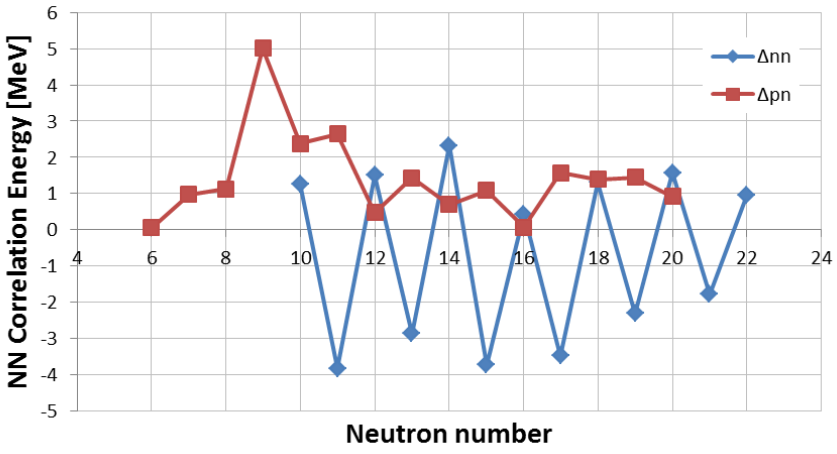

Figure 1-16 – The nucleon-nucleon (NN) correlation energy of fluorine isotopes.

The experimental data of proton knockout reaction are limited for fluorine isotopes because it has only one stable isotope [40], and it is difficult to access exotic nuclei with sufficient intensity for a successful study in the past. A ^{19}F(e,e′p) reaction was performed but it does not discuss neither single-particle state nor spectroscopic properties [73]. A ^{19}F(p,2p) knockout reaction reported only the 2s-shell proton was observed [74]. A proton knockout reaction on unstable fluorine isotopes using a ^{12}C target was performed a decade ago by M. Thoennessen *et al*. [75]. The study focused on the valance orbit of exotic fluorine isotopes using ^{12}C(^{24,25,26}F,^{23,24,25}O) reactions at 50*A* MeV. The exclusive scattering experiment found that the spectroscopic factors for ^{12}C(^{24}F,^{23}O), ^{12}C(^{25}F,^{24}O), and ^{12}C(^{26}F,^{25}O) are 0.9 ± 0.1, 0.49 ± 0.08, and 0.5 ± 0.2 respectively. Besides the valance state, the $1p_{1/2}$ and $1p_{3/2}$ orbits was stated (Figure 1-3) in Reference [23], but no reference was given.

The only stable isotope of fluorine is ^{19}F, it has low-laying negative parity excited states, which indicate a strong state mixing. According to the normal shell ordering, the $1d_{5/2}$ state is the lowest energy state in the sd-shell. The sd-shell proton of the ^{19}F should be in the $1d_{5/2}$ state and the two neutrons in the $1d_{5/2}$ state couple to a total spin zero. Thus, the ground state spin of ^{19}F should be 5/2. In fact, its ground state spin-parity is $1/2^+$ instead of $5/2^+$. The low laying negative parity excited states and abnormal ground state spin suggest that ^{19}F is deformed [76] or the $2s_{1/2}$ state is more tightly bound than the $1d_{5/2}$ state [74].

A common way to study the proton valance state and excited states of fluorine is using the proton transfer reaction on the oxygen isotopes ^{16,17,18}O, such as the (d,n), (^{3}He,d), and (α,t) reactions. The proton excited state of ^{19}F was studied using a ^{18}O(d,n)^{19}F reaction at 25 MeV and the spectroscopic factors of the $2s_{1/2}$ of ^{19}F up to 14 MeV was reported to be 0.72 ± 0.41 [77]. A ^{18}O(^{3}He,d)^{19}F reaction reported that the spectroscopic factor of the valance $2s_{1/2}$ proton at ground state is 0.42 [78]. The proton states on the sd-shell were studied by an (α, t) reaction on ^{16,17,18}O at 65 MeV [79]. The experimental cross-sections were compared with an exact-finite-range distorted wave Born approximation (DWBA) calculation. The spectroscopic factors of the valance proton of ^{17,18,19}F up to 14 MeV are 1.3, 1.38, and 1.13 respectively. The spectroscopic strength of the proton valance state of even-neutron fluorine isotopes are shown in Figure 1-17.

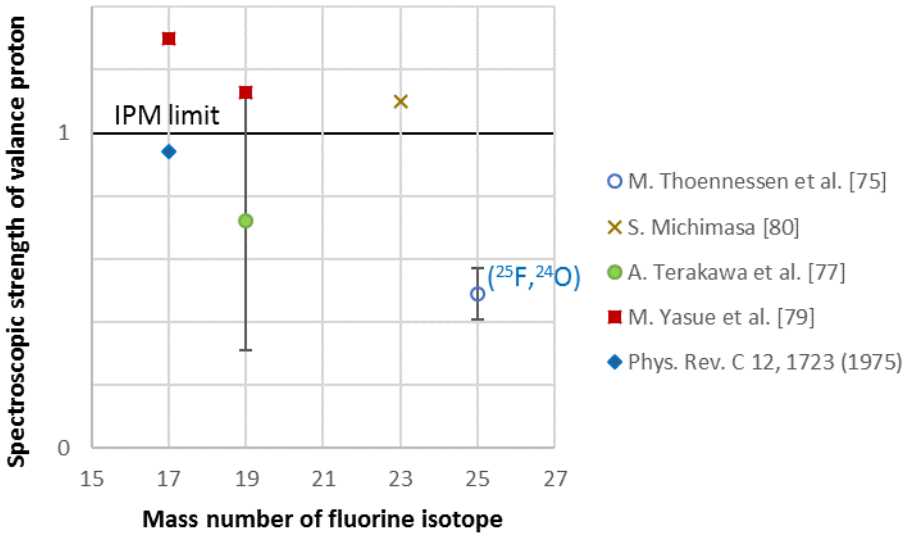

Figure 1-17 – The spectroscopic strength of the valance proton of ground state of even-neutron fluorine isotopes [75] [77] [79] [80].
The solid dots are full strength of the valance proton. The hollow dot is partial strength of the valance proton. The cross is the result from S. Michimasa [80]. Note that the data were collected under different reactions and energies.

The excited states or the valance state of unstable fluorine isotopes were studies using either β^- decay from unstable oxygen isotopes [81] or proton transfer reactions. S. Michimasa *et al.* studied the ^{23}F using γ-ray spectroscopy via a proton transfer reaction from ^{4}He to the ^{22}O [82], the study showed pure proton excited states at 2.27 MeV ($j^\pi = 1/2^+$) and 4.06 MeV ($J^\pi = 3/2^+$) above the ground state. The spin-orbital splitting between the $1d_{3/2}$ and $1d_{5/2}$ orbits was found to be 4.06 MeV by assuming that there was no fragmentation for those states. The experimental cross sections were compared with the DWBA calculation, and the spectroscopic strength of the ground state ($J = 5/2$) and the 4.06 MeV ($J = 3/2$) state were found to be 6.6 and 1.2 respectively [80]. The experimental excited levels were compared using shell-model calculation with USDB interaction [83]. They also found that the shell gap energy of the proton $1d_{5/2}$ and $1d_{3/2}$ orbits have to be increased by 1.2 MeV to reproduce the experimental spin-orbit splitting. The left figure of Figure 1-18 shows the evolution of the proton $1d_{5/2}$ state and $2s_{1/2}$ state with respect to neutron numbers [81]. The right figure of Figure 1-18 shows the level scheme on ^{25}F obtained by Zs. Vajta *et al.* [84].

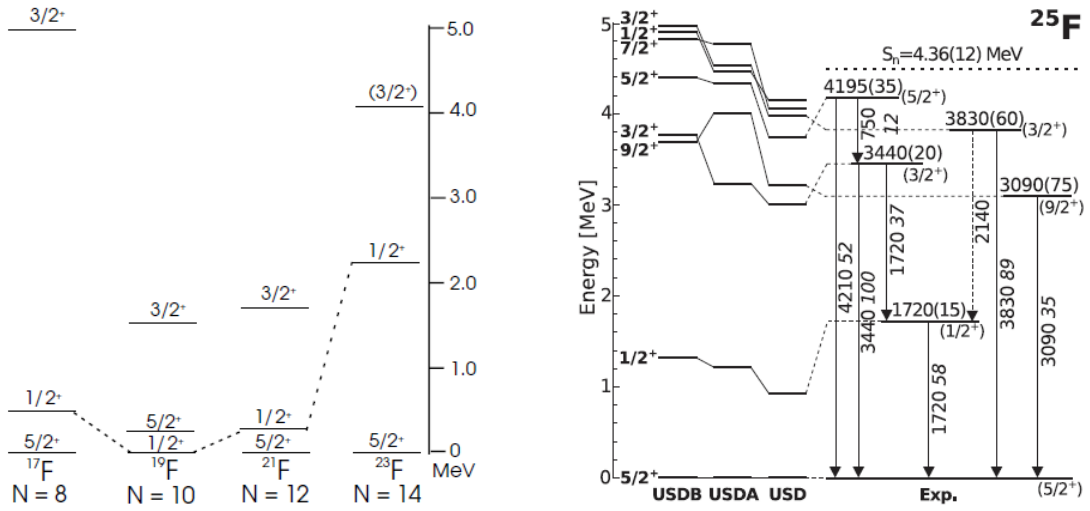

Figure 1-18 – The experimental proton unoccupied shell structure of fluorine isotopes [81] [84].

1.1.5 Prediction of the Shell Model Calculation

From the change of the neutron dripline between oxygen and fluorine, we could expect the sd-shell proton affects the sd-shell neutrons and changes the neutron shell structure. In a simplest model, assuming the sd-shell proton is always in the $1d_{5/2}$ orbit as the ground state spin of most even-neutron fluorine isotopes are 5/2, the wavefunction of fluorine can be written as a coupling between the $1d_{5/2}$ proton $|\pi 1d_{5/2}\rangle$, the sd-shell neutrons $|vsd\rangle$, and the inert ^{16}O core $|^{16}\mathrm{O}\rangle$, such that

$$|\mathrm{F}\rangle_{J_F} = \left[\left|\pi 1d_{\frac{5}{2}}\right\rangle |vsd\rangle \left|^{16}\mathrm{O}\right\rangle\right]_{J_F} = \left[\left|\pi 1d_{\frac{5}{2}}\right\rangle |\mathrm{O}_{bound}\rangle\right]_{J_F}. \qquad (1.1.19)$$

Because the neutron shell changed from oxygen to fluorine, the wavefunction of the bound oxygen is not as same as that of the free oxygen, so that the overlap of the wavefunctions between the ground state oxygen and fluorine is not 100%. Also, the bound oxygen wavefunction has to be expressed from many excited state of oxygen, and then the quasi-proton state should be fragmented.

We used the shell model calculation to investigate the shell structure of ^{22,24}O and ^{23,25}F with OXBASH [85]. The calculations were carried out in isospin formalism in the psd model space with the SFO Hamiltonian [86]. Sixty wavefunctions were calculated up to $2\hbar\omega$ excitation, so that the maximum excitation energy was roughly 22 MeV. The SFO Hamiltonian was made to give good predictions on the excitation energy and the B(GT) value among the p-shell exotic light nuclei. The calculation shows that the p-shell is always filled in the ground state of fluorine and oxygen. We assumed that the sd-shell proton is always in $1d_{5/2}$ shell, because the occupation numbers of (^{23}F,^{22}O) and (^{25}F,^{24}O) are 0.9. Thus, we can extract the neutron configuration even in the isospin formalism.

Since the p-shell is always filled in the ground state, we also use different model spaces and interactions to explore the model space and interactions dependency. The sd-shell model space with the USDB [83] interaction and the sdpf-shell model space with the SDPF-MU [87] interaction are used. The probabilities of different configurations of the ground state of ^{22,24}O and ^{23,25}F from the shell model calculation are shown in Table 1-2 and Table 1-3. The calculation of the ground state of ^{16,22}O and ^{15,21}N are also done and the results are shown in Table 1-4.

Table 1-2 – Neutron shell configurations of ^{23}F and ^{22}O from the shell model calculation. The number represents the number of neutron in each orbit. For example, "425130" means 4 neutrons in $1p_{3/2}$, 2 neutrons in $1p_{1/2}$, 5 neutrons in $1d_{5/2}$, 1 neutron in $2s_{1/2}$, 3 neutrons in $1d_{3/2}$, and 0 neutron in $1f_{7/2}$. SF stands for spectroscopic factor.

Neutron	SFO		USDB		SDPF-MU	
Configuration	^{23}F [%]	^{22}O [%]	^{23}F [%]	^{22}O [%]	^{23}F [%]	^{22}O [%]
42420	45.14	66.32	12.57	13.72	14.46	14.44
42321	12.56	3.40	2.45	–	2.32	–
42222	9.65	7.97	1.57	1.18	2.78	1.90
42510	9.20	–	8.74	–	5.15	–
42600	7.37	10.01	56.92	75.01	47.04	66.57
42411	4.32	1.14	4.95	3.31	3.08	1.55
42402	3.53	2.55	6.56	5.9	10.50	9.04
42330	3.12	–	–	–	–	–
42312	2.28	–	–	–	–	–
42501	1.13	–	4.76	–	3.46	–
424002	–	–	–	–	1.99	1.97
SF	0.62 (0 MeV, 0^+)		0.92 (0 MeV, 0^+)		0.89 (0 MeV, 0^+)	
	0.30 (1.9 MeV, 2^+)		0.16 (3.2 MeV, 2^+)		0.11 (3.6 MeV, 2^+)	

Table 1-3 – Neutron shell configurations of ^{25}F and ^{24}O from the shell model calculation.

Neutron	SFO		USDB		SDPF-MU	
Configuration	^{25}F [%]	^{24}O [%]	^{25}F [%]	^{24}O [%]	^{25}F [%]	^{24}O [%]
42620	67.05	83.71	79.58	91.00	57.4	74.16
42422	15.85	10.50	7.62	6.25	11.47	9.53
42521	9.27	–	6.25	2.29	4.65	–
42611	1.82	–	–	–	–	–
42602	1.63	–	3.90	–	7.89	4.71
42512	1.54	–	–	–	–	–
424202	–	–	–	–	1.84	1.67
426002	–	–	–	–	2.37	2.16
SF	0.90 (0 MeV, 0^+)		1.01 (0 MeV, 0^+)		0.95 (0 MeV, 0^+)	

Table 1-4 – Neutron shell configurations of ^{16}O, ^{15}N, ^{22}O, and ^{21}N from the shell model calculation.

Neutron Configuration	SFO ^{16}O [%]	SFO ^{15}N [%]	Neutron Configuration	SFO ^{22}O [%]	SFO ^{21}N [%]
42000	81.80	85.18	42420	66.32	63.09
31101	5.57	4.24	42600	10.01	5.70
40200	4.15	2.50	42222	7.97	10.88
22101	2.20	2.39	42321	3.40	6.14
31200	2.05	1.70	42402	2.55	2.14
22200	1.27	1.25	42411	1.14	1.80
			32420	–	3.45
			32231	–	2.12
			32510	–	1.90
SF	0.95 (0 MeV, 0^+)			0.93 (0 MeV, 0^+)	

From the configuration, the neutron shell structure changes a lot from oxygen to fluorine, but not from nitrogen to oxygen. This indicates the $1d_{5/2}$ proton strongly affects the sd-shells neutrons. This is only possible if the proton interacts strongly with the neutrons.

The strong interaction explained the difference of the position of the neutron dripline between oxygen and fluorine. Figure 1-19 demonstrates the idea. In oxygen, the sd-shell neutrons are bound by the mean field of ^{16}O and themselves except the $1d_{3/2}$ orbit. However, in fluorine, the interaction between $\pi 1d_{5/2}$ and $\nu 1d_{3/2}$ lowers the energy of the $1d_{3/2}$ neutron orbit and the dripline extended. In fact, the isoscalar monopole energy [38] of the $\pi 1d_{5/2}$ and $\nu 1d_{3/2}$ of the SFO, USDB, and SDPF-MU interactions are -3.6 MeV, -3.7 MeV, and -3.2 MeV respectively, and the experimental neutron separation energy of ^{25}O is -0.78 MeV (unbound). Therefore, the $1d_{5/2}$ proton can make the $1d_{3/2}$ neutron bound theoretically. The experimental neutron separation energy of ^{26}F is 0.77 MeV.

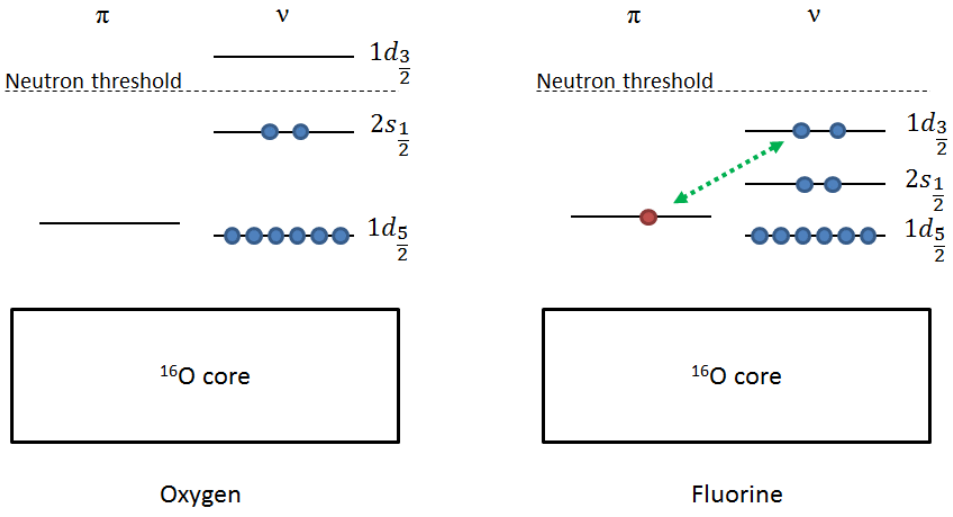

Figure 1-19 – Illustration of the change of the neutron shell caused by the $1d_{5/2}$ proton. See main text for explanation.

The levels of the excitation energy of ^{22,24}O and ^{23,25}F are shown in Figure 1-20, Figure 1-21, Figure 1-22 and Figure 1-23 respectively. The USDB interaction has better agreement with the experimental excitation-energy levels.

Figure 1-20 – Level scheme of ^{22}O.

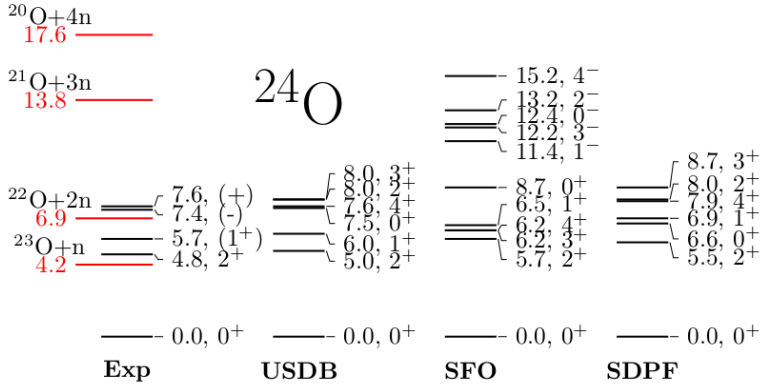

Figure 1-21 – Level scheme of ^{24}O.

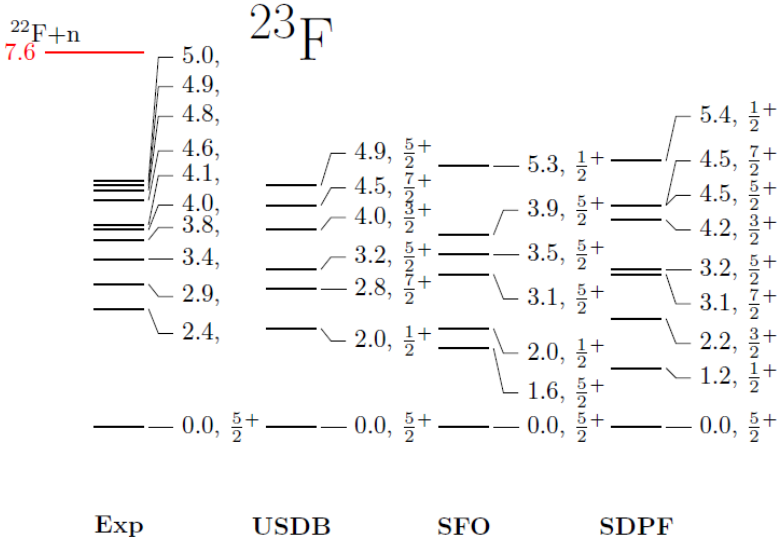

Figure 1-22 – Level scheme of ^{23}F.

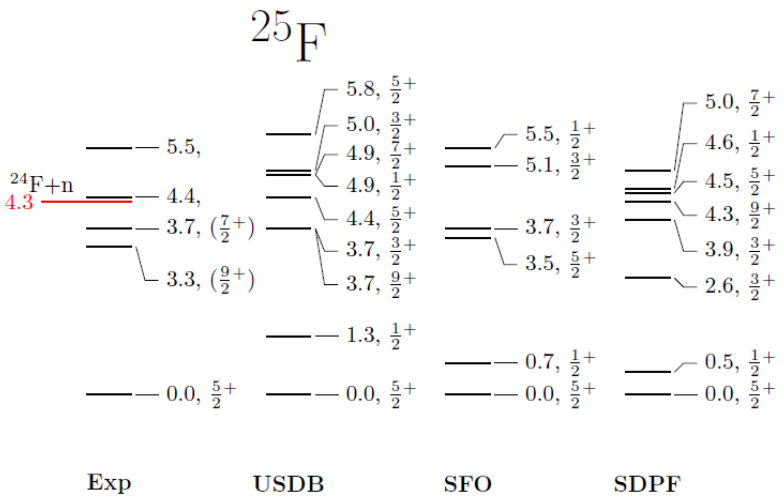

Figure 1-23 – Level scheme of ^{25}F.

A good shell model interaction should able to reproduce the experimental binding energy BE_{exp}. The binding energy of the core $BE(core)$ has to be added on the binding energy E, that calculated from the shell model interaction, to get the total binding energy $BE_{sh} = E + BE(core)$. The results show in Table 1-5 and Table 1-6. In the case of SFO interaction, the particle threshold (~ 20 MeV) should be subtracted. The calculated binding energies of ^{23,25}F are worse than that of ^{22,24}O from the experimental value. This is due to the Coulomb force is missing that the single-particle energies of proton and that of neutron are the same, but in fact, the neutron single-particle energies are always lower than that of protons because of the Coulomb interaction. The USDB interaction with Coulomb force has a very good agreement with experimental binding energy [83].

Table 1-5 - Binding energies [MeV] of ^{22}O and ^{23}F.

	SFO, BE(^{4}He) = 28.3 MeV		USDB, BE(^{16}O)=127.6 MeV		SDPF-MU	
	^{23}F	^{22}O	^{23}F	^{22}O	^{23}F	^{22}O
E	166.4	150.8	51.2	34.5	53.0	35.5
BE_{sh}	194.7	179.1	178.8	162.1	180.6	163.1
BE_{exp}	175.3	162.0	175.3	162.0	175.3	162.0
diff.	19.4	17.1	3.5	0.1	5.3	1.1

Table 1-6 – Binding energies [MeV] of ^{24}O and ^{25}F.

	SFO, BE(^{4}He) = 28.3 MeV		USDB, BE(^{16}O)=127.6 MeV		SDPF-MU	
	^{25}F	^{24}O	^{25}F	^{24}O	^{25}F	^{24}O
E	180.9	163.2	59.6	41.2	62.2	42.7
BE_{sh}	209.2	191.5	187.2	168.8	189.8	170.3
BE_{exp}	183.4	170.4	183.4	170.4	183.4	170.4
diff.	25.8	21.1	3.8	-1.6	6.4	-0.1

1.2 Experimental Method

Transfer, pick-up, and knockout reactions are used to study the single-particle properties and the nucleon-nucleon interaction [88]. Transfer reaction focuses on the unoccupied states [82] [55] and measures the emptiness of a state. Pick-up and knockout reactions focus on the occupied states. Both transfer and pick-up reactions require momentum matching, that has to be included in the reaction mechanism. Some pioneering works on the proton occupied states are done using (e,e′p) [57] [89], (p,2p) [74] [90] [91] [92] [56], (d,^{3}He) [93] and other single-proton knockout experiments [75]. One of the findings is the spectroscopic factors are around 20% to 40% smaller than the shell limit for most stable nuclei [58]. This indicates that the nucleon-nucleon correlation cannot be ignored and the independent particle model is merely a first order approximation.

To study the proton spectroscopy of ^{23,25}F, it is better to use a direct knockout reaction [25]. There are many types of knockout experiments designed to measure the single-particle energy of the orbital/bound protons. For example, (e,e′p) reaction uses the Coulomb force and only sensitive to proton. It is widely used on stable nuclei [57] [89]. (n,d) reaction is not easy because of many technical issues, like the small efficiency of neutrons detection. The (p,2p) reaction uses a proton to knockout an orbital proton [56] [74] [94] [90]. In this type of experiment, a spin-polarized proton can be used to distinguish the $J_> = l + s$ state and $J_< = l - s$ state by measuring the asymmetry in the differential cross section, for example ^{16}O(p,2p)^{15}N [95] [96]. There are also inverse knockout experiments on nuclear targets [93] [75].

The (p,2p) reaction in inverse kinematics at medium energy was chosen with four reasons: 1) ^{23}F and ^{25}F are unstable and short life time, they have to be produced by nuclear reaction and accelerated to relativistic speed to increase the life time in the laboratory frame, 2) proton is the cleanest probe that it will not be excited and the proton-proton bound state does not exist, and 3) medium energy proton should be able to probe the deeply bound states and ensure direct reaction. The impulse approximation is applicable at medium energy, so that the knockout reaction can be treated quasi-freely, and the reaction mechanism can be simplified [50] [51].

1.2.1 Knockout Reaction and Single-Particle State

A knockout reaction with the impulse approximation can be used to probe the single-particle state because the reaction matrix T is

$$T \propto \langle \phi_1 \phi_2 B | V_{NN} | A \phi_0 \rangle = \langle \phi_1 \phi_2 | V_{NN} | \langle B | A \rangle \phi_o \rangle = \langle \phi_1 \phi_2 | V_{NN} \sum_{nlj} \beta_{nlj}(A,B) | nlj \rangle | \phi_o \rangle, \quad (1.2.1)$$

where ϕ are proton distorted waves, V_{NN} is the nucleon-nucleon interaction, A and B are the wavefunctions of the nuclei A and B respectively. The second step used the impulse approximation that the reaction can be treated quasi-freely as proton-proton scattering. The last step of equation (1.2.1) used equation (1.1.7). The reaction matrix is proportional to the quasi-particle state; therefore, the reaction cross-section can be used to probe the spectroscopic factor. Note that the degree of freedom of the incident proton is the intrinsic spin only. If the incident particle contains many nucleons, the internal degree of freedom has to be considered, and the reaction matrix element is not only connected to the spectroscopic factor of nucleus A but also that of the incident particle because of the exchange terms in the incident channel that introduced from anti-symmetric requirement.

The reaction can be treated quasi-freely and be applied the impulse approximation because the incident energy is high enough [50]. The high incident energy implies short reaction time when compare with nucleon motion, so that the nucleons can be treated as stationary. For a 300 MeV proton, the speed is 2 fm per 10^{-11} ps. The diameter of ^{23}F is about 7 fm, therefore the proton travelling time inside the nucleus is at most 4×10^{-11} ps. The Fermi energy of a nucleon is ~35 MeV, or 1 fm per 130×10^{-11}ps. Within the proton travelling time, the nucleons are moved 0.03 fm, therefore the nucleon motion is almost freeze.

High incident energy also implies a short de Broglie wavelength, which is 1.5 fm for 300 MeV proton. In such a short wavelength and negligible nucleon motion, the incident proton can only interact with one or two nucleon and the rest nucleons does not participate in the reaction. Because of this, the reaction is mostly on the nuclear surface as the incident proton will be scattered. The energy-time uncertainty also allows an energy fluctuation larger than the binding energy, so that the energy conservation can be neglected during the very short reaction time [51]. The reaction time is at most 4×10^{-11} ps, and the energy fluctuation is ~30 MeV, which is larger than the separation energy. Since the binding energy was neglected during the time of reaction, the reaction can be treated as free proton-proton scattering that the calculation of the reaction matrix only has kinematics and phase-space components. The reaction is not exactly free but quasi-free because the energy must be balanced in the kinematics eventually.

1.2.2 Kinematics of Knockout Reaction

In the reference frame of the fluorine nucleus, the proton approaches at medium kinetic energy T. An orbital (or bound) proton is knocked out quasi-freely, and then an oxygen nucleus is left behind in ground state or excited states. A classical picture of the (p,2p) knockout reaction is illustrated in Figure 1-24. A round rectangle is inserted in the figure to illustrate the kinematics in the frame of center of momentum (C.M. frame).

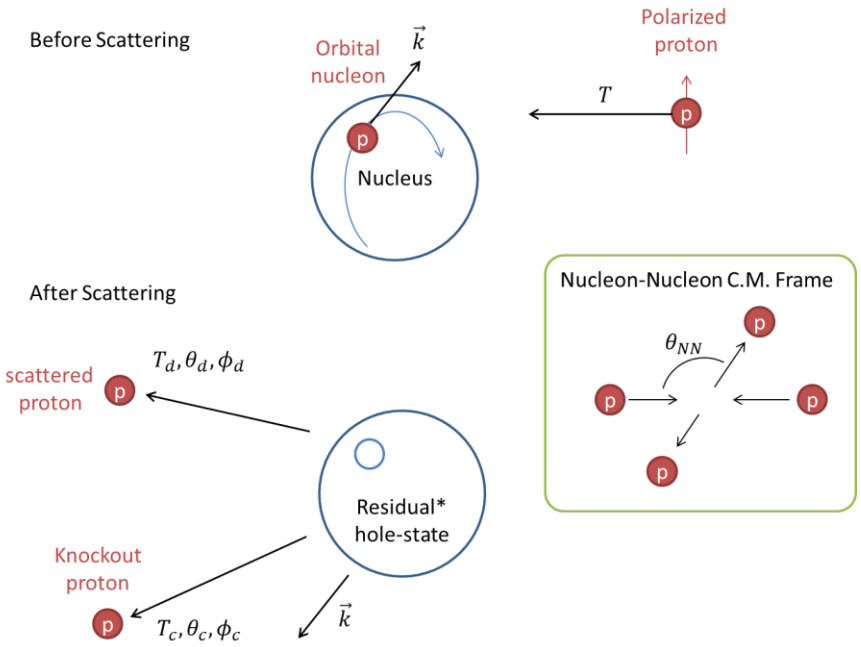

Figure 1-24 – Illustration of a (p,2p) knockout reaction in the nuclear frame.

The reaction in nuclear rest frame is notated as $A(a, cd)B$ and $A = B + b$, where A is the target nucleus, a is the incident proton, c and d are the scattered and knocked out proton, B is the reaction residue, and b is the orbital proton. The proton b is knocked out from nucleus B after being directly struck by the proton a, and the proton a and b become c and d respectively. Since our experiment uses inverse kinematics, we use another notation $T(F, O)12$ and $F = O + k$ to avoid confusion, where T is the proton target, F is the fluorine nucleus, O is the oxygen residual, k is the bound proton, and 1 and 2 are the scattered and knocked out protons, respectively when working in the laboratory reference frame. The relativistic four-momenta $\mathbb{P}$, of the reaction in the nuclear rest frame are

$$\mathbb{P}_A + \mathbb{P}_a = \mathbb{P}_c + \mathbb{P}_d + \mathbb{P}_B, \qquad \mathbb{P}_b = \mathbb{P}_A - \mathbb{P}_B, \tag{1.2.2}$$

and in the laboratory reference frame

$$\mathbb{P}_F + \mathbb{P}_T = \mathbb{P}_1 + \mathbb{P}_2 + \mathbb{P}_O, \qquad \mathbb{P}_k = \mathbb{P}_F - \mathbb{P}_O. \tag{1.2.3}$$

We can rearrange equation (1.2.2) into

$$\mathbb{P}_b + \mathbb{P}_a = \mathbb{P}_c + \mathbb{P}_d. \tag{1.2.4}$$

Note that the four-momentum $\mathbb{P}_b$ is a quasi-proton and its mass is defined from equation (1.2.2) that it is different from the mass of a free proton. Since $\mathbb{P}_A$ is stationary, the magnitude of the momentum of $\mathbb{P}_b$ is equal to that of the residue $\mathbb{P}_B$ but opposite direction. There are 6 unknowns in the reaction: the momentum of the residue $\overrightarrow{p_B} = \vec{k}(k, \theta_k, \phi_k)$, the separation energy for an orbital proton s_p, and the scattering angles (θ_{NN}, ϕ_{NN}) at the rest frame of the nucleon-nucleon center of momentum (the small picture of Figure 1-24). By measuring the scattering angles and the kinetic energy of the scattered protons, the four-momenta of the scattered proton $\mathbb{P}_1(T_1, \theta_1, \phi_1)$ and the knockout proton

$\mathbb{P}_2(T_2, \theta_2, \phi_2)$ can be reconstructed, then the four-momentum $\mathbb{P}_b$ can be reconstructed. And then the separation energy can be deduced by

$$s_p = m(\mathbb{P}_O) + m(\mathbb{P}_T) - m(\mathbb{P}_F), \tag{1.2.5}$$

where $m(\mathbb{P})$ is the mass of a four-momentum $\mathbb{P}$.

1.2.3 Kinematics Calculation

A kinematics of the ^{23}F(p,2p) knockout reaction was calculated as shown in Appendix A.1. In the calculation, the incident energy of the proton in the nuclear frame is 290 MeV. The scattering angle in the reference frame of the center of momentum of the incident proton and orbital proton θ_{NN} ran from 0° to 360° and $\phi_{NN} = 0°$ (Figure 1-24). Figure 1-25 shows the scattered energy of proton versus the scattering angle in the frame of laboratory with fixed $k = 100$ MeV/c, $\theta_k = 60°$, and $\phi_k = 0°$ on different values of s_p. The different colors loci in Figure 1-25 represent different values of s_p. When θ_{NN} runs from 0° to 360°, the loops start at maximum energy and run clockwise. The scattered angle for maximum kinetic energy is not zero because of $\theta_k = 60°$. The shapes of the locus are different for different separation energies. This is reasonable as some energies is lost to the separation energy. This simple kinematics calculation shows that the scattering angle ranges from 0° to 80° in the laboratory reference frame, but the energy can vary with different kinematic conditions.

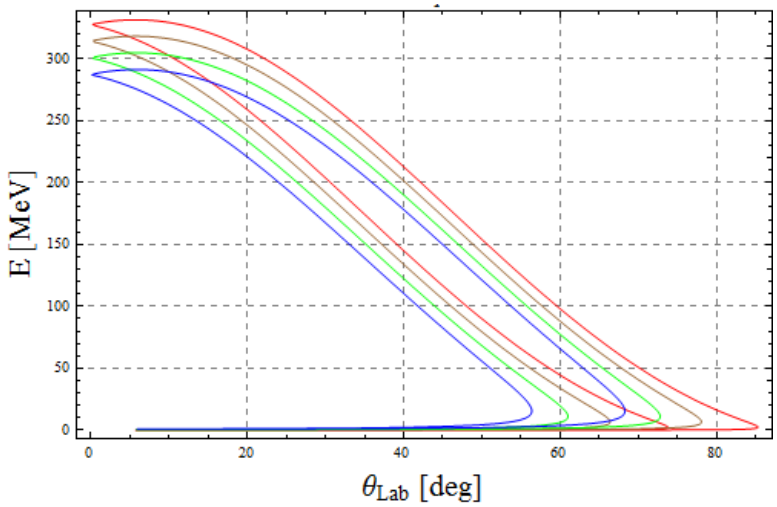

Figure 1-25 – Kinetic energy vs scattering angle in the laboratory reference frame.
The red, brown, green, and blue curves correspond to s_p = 0, 10, 20, and 30 MeV respectively. The momentum of the residue is 100 MeV/c, and the $\theta_k = 60°$. This is kinematics calculation and no detector acceptance is considered.

1.2.4 Estimation of Differential Cross Section

Differential cross section is calculated by a DWIA method from the code THREEDEE [50] [97]. The code calculates the kinematics in the nuclear frame. The kinematics inputs are the incident energy of

the proton (T_a), the separation energy (s_p), the kinetic energy of a scattered proton (T_c), the scattered angles of recoil protons (θ_c, θ_d) and the non-planar angle ($\beta_d = \phi_d - \phi_c$). The knockout reaction of the type $A(a, cd)B$, $A = B + b$ are separated into 4 channels: the $a + A$, $c + B$, $d + B$, and $b + B$. The other inputs are the optical potential parameters, nuclei spins, mass number, and charge number for each channel.

1.2.4.1 Formulism

The triple differential cross section and the scattering amplitude f are

$$\frac{d\sigma}{d\Omega_c d\Omega_d dE_c} = |f|^2, \qquad f \propto \int \chi_c^* \chi_d^* \, \Phi_B^* V_{ab} \chi_a \Phi_A dr_A dr_a, \tag{1.2.6}$$

where χ_a, χ_c, and χ_d are the distorted wave of the incident particle a, the scattered particle c, and the knocked out particle d. r_A is the coordinates of all nucleons of the nucleus A. r_a is the relative position of the particle a to the nucleus A. Because of the impulse approximation, the particle a only interacts with an orbital nucleon b with free-space potential V_{ab}. The intrinsic wavefunctions Φ_A and Φ_B represent the nucleus A and B, so that

$$\int \Phi_B^* \Phi_A dr_A = \int \phi_{nlj} dr_b. \tag{1.2.7}$$

Here, ϕ_{nlj} is the wavefunction of the orbital (or bound state) nucleon b with coordinate r_b. The orbit was labeled by the 3 quantum number n (principle quantum number), l (orbital angular momentum), and j (total angular momentum). The scattering amplitude reduced to

$$f \propto \int \chi_c^* \chi_d^* \, V_{ab} \chi_a \phi_{nlj} dr_b dr_a. \tag{1.2.8}$$

We can understand it better by replacing the distorted waves with plane waves.

$$f \propto \int e^{-ik_c r_c} e^{-ik_d r_d} \, V_{ab}(r) e^{ik_a r_a} \phi_{nlj} dr_b dr_a. \tag{1.2.9}$$

Notes that the coordinates are related by (Figure 1-26)

$$\begin{aligned} r_a &= \frac{M_A - 1}{M_A} r_b - r, \\ r_c &= r_b - r, \\ r_d &= r_b, \end{aligned} \tag{1.2.10}$$

where M_A is the mass of nucleus A, and r is the relative position between particle a and orbital nucleon b. Rearranging the equation, we found that

$$f \propto \int e^{-i(k_a - k_c)r} V_{ab}(r) dr \int e^{-i\left(k_c + k_d - k_a \frac{A-1}{A}\right) r_b} \, \phi_{nlj} dr_b. \tag{1.2.11}$$

The scattering amplitude contains two parts, one is the free-space scattering, and another is the bound state.

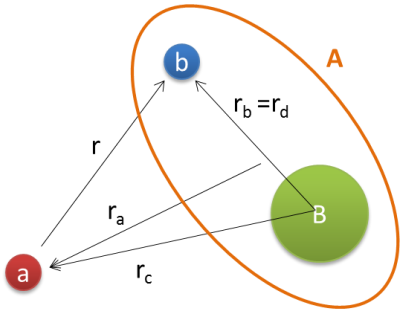

Figure 1-26 – A diagram of coordinates of the A(a,cd)B , A=B+b reaction.

The outputs of the calculation are a triple differential cross section

$$\frac{d^3\sigma_{DWIA}}{dT_c d\Omega_c d\Omega_d} \quad \text{and} \quad A_y \tag{1.2.12}$$

where T_X and Ω_X are the kinetic energy and the solid angle of the particle X respectively. A_y is the analyzing power that related to the asymmetry of the differential cross section when the nuclear spin has fixed orientation.

1.2.4.2 Optical Potential

Nuclear potentials are need for the code THREEDEE to calculate the differential cross section. The Dirac phenomenological potential with EDAD2 (energy-dependent-A-dependent) global parameter set was used [97]. We denote this potential as Dirac-Cooper global potential. This parameter set is obtained from fitting the proton scattering data with energy ranging from 20 MeV to 1040 MeV using ^{12}C, ^{16}O, ^{24}Mg, ^{28}Si, ^{40}Ca, ^{48}Ca, ^{56}Fe, ^{60}Ni, ^{90}Zr, and ^{208}Pb nuclei. The fitting of the parameter set has at most 3% systematic error. The optical potentials (central and spin-orbital terms) of ^{23}F + p and ^{25}F + p are shows in Figure 1-27. The magnitude of the spin-orbital terms is smaller than that of the central term.

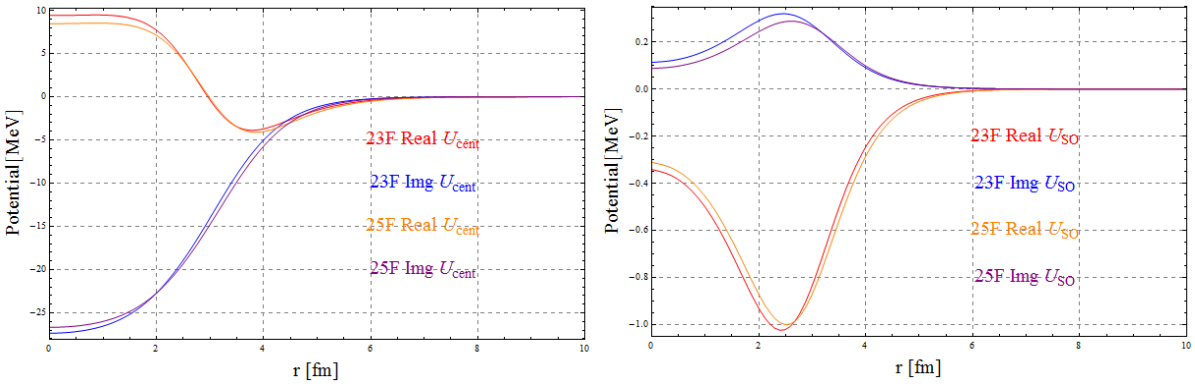

Figure 1-27 – Optical potential of ^{23}F at the proton energy 289 MeV and ^{25}F at the proton energy 277 MeV from-Cooper potential.

The radius and diffuseness of the real and imaginary, central and spin-orbital optical potentials of ^{22}O + p system are set to be 1.27 $A^{1/3}$ fm and 0.67 fm respectively for calculating the bound state of the proton [39]. The charge radiuses of all channels are set to 1.25 $A^{1/3}$ fm. A non-locality parameter

caused by the exchange term was switched off in the calculation. The calculation included a damping (Perey factor) of the proton wavefunctions that is caused by the nucleus and can be traced back to the Darwin term of relativistic scattering theory.

1.2.4.3 Integrated Cross Section

The quantities in the nuclear frame $T_C, \theta_c, \phi_c, \theta_d, \phi_d$ are used to calculate the quantities in the laboratory frame $T_1, \theta_1, \phi_1, T_2, \theta_2, \phi_2$. An acceptance filter (defined by detectors) was applied with additional kinetic energy filter $350 > T_1, T_2 > 30$ MeV. The energy of the scattered proton (T_c) was varied from 10 MeV to 300 MeV, with step 20 MeV. The scattering angles (θ_c, θ_d) are varied from 0° to 180° with step 10°, and ϕ_c, ϕ_d are varied from -24° to 24° with step 4°. Smaller step size was checked and gave no significant difference. The energy filter was determined by energy loss due to multiple scattering when a proton passes through 72-mm N_2 gas, two 128-μm Kapton films, and at least 1-meter-thick air (see Appendix A.5). The integrated cross-section is calculated using the formula

$$\begin{aligned}\sigma_{DWIA} &= \int_{30}^{350}\int_{20^\circ}^{70^\circ}\int_{-\phi}^{\phi}\frac{d^3\sigma}{dT_c d\Omega_c d\Omega_d}\sin\theta_c \sin\theta_d \, d\phi_c d\phi_d \, d\theta_c \, d\theta_1 dT_c \\ &= \sum_i \left[\left(\frac{d^3\sigma}{dT_c d\Omega_c d\Omega_d}\right)_i \sin\big(\theta_c(i)\big)\sin\big(\theta_d(i)\big)\, \Delta T_c \Delta\theta_c \Delta\theta_d \Delta\phi_c \Delta\phi_d\right],\end{aligned} \tag{1.2.13}$$

where Δ means the step size of each qualities. The integrated cross section in the frame of laboratory is as same as that of the frame of nucleus because of the acceptance filter.

We found that the cross-section is insensitive to the strength of the spin-orbital potential. The theoretical cross-section is increased by 30% if the Perey factor turned off.

1.2.4.4 Detector Acceptance

We simulated the energy emittance that limited by angular acceptance using a Monte Carlo method for both ^{23}F (at 290 MeV) and ^{25}F (at 277 MeV). The initial inputs are the separation energy, the Fermi momentum vector, and the proton-proton center of momentum frame scattering angles. The separation energy of ^{23}F was set to be 13.26 MeV or 30 MeV, and that of ^{25}F was set to be 14.43 MeV. The magnitude of the Fermi momentum was approximated as a triangular distribution with base ranging from 0 MeV/c to 250 MeV/c and peaked at 100 MeV/c. The direction of the Fermi momentum and the scattering angles were set to be spherically isotopic. We generated 50,000 events and then gated those events with the detector angular acceptance. There are about 5,000 events left. The resulting acceptance are plotted over Figure 1-25 and shown in Figure 1-28. We can see there are almost no events below 30 MeV. In fact, there are only 8 events out of ~5000 events below 30 MeV. When the separation energy increase, the opening angle reduces (Figure 1-29). A similar energy emittance for ^{25}F(p,2p) reaction was obtained and shown in Figure 1-30.

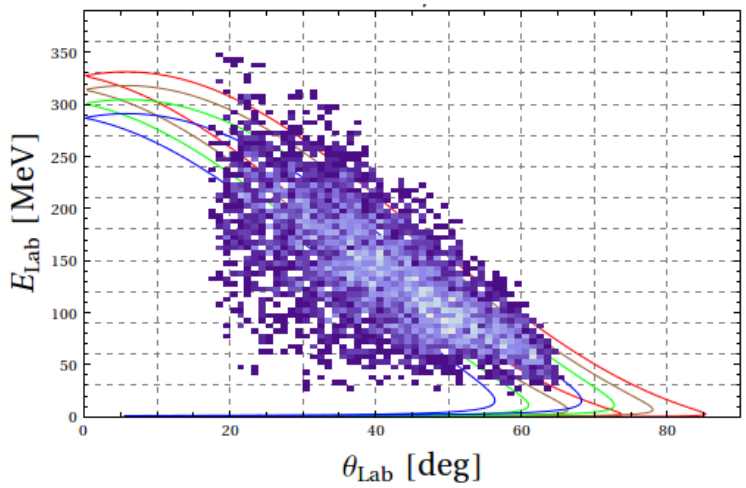

Figure 1-28 – The angular and energy acceptance of ^{23}F(p,2p) reaction at 290*A* MeV for separation energy of 13.6 MeV.

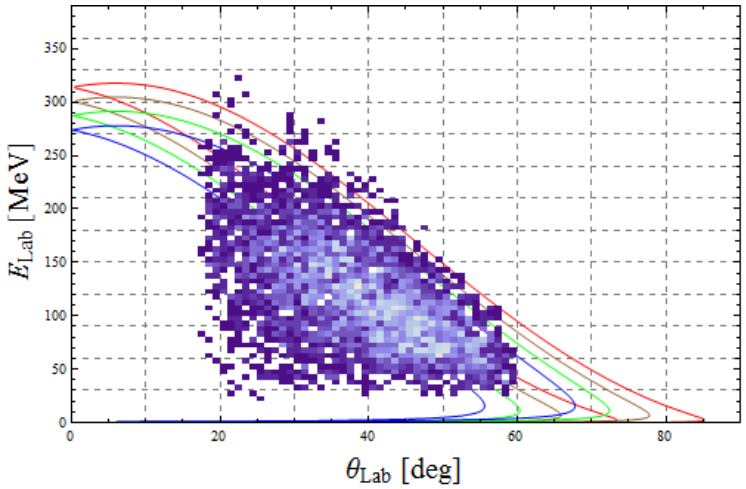

Figure 1-29 – The angular and energy acceptance of ^{23}F(p,2p) reaction at 290*A* MeV for separation energy of 30 MeV.

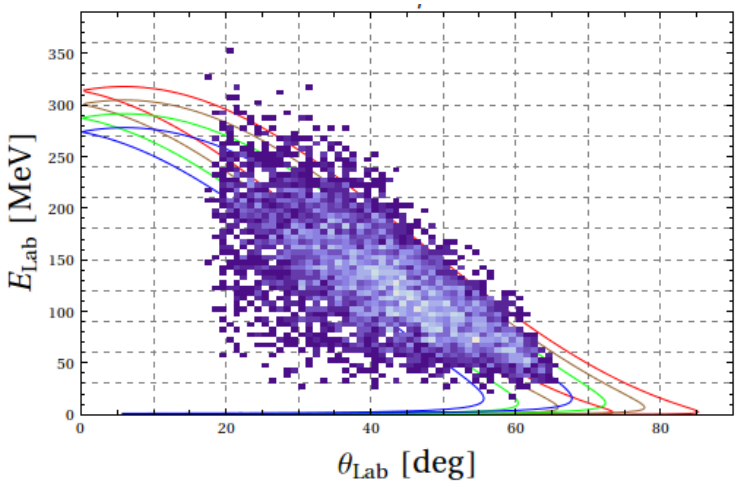

Figure 1-30 – The angular and energy acceptance of ^{25}F(p,2p) at 277*A* MeV for separation energy of 14.4 MeV.

The result can be understood using the momentum transferred and Fermi momentum. The Fermi momentum of a nucleon is ranging from 0 to 260 MeV/c. In quasi-free knockout approximation in the nuclear frame, the minimum momentum transfer is on the forward angle (40°) and equal 550 MeV/c for 300 MeV proton. Thus, the minimum momentum of the knockout proton would be 290 MeV/c or 44 MeV. Although the above explanation is in the nuclear frame, this gives the idea that there is a minimum kinetic energy of the scattered proton due to large transferred momentum.

1.2.5 Orbit Identification

The orbit identification is needed for knowing the orbit of the knocked out proton. Because the momentum of the orbital proton has same magnitude of that of the residual nucleus, and the momentum distribution depends on the orbital angular momentum. Momentum distributions from different orbits were calculated using the code THREEDEE with fixed $\theta_{NN} = 70°$, $\theta_k = 60°$, and $\phi_{NN} = \phi_k = 0°$. The result is shown in the upper plot of Figure 1-31. The strength of the s-orbit is concentrated on the low momentum region and the strength of the d-orbits have peaks around 120 MeV/c. The orbital angular momentum can be identified by the peak position on the momentum distribution. The $J_>$ or $J_<$ can be distinguished from the analyzing power (lower plot of Figure 1-31).

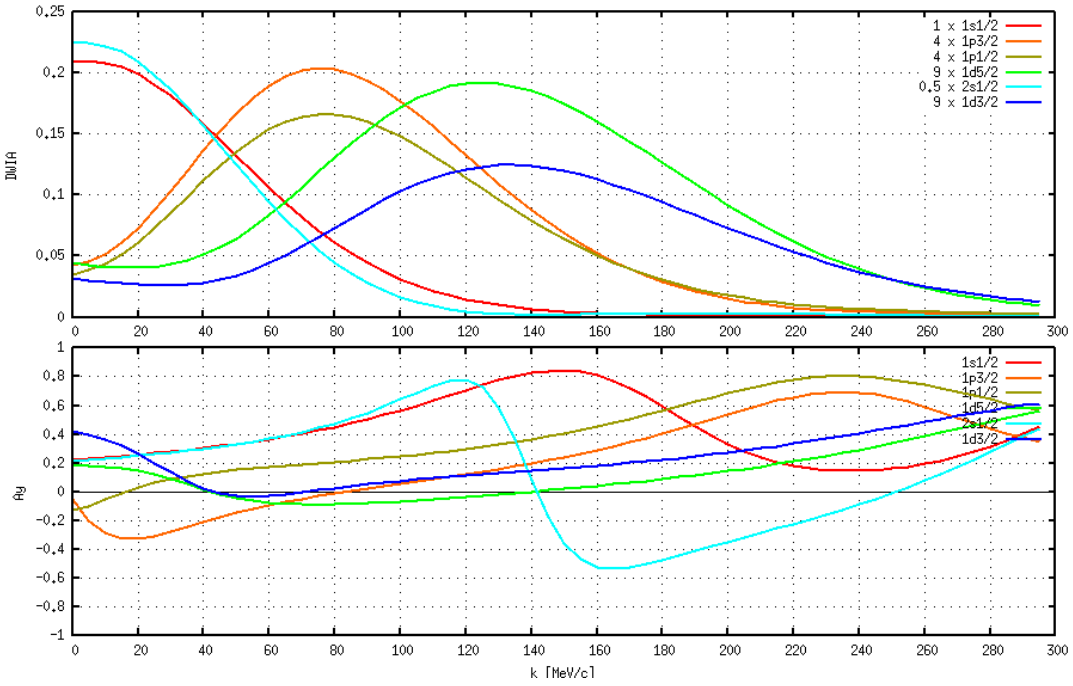

Figure 1-31 – Momentum distribution in the nuclear frame for different orbital angular momenta. The upper plot is the DWIA triplet differential cross section and the lower plot is the analyzing power. The cross section is scaled. The separation energy is 10 MeV, θ_{NN} is 70° and θ_k is 60° and the incident energy of the proton is 290 MeV.

Generally, non-zero analyzing power (or asymmetry of cross section) exists in scattering experiments due to symmetries (parity, rotation, and time reversal) [98]. The physical origin of the asymmetry of

the cross section in the knockout reaction is due to the proton-proton interaction and multiple scattering or absorption of the scattered proton inside the nucleus [99]. Because of the proton-proton interaction and symmetries, the scattering cross section σ takes the form [98]

$$\sigma = \sigma_0\big(1 + P_y A_y + P_y^T A_y^T + P_x P_x^T C_{xx} + P_z P_x^T C_{zx} + P_x P_z^T C_{xz} + P_y P_y^T C_{yy} + P_z P_z^T C_{zz}\big), \tag{1.2.14}$$

where σ_0 is the scattering cross section for the non-polarized beam and target, P_i is the polarization along the i-axis, the superscript T stands for the target, A_y is the analyzing power along the y-axis, and C_{jk} is the spin-spin correlation coefficient between the projectile with spin on the j-axis and the target with spin on the k-axis. In the nuclear frame, a y-axis polarized proton hits on a bound proton inside the nucleus. Under the impulse approximation, the effective interaction can be approximated by the free proton-proton interaction. The cross section reduces to

$$\sigma = \sigma_0\big(1 + \big(P_y + P_y^T\big)A_y + P_y P_y^T C_{yy}\big). \tag{1.2.15}$$

Therefore, only the bound proton with a spin on the y-axis can be knocked out. The experimental value for the coefficient C_{yy} is positive. It is close to unity for incident energy of 300 MeV and scattering angle in the frame of the center of momentum between 20° to 160° [100]. A simple reason for the coefficient C_{yy} to be positive is the nucleon-nucleon spin-orbit coupling, in which the total spin of the two protons have to be parallel (or S = 1). The coefficient A_y has a maximum value of 0.3 for incident energy of 300 MeV. The acceptance of the detectors limited the scattering angle from 40° to 140° in the center-of-momentum frame. Therefore, the bound proton most likely spins in the same direction to produce a large cross-section.

The second reason for the asymmetry of the cross section in the knockout reaction is due to the multiple scattering or absorption as the scattered proton passes through the nucleus [99]. Figure 1-32 shows a classical picture of a knockout reaction. The scattered proton (k_2 in the figure) from the left and has to pass through the nucleus. The mean free path [101] of a slow proton (large θ_2) is smaller than the nuclear radius, and then the proton suffers from multiple scattering when passing through the nucleus. Therefore, the cross section at this outgoing angle (small θ_1 and large θ_2) is reduced. Now, when the θ_1 becomes large, θ_2 becomes small, the path through the nucleus reduces, and the cross section increases as there is no multiple scattering. The consequence is a front-back or left-right asymmetry (due to the correlation of θ_1 and θ_2) of the cross section. This is reflected in the analyzing power A_y, as A_y must be an odd function of θ_1 caused by time reversal symmetry.

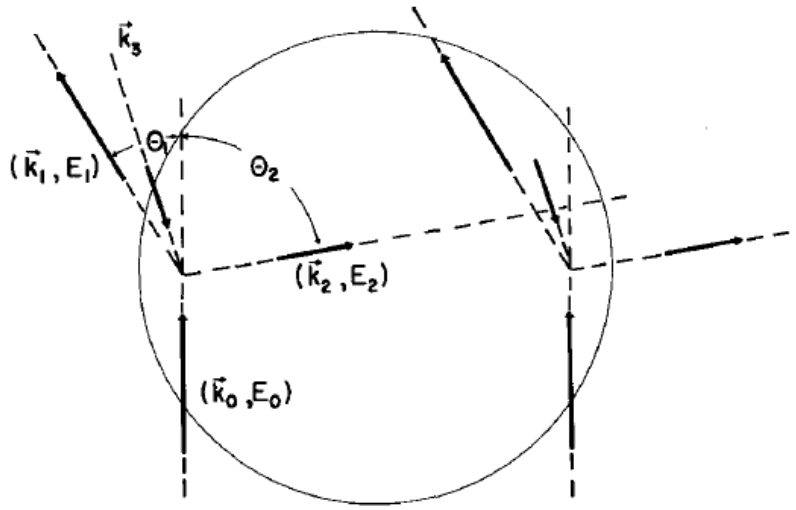

Figure 1-32 – Classical kinematic picture of a knockout reaction [99].

Without loss of generality, we can assume the projectile proton is spin up (pointing out of the paper). The projectile proton can knock out a bound proton from the left side or the right side. Recalling that the bound proton has to be the same spin (pointing out of the paper) for the spin-orbit coupling to act upon. Therefore, the bound proton being knocked out on the left side has total spin $J_> = l + s$ and it has total spin $J_< = l - s$ when it was knocked out from the right. From the above discussion, the analyzing power for $J_>$ and $J_<$ has opposite sign. However, in reality, the knock out could take place anywhere in the nucleus, which makes the relation of the analyzing power between $J_>$ and $J_<$ complicated. As Figure 1-31 shows, the analyzing powers from the $1p_{1/2}$ and $1p_{3/2}$ orbits have same sign at high momentum k.

Chapter 2

Experimental Setup

This chapter focuses on the experimental setup from the beam production to the details and performance (resolution and efficiency) of the detectors. The scattered protons were detected by two sets of detectors, placed on the left and right sides of the target. The residue identification was also important; it was done using the SHARAQ spectrometer.

2.1 Beam Production and Beam Time

A primary beam of ^{48}Ca was accelerated to 345 MeV/nucleon with an intensity of 200 pnA using the Super-conductive Ring Cyclotron of RIKEN Nishina Center. The cyclotron was operated at 37 MHz. The ^{48}Ca beam hit on a ^{9}Be target with thickness of 30 mm and then fragments were produced. An aluminum degrader with thickness of 8 mm was used to improve purity. The BigRIPS in-flight fragment separator [102] (Figure 2-1) separated the fragments according to the mass-to-charge (A/Q) ratio and momentum. Because the fragments have similar A/Q ratios, the secondary beam was a cocktail beam. The detail of the secondary beam production is listed in Table 2-1.

Table 2-1 – The list of secondary beam production.

Magnetic rigidity	Total rate of secondary beam	Intensity of primary beam	Production target		Degrader	
			Material	Thickness	Material	Thickness
7.13 Tm	70 kcps	200 pnA	^{9}Be	30 mm	Al	8 mm

2.1.1 Experiment Flow

The experiment was started at 9 am, May 28th, 2012. A pure proton beam was used for optical alignment in the first 6 hours, and proton-proton elastic scattering was measured for the next 6 hours. The elastic scattering was performed to determine the absolute magnitude of the polarization of the spin-polarized proton target. Detector was calibrated using the data from the proton-proton elastic scattering runs.

A beam tuning for the secondary beam was started at 9 am, May 29th, 2012. The physical runs of the ^{23}F(p,2p) reaction on a cocktail beam (35% of ^{23}F, 18% of ^{22}O) were started at 12 am midnight, May 30th. The ^{23}F cocktail beam was ended at 9:08 pm, May 31th. A ^{25}F cocktail beam was delivered and the

^{25}F(p,2p) reaction was measured from June 2nd to June 4th. Spin-up and spin-down of the orientation of the proton polarization were measured for each beam. The beam times is summarized in Table 2-2.

Table 2-2 – Beams and their measurement duration.

Beam	Target Polarization Direction	Total Beam Intensity [cps]	Total Measurement Duration [hh:mm:ss]	Date (start, end)
Proton (Pure)	Down	1.27×10^5	2:44:58	28th May, 20:46:02
	Up	1.27×10^5	1:54:16	29th May, 9:00:07
^{23}F / ^{22}O	Up	1.28×10^5	11:32:14	30th May, 0:26:31
	Down	1.16×10^5	3:11:22	31st May, 9:08:32
^{25}F / ^{24}O	Up	1.78×10^4	14:49:43	2nd Jun, 19:56:44
	Down	2.16×10^4	12:51:27	4th Jun, 9:00:00

2.2 Particle Transportation

Figure 2-1 shows the BigRIPS and the SHARAQ spectrometer [103] in the Radioactive Isotopes Beam Facility (RIBF) of RIKEN Nishina Center. The BigRIPS starts from focal plane F0 that was the positon of the primary target, and continues until the STQ-H19 (Super-conducted Triplet Quadrupole) that was just before the focal plane F-H10. Particle identification was done using the time-of-flight (TOF) from the F3 to F-H9 focal planes and the energy loss in F-H9 (or F3). Two drift-chambers (DCX1 and DCX2) were placed between the STQ-H19 and the target chamber for beam trajectory tracking. The F6 focal plane was a momentum dispersion plane with momentum dispersion of 75 mm/1%. A PPAC (F6-PPAC) was placed at the F6 focal plane for measuring the momentum of the secondary beam. The F6-PPAC was used only in the optical runs for beam tuning and ^{25}F runs, because the momentum spreading of the ^{23}F beam was 0.2% (Section 3.1.2).

The SHARAQ spectrometer (Figure 2-2) was continuous from F-H10 (or S0). It consists of a superconductive double quadruple magnet (SDQ), two dipole magnets (D1 and D2), and a quadruple magnet (Q3). In this experiment, only the SDQ and the D1 were used. The position just before the SDQ is labeled as S0D (S0 downstream) and the focal plane after D1 is labeled as S1.

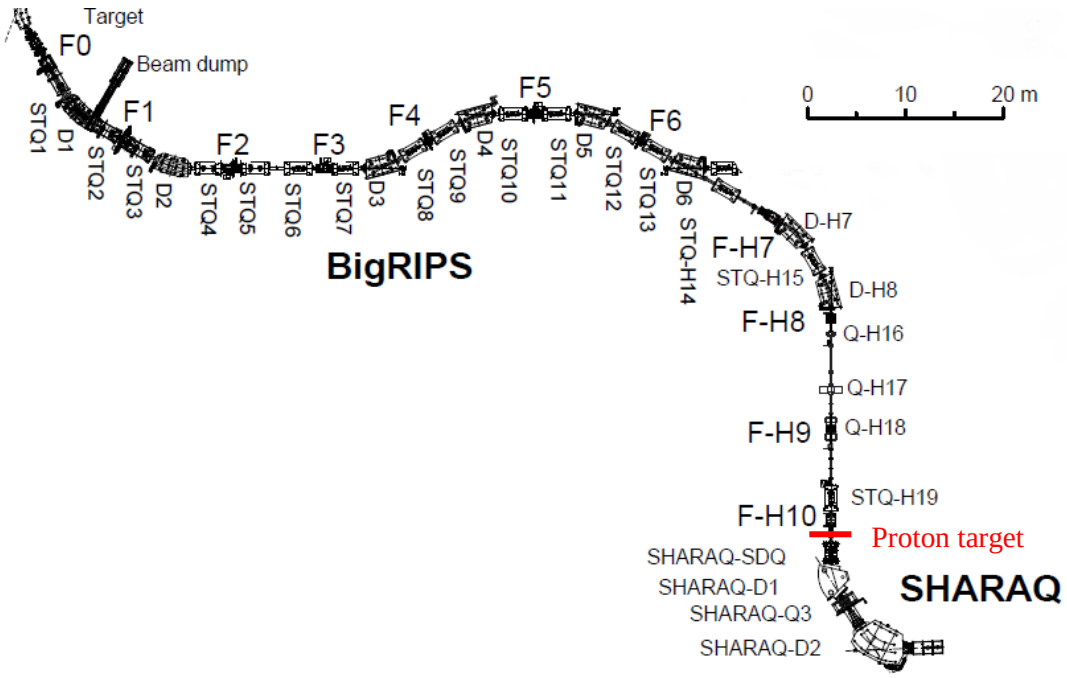

Figure 2-1 – The beam transportation system, the BigRIPS and the SHARAQ spectrometer. The primary target (^{9}Be) was placed at F0. The secondary target (proton) was placed between F-H10 and SHARAQ-SDQ, it is labeled as a red line.

2.3 Particle Detectors

The following is a brief summary of the detector setup on the detector type and location. An illustration of the setup near SHARAQ is drawn in Figure 2-2. A plastic scintillator was located at the F3 focal plane (F3PL), a PPAC (F6-PPAC) [104] was located at the F6 momentum dispersion plane, a plastic scintillator was located at F-H9 focal plane (FH9PL), and two drift chambers (DCX1 and DCX2 [105]) were located after the STQ-H19 (Figure 2-1). These detectors were upstream (of the target) detectors. They provided information of the beam such as charge state, kinetic energy, and beam trajectory. The target position is labeled as S0. The downstream (of the target) detectors consisted of two set of detectors placed on left and right sides and series of residue detectors. Each set of left/right detectors had a multi-wire drift chamber (MWDC [106]) and a trigger plastic scintillator (Tpla). The residual nuclei had passed through a plastic scintillator (S0DPL) and a drift chamber (DCS0D) before entering the SHARAQ spectrometer [103]. The residues were then deflected by the SHARAQ-D1 magnet according to their masses, charge states, and momenta. The focal plane after the SHARAQ-D1 magnet is labeled as S1. The residues were detected using a MWDC-S1 (MWDC located at S1) and a Hodo array (plastic scintillators hodoscope). A spin-polarized solid proton target [107] [108] was used. A carbon target was placed 160 mm downstream of the target for carbon background subtraction. The order of locations and corresponding detectors are listed in Table 2-3.

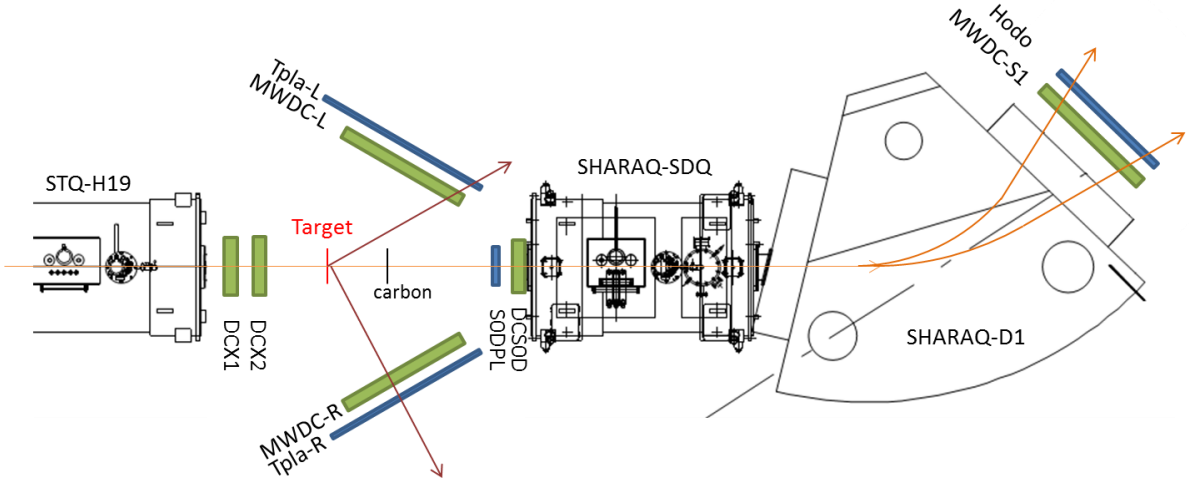

Figure 2-2 – The layout of particle detectors after focal plane F-H9.
The green boxes are drift chambers. The blue are plastic scintillators. The orange arrow is the beam direction. The cerise arrows are the scattered protons.

Table 2-3 – List of detectors and their order of location.

Location	Detectors
F3	F3PL
F6	F6PPAC
F-H9	DC91 FH9PL
Before target	DCX1, DCX2
S0	Target (not a detector)
After target	Tpla-L, Tpla-R MWDC-L, MWDC-R
S0 downstream	S0DPL DCS0D
S1	MWDC-S1 Hodo

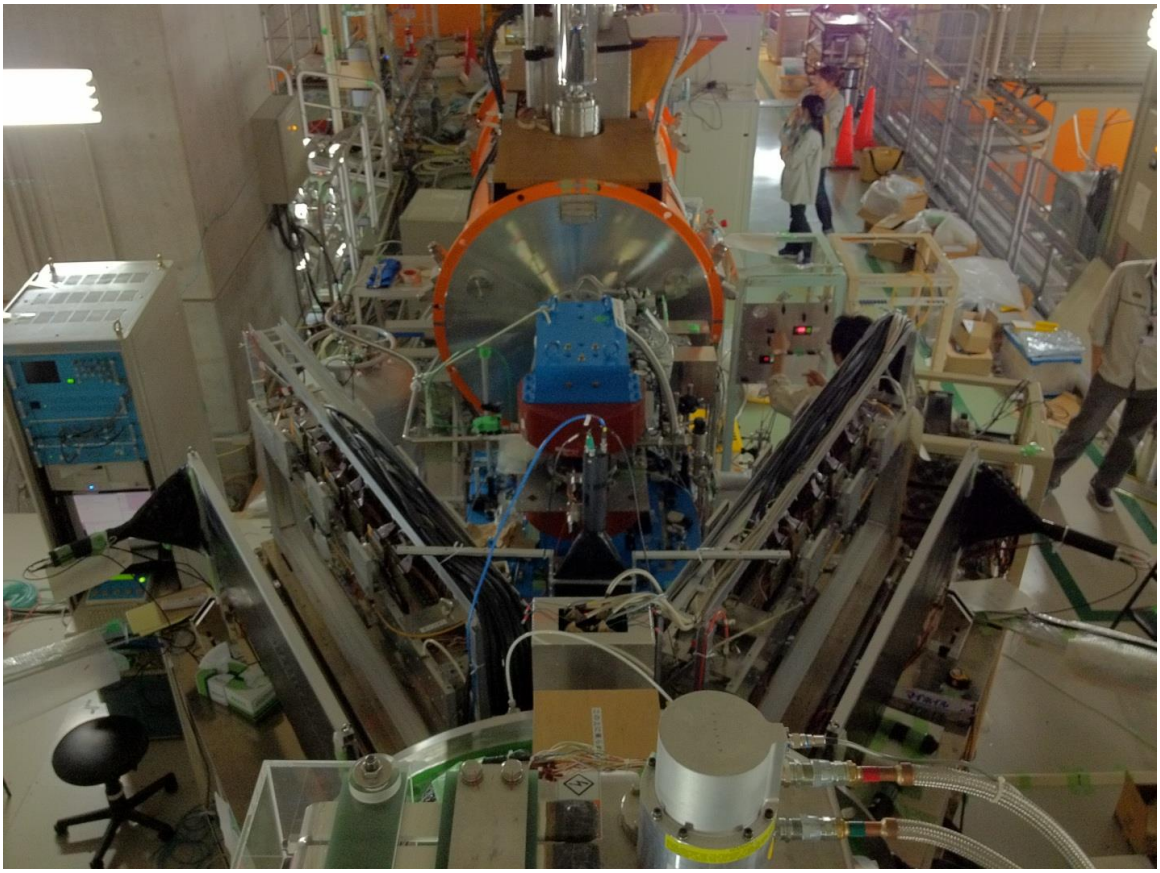

Figure 2-3 – Experiment set-up at F-H10, viewed from the top of the SHARAQ-SDQ. The beam is coming from top of the picture. The orange cylinder is STQ-H19.

2.3.1 Plastic Scintillator (F3PL, FH9PL, Tpla-L, Tpla-R, and S0DPL)

There were five plastic scintillators along the BigRIPS and SHARAQ beam line. The F3PL and the FH9PL were focal plane plastic scintillators, and they were located at focal plane F3 and FH9, respectively. The Tpla-L and the Tpla-R were trigger plastic scintillators placed behind the MWDC-L and the MWDC-R respectively. They acted as the time reference for the MWDCs. They also provided the energy of the scattered proton from the TOF measurement. The S0DPL was a downstream plastic scintillator for the reaction residues. When we do not distinguish the left or right detector, we use Tpla and MWDC.

All these five plastic scintillators were connected with a photo-multiplier tube (PMT) on each ends. The leading time of each PMT was recorded using time-to-digital converters (TDCs). The timing of a plastic scintillator was defined as the arithmetic average of the leading time of the PMTs in both ends. The light output, which is related to the energy loss, in the plastic scintillator was recorded by analogy-to-digital converters (ADCs). The energy loss was defined as the geometric mean of the energy loss of the PMTs in both ends. The timing and energy loss are shown in Figure 2-4. The blue box represents a plastic scintillator with length L. The black arrow is the path of a particle that passed through the scintillator at position x and creates scintillation light at time T with light output Q_0. The two opposite

dotted yellow arrows are the scintillation light. The leading time t_i and the light output Q_i were recorded. The timing t and the energy loss Q were defined using arithmetic mean and geometric mean respectively. The symbol βc is the speed of light in the plastic scintillator, typical value is 0.67 of speed of light in vacuum. The symbol a is the attenuation length of the plastic scintillator, typical value is 1 to 2 meters.

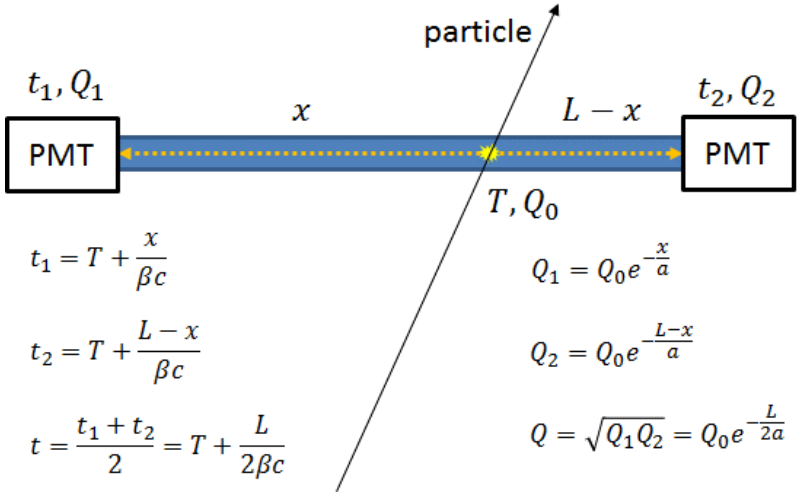

Figure 2-4 – Definition of the timing *t* and energy loss *Q* in a plastic scintillator. See main text for detail.

An illustration of the connections of the plastic scintillators to the TDCs are shown in Figure 2-5. The F3PL was connected to two TDCs – V1190 (time windows = 200 ns) and V775 (time windows = 200 ns). The FH9PL was connected to another two TDCs – model V1190 (time windows = 4500 ns) and V775 (time windows = 170 ns). The TDC V1190 is a multi-hit TDC with channel-to-ns (ch2ns) factor about 100 ps/channel. The TDC V775 is a signal-hit TDC with channel-to-ns factor about 80 ps/channel. All TDCs V775 were set at common stop mode.

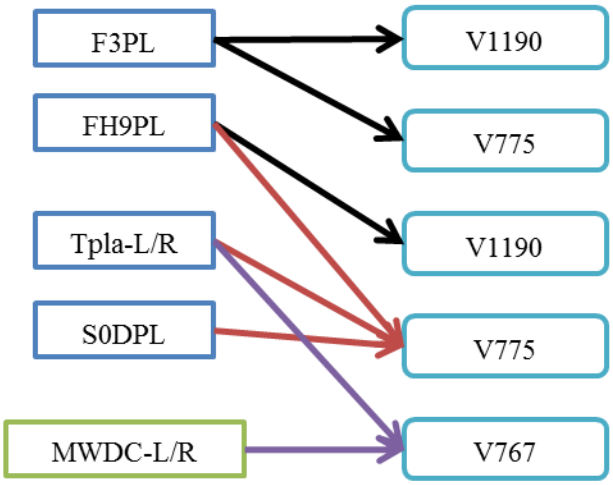

Figure 2-5 – Detectors and TDC connections. The colored arrows are only for clear presentation. The blue boxes are plastic scintillators. The green box is MWDC. The boxes with rounded corners are TDCs.

The Tpla-L and Tpla-R were the trigger plastic scintillators behind the MWDC-L and the MWDC-R respectively. The perpendicular distance from the Tpla-L (or Tpla-R) to the target was 1400 mm. There were two PMTs at the ends of each trigger plastic scintillator. The PMT with a forward angle is labeled by F, and of backward angle is labeled by B. For example, PMT-LB is the PMT on the Tpla-L and with the backward angle. Both plastic scintillators were 1500 mm wide, 13 mm thick and 500 mm high. Since the Tpla-L and Tpla-R provided the trigger signal, the acceptance was then defined by their geometry. The height of the Tpla was not large enough to fully cover the height of the MWDC, therefore we cannot detect events on the edge of MWDCs (Figure 2-6).

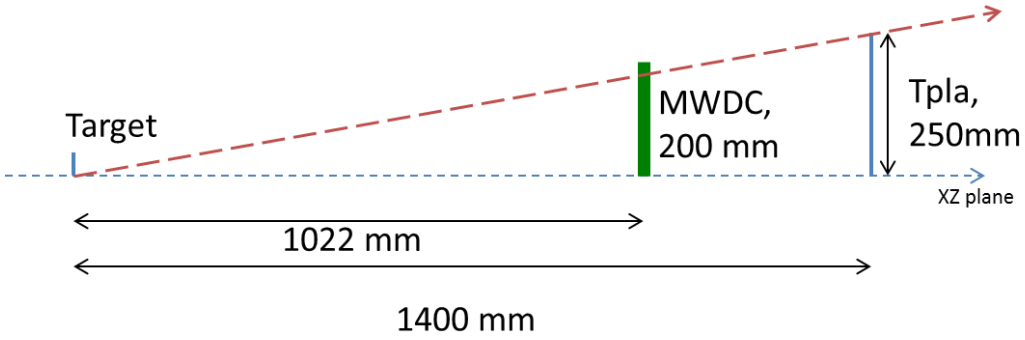

Figure 2-6 – The geometry of the MWDC and the Tpla.
The height of the Tpla was not fully covered by the height of the MWDC. The MWDC was 17.5 mm higher. Note that the experimental setup was symmetric on the XZ plane, the figure only shows the upper half.

The S0DPL was placed 1457 mm downstream of the target and in front of the DCS0D (Figure 2-2). It and the FH9PL formed a primary residue particle-identification (PID) by ΔE-TOF method. However, the high voltage of the S0DPL was not well set so it was difficult to separate the charge number. A detailed residue PID was analyzed by using the SHARAQ spectrometer, the MWDC-S1, and the Hodo array.

2.3.1.1 Time Calibration

Time calibration only ran for the TDC V775 that connected to the FH9PL, the Tpla-L, the Tpla-R, and the S0DPL but not the F3PL. The channel-to-ns (ch2ns) conversion factors were calibrated using a time calibrator. It was set to a period of 10 ns with a time range of 120 ns. By subtracting the channel number of the 13^{th} peak and the 1^{st} peak and dividing by 120, we obtained the factor for each PMT. The linearity was also checked. The values of ch2ns for each TDC channel are listed in Table 2-4. The negative value means that the TDC was in common-stop mode.

Table 2-4 – Channel-to-ns used for the TDC modules.

	*TDC V1190 / #TDC V767		TDC 775 (calibrated)	
	Left-PMT	Right-PMT	Left-PMT	Right-PMT
F3PL*	0.09765625	0.09765625	0.051882	0.0049554
FH9PL*	0.09765625	0.09765625	-0.07742	-0.07732
S0DPL	NA	NA	-0.07562	-0.07782
Tpla-L#	0.8	0.8	-0.07747	-0.07787
Tpla-R#	0.8	0.8	-0.07687	-0.07702

The absolute values of the TOF were calibrated using the proton beam runs because the kinematics of the proton-proton elastic scattering is well known. From now on, we adapt a notation that TOF(A-B) is the time-of-flight from point or detector A to point or detector B. The TOF(target-Tpla) and scattering angle are correlated, as shown in Figure 2-7. The broad distribution was caused by the time resolution, reactions with carbon, and multiple scattering.

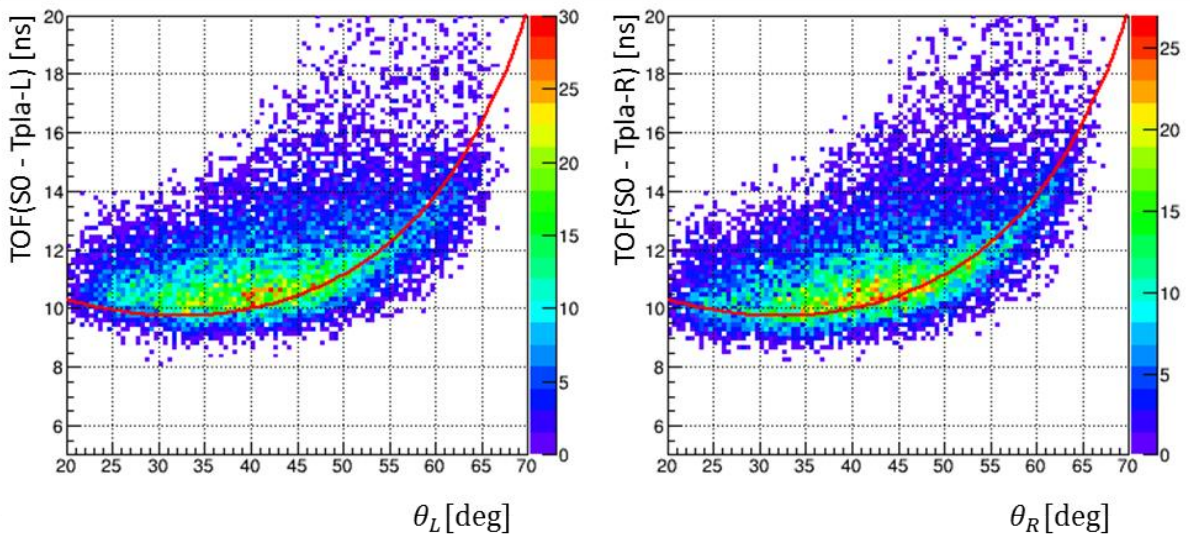

Figure 2-7 – Correlation between the scattering angle and the TOF(target-Tpla) in the proton-proton elastic scattering.
The left plot is from the Tpla-L and the right plot is from the Tpla-R. The red line is the theoretical curve. The unit of the y-axis is nano-second.

2.3.1.2 Time Resolution

The time resolution was only calculated for the FH9PL, the Tpla-L, and the Tpla-R. It was based on the standard deviation of the fitting of a Gaussian distribution on the experimental distribution of the time-difference between the leading times from the two PMTs at the end of each plastic scintillator. The detailed description of the time resolution calculation is shown in Appendix A.2. The time resolution of the F3PL was ignored because it did not affect the energy resolution of the scattered proton much {we can see it later in section 3.7. The effect of the time resolution was only ~10% of the target-hit-time [equation (3.73)]}. Also the momentum spread of the ^{23}F beam was only 0.3% (sigma, Figure 3-2),

therefore, the energy resolution of the beam was high enough that the event by event calculation of beam energy from TOF(F3PL-FH9PL) was not necessary.

The time resolution of the FH9PL from the TDC V775 was deduced by tracking from a drift chamber, which was located 15 mm in front of the FH9PL. Figure 2-8 shows the position dependence of the time-difference. By selecting a narrow position width, the time resolution of each position can be deduced. The average time resolution of the FH9PL was 220 ps. The time resolutions of the Tpla-L and the Tpla-R were deduced with the tracking result of the MWDC-L and the MWDC-R respectively. The average time resolutions of the Tpla-L and the Tpla-R are 500 ps and 600 ps respectively (Figure 2-9 and Figure 2-10).

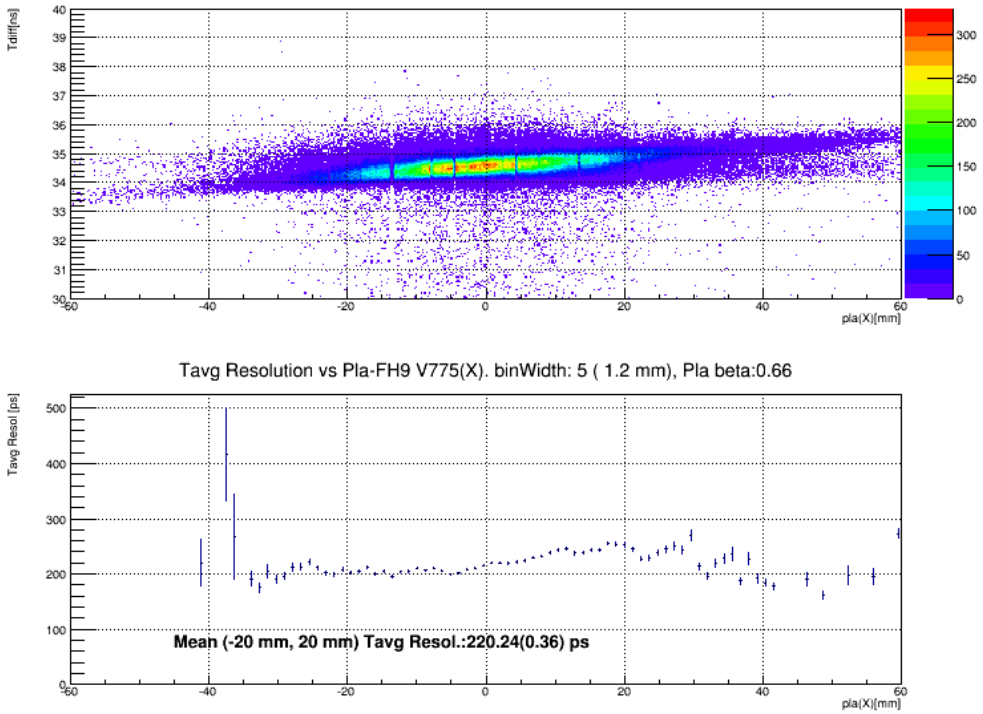

Figure 2-8 – Time resolution of the FH9PL from TDC V775 using the DC91.
The x-axes are the projected position on the FH9PL from the tracking result of the DC91. The y-axis on the upper figure is the time difference between the PMTs of the FH9PL. The y-axis on the lower figure is the time resolution.

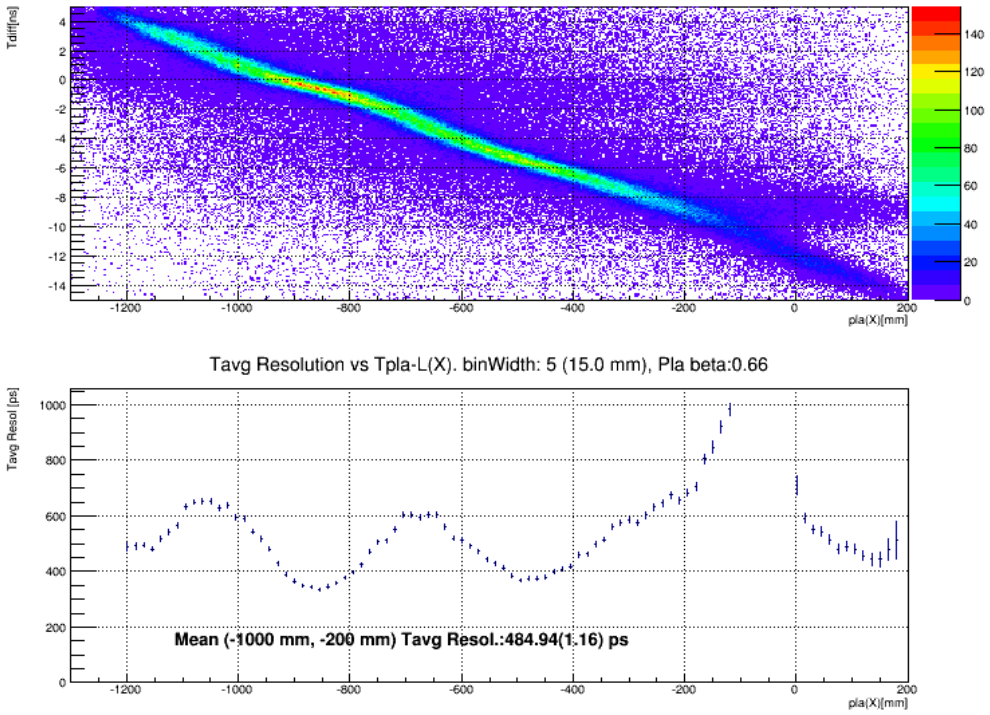

Figure 2-9 – Time resolution of the Tpla-L.
The x-axes are the position on the Tpla-L calculated from the projection of the tracking result of the MWDC-L. The y-axis on the upper figure is the time difference between the PMTs at the Tpla-L. The y-axis on the lower figure is the time resolution.

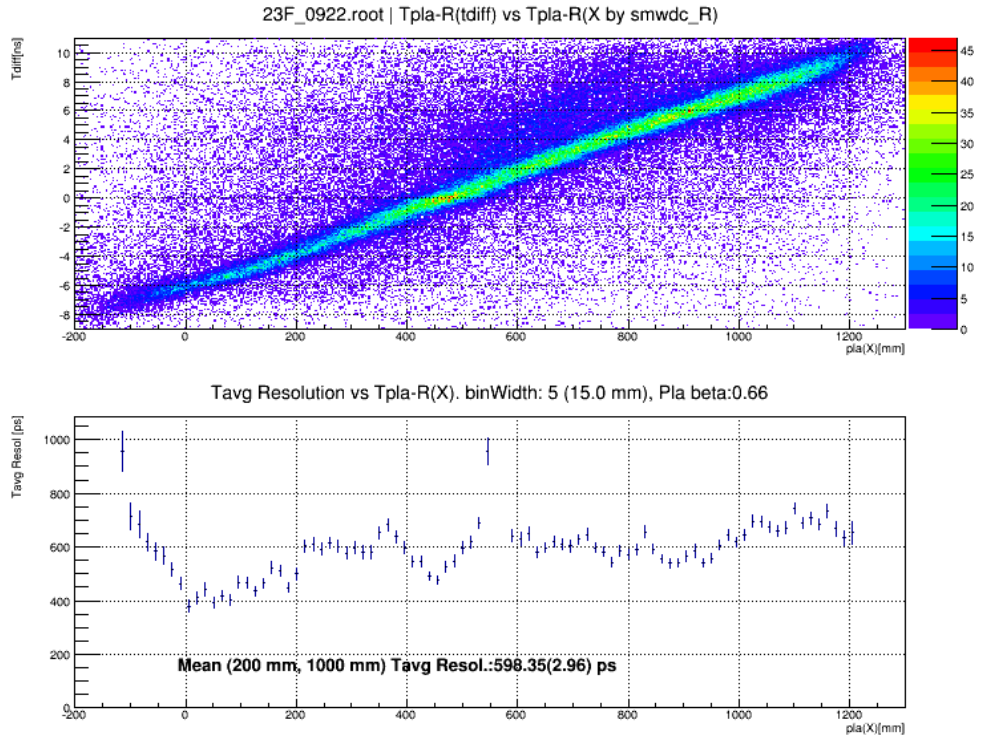

Figure 2-10 – Time resolution of the Tpla-R.
The x-axes are the position on the Tpla-R calculated from the projection of the tracking result of the MWDC-R. The y-axis on the upper figure is the time difference between the PMTs at the Tpla-R. The y-axis on the lower figure is the time resolution.

2.3.2 Drift Chamber (DCX1 and DCX2)

The DCX1 and DCX2 were used for tracking the trajectory of the secondary beam. The trajectory was used to deduced the size of the beam spot on the target. The DCX1 has three planes: X (24 wires), U (24 wires), and Y (16 wires). The DCX2 has four planes: U (24 wires), V (24 wires), V′ (24 wires), and U′ (16 wires). The time reference for the drift-time was taken from the FH9PL with the TDC V775. The configurations are listed in Table 2-5. The "Plane Pos." is the abbreviation of plane position.

Table 2-5 – Configuration of DCX1 and DCX2.

	DCX1			DCX2			
Size [mm^2]	144 × 216			144 × 216			
Plane label	X	U	Y	U	V	V′	U′
Wire angle [deg]	0	30	-45	-30	30	30	-30
Plane Pos. [mm]	-877	-868	-859	-613.5	-604.5	-595.5	-586.5
Cell width [mm]	9	9	9	9	9	9	9
Center [wire]	-12.5	-12.5	-8.5	-12.5	-12	-12.5	-13
Number of wire	24	24	16	24	24	24	24

The drift-time-to-drift-length conversion was deduced by integrating the drift-time distribution, so that the resulting drift-length distribution was uniform. We found that the alignment of the DCX2 was off-set by 2.1 mm vertically during experiment. This offset was included in the tracking algorithm. The two drift chambers were combined as a single 7-plane detector in the tracking algorithm, which was multi-dimension linear regression. The outline of the theory of the regression is shown in Appendix A.3. Since the DCX1 and DCX2 were regarded as a single detector, we denote it as DCX1X2. The tracking gave the usual ray parameters (X, A, Y, B), where X and Y are the x and the y position on the target respectively, A and B are the incident angles on the x-z plane and the y-z plane respectively.

The detection efficiency was defined as the number of tracked events over the number of particles that passed through. We assumed the transmission rate from the FH9PL to the DCX1X2 was 100%. The number of particles that passed through was the event count on the FH9PL. The detection efficiency of the DCX1X2 was 93.4%.

The tracking uncertainty of each of the ray parameters was deduced by the sum of square of residues and the covariance matrix from the regression [109]. Figure 2-11 shows the distribution of the tracking uncertainties. The uncertainties of X and Y are 0.8 mm and 1.6 mm respectively. The uncertainties of A and B are 1.4 mrad and 2.4 mrad respectively.

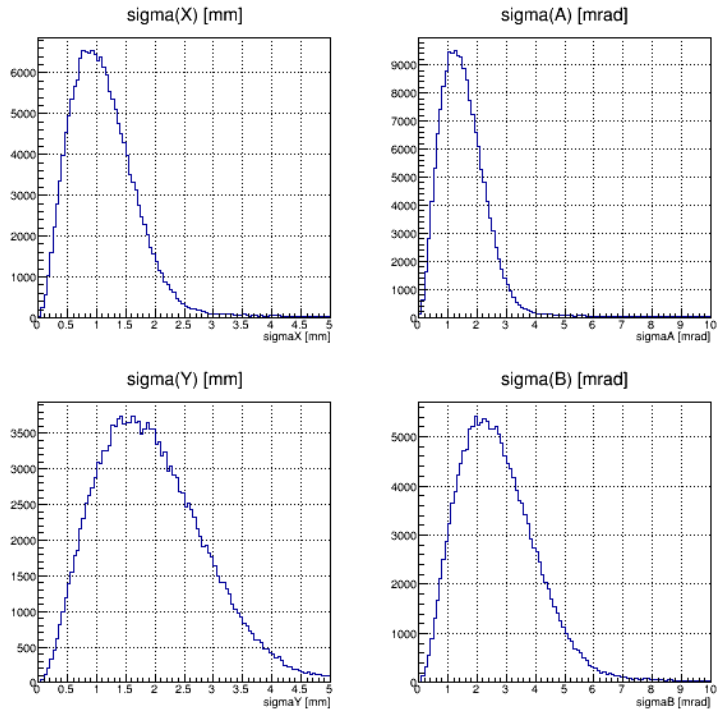

Figure 2-11 – The uncertainty of estimated parameters of the DCX1X2.

2.3.3 Multi-Wire Drift Chamber (MWDC-L and MWDC-R)

The MWDC was 1740 mm in width, 640 mm in height, and 250 mm in depth. The schematic of the MWDC is shown in Figure 2-12. It has 6 planes, labels as XX′UU′VV′. The detection area was 400 mm × 1120 mm (for the X plane). The number of wires of the X and X′ planes, U and U′ planes, and V and V′ planes were 56, 44, and 44 receptivity. The primed planes were shifted by ¼ cell (5 mm).

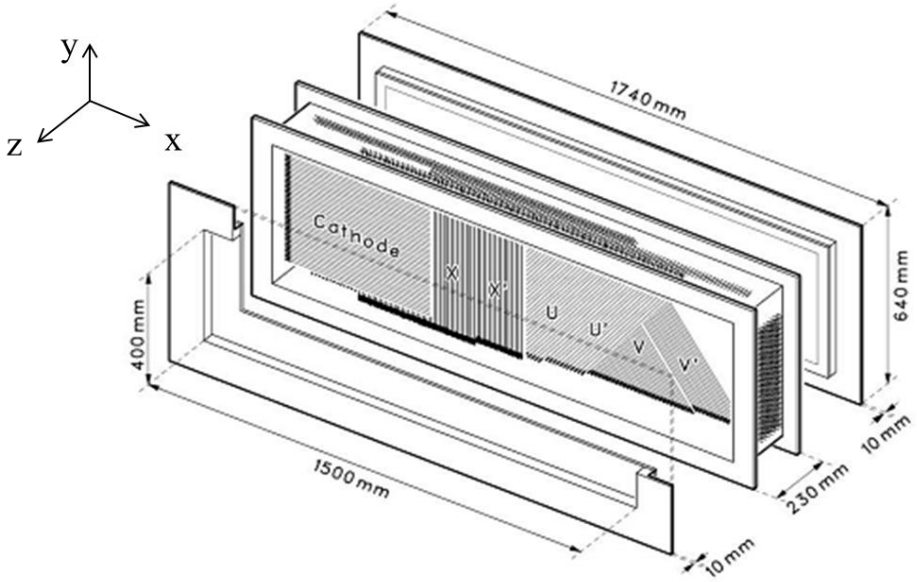

Figure 2-12 – Schematics view of MWDC structure [106].
The MWDC's local coordinate is shown on upper left with small letters. The local y axis was parallel with the y-axis of the laboratory frame.

The wire directions of the X and X′ planes were vertical (Figure 2-12) i.e. parallel to the laboratory's Y-axis (Figure 2-14). The UU′ wires and VV′ wires made angle of 36.87° [$\cos^{-1}(0.8)$] with respect to the XX′ wires. Because of this configuration, the corners were only covered by 4 planes. All cell sizes (perpendicular to wire direction) were 20 mm × 16 mm. The cells of the X′ and V′ planes were shifted toward the positive x-axis. The U′ plane was shifted to the negative x-axis. The wire alignment is shown in Figure 2-13. The voltage supply for the MWDC-L was 2900 V for the cathode and 3100 V for the potential line, it was 3000 V for the cathode and 3150 V for the potential line for the MWDC-R. The counter gas was 60% Ar + 40% C_2H_6.

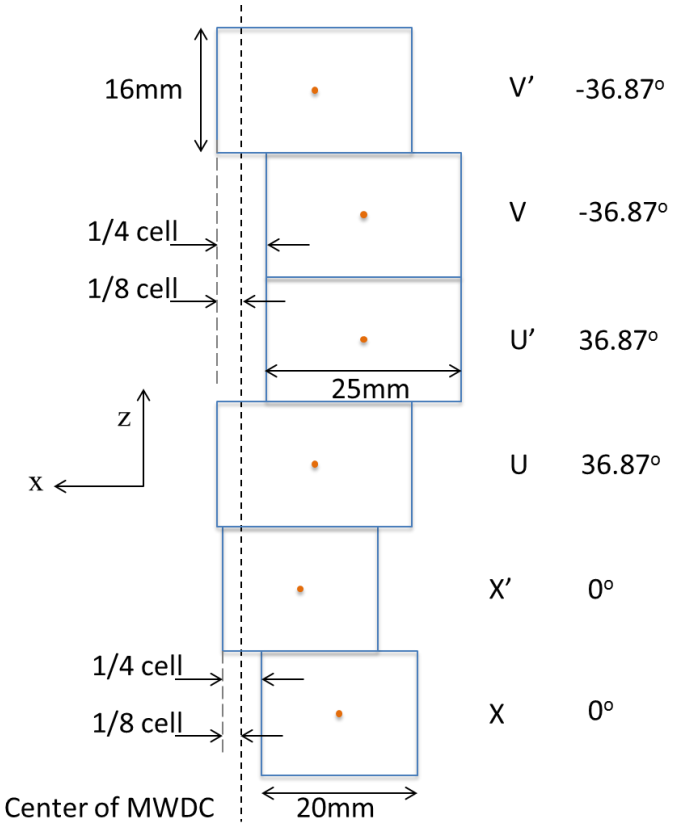

Figure 2-13 – Illustration of the MWDC wire plane configuration.
The orange dots are wire. Note that this is a cross section on the x-z plane, the width of the cell size of the U, U′, V, and V′ planes are 25 mm because the wire directions are not perpendicular to the x-z plane.

Table 2-6 – MWDC configuration.

	MWDC					
Size [mm^2]	1120 × 400					
Plane label	X	X′	U	U′	V	V′
Wire angle [deg]	0	0	36.87	36.87	-36.87	-36.87
Plane Pos. [mm]	-40	-24	-8	8	24	40
Cell width [mm]	20	20	20	20	20	20
Center (L) [wire]	48.143	47.893	37.9894	38.2394	37.9894	38.2394
Center (R) [wire]	9.107	8.857	6.7606	7.0106	6.7606	7.0106
Number of wires	56	56	44	44	44	44

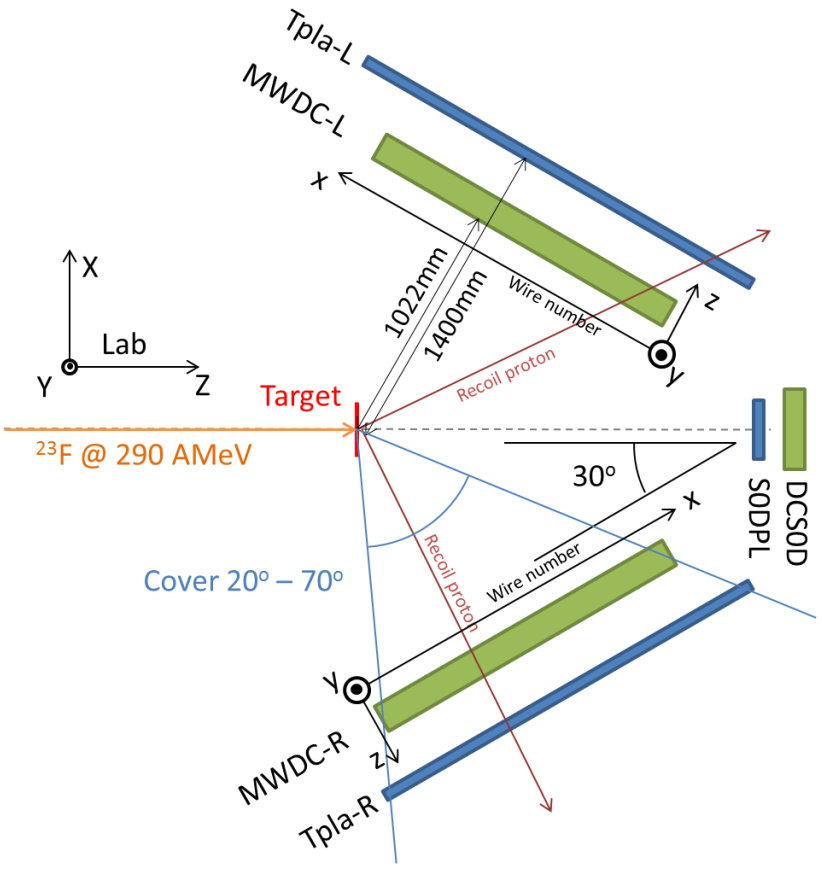

Figure 2-14 – The geometry of target, MWDCs, and Tplas.
The coordinate systems of the laboratory and the MWDC frames are shown. The laboratory frame coordinates are labeled by capital letters. The coordinates of the MWDC frame are labeled by small letters.

The global positions of the MWDC-L, MWDC-R, Tpla-L, Tpla-R, S0DPL, and DCS0D are shown in Figure 2-14. In the laboratory reference frame, the x-y plane of the MWDC made 30º with the beam line. The closed distance from the target to the MWDC mid-plane was 1022 mm at 60º forward angle. The angular acceptance covered from 20º to 70º.

2.3.3.1 Data Selection

The timing and energy of each wire were recorded by TDC and ADC respectively. A data selection was necessary because it ruled out the noise signals, improve the tracking quality, and reduce the calculation time by reducing the number of combinations between planes and wires. The time reference of the drift-time was the timing of the Tpla by TDC V767. Although the Tpla was located 378 mm away, the time delay of the scattering protons with energy ranging from 20 to 350 MeV was 6 ns at most. The drift-velocity was approximately 5 mm per 100 ns. Therefore, the timing of the Tpla did not affect the drift-time significantly. The drift-time distribution is shown in the left plot of Figure 2-15. The events with drift-time below -150 ns were counted as noise and discarded. The drift-time was selected from -150 ns to 160 ns. The energy loss distribution is shown in the right plot of Figure 2-15. The signal between 10

- 20 ch cannot produce any tracking with small sum of square of residual. They were probably noise and caused by scattered electrons (delta ray). Therefore, the energy loss was selected between 20 ch and 4000 ch.

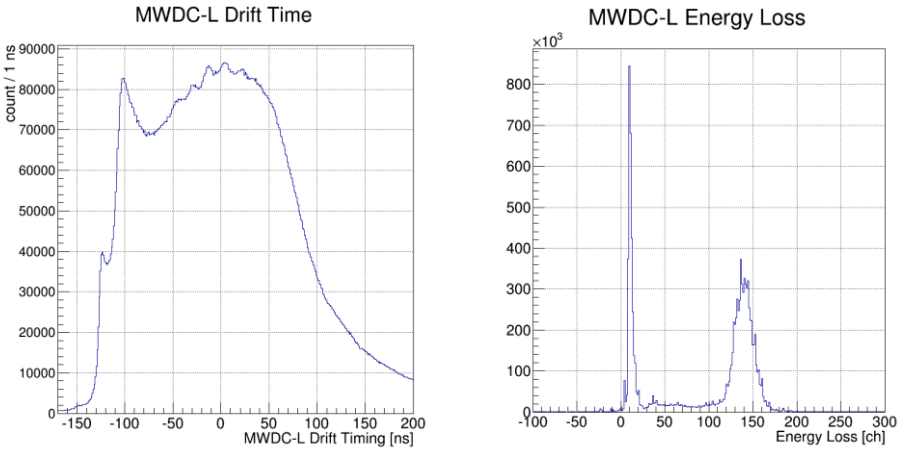

Figure 2-15 – Distribution of the drift-time (left) and the energy loss (right) in MWDC-L.

2.3.3.2 Ray Tracking Algorithm

Ideally, six values from all wire planes were recorded when a charged particle passed through the MWDC. The goal of the ray tracking is to obtain the tracking parameters: the hit positions (X, Y) and the incident angles (A, B), from those six values. The tracking algorithm can be formulated using linear algebra and matrix formulism, in which the positions and the incident angles are used to form the ray vector $\beta = (X, A, Y, B)$.

A wire vector $\vec{w} = (w_X, w_{X'}, w_V, w_{V'}, w_U, w_{U'})$ is the fired wire ID of each plane. The drift-length (DL) is calculated from a drift-time-to-drift-length function $f(DT)$, where DT is the drift-time. The function f is not necessarily the same for each plane. In each event, all possible combination of positions vector $\overrightarrow{\mathcal{P}_q} = \vec{w} + c_q|\overrightarrow{DL}|$ is constructed, where $\overrightarrow{\mathcal{P}_q}$ contains the position information from all planes, c_q is the left-right ambiguity vector with elements either +1 or -1, $\overrightarrow{DL} = (DL_X, DL_{X'}, DL_V, DL_{V'}, DL_U, DL_{U'})$ is the drift-length vector, and q is the index of possible combination, such that $q = 1,2, \dots, 2^n$, for n fired planes. The size of the vectors is equal to the number of fired plane, which could be 5 or 6. Then the best estimated ray vector $\hat{\beta}_q = (X, A, Y, B)_q$ and the sum of square of residues (SSR) SSR_q for each possible position $\overrightarrow{\mathcal{P}_q}$ is calculated by multi-dimension linear regression (Appendix A.3). The combination with minimum SSR is the most probable ray vector. In cases of multi-hits on each plane, all possible combinations of wires are calculated.

2.3.3.3 Incident Angle Correction

The theory of linear regression assumed that the drift-lengths are measured on the wire planes, but this assumption was broken by the cylindrical electric potential and the particles with large incident angles. The particles with scattering angle of 60º hit the MWDC normally, and the particles with scattering angle of 20º hit the MWDC at 40º with respect to the local z-axis of the MWDC (Figure 2-14). Figure 2-16 illustrates the situation. A trajectory with a ray vector β (black arrow) passes through a cell. The drift-length DL is not parallel with the wire plane, because the shape of the electric potential is cylindrical. Therefore, the drift-length DL is not the desired drift-length DL_Z (which is from the point P to the position of the wire w, Figure 2-16), and breaks the assumption of linear regression. The true ray vector β can only be correctly deduced by using DL_z. If we use DL and put it into the tracking algorithm, we get an incorrect ray vector $\hat{\beta}$ (the green arrow).

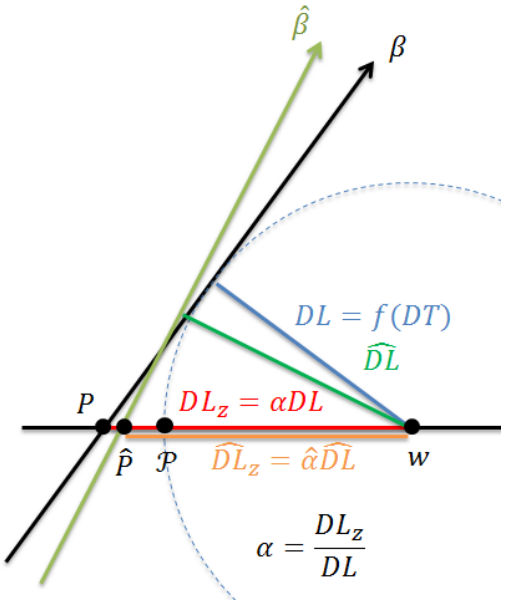

Figure 2-16 – Illustration of large incident angle.
***w* is the wire postion. The dotted circle is the equal potential surface. See main text for detail.**

An iteration method was introduced to approximate the drift-length on the wire plane DL_Z. We first used the position vector $\vec{\mathcal{P}} = \vec{w} + c\left|\overrightarrow{DL}\right|$, with incorrect drift-length DL to calculate a first approximation of the ray vector $\hat{\beta}^0 = (X^0, A^0, Y^0, B^0)$. A correction parameter α was constructed from this ray vector as

$$\hat{\alpha}^0(i) = \sqrt{1 + (A^0 \cos\theta_i + B^0 \sin\theta_i)^2}, \qquad (2.1)$$

where $\hat{\alpha}$ is the best estimator of α, i is the index of the planes, and θ is the wire angle. Then we had a first correction of the position vector $\overrightarrow{\mathcal{P}^1} = \vec{w} + c\left|\overrightarrow{DL}\,\alpha^0\right|$, and then used it to calculate the second approximation of the ray vector $\hat{\beta}^1$, and $\hat{\alpha}^1$, and then $\overrightarrow{\mathcal{P}^2} = \vec{w} + c\left|\overrightarrow{DL}\,\alpha^1\right|$, and so on. The iteration is shown in Figure 2-17. The DL_z after 5 iterations in the MWDC-L is shown in Figure 2-18. A smaller

wire ID corresponds to a large incident angle and the maximum DL_z can be larger than half of the cell size (10 mm).

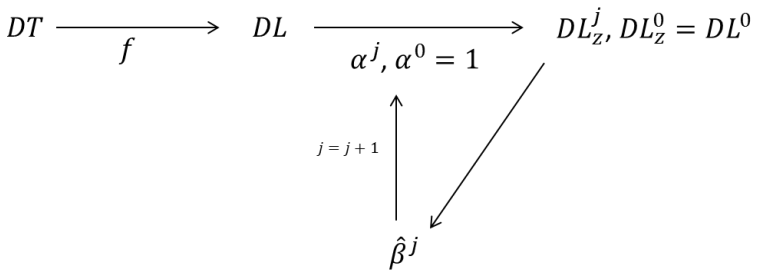

Figure 2-17 – Iteration for incident angle correction.

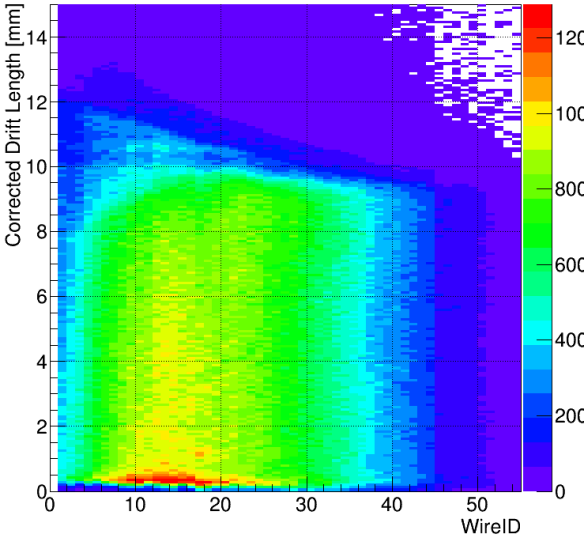

Figure 2-18 – The corrected drift length versus wire ID from MWDC-L.
According to the geometry, the wire ID 45 is for normal incident, and wire ID 0 is for largest incident angle.

The results of before and after the iteration on the tracking are shown in Figure 2-19. The tracking parameters X and A are related because the target can be approximated as a point source. In the MWDC frame (Figure 2-14), the relation between X and A was $X = 1022\,A$, and the target image should be a straight line (Figure 2-19). The result of no iteration was stripped at larger incident angle region, where the x-position was smaller than -400 mm. The strips disappeared after 5 iterations. This indicates that the iteration method improved the tracking.

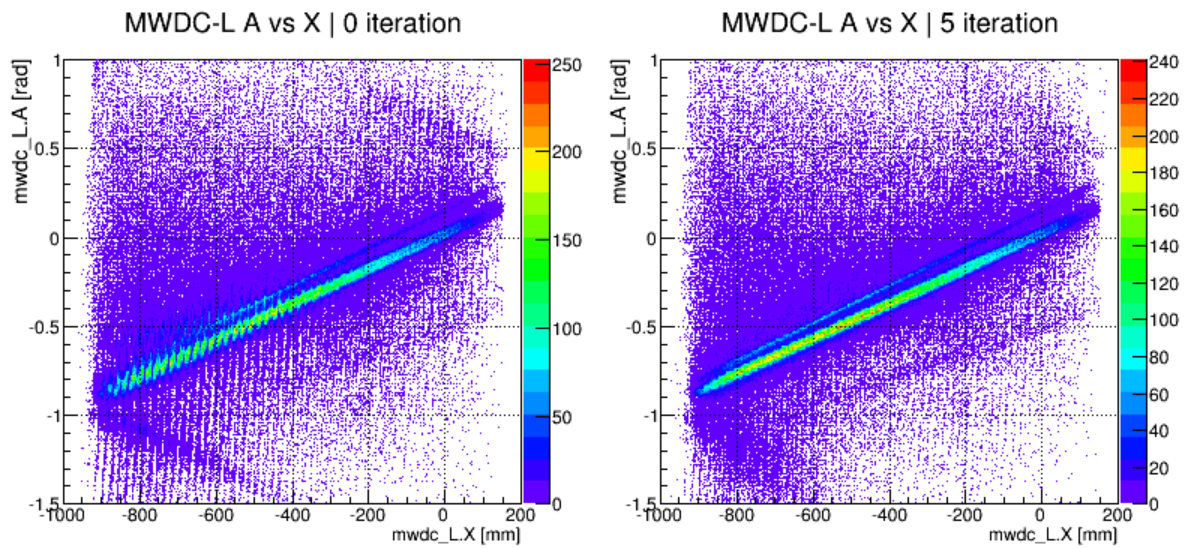

Figure 2-19 – Comparing ray tracking between iteration and without for the MWDC-L. There are three main loci. The top and thin locus is originated from the carbon target. The middle line above the bottom locus is originated from the NMR coil, which was in front of the target. The bottom line is originated form the target. The normally incident protons hit at $x = 0$ mm. The results with no iteration and 5 iterations are shown on the left and right respectively. The zip-zig pattern around $x = -700$ mm was gone. The large incident-angle protons hit that region.

2.3.3.4 Drift-Time to Drift-Length Conversion

The drift-length distribution should be uniform within a cell due to a small angular acceptance. A typical method to deduce the drift-time-to-drift-length function f is using the drift-time distribution. The integration of the drift-time distribution should be the desired function, because it results in a uniform drift-length distribution.

Any two distributions $h(x)$ and $g(y)$ can be related by

$$h(x)\Delta x = g(y)\Delta y. \tag{2.2}$$

If one of the distribution is uniform, say $g(y) = conts$, then the other distribution is calculated using

$$\frac{dy}{dx} \propto h(x), \qquad y \propto \int h(x)dx. \tag{2.3}$$

However, this method does not always work, for example, the drift-length distribution should not be uniform for a focused beam, or the drift-length depends on the incident angle, which was the case in our experiment.

We used the "omitted plane method" to deduce the drift-time-to-drift-length function f. For an event with 6 planes fired and traceable, we omitted one of the plane, and then performed a 5-plane ray tracking (5-PRT) with the incident angle correction. On one hand, the 5-PRT gave a ray vector, and then we could use this ray vector to estimate the drift-length on the k-th omitted plane $\widehat{DL_{zk}}$ and $\widehat{DL_k}$. On the

other hand, the 6-plane ray tracking (6-PRT) with the incident angle correction gave others estimations on the drift-length $\widehat{DL_Z}$ and $\widehat{DL}$. If the drift-time-to-drift-length function f was correct, the $\widehat{DL}$ and $\widehat{DL_k}$ should be the same. By comparing the $\widehat{DL}$ and $\widehat{DL_k}$, we could get the true conversion function.

The flow of the omitted plane method is shown in Figure 2-20. We used equation (2.3) to make the initial guess of the conversion function f^0. The flow contains two loops. The red loop in Figure 2-20 is for the incident angle correction (Figure 2-19). This loop is necessary for giving a more reliable DL_z and then a better estimation of $\widehat{DL}_{zk}$. The outer loop is for the conversion function. The factor of the incident angle correction in the 5-PRT is $\hat{\alpha}_k$. It can be replaced by $\hat{\alpha}$ from the 6-PRT. The goal for the iteration is to obtains as small $DL - \widehat{DL}_k$ as possible.

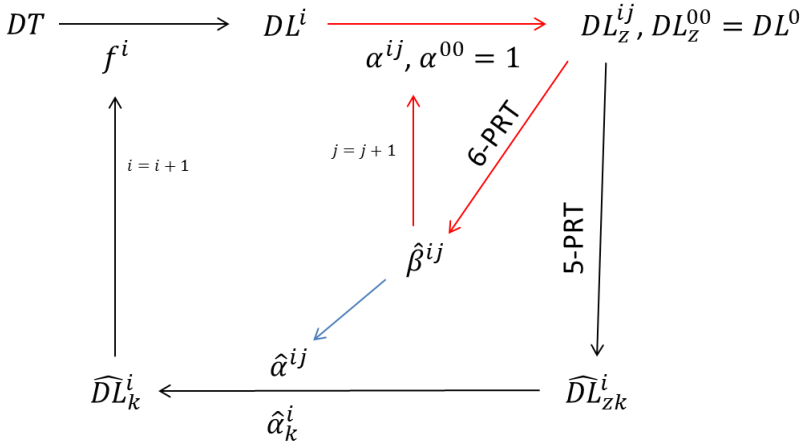

Figure 2-20 – The procedure of finding drift-time-to-drift-length conversion function. The subscript *k* means omitting the k-th plane.

2.3.3.5 Detection Efficiency

The detection efficiency contained two parts: fired efficiency and tracking efficiency. The fired efficiency is the ratio of the number of events for which at least one plane was fired over number of charged particles that passed through. Assuming the fired efficiency of each plane is ϵ and the total number of charged particles that passed through is N, the number of planes fired is following the binomial distribution $N_i = NC_i^6\epsilon^i(1-\epsilon)^{6-i}$, where N_i is the number of events for which i planes were fired, $C_i^6 = 6!/(i!\,(6-i)!)$ is the binomial factor. The fired efficiency is $\epsilon_{fired} = 1-(1-\epsilon)^6$. The count of 0 plane fired was ignored, because the Tpla can be fired by gamma ray. The fired plane distribution is shown in Figure 2-21. The distribution does not exactly follow binomial distribution. This is because of the wire configuration and also the fired efficiencies of each plane may be different. The efficiency was only deduced for the central area, because the corners were not covered by 6 planes but 4 planes (Figure 2-12). We also restricted that the energy loss of Tpla had to be larger than 1000 ch to ensure charged particle was passing through. The fitting with a binomial distribution showed that the fire efficiencies of each plane of the MWDC-L and MWDC-R were 0.968 and 0.933 respectively.

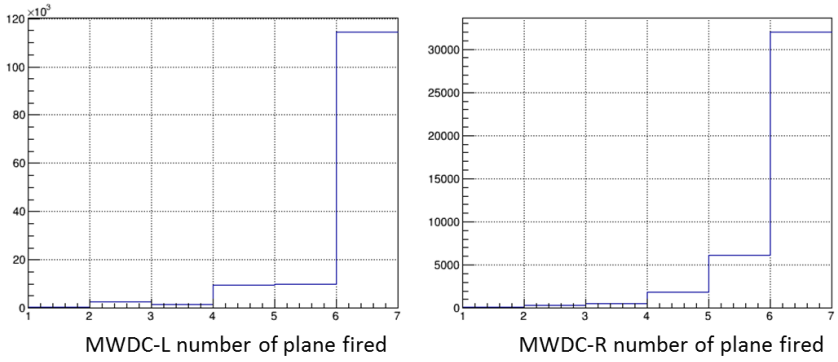

Figure 2-21 – Distribution of number of fired planes for the MWDCs.

The tracking efficiency is defined as the ratio of the number of tracked events over the number of events for which at least one plane was fired. The result is shown in Figure 2-22.

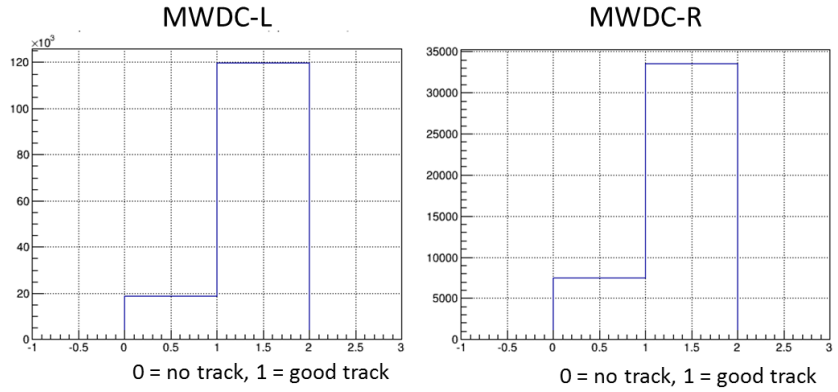

Figure 2-22 – Distribution of tracked events.
No track means the SSR is larger than 10 mm^2.

The individual detection efficiencies were 80% and 78% for the MWDC-L and the MWDC-R respectively. The combined detection efficiency was a simple product because the two MWDC were operating independently. The detection efficiency is listed in Table 2-7. Note that the efficiency depended on the hit position, an average value was taken and the result had approximately 3% uncertainty.

Table 2-7 – Detection efficiency of MWDC.

	MWDC-L	MWDC-R
Fire eff. (plane)	0.968	0.933
Fired eff.	1.0	1.0
Tracking eff.	0.80	0.78
Detection eff.	0.80	0.78
Combined eff.	0.624	

2.3.3.6 Position and Angular Resolution

The resolution can be calculated by equation (A.3.15) (see Appendix A.3 for more detail). The distributions of the uncertainty of the best estimated ray parameters X, A, Y, B are shown in Figure 2-23. Because the degree of freedom can be two in the 6-PRT or one in the 5-PRT, the distribution was a mixture of chi distributions with degree of freedom of two and one. The estimated standard error of each ray parameter was the peak value of the corresponding distribution.

The drift velocity of the electrons in the MWDC was approximately 5 mm/100 ns. The time resolution of the drift time was 1 ns at most. Therefore, the drift-length resolution should be at least 0.05 mm. The experimental resolution of the X position was 0.1 mm, the additional uncertainty was caused by the tracking, the approximation methods, and the time delay caused by the distance between the MWDC and the Tpla.

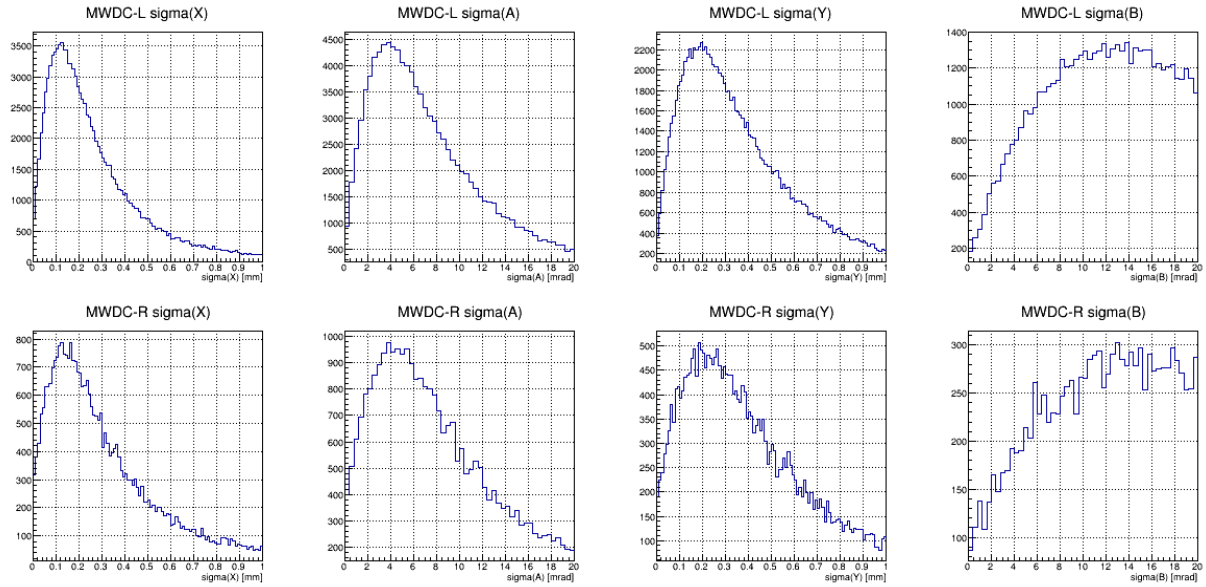

Figure 2-23 – Distribution of the uncertainties of the ray parameters.

2.3.4 Drift Chamber DCS0D

The DCS0D was located around 1.5 m downstream of the target and behind the S0DPL. The configuration is shown in Table 2-8. Due to the configuration, the DCS0D can only track the positions (X, Y). The time reference of the DCS0D came from the S0DPL. The drift-time-to-drift-length conversion table was deduced by integrating the drift-time distribution. The detection efficiency was 95.9% for oxygen, which was selected from the Hodo array.

Table 2-8 – Configuration of the DCS0D.

	DCS0D			
Size [mm^2]	144 x 216			
Plane label	X	X′	Y	Y′
Wire angle [deg]	90	90	0	0
Plane Pos. [mm]	-15	-5	5	15
Cell width [mm]	12	12	12	12
Center [wire]	21	21.5	11	11.5
Number of wires	40	40	20	20

2.3.5 Hodo Array and MWDC-S1

The Hodo array and the MWDC-S1 were placed at the exit of the SHARAQ-D1 magnet (or D1 magnet for short, Figure 2-2). They were used for the residue identification. The relative position of the MWDC-S1 and the Hodo array are shown in Figure 2-24. The Hodo array was a hodoscope consisting of 14 identical plastic scintillators. Each scintillator is labelled as Hodo-0 to Hodo-13. We call anyone of them as Hodo when no label is specified and Hodos for multiple of them. Each Hodo was 85 mm in width, 180 mm in height, and 5 mm in depth. Each of them was connected to one PMT, and the timing and the energy loss were recorded. The even labelled Hodos were 10 mm downstream from the odd labelled Hodos. Adjacent Hodos were overlapped by 5 mm. The model of the MWDC-S1 was basically as same as the MWDC-L and the MWDC-R. The MWDC-S1 made a 13.5 degree with respect to the optical axis and paralleled to the exit plane of the D1 magnet. The Hodo array paralleled to the MWDC-S1. The timings of the MWDC-S1 and each Hodo were recorded by TDC V1190.

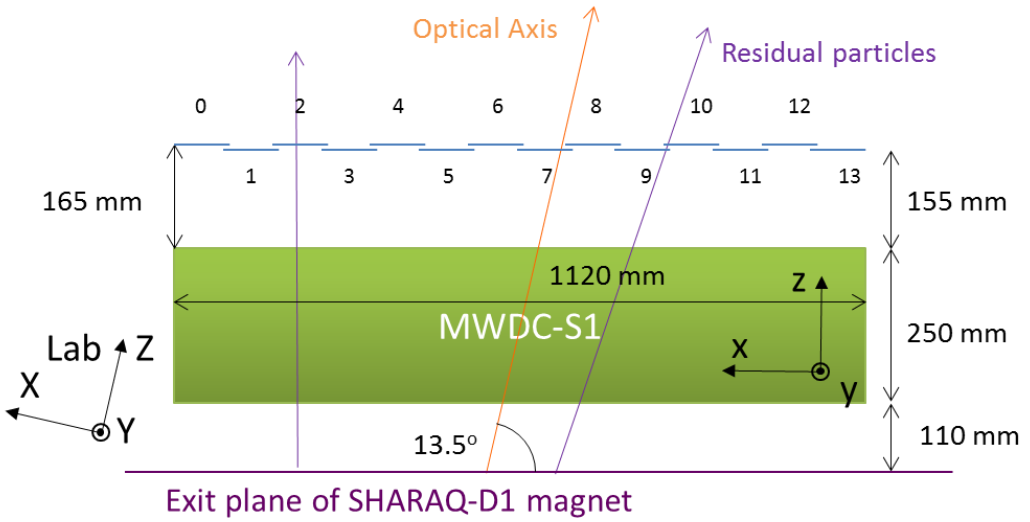

Figure 2-24 – Relative position of the MWDC-S1 and the Hodo array.
The thin blue lines represent each Hodo. The normal of the exit plane of the SHARAQ-D1 magnet makes 13.5° with the optical axis of the beam. The laboratory's coordinate is shown in the left side with capital letters. The local coordinate of the MWDC-S1 and the Hodo array is inside the MWDC-S1 with small letters.

2.3.5.1 Hodo Array

The multiplicity of the Hodo array is shown in Figure 2-25. There were 72% single-hit events. In the multi-hit events, 73% were caused by adjacent-hit. Only 7.8% of multi-hit events were true multi-particle-hit.

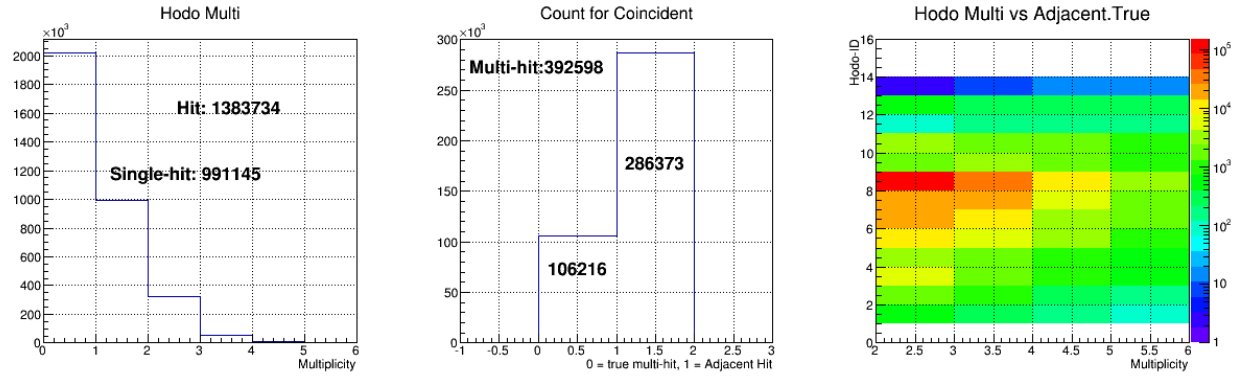

Figure 2-25 – Multiplicity of Hodo.
(Left) Multiplicity, (middle) Adjacent-Hit, (Right) Hodo-ID vs multiplicity.

The timing was recorded by TDC V1190 with a 2.8 μs time window. The true events were selected using a time gate (-270 ns to -210 ns). The TOF(S0DPL-Hodo) was calibrated for the Hodo-7 and the Hodo-8 by ^{23}F and ^{22}O. The time offsets of the rest of the Hodos were calibrated using the overlap area between the adjacent Hodos. The time offsets and the channel-to-nano-second conversion factors are listed in Table 2-9. Note that the Hodo-13 was not used because the number of counts was very small.

Table 2-9 – Hodo time offset and ch2ns conversion factors.

	Offset	ch2ns
Hodo-00	50.18	0.09765625
Hodo-01	49.28	
Hodo-02	49.58	
Hodo-03	50.28	
Hodo-04	50.58	
Hodo-05	50.08	
Hodo-06	50.18	
Hodo-07	49.02	
Hodo-08	46.45	
Hodo-09	44.48	
Hodo-10	44.78	
Hodo-11	44.48	
Hodo-12	41.98	
Hodo-13	0.00	

We found that the energy loss of each Hodo depended on the timing. The left plot in Figure 2-26 shows the energy loss versus timing in the Hodo-8. This correlation was because the recording time window of the ADC overlapped with signals marginally. The time window depended on the trigger time and the timing of a Hodo was $t_{Hodo} = t_{raw} - t_{trig}$, where t_{trig} was the trigger time of the DAQ, and it was

from the Tpla in the ppcoin trigger (see Section 2.4.1). When the trigger time came earlier, the time window covered a whole signal, and the recorded energy was independent from the timing. But when the trigger time was late, the time window only covered portion of a signal and only recorded part of the energy loss. Therefore, the recorded energy loss depended on the timing. This was corrected by normalizing the signal with a function of time. The left plot in Figure 2-26 shows 9 loci, from the top is fluorine, the next on is oxygen, then nitrogen, and so on. The function was extracted by using the locus of the oxygen. The result of the correction of the Hodo-8 is shown in the middle plot of Figure 2-26.The energy projection of the middle plot is shown in the right plot.

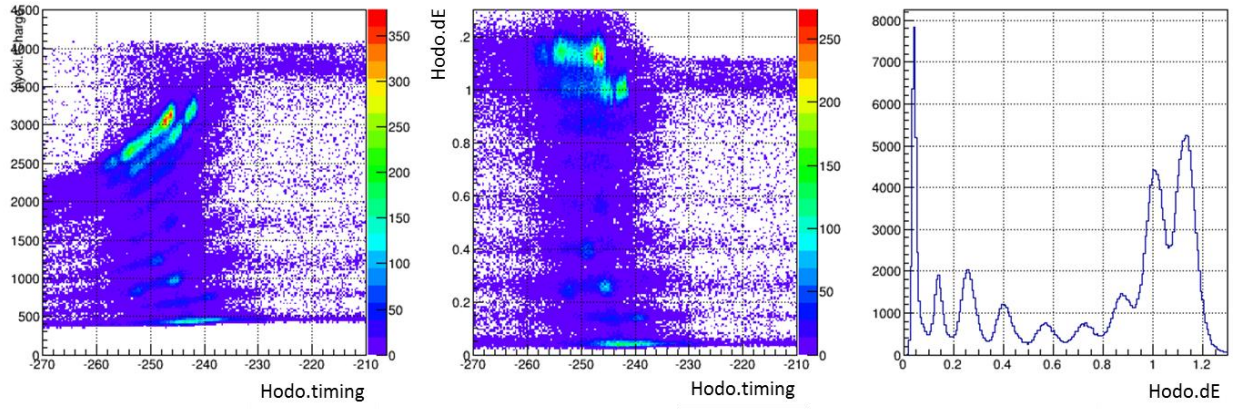

Figure 2-26 – Correction between the energy loss and the timing from the Hodo-8. The energy loss vs timing before (left) and after (middle) correction. The right figure is the projection on the corrected energy loss. Note that the left plot is not a PID plot but simply energy loss versus timing of the Hodo-8.

2.3.5.2 MWDC-S1

The MWDC-S1 was a 6-plane multi-wire drift chamber similar to the MWDC-L and the MWDC-R, except the configuration of the X and X′ planes were swapped. The time reference came from the Hodo timing. Because of the multiplicity of the Hodo, the timing with largest energy loss was selected as the reference timing (see Appendix 0 for a detailed explanation). The detection efficiency of the MWDC-S1 was 95.9%. The tracking results are shown in Figure 2-27. The relation between the ray parameters X and A was almost linear because of the point source nature of the target. and the D1 magnet can be regarded as a simple magnifying lens. The value of A was $-0.24 = -\tan(13.5°)$ at X = 0 mm reflected that the x-y plane of the MWDC-S1 made a 13.5 degrees with the optical axis. The image of Y versus X shows the image of the Hodo array (the upper right plot of Figure 2-7). The resolutions of the tracking parameters are shown in Figure 2-28.

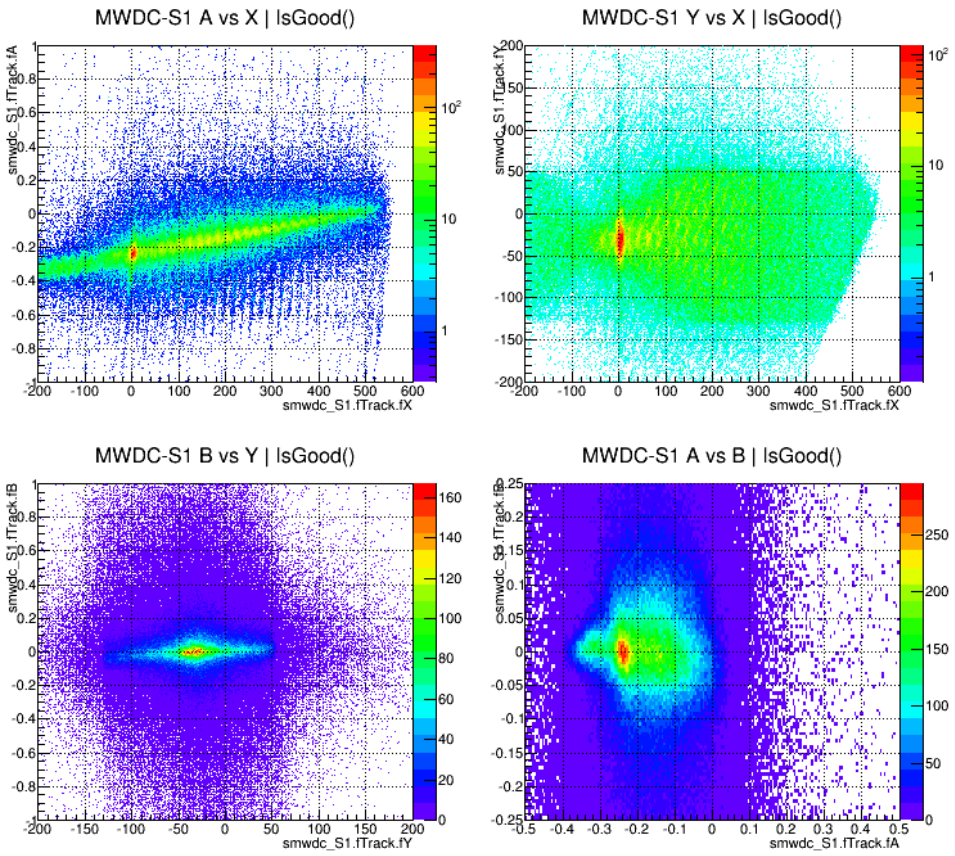

Figure 2-27 – The coincident plots for the tracking parameters from the MWDC-S1.

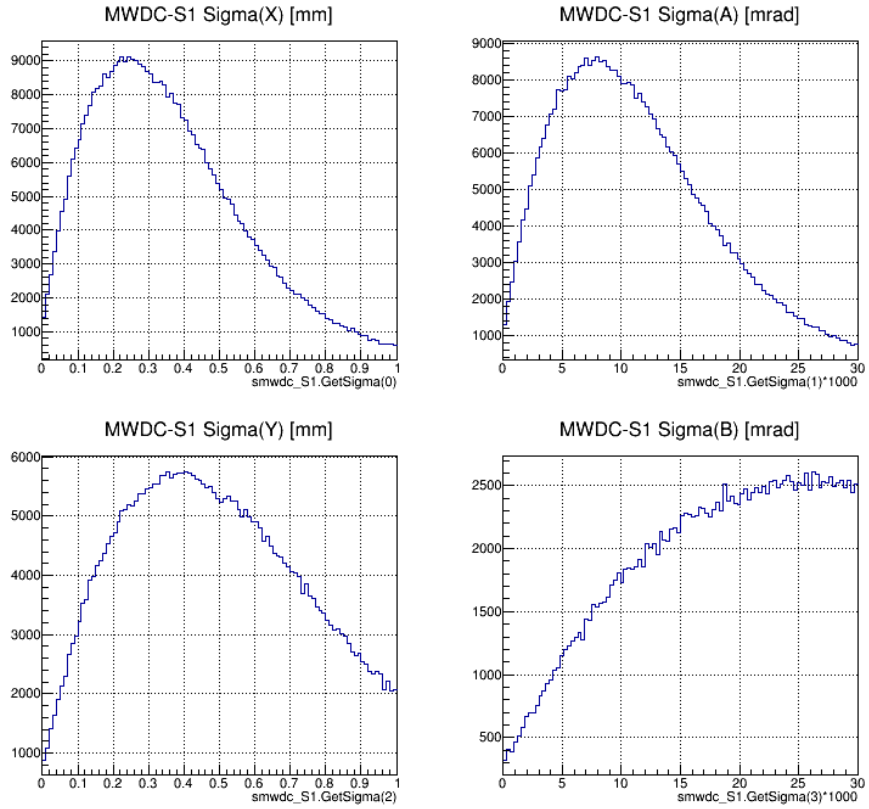

Figure 2-28 – The distributions of the standard error of tracking parameters from the MWDC-S1.

2.3.6 Detectors Performance

The efficiencies of all plastic scintillators and the Hodo array were assumed to be 100%. The time resolutions of plastic scintillators were calculated with the help of nearest drift-chambers. The detectors performances are summarized in Table 2-10.

Table 2-10 – Detectors efficiencies and resolutions.

Detector	Efficiency	Resolution [sigma]
F3PL	100%	NA
FH9PL	100%	220 ps
Tpla-L	100%	500 ps
Tpla-R	100%	600 ps
S0DPL	100%	NA
DCX1X2	90.2%	σ(X) = 0.8 mm, σ(Y) = 1.4 mm σ(A) = 1.4 mrad, σ(B) = 2.4 mrad
MWDC-L	80%	σ(X) = 0.1 mm, σ(Y) = 0.2 mm σ(A) = 4 mrad, σ(B) = 13 mrad
MWDC-R	78%	σ(X) = 0.15 mm, σ(Y) = 0.2 mm σ(A) = 4 mrad, σ(B) = 13 mrad
DCS0D	95.9%	NA
MWDC-S1	95.9%	σ(X) = 0.25 mm, σ(Y) = 0.4 mm σ(A) = 8 mrad, σ(B) = 27 mrad
Hodo array	100%	NA

2.4 Data Acquisition System

Many triggers were used in the experiment. We will only focus on 2 triggers: beam trigger and proton-proton coincident (ppcoin) trigger. The beam trigger was a down-scaled trigger from the FH9PL. The down-scaled ratio was 1/40, or one in 40 events was recorded. The ppcoin trigger was fired when both of the Tpla-L and the Tpla-R were triggered. The triggers were not mutually exclusive.

2.4.1 Circuit Diagram of The ppcoin Trigger

The ppcoin trigger was the tag of the (p,2p) events. The circuit diagram of the ppcoin trigger is shown in Figure 2-29. The orange colored boxes represent PMTs of the Tpla. The PMTs were the starting points of the signals. The arrows represent the flow of signals. The signals from the PMT-LB, LF, RB, and RF were fed into discriminators with threshold of -19 mV and output time width of 80 ns. The light traveled at 0.66c inside the Tpla of 1500 mm long, the maximum time difference between the forward and the backward signals should not be more than 10 ns. The forward PMTs, LF and RF, were delayed

by 20 ns so that the time reference was always the forward PMTs. The delayed forward signal and the backward signals were combined in a coincident module. The signal of the Tpla-R was fed into a gate generator to give a 50 μs time gate. The combined signal of the Tpla-L was further delayed by 210 ns because of the cable length. Therefore, the reference time of the ppcoin trigger was the signal from the PMT-LF. The signals from the PMTs were duplicated by fan-in-fan-out units (L.FIFO). Each signal was delayed by 600 ns, and fed into QDC V792 for recording the energy loss in the Tpla.

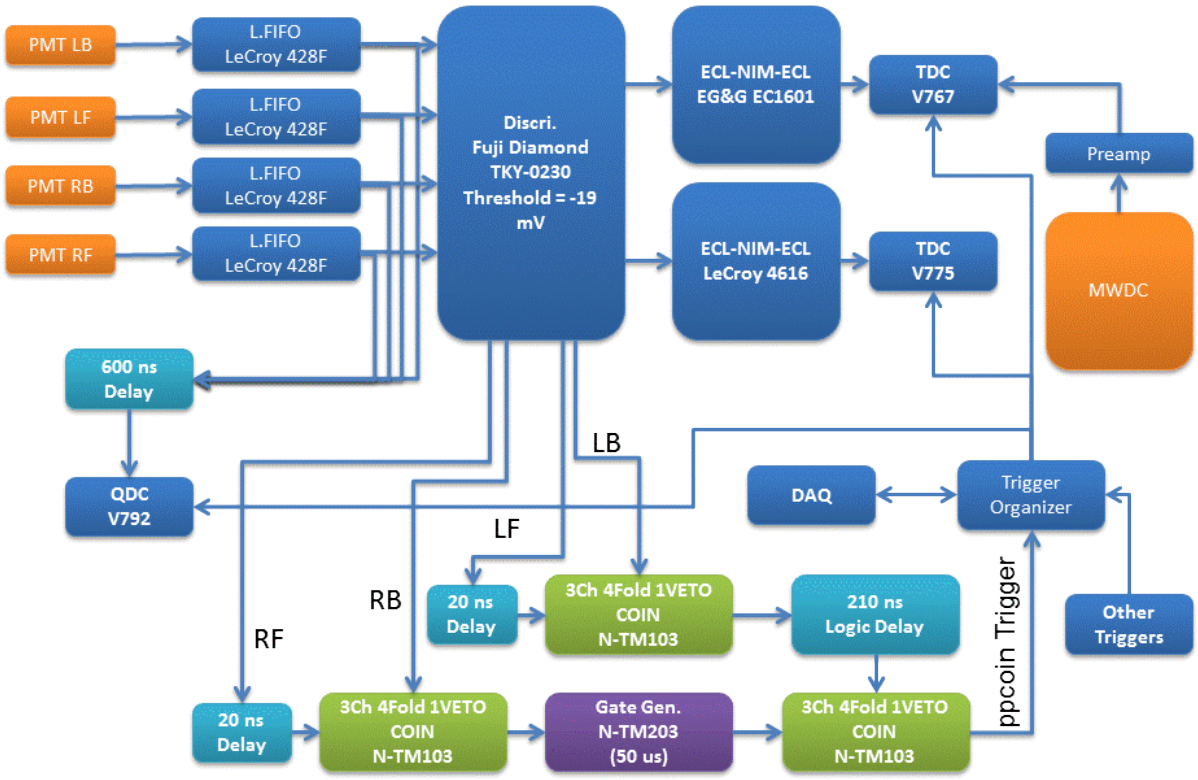

Figure 2-29 – Circuit diagram for the ppcoin trigger.
See main text. The single arrow to the QDC V792 did not mean signals were combined, each signal was recorded separately in the QDC.

2.5 Spin-Polarized Solid Proton Target

The spin-polarized target was installed to provide an asymmetry on the differential cross section so that the $J_> = l + s$ and $J_< = l - s$ orbits of the bound proton can be distinguished [96]. However, Because of the insufficient yield and small absolute polarization (30%) [110], the asymmetry cannot be extracted with sufficient accuracy and precision (Appendix C.9). Therefore, the target system is not presented in here, but detailed reports can be found in References [111] [112] and Appendix C.

Chapter 3

Data Analysis and Results

The objectives of the analysis are to obtain the excitation energy of the reaction residue, then deduce the cross section, the spin state, and the spectroscopic factor. We present the ^{23}F(p,2p) analysis first, the analysis method of the ^{25}F(p,2p) reaction was the same and the results are shown after. The reaction identification was the first step of the analysis. After that, the excitation-energy spectrum of the reaction residue was extracted. The integrated cross-sections and the spectroscopic factors were then deduced. Italic font is used for gates to avoid confusion.

3.1 Properties of the Incident Beam

3.1.1 Particle Identification

Since the F6-PPAC was switched off in physical runs of ^{23}F, the particle identification was done by ΔE-TOF method and the plot is shown in Figure 3-1. The gate on ^{23}F is shown in the red square. The ^{23}F nucleus was selected between $5680 < \Delta E < 6060$ ch and $-1465 < \mathrm{TOF} < -1460$. The purity of ^{23}F was 36.5% from event by event identification.

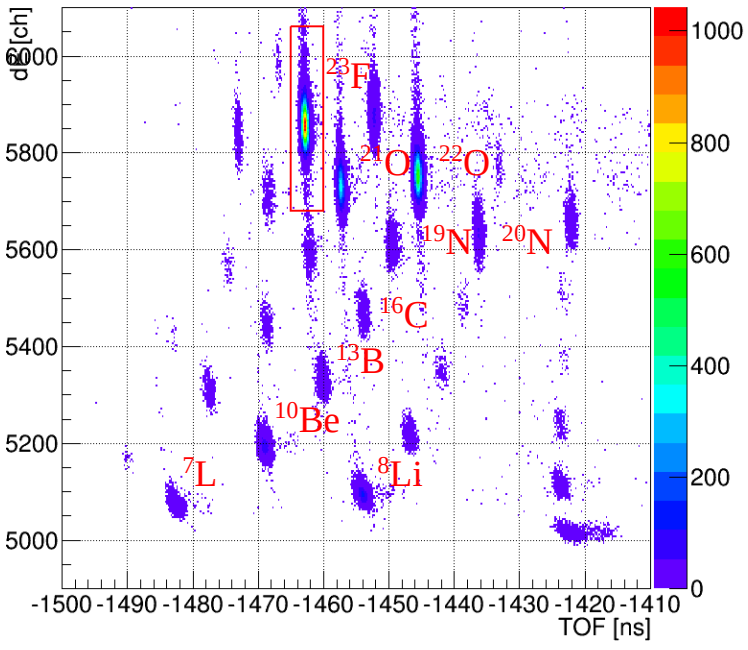

Figure 3-1 – The ΔE-TOF plot upstream PID. The *^{23}F* gate is inside the red rectangle.

3.1.2 Kinetic Energy

The distribution of kinetic energy per nucleon (KE/A) of ^{23}F was obtained from the optics runs and is shown in Figure 3-2. The spread of the kinetic energy was ± 0.7 MeV/nucleon or ± 0.2%.

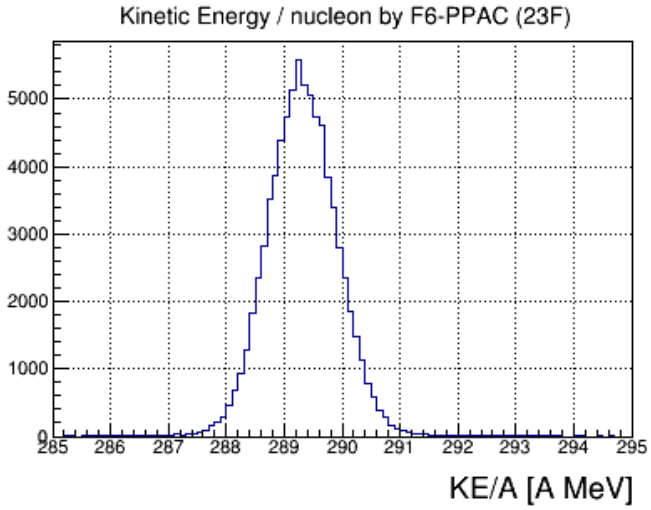

Figure 3-2 – The distribution of the kinetic energy per nucleon obtained from the F6-PPAC.

3.1.3 Beam Profile

The beam profile on the target was deduced from the tracking of the DCX1X2. The beam profile under the beam trigger is shown in Figure 3-3. The left plot is the position distribution and the right plot is the angular distribution under the ^{23}F gate and the beam trigger. The circle in the left figure shows the position of the target crystal (Section 3.3). The target-hit-ratio was defined as the number of events within the circle over the number of tracked events by the DCX1X2, and it was 61.3%.

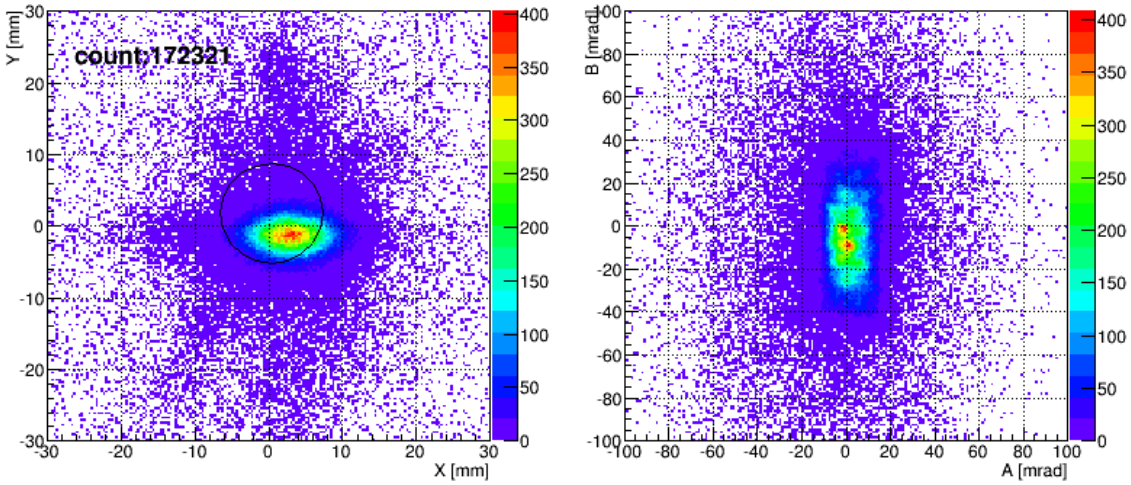

Figure 3-3 – Bema Profile on the target deduced from ray tracking of DCX1X2.
(Left) The beam image on the target crystal, where X and Y is the x and y positions. (Right) The incident angles A and B of the beam.

3.2 Reaction Vertex and Carbon Background

The reaction vertex was back-tracked using the MWDC-L and the MWDC-R together with the tracking of the DCX1X2. The 3-dimension coordinates of the reaction vertex are denoted as vertex(X), vertex(Y), and vertex(Z). The vertex(X) and vertex(Y) are also denoted as S0.X and S0.Y respectively. The vertex(X) and vertex(Y) were calculated using the tracking results of the DCX1X2. Using the ray-tracking results [X and A (Figure 2-19)] of each MWDC, an interception of the ray on the laboratory Y-Z plane and the vertex(X) was calculated. The Z-position of the interception was the vertex(Z). Since the interception was an extrapolation of the tracking results, the interceptions from the MWDC-L and the MWDC-R could be different and an uncertainty-weighted average was used as the vertex(Z). The resolution of vertex(X) and vertex(Y) were approximately 1 mm, and the resolution of vertex(Z) was approximately 15 mm.

The vertex(Z) under $^{23}F \cap$ *ppcoin* $\cap$ *vertexXY* $\cap$ *tofS0dS1* $\cap$ *pidZ* gates is shown in Figure 3-4. The peak around vertex(Z) = 10 mm is the target crystal. A *vertexZ* gate for the target was defined as |vertex(Z)-10|<30 mm. A clear target and carbon peaks are shown in Figure 3-4. The *vertexZ* gate cover 95% of the Gaussian with central at 10 mm.

A carbon target was placed at 160 mm downstream of the target. It provided an estimation for the carbon contamination. The carbon target was identified from the vertex(Z). In Figure 3-4, the peak around vertex(Z) = 170 mm is from the carbon target. A carbon gate was defined as |vertex(Z)-160|<30 mm and is called as *vertexZc*. We define a *Common* gate in here for future discussion. The *Common* gate is formed by a union of the ^{23}F gate and the ppcoin trigger.

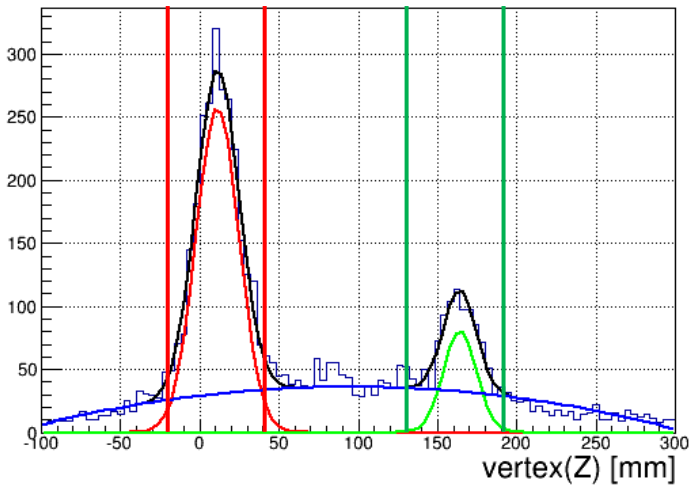

Figure 3-4 – vertex(Z) under $^{23}F \cap$ *ppcoin* $\cap$ *vertexXY* $\cap$ *tofS0dS1* $\cap$ *pidZ* gates.
The gate definitions are listed on Table 3-2. The histogram was fitted with 2 Gaussians and a second-order polynomial. The reduced chi-squared is 1.8. The *vertexZ* gate is defined between the red lines. The *vertexZc* gate is defined between the green lines.

3.3 Target Position and TOF(S0D-S1)

The target was surrounded by a thick hydrogen free target holder (made from PCTFE, polychlorotrifluoroethylene, $[CF_2\text{-}CFCl]_n$). Since the beam trigger and the ppcoin trigger are not exclusive, the target position cannot be determined by comparing the beam profile from the beam trigger and that from the ppcoin trigger. The other way was using the different in energy losses between the residues with large charge number and small charge number.

Whenever the ^{23}F beam hit on the 8 mm thick target holder and 2 scattered protons were detected by the Tplas, residues were produced. The residues with large charge number lost more energy in the target holder than the residues with small charge number because of the Bethe's formula. Therefore, from the target holder, only residues with small charge number can reach to the Hodo array. Because the target crystal was 1 mm thin, the energy losses for all residues were small, hence, most of them can reach to the Hodo array. Therefore, by gating on the residue with charge number > 5 from the Hodo array, the position of the target crystal can be revealed. The left plot of Figure 3-5 shows the target position. We define a gate for the residue with large charge number in the Hodo array, and called it as *Hodo-charge* gate. The plot was calculated by dividing 2 plots - a plot with the *Hodo-charge* gate ∩ *vertexZ* gate ∩ *Common* gate divided by a plot with the negation of the *Hodo-charge* gate ∩ *vertexZ* gate ∩ the *Common* gate. The target crystal was a circle, which centered at (X,Y) = (0.4, 1.8) mm with radius of 7 mm. We define a *vertexXY* gate as the circle of the target crystal.

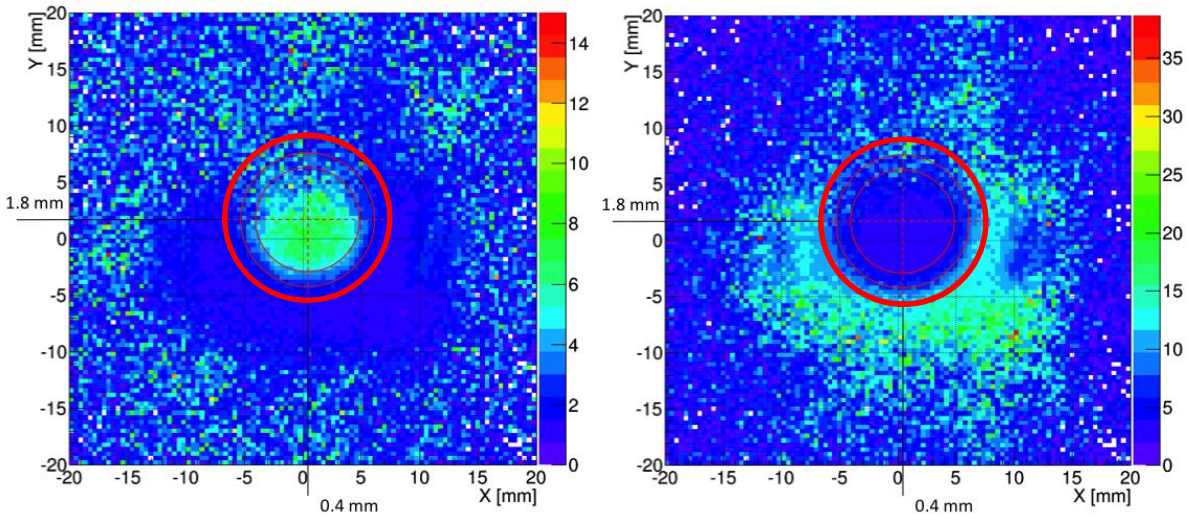

Figure 3-5 – Images of target crystal position.
See main text. The right figure is an inverse of the left figure. The guided circles are red in color. The largest red circle is 14 mm diameter. This circle is also the *vertexXY* gate.

The target position was cross checked with another method. Residues lost more energy in the target holder than in the target crystal, due to the different thicknesses, that resulted in a longer TOF(S0D-S1) on the target holder. Therefore, the position of the target crystal can also be revealed using a gate on the

TOF(S0D-S1). Figure 3-6 shows the correlation between the S0.X and the TOF(S0D-S1). The target crystal ranged from S0.X ∈ (-7, +7) mm. The TOF was longer at outside because of the thick target holder. A *tofS0DS1* gate was defined as 32 ns < TOF(S0D-S1) < 35 ns to eliminate most events from the target holder. Figure 3-7 shows that the crystal position deduced from the *tofS0DS1* gate. The result was consistent with Figure 3-5.

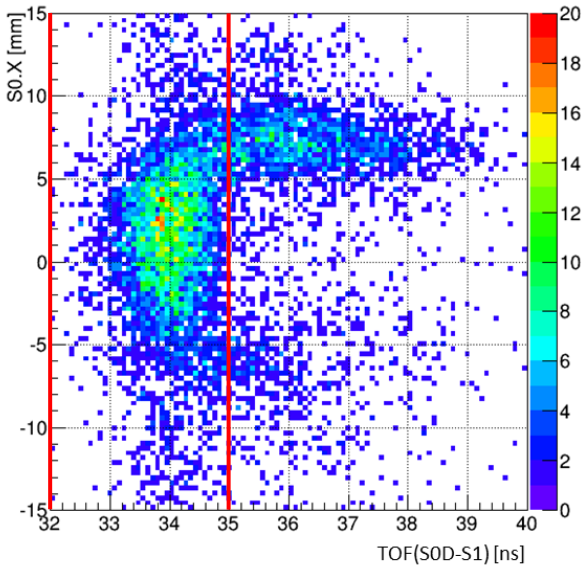

Figure 3-6 – The plot of S0.X versus TOF(S0D-S1).
The plot was gated on a union of the oxygen gate from the Hodo array, |vertex(Z)| < 7 mm, and |S0.Y| < 2 mm. The *tofS0DS1* gate is defined from 32 ns to 35 ns, or between the red lines.

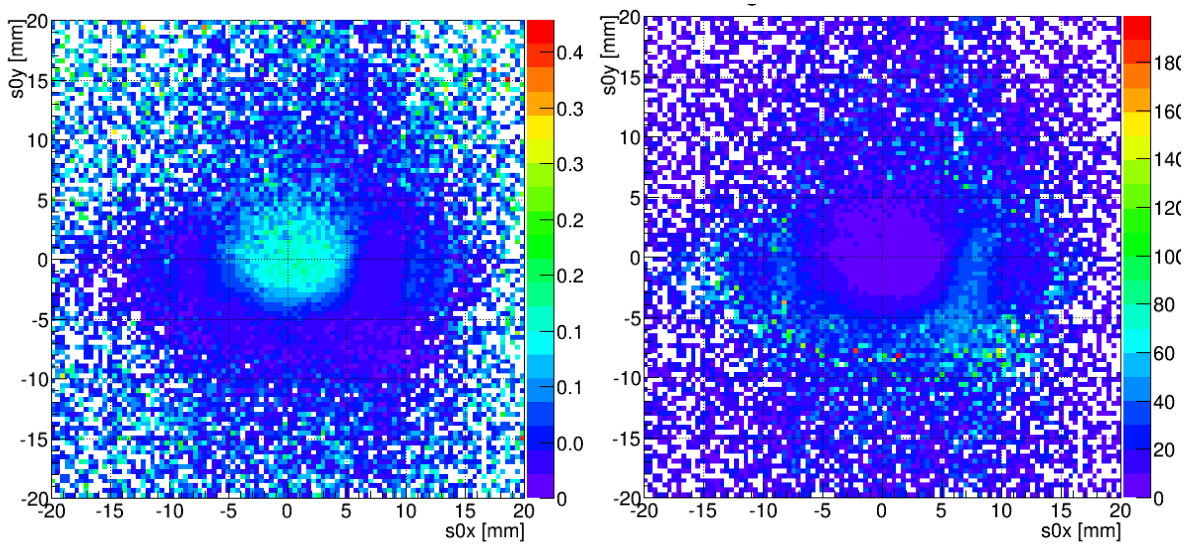

Figure 3-7 – The crystal position revealed using the *tofD0DS1* gate.
See main text. The right plot is the inverse of the left plot.

3.4 Residue Identification

The target crystal contained carbon atoms and the size of the beam spot was larger than the size of the target crystal, therefore, many kinds of residual nuclei were produced in the target and in the target

holder. The SHARAQ spectrometer was used to identify the residues. We had tried two methods, one was using the magnetic rigidity of the SHARAQ spectrometer, TOF, and flight-length. Another was a phenomenological approach using the tracking results from the MWDC-S1 and the DCS0D, and the TOF(S0D-S1). It turned out that the phenomenological approach gave better mass resolution.

3.4.1 Analysis of Downstream PID with the SHARAQ spectrometer

A phenomenological approach is presented in here. The calculation involved the S0DPL, the DCS0D, the MWDC-S1, and the Hodo array. The flow chart of the Z and the A/Q deduction is shown in Figure 3-8. We will explain the process of multi-hit data from the Hodo array first.

There were 14 Hodos, the data of each event was a 3 columns and 14 row multi-dimensional array. Each row for a Hodo and stored the charge number (Hodo.Z, this was empty at the beginning), the energy loss (Hodo.ΔE), and the timing (Hodo.ch). The goal is to reduce the multiplicity into one by selecting a particular row from the data. The energy loss was corrected to Hodo_Corr.ΔE as shown in Section 2.3.5.1. Hodo_Corr.ΔE was converted into charge number Hodo.Z using a simple scaling. A proper range of the timing of each Hodo was selected and gave the true event (Hodo_trueEvent). The Hodo_trueEvent still contained data from multiple Hodos. The multiplicity was reduced to 1 by selecting the largest Hodo.Z among the 14 Hodos. This was called “Largest Z selection”. The data Hodo_U only contained the charge number and the timing. The Z number was Hodo_U.Z.

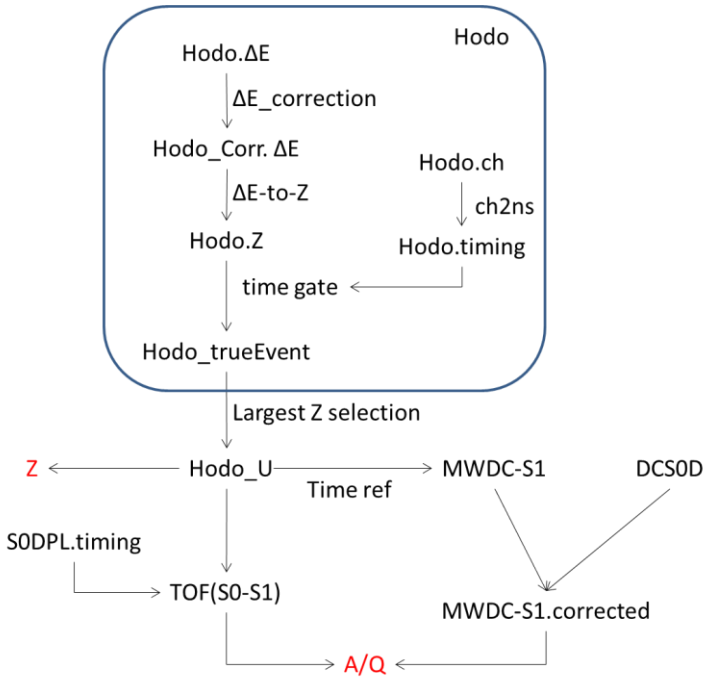

Figure 3-8 – The flow chart of calculating the Z and A/Q value.
See main text for detail explanation.

The deduction of the A/Q value was using the MWDC-S1, the DCS0D, and the TOF(S0D-S1). The timing from Hodo_U was used as the time reference for the drift-time of the MWDC-S1. It also formed the TOF(S0D-S1) with the timing from the S0DPL. The correlation between the x-positions of the MWDC-S1 and DCS0D can eliminate the angular dependence. The correlation between the x-position of the MWDC-S1 and TOF(S0D-S1) can eliminate the momentum dependence. The corrected x-position of the MWDC-S1 would be independent of incident angle and momentum and then it is related to the A/Q value.

We applied a charge number gate $|Z - 8| < 0.6$ to select the oxygen isotope. Under this gate, the x-position of the MWDC-S1 x_{S1} was made to be independent of the x-position of the DCS0D x_{S0D} (Figure 3-9) using formula

$$x = \frac{x_{S1} + 0.1296 x_{S0D}}{1 - 0.04874 x_{S0D}}, \tag{3.4.1}$$

where x is the corrected x-position of the MWDC-S1. Under the same charge number gate, a correlation can be seen between the corrected x-position of MWDC-S1 and the TOF(S0D-S1) (Figure 3-10). We fitted the data with a 2-dimenstion function to get the A/Q value

$$\frac{A}{Q} = 0.75409 - 0.0021946x + 1.64 \times 10^{-6} x^2 + 0.05327t, \tag{3.4.2}$$

where t is the TOF(S0D-S1). The constant term in equation (3.4.2) was set so that the value of A/Q of ^{23}F is 23/9.

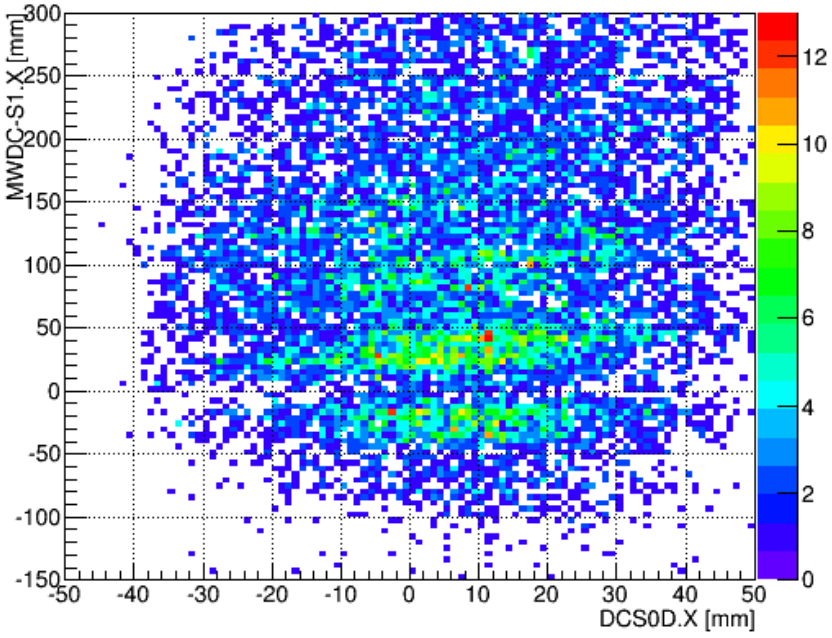

Figure 3-9 – Correlation between the x-position of MWDC-S1 and that of DCS0D.

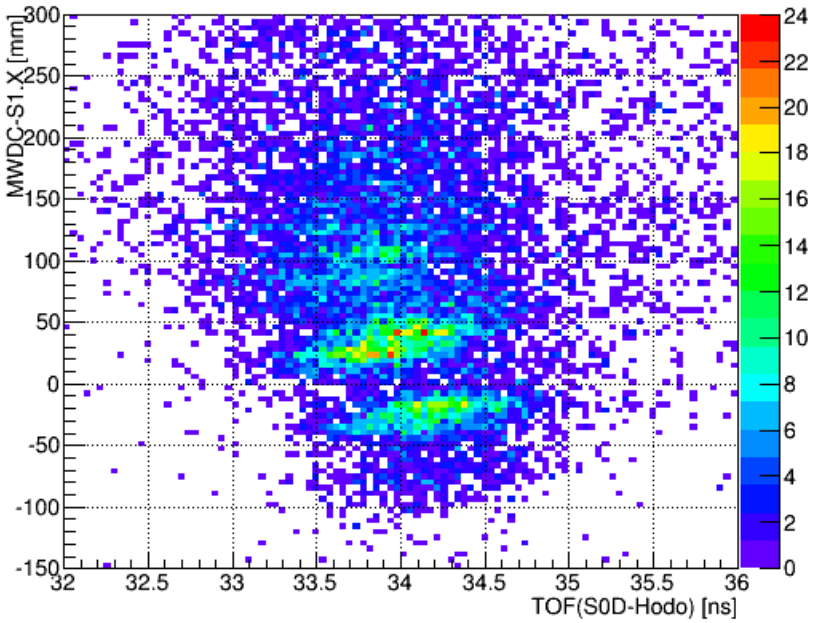

Figure 3-10 – Correlation between the corrected x-position of the MWDC-S1 and the TOF(S0D-Hodo).

Figure 3-11 shows the Z number distribution. The standard deviations of the Z number from the fitting of multiple Gaussians were 0.3, except for the fluorine. The number of channel in the Hodo was ranging from ~500 to ~4000, roughly 500 channels for one element. Standard deviation of 0.3 corresponds to the resolution of energy loss of 150 channels. Thus, the relative energy resolution of the Hodo was ~5% for oxygen. The Z - A/Q plot of the residues is shown in Figure 3-12.

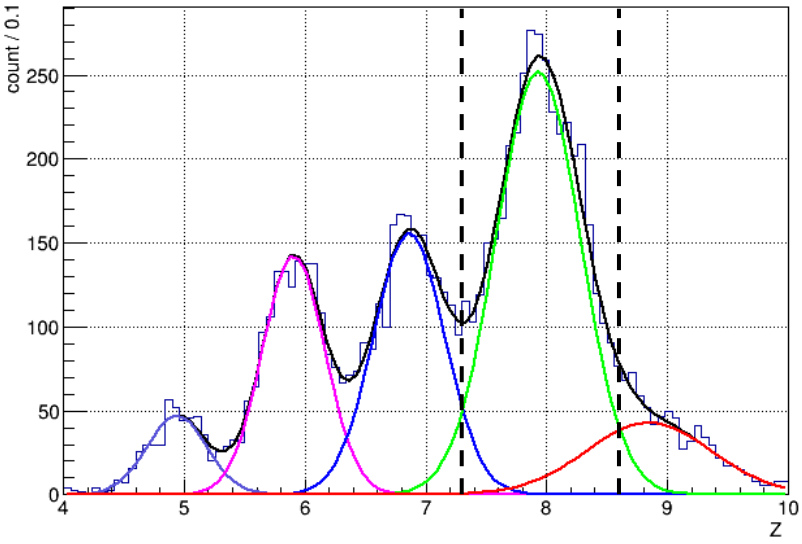

Figure 3-11 – Charge number distribution from the Hodo array.
The plot was gated under the ^{23}F gate and the ppcoin trigger. The small fraction of Z = 9 comes from accidental events. A *pidZ* gate is defined between the dashed black lines, or from Z = 7.3 to Z = 8.6. The gate covered 95% of the oxygen strength.

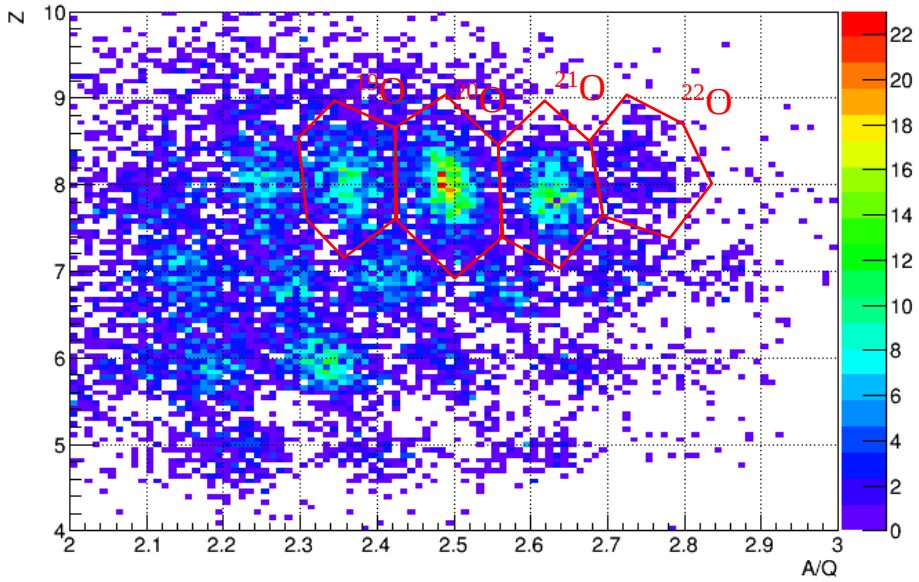

Figure 3-12 – A Z-A/Q plot of the residues.
The plot was under union of the *vertexXY* gate, the *tofS0DS1* gate and the *vertexZ* gate. The irregular hexagons are the gates for residual oxygen.

The plot of the mass number of the oxygen isotopes is shown in Figure 3-13. The standard deviations of the mass number from the fitting with multi-Gaussians were 0.2 for most of the peaks except for ^{22}O and ^{18}O. The standard deviation of the mass number can be checked using $A = Q\frac{c}{u\gamma\beta}B\rho\left(1+\frac{x}{\langle x|\delta\rangle}\right)$, where Q is the charge state, c is the speed of light in vacuum in mm/ns, u is 931.5 MeV/c^2, $B\rho$ is the magnetic rigidity of the SHARAQ-D1 magnet, $\gamma\beta$ is the Lorentz factor of the particle, x is the position on the focal plane, and $\langle x|\delta\rangle$ is the momentum dispersion. Using $\sigma(A) = \frac{A}{\langle x|\delta\rangle}\sigma(x)$, $\sigma(x)$~15 mm was the position resolution of an isotope (Figure 3-9), the dispersion was then ~1650 mm/100%. This value agreed with the theoretical dispersion of 1350 mm/100%.

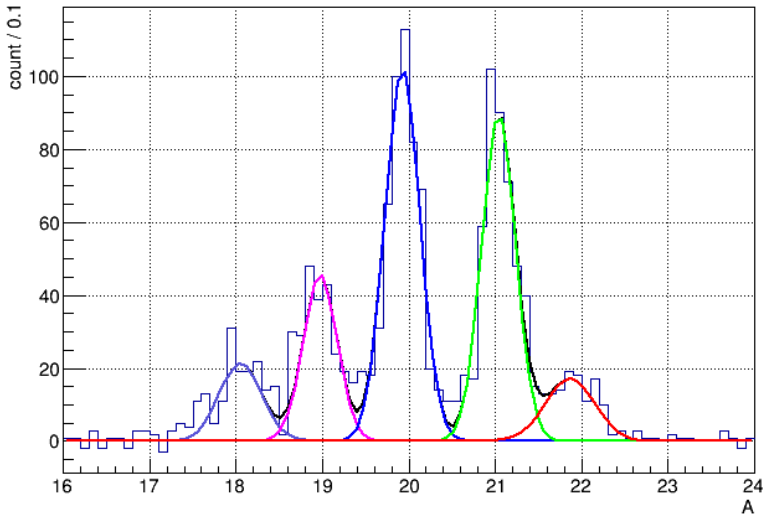

Figure 3-13 – The mass number of oxygen isotopes under the *pidZ* gate.
The *pidZ* gate was defined in Figure 3-11. The standard deviations of each peak is 0.2, except for ^{22}O and ^{18}O.

3.5 Residue Disintegration – Neutron Emission

The residue ^{22}O can be highly excited after a proton was knocked out from the 1p-shell or the 1s-shell. When the excitation energy is higher than the particle thresholds, nucleon(s) emission could happen, especially for the direct reaction. The neutron separation energy of ^{22}O is 6.85 MeV. Therefore, if the excitation energy of ^{22}O residue from the ^{23}F(p,2p) reaction is larger than 6.85 MeV, the residue ^{22}O will be excited, emit a neutron, and become ^{21}O. Similarly, ^{20,19}O can be detected when the excitation energy of the residue ^{22}O is higher than 2- or 3-neutron threshold. The multiple-neutron thresholds for ^{22}O and ^{24}O are shown in Table 3-1. The excitation-energy spectrum was partitioned by selecting different oxygen isotopes. For example, selecting (^{23}F,^{21}O) restricts the excitation energy of ^{22}O from 6.8 MeV to 10.7 MeV.

Table 3-1 – Multiple-neutron thresholds of ^{22}O and ^{24}O in MeV.

	^{22}O	^{24}O
1-neutron threshold	6.8	4.2
2-neutron threshold	10.7	6.9
3-neutron threshold	18.3	13.8
4-neutron threshold	22.2	17.6
5-neutron threshold	30.3	25.2

3.6 Reaction Identification

The reaction identification of the ^{23}F(p,2p)^{22}O* reaction required selecting the ^{23}F, the protons in the target crystal, the ppcoin trigger, and the oxygen isotopes. The ^{23}F was selected by the upstream PID (Figure 3-1). The ppcoin trigger was the coincident trigger of both of the Tpla-L and the Tpla-R (Section 2.4.1). Although the ppcoin trigger contained proton-gamma or gamma-gamma accidental events, those gamma events were ruled out by the tracking of the MWDC-L or the MWDC-R, because MWDCs are not sensitive to gamma ray. The oxygen isotopes were selected by the residue PID (Section 3.4).

The (p,2p) condition was checked using the angular correlation of the scattered protons. Figure 3-14 shows the correlation. The left plot is from the target; it clearly shows a correlation. The right plot is from the carbon target; it does not show any correlation.

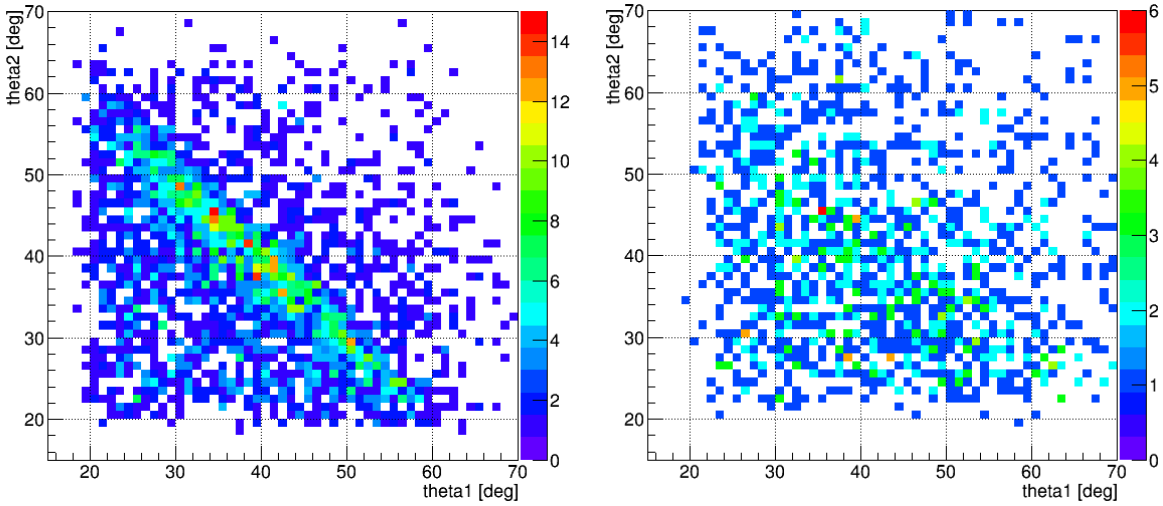

Figure 3-14 – Correlation of the scattered protons.
The left plot is gated on the ^{23}F, *Target*, and *pidZ* gates. The right plot is gated on the ^{23}F, *Carbon*, and *pidZ* gates. The *ppcoin* gate is implicitly included.

Because the target crystal was made of $C_{10}H_8$ molecules (Figure B-1), elimination and estimation of carbon background were necessary. We defined serval gates and list them in Table 3-2. The *vertexXY* gate selected the target crystal and excluded the target holder (Figure 3-5). The *tofS0DS1* gate also applied to rule out possible contamination from the target holder (Figure 3-6). The *vertexZ* gate was necessary to separate the target crystal and the carbon target (Figure 3-4). The union of the *vertexXY* gate and the *vertexZ* gate set a 3-dimensional gate on the target crystal to exclude the background from target holder and surrounding materials. A *vertexZc* gate selected the position of the carbon target for carbon background estimation.

Table 3-2 – Gates definition of the ^{23}F(p,2p) reaction.

Category	Gate Name	Description	Figure
Upstream PID	^{23}F	Graphical cut	Figure 3-1
2p	*ppcoin*	Selected from trigger condition	
Target	*vertexXY*	Circle of radius 7 mm and centered at (0.4, 1.8) mm in	Figure 3-5
	tofS0DS1	35 ns >TOF(S0D-S1) > 32 ns	Figure 3-6
	vertexZ	|vertex(Z) – 10| < 30 mm	Figure 3-4
	vertexZc	|vertex(Z) – 160| < 30 mm	Figure 3-4
Downstream PID	*pidZ*	8.6 > Z > 7.3	Figure 3-11
	^{22}O	Graphical cuts	Figure 3-12
	^{21}O		
	^{20}O		

The signal and background gates are defined in Table 3-3. The "*Target*" gate was defined as a union of the *vertexXY* gate, the *vertexZ* gate and the *tofS0DS1* gate. The "*Carbon*" gate was a union of the *vertexXY* gate, the *vertexZc* gate, and the *tofS0DS1* gate. The "*Common*" gate was redefined as the union of the ^{23}F gate and *ppcoin* gate. The signal gate for the ^{22}O ground state was a union of the *Common* gate, the *Target* gate, and the ^{22}O gate from the residue PID. The corresponding carbon background

gate was union of the *Common* gate, the *Carbon* gate, and the ^{22}O gate. Similar signal and background gates were defined for excited states of ^{22}O.

Table 3-3 – Definition of signal and background gates of the ^{23}F(p,2p) reaction.

	Signal gate	Carbon background gate
Target	*vertexXY* ∩ *vertexZ* ∩ *tofS0DS1*	/
Carbon	/	*vertexXY* ∩ *vertexZc* ∩ *tofS0DS1*
Common	^{23}F ∩ *ppcoin*	
$^{22}O_{g.s.}$	*Common* ∩ *Target* ∩ ^{22}O	*Common* ∩ *Carbon* ∩ ^{22}O
$^{22}O^* \rightarrow {}^{21}O+n$	*Common* ∩ *Target* ∩ ^{21}O	*Common* ∩ *Carbon* ∩ ^{21}O
$^{22}O^* \rightarrow {}^{20}O+2n$	*Common* ∩ *Target* ∩ ^{20}O	*Common* ∩ *Carbon* ∩ ^{20}O

3.7 Excitation-Energy Spectrum

The experimental proton separation energy $s_p(nlj)$, which is the energy required to knock out a proton from the $|nlj\rangle$ orbit. It can be calculated from the four-momenta of the incident fluorine nucleus $\mathbb{P}_F$, the target proton $\mathbb{P}_T$, and the scattered protons $\mathbb{P}_1$ and $\mathbb{P}_2$. In order to construct the four-momenta, the energy and the direction of the particles have to be deduced. Note that the experimental proton separation energy is different from the usual proton separation energy S_p, which is calculated from the experimental binding energies.

The energy can be deduced from the time information and the length of the flight length. The TOF from the target to the Tpla was found by following steps. The average time (Tavg) from the F3PL and the FH9PL gave the TOF(F3-FH9) with a proper time offset

$$\mathrm{TOF(F3-FH9)} = t_{FH9} - t_{F3} + \tau_1 + TOF(B\rho_0), \tag{3.7.1}$$

where t_i were the Tavg of the i detector, τ_1 was the time offset which set the $t_{FH9} - t_{F3}$ to be zero, and $TOF(B\rho_0)$ was the TOF that calculated from the magnetic rigidity $B\rho_0$ of the BigRIPS. It turned out that the value of $\tau_1 + TOF(B\rho_0)$ was the same for the proton, ^{23}F, and ^{25}F beams. It was not surprised but expected as the total time offset should be a constant. The TOF(FH9-target) was calculated using the TOF(F3-FH9) with the known positions of the F3 focal plane, the FH9 focal plane, and the target

$$\frac{\mathrm{ToF(FH9-target)}}{\mathrm{ToF(F3-FH9)}} = \frac{\mathrm{L(FH9-target)}}{\mathrm{L(F3-FH9)}} = \frac{10.865[\mathrm{m}]}{74.075[\mathrm{m}]} = 0.1467, \tag{3.7.2}$$

where L(A-B) was the flight length from point A to point B. There were some thin detectors from F3 to FH9, but the energy loss should be small as the kinematic energy of the beam is high. Thus, the TOF should not be affected much. The target-hit-time was

$$t_{target} = t_{FH9} + \mathrm{TOF(FH9-target)}. \tag{3.7.3}$$

The TOF from the target to the Tpla or to the S0DPL were then calculated from

$$\mathrm{TOF(target-X)} = t_X - t_{target} = \mathrm{TOF(FH9-X)} - \mathrm{TOF(FH9-target)} + \tau_X, \quad (3.7.4)$$

where X can be the Tpla or the S0DPL, and τ_X is the time offset for each X.

The flight length from the target to the Tpla can be found using the tracked position on the MWDC and the reaction vertex. The four-momenta of the scattered protons $\mathbb{P}_1$ and $\mathbb{P}_2$ were constructed from the TOF(target-Tpla), the flight length L(target-Tpla), and the scattering angles(θ, ϕ). The four-momenta were further corrected from the deflection caused by the polarization magnet and the incident angles of ^{23}F.

The four-momentum of the incident fluorine nucleus $\mathbb{P}_F$ was constructed from the incident energy and the tracking of the DCX1X2. The incident energy was obtained using the TOF(F3-FH9) for the ^{23}F runs or the F6-PPAC for the ^{25}F runs (Section 3.1.2). The experimental separation energy was calculated by equation (3.7.5). The excitation energy of the reaction residue was then deduced by subtracting the experimental separation energy from the proton separation energy of the fluorine nucleus. The flow of the calculation is shown in Figure 3-15.

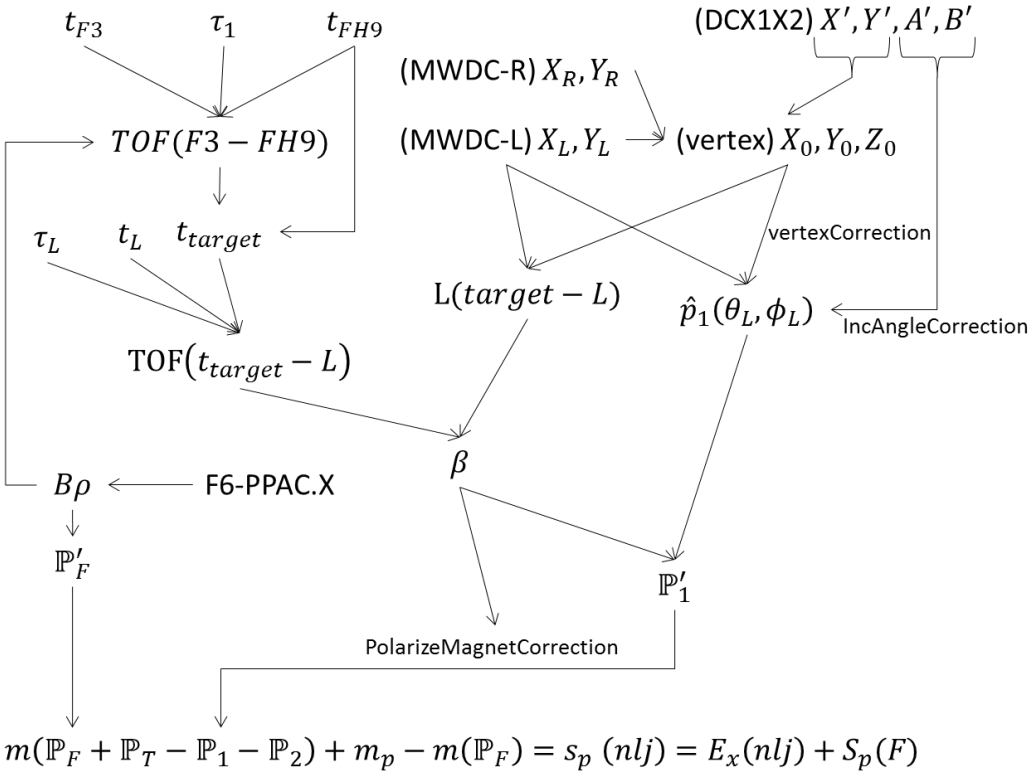

Figure 3-15 –Flow chart of the calculation of the experimental proton separation energy.
The chart only shows the calculation for $\mathbb{P}_1$, the same calculation also applied for $\mathbb{P}_2$. *L* stands for left. The $\mathbb{P}_T$ is the four-momentum of a proton at the target. $\hat{p}$ is the unit vector of momentum. β is the velocity of the scattered proton over the speed of light. $s_p(nlj)$ is the separation energy of a proton knockout from *nlj* orbit, $m(\mathbb{P})$ is the mass of a four-momentum $\mathbb{P}$, E_x is the excitation energy of the residue with *nlj*-hole state, and $S_p(F)$ is the proton separation energy of fluorine.

The calculation formula of the experimental separation energy s_p and the excitation energy E_x are

$$s_p = m\left(^{22}O^*\right) + m_p - m(^{23}F) = m(\mathbb{P}_F + \mathbb{P}_T - \mathbb{P}_1 - \mathbb{P}_2) + m_p - m(\mathbb{P}_F), \quad (3.7.5)$$

$$E_x = s_p - S_p\left(^{23}F\right). \quad (3.7.6)$$

Here $m(X)$ is the mass of the four-momentum X, m_p is the mass of proton, and $\mathbb{P}_i$ is the four-momentum, in which i can be: F for the fluorine nucleus, T for the proton in the target, 1 and 2 for the scattered protons. The proton separation energy of ^{23}F is 13.26 MeV. The accuracy of the formula was checked with the proton-proton elastic scattering [110]. Values of masses were taken from Reference [72]. Figure 3-16 shows the coincident plot of the excitation energy and the oxygen mass number for the ^{23}F(p,2p) reaction. The loci of the excitation energies are well isolated by mass number.

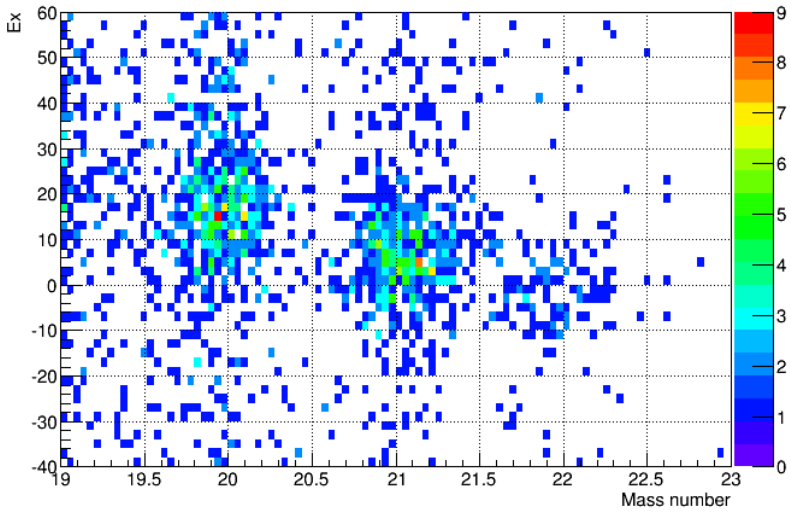

Figure 3-16 – The coincident plot of excitation energy versus oxygen mass number for ^{23}F(p,2p) reaction with $^{23}F \cap$ *ppcoin* $\cap$ *Target* gates.

The excitation-energy spectrum with carbon background subtraction for the ^{23}F(p,2p) reaction is shown in Figure 3-17. The scaling factor of the carbon background was 1, which was adjusted so that the average strength of the negative part of the energy spectrum was zero. The carbon target was 0.6 mm thick and the density was ~2 g/cm^3. The particle density of the carbon in the carbon target was $0.01N_A$ cm^{-2}, where N_A is the Avogadro's number The particle density of carbon in the target was $0.9 \times 10^{-2}N_A$ cm^{-2} [equation (3.8.2)]. Thus, the scaling factor was reasonable. Figure 3-17 shows three histograms using ^{22}O (red), ^{21}O (green), and ^{20}O (blue) gates. The experimental resolution (~5 MeV) was consistent with the detector resolutions. The main contribution of the resolution was the uncertainty of the TOF(target-Tpla), which was ~500 ps. Because of the insufficient energy resolution, we can only fit with a single Gaussian for each histogram. The results of the fits and the counts are listed in Table 3-4. The statistical error was included in the fitting. The error bar is not shown in the plot for clear presentation. The notation (^{23}F,^{A}O) means the residual ^{A}O was selected.

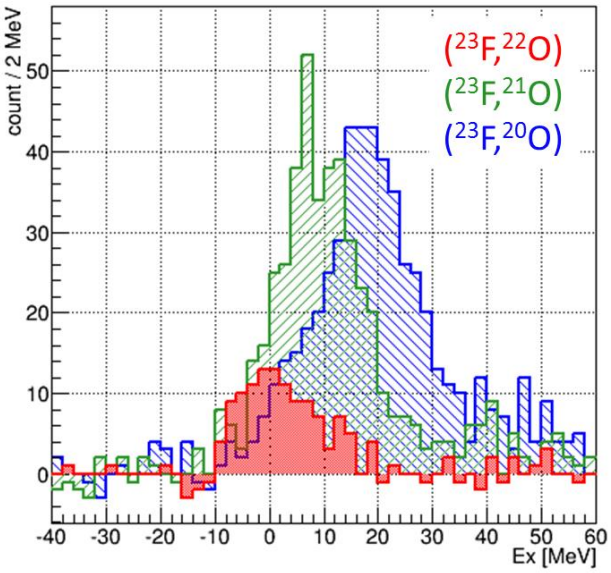

Figure 3-17 – Excitation-energy spectrum of ^{22}O from the ^{23}F(p,2p) reaction. The red, green, and blue color stands for ^{22}O gate, ^{21}O gate, and ^{20}O gate respectively.

Table 3-4 – The fitting results and counts of the ^{23}F(p,2p) reaction.

Partition	Ex [MeV]	Width [MeV]	Count
(^{23}F, ^{22}O)	1.0(8)	6.0(6)	110(15)
(^{23}F, ^{21}O)	9.5(4)	7.9(4)	386(29)
(^{23}F, ^{20}O)	18.0(5)	9.7(5)	442(32)

3.8 Integrated Cross-Section

The integrated cross-section was calculated by

$$\sigma = \int \frac{d^3\sigma}{d\Omega_1 d\Omega_2 dT_1} d\Omega_1 d\Omega_2 dT_1 = \frac{\text{Count}}{N_T N_B P_B H \lambda \epsilon t}, \quad (3.8.1)$$

where the count is taken from Table 3-4, section 3.7. The count was integrated on the detector angular acceptance and energy acceptance. The energy acceptance was defined by the TOF(target-Tpla) window. The window was ranging from 0 ns to 50 ns, which was corresponding to minimum energy of 4 MeV. The minimum theoretical kinetics energy of the scattered proton was 30 MeV (Figure 1-28). And the average energy loss caused by multiple scattering was 10 MeV (Figure A-10). Therefore, the TOF windows was able to covered the lowest energy proton. The experimental energy-angular acceptance is shown in Figure 3-18.

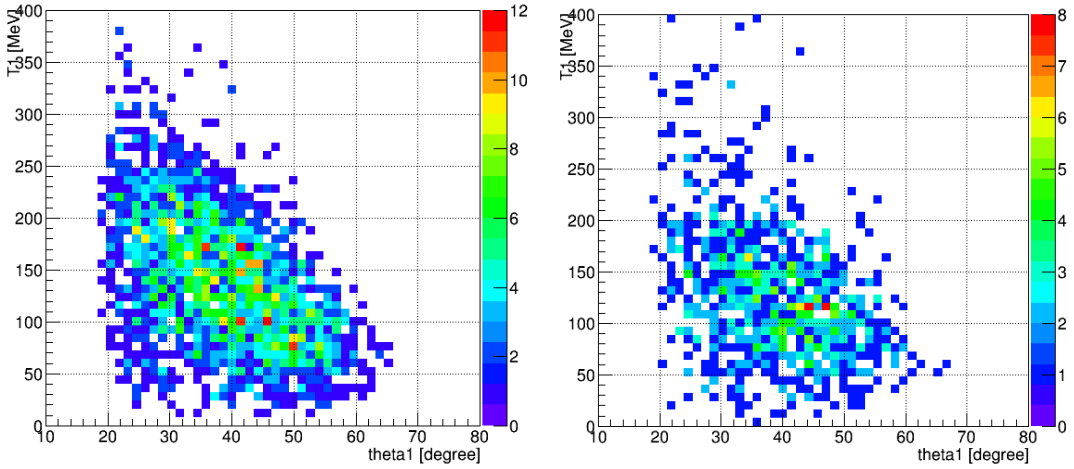

Figure 3-18 – The experimental acceptance of ^{23}F(p,2p) (left) and ^{25}F(p,2p) (right). The plots are gated by *Common*, *Target*, and *pidZ* gates. The carbon background did not remove.

In equation (3.8.1), N_T was the number of protons in target, N_B was the number of particles of the (secondary) beam, P_B was the purity of ^{23}F isotope, H was the target-hit-ratio, λ was the DAQ live time, ϵ was the total detection efficiency and t was the transmission rate from S0D to S1. The calculation elements in the denominator and their relative errors are listed in Table 3-5. The target thickness was 1.0 ± 0.1 mm. The molar mass of naphthalene ($C_{10}H_8$) is 128.17 g/mol. The density of the target crystal is 1.14 g/cm^3. Each naphthalene molecule has 8 protons. The number of protons N_T in the target crystal was

$$N_T = \frac{1.14}{128.17} \times 8 \times 0.1 \times N_A = 4.285 \times 10^{21}\ \text{cm}^{-2}, \qquad (3.8.2)$$

where N_A is the Avogadro's number. The relative error of N_T is 10%, which was came from the thickness of the target. The rate of event was uniform from beginning to the end of the experiment, therefore, the thickness of the target was the same throughout the experiment.

The beam luminosity was the sum of the product of N_B and λ for each runs. The beam purity was deduced in Section 3.1.1. The target-hit-ratio H was calculated from the tracking result of the DCX1X2 (Figure 3-3). The relative error of H came from the tracking uncertainty of 1 mm. Because the beam spot was larger than the crystal and off–centered, the uncertainty of the target radius or center resulted in a significant change of the number of events. The efficiencies of each detector were discussed in Chapter 2. The relative errors of the efficiency of most of the detectors were assumed to be zero, except for the MWDC-L and the MWDC-R, because their efficiency slightly depended on the position.

The transmission rate from S0D to S1 were checked by the XY image of the MWDC-S1 and the image was shown in Figure 3-19. The Y-detection range was between -130 mm and 50 mm (Figure 2-27). The oxygen isotopes were within the detection range and concentrated around the optical axis (X = 0), so that they did not hit any obstacle, thus the transmission rate was 100% for oxygen isotopes. There are

two loci on the figure. This is because the A/Q ratios of the oxygen isotopes are around the A/Q ratio of the beam (^{23}F) and the image of the beam was gated out by ppcoin trigger.

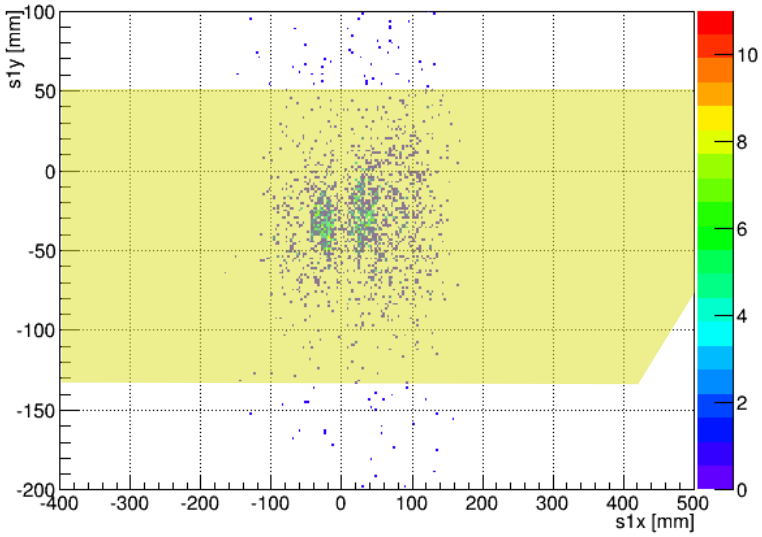

Figure 3-19 – The XY image of MWDC-S1 after gates.
The yellow region is the acceptance. It is clear that the oxygen isotopes are fully captured. The gate is a union of the *Common*, *Target*, *pidZ*, and 60>Ex>-40 MeV gates.

The elements of the calculation of the integrated cross-section are listed in Table 3-5. The systematic errors due to the reaction identification in the ^{23}F(p,2p) reaction was small. The ^{23}F gate was clean, so the graphical cut would not be a problem. The systematic error of the *vertexXY* gate was included in the Target-Hit-Ratio. The systematic error of vertexZ gate was small, because the gate covered 98% strength from the crystal (Figure 3-4). The systematic error of the graphical cut of the downstream PID was small. In Figure 3-16, the coincident plot between the excitation energy and mass number shows a clear separation in mass number. Thus, the total systematic relative error contained only the errors in Table 3-5 and it was 18.5%. The cross section was then calculated and listed in Table 3-6. The uncertainties in the "count" column are only statistical, but the uncertainties of the cross sections included the systematic error.

Table 3-5 – Value of calculation elements in ^{23}F.

		Value	Relative error
Number of protons [cm^{-2}]	N_T	4.285×10^{21}	10%
Beam luminosity	$\sum N_B \lambda$	3.63×10^{9}	/
Beam purity	P_B	0.37	/
Target-Hit-Ratio	H	0.61	15%
Eff. Of DCX1X2	ϵ (DCX1X2)	0.90	/
Eff. Of MWDC-L	ϵ (MWDC-L)	0.80	3.0%
Eff. Of MWDC-R	ϵ (MWDC-R)	0.78	3.0%
Eff. Of DCS0D	ϵ (DCS0D)	0.977	/
Transmission(S0D-S1)	T	1.0	/
Eff. Of MWDC-S1	ϵ (MWDCs)	0.96	/

Table 3-6 – The experimental integrated cross-section of the ^{23}F(p,2p) reaction. The systematic errors from Table 3-5 were included in the error of cross section.

Partition	E_x [MeV]	Count	Integrated Cross-section [ub]
(^{23}F, ^{22}O)	1.0(8)	110(15)	61(14)
(^{23}F, ^{21}O)	9.5(4)	386(29)	213(44)
(^{23}F, ^{20}O)	18.0(5)	442(32)	243(50)

3.9 Identification of Orbital Angular Momentum

The orbital angular momentum of each partition can be identified using the momentum distribution of the residue in the fluorine nuclear frame, in which the momentum of the residue $\vec{k}$ has the same magnitude of the knocked out proton. The four-momentum of the residue in the laboratory frame is

$$\mathbb{P}_R = \mathbb{P}_F + \mathbb{P}_T - \mathbb{P}_1 - \mathbb{P}_2. \tag{3.9.1}$$

The four-momentum of the residue in the fluorine nuclear frame was calculated by a Lorentz transformation $L\left(-\overrightarrow{\beta_F}\right)$

$$\mathbb{P}'_R = L\left(-\overrightarrow{\beta_F}\right) \cdot \mathbb{P}_R, \qquad \overrightarrow{\beta_F} = \frac{\overrightarrow{p_F}}{E_F}, \quad \mathbb{P}'_R = \left(E_R, \vec{k}\right) \tag{3.9.2}$$

where $\overrightarrow{\beta_F}$ was the Lorentz boots vector of the incident fluorine nucleus and E_R was the total energy of the residue. The $\mathbb{P}_F = (E_F, \overrightarrow{p_F})$ was the four-momentum of fluorine nucleus, $\overrightarrow{p_F}$ was momentum vector, and E_F was the total energy. The uncertainty of the magnitude of the experimental missing momentum k was approximately 15 MeV/c.

The momentum distributions for each partition in Figure 3-17 are shown in the left plot of Figure 3-20, Figure 3-21, and Figure 3-22. Momentum distributions of different orbits from the DWIA calculation (Section 1.2.4) are included in the plot. The analytical form of the theoretical momentum distribution is very complicated. The theoretical momentum distributions were approximated with a phenomenological model function

$$G_L(x) = A\, e^{-\frac{\alpha}{x_0}(x - x_0)} \frac{x^\alpha}{x_0^\alpha} + \delta_{L0} Gauss, \tag{3.9.3}$$

where A is the maximum value, x_0 is the peak position, α is a parameter for controlling the width, L is the angular momentum, δ_{ij} is the Kronecker delta, and $Gauss$ represent a Gaussian function. The angular momentum is implicitly included in the parameters α and x_0. The peak position for a fixed orbit is almost the same and slowly depends on the excitation energy according to code THREEDEE calculation. The peak position for the d-shell varies from 130 to 145 MeV/c for $E_x = 0$ to 20 MeV. The peak position for the p-shell varies from 90 to 105 MeV/c for $E_x = 0$ to 20 MeV. The first term of the function is not accurate to describe the 2s-shell, because the function has no node, therefore, a Gaussian

is added in the case for the 2s-shell. Since the uncertainty of the missing momentum was 15 MeV/c, we did not convolute the model function with the uncertainty, because the effect is small as the variance of the model function is ~ (60 MeV/c)^2 that an additional variance of (15 MeV/c)^2 can be neglected. Examples of the fitting of the phenomenological model function is shown in left plot of Figure 3-20 and Figure 3-21.

By simple inspection, there was no significant s-shell component in all partitions, and the $1p_{3/2}$ and $1p_{1/2}$ distribution had the same shape but different in amplitude. In order to evaluate the orbital angular momentum of each partition, after fitted the model function G to the theoretical distribution, the experimental momentum distribution was tested with the null hypothesis of a combined function $aG_1(x) + bG_2(x)$, where a and b are the testing parameters, $G_1(x)$ is the $1d_{5/2}$ distribution, and $G_2(x)$ is the $1p_{3/2}$ distribution. The goal of the test is to obtain the reduced chi-squared χ^2/ndf of 1. The reduced chi-squared of different a and b are shown in the right plots of Figure 3-20, Figure 3-21, and Figure 3-22. In the figures, the lowest value of the reduced chi-squared was marked and the corresponding a and b were shown.

The total number of bin was 40 and the two parameters were fitted. The degree of freedom is 38. According to the reduced chi-squared distribution, the 90% two-tailed confident interval of the reduced chi-squared ranges from 0.65 to 1.4. If the reduced chi-squared is smaller than 0.65, the fitting is too good to be true. If it is larger than 1.4, the fitting is no different from chance. There errors of a and b was taken as a one-sigma width. It corresponds to the value with $\chi^2_{min} + 1$. The error of b is then 0.15. Since the contour ellipse rotated 45 degrees, thus the error of a is also 0.15. The portion of the cross section from $1d_{5/2}$ orbit and p-orbit are also shown in Table 3-7. The first error is the total uncertainty and the second error is the uncertainty from the testing parameters.

Table 3-7 – The value of minimum reduced chi-squared, a, and b.

Partition	χ^2/ndf	a	b	$\sigma_{exp}(1d_{5/2})$ [μb]	σ_{exp}(p-orbit) [μb]
(^{23}F, ^{22}O)	0.75	0.50 ± 0.15	0.15 ± 0.15	47 ± 11 ± 14	14 ± 3 ± 14
(^{23}F, ^{21}O)	0.77	0.32 ± 0.10	0.40 ± 0.10	95 ± 20 ± 30	118 ± 24 ± 30
(^{23}F, ^{20}O)	0.93	0.36 ± 0.10	0.62 ± 0.10	89 ± 18 ± 25	154 ± 32 ± 25

We also used the excitation energy and parity of known states to determine the orbit. In the (^{23}F,^{22}O) partition, the mean excitation energy was close to 0 MeV and the known states are positive parity. Therefore, we assign the (^{23}F,^{22}O) partition to be originated from $1d_{5/2}$ distribution. In the (^{23}F,^{21,20}O) partitions, the excitation energy was large. The mean excitation energy of the (^{23}F,^{21}O) partition was consistent with the shell gap between $1d_{5/2}$ and $1p_{1/2}$ orbits. Therefore, these two partition should be dominated by p-orbit but mixed with little d-orbit.

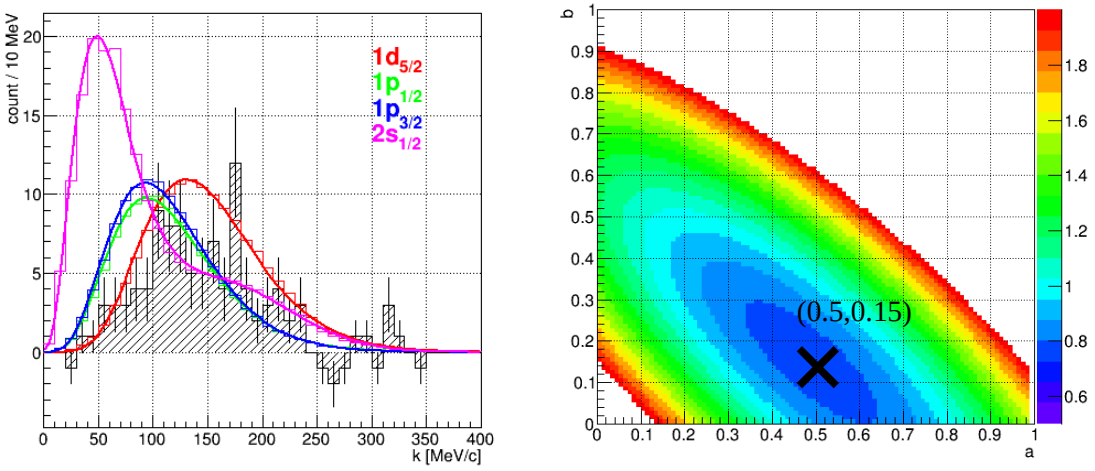

Figure 3-20 – Momentum distribution of residue for the (^{23}F,^{22}O) partition.
The solid curves and colored histograms are calculated from code THREEDEE. The excitation energy of 0 MeV was used in the calculation. The cross marks the minimum reduced chi-squared.

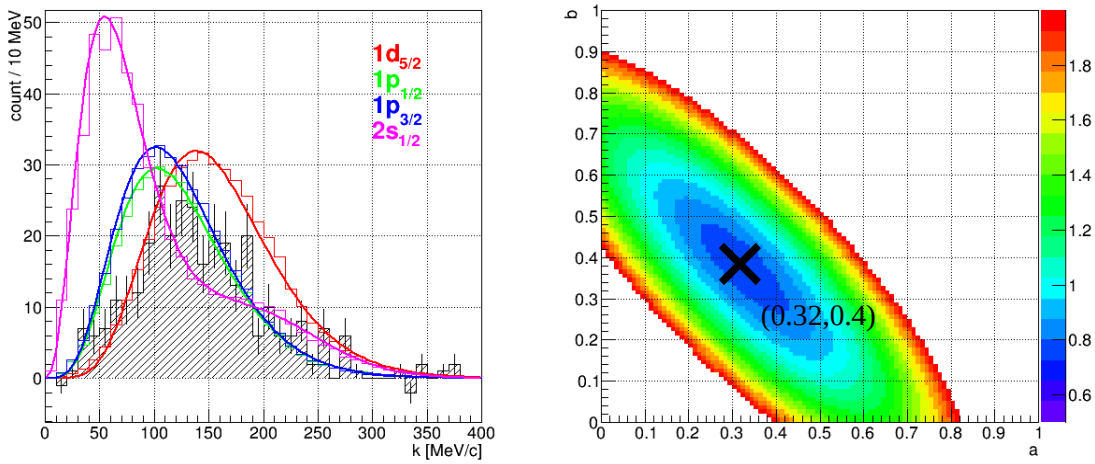

Figure 3-21 – Momentum distribution of residue for the (^{23}F,^{21}O) partition.
The solid curves and colored histograms are calculated from code THREEDEE. The excitation energy of 10 MeV was used in the calculation. The cross marks the minimum reduced chi-squared.

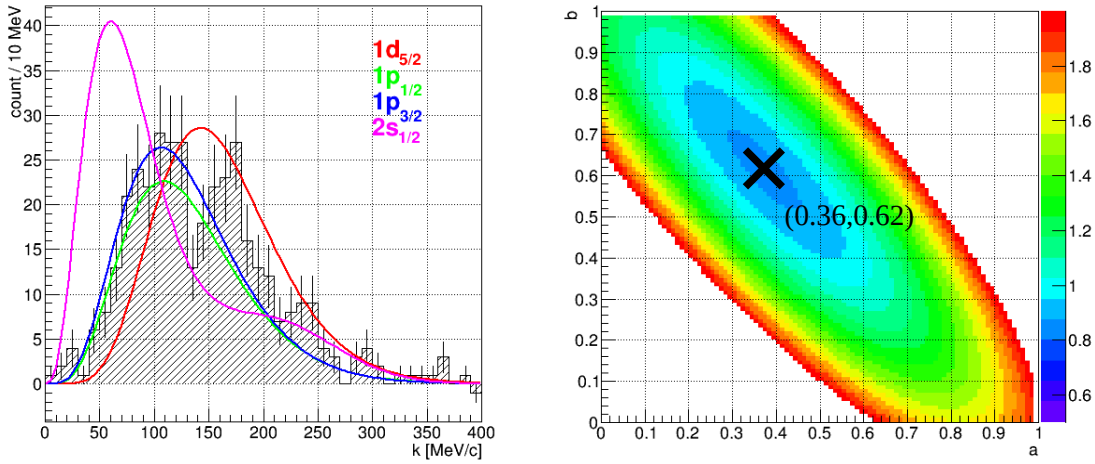

Figure 3-22 – Momentum distribution of residue for the (^{23}F,^{20}O) partition.
The solid curves are calculated from code THREEDEE. The excitation energy of 20 MeV was used in the calculation. The cross marks the minimum reduced chi-squared.

3.10 Analysis Result of ^{25}F

The ^{25}F(p,2p) reaction was analyzed and the excitation-energy spectrum of ^{24}O was extracted through the same analysis procedure as in the ^{23}F(p,2p) reaction. The incident energy of ^{25}F was 277*A* MeV with an uneven momentum spread of 2%. Therefore, the incident energy was calculated in event by event basic using F6-PPAC. The upstream particle identification of ^{25}F was done by the Z-A/Q plot, where Z is the charge number and A/Q is the mass to charge ratio. The plot was calculated using the energy loss in the FH9 plastic, the TOF(F3-FH9), F6-PPAC, and the magnetic rigidity of the BigRIPS. The upstream PID and downstream PID are shown in Figure 3-23 and Figure 3-24, respectively.

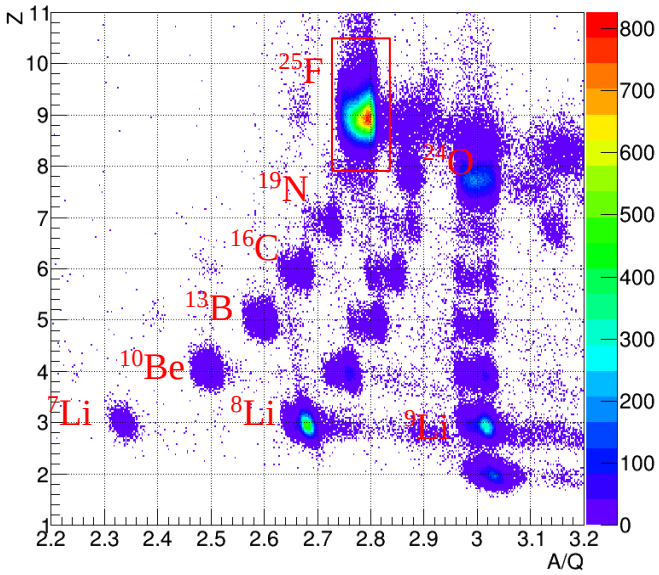

Figure 3-23 – The Z - A/Q plot from optics runs of the ^{25}F beam. The *^{25}F* gate is the red square.

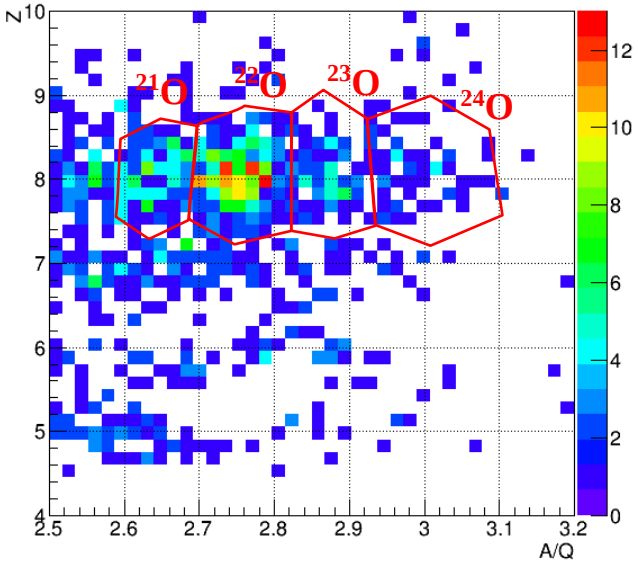

Figure 3-24 – Downstream PID plot of the ^{25}F(p,2p) reaction.
The gates of oxygen residues show in the irregular hexagons. This plot was gated on *Common* ∩ *Target* gates.

The charge distribution of the downstream PID is shown in Figure 3-25. The mass number of oxygen isotopes is shown in Figure 3-26. The downstream PID was merely enough to separate the mass number of the oxygen isotopes as the mass separation only 4σ. The isotopes were selected using graphic cuts on Figure 3-24.

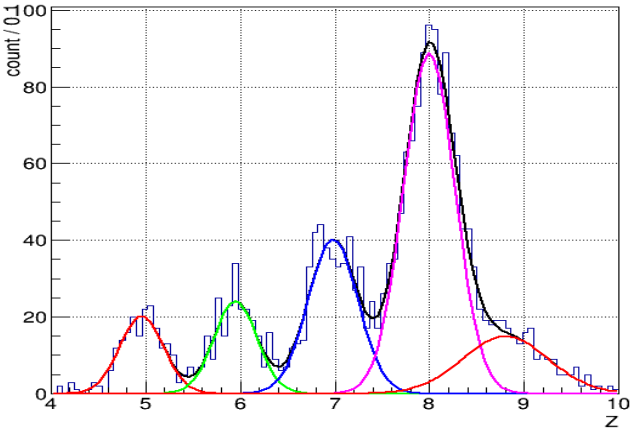

Figure 3-25 – Distribution of the charge number in downstream PID.
The standard deviations of each peak are 0.3. This plot was gated on *Common* ∩ *Target* gates.

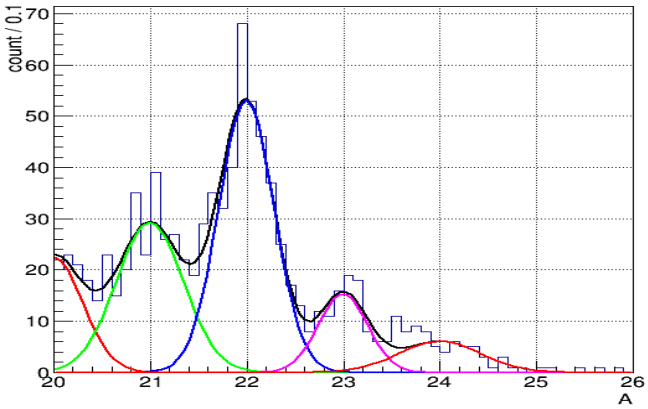

Figure 3-26 – The distribution of the oxygen mass number in downstream PID.
This plot was gated on *Common* ∩ *Target* gate and 60 MeV>E_x>-40 MeV gate. The standard deviations of each peak are 0.25, except for the ^{24}O peak.

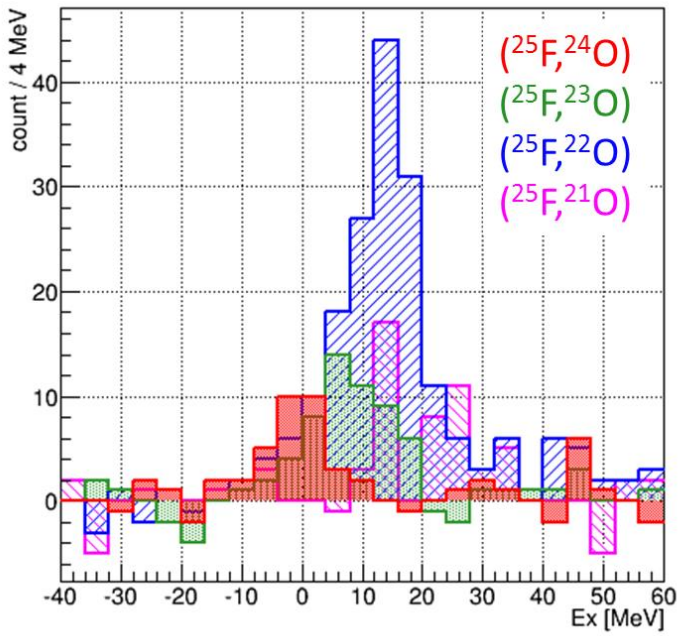

Figure 3-27 – Excitation-energy spectrum of ^{24}O from the ^{25}F(p,2p) reaction.
The red, green, blue, and pink color stand for ^{24}O gate, ^{23}O gate, ^{22}O, and ^{21}O gate respectively.

The excitation-energy spectrum of the ^{24}O from the ^{25}F(p,2p) reaction is shown in Figure 3-27. The red, green, blue, and pink histograms were deduced using ^{24}O, ^{23}O, ^{22}O and ^{21}O gates respectively. A single Gaussian was fitted for each partition due to the insufficient energy resolution. Note that the fitting of the (^{25}F,^{21}O) partition was not good as a strong peak located at 14 MeV was not fitted. However, the 14 MeV peak was included in counting. The elements for the cross section calculation are listed in Table 3-8.

Table 3-8 – Value of calculation elements in ^{25}F.

		Value	Relative error
Number of protons [cm^{-2}]	N_T	4.285×10^{21}	10%
Beam luminosity	$\sum N_B \lambda$	1.50×10^{9}	/
Beam purity	P_B	0.42	/
Target-Hit-Ratio	H	0.47	21%
Eff. Of DCX1X2	ϵ (DCX1X2)	0.90	/
Eff. Of MWDC-L	ϵ (MWDC-L)	0.80	3.0%
Eff. Of MWDC-R	ϵ (MWDC-R)	0.78	3.0%
Eff. Of DCS0D	ϵ (DCS0D)	0.977	/
Transmission (S0D-S1)	T	1.0	/
Eff. Of MWDC-S1	ϵ (MWDCs)	0.96	/

Since the downstream PID in the ^{25}F(p,2p) reaction was not as good as that of the ^{23}F(p,2p) reaction. The excitation energy was plotted against the oxygen mass number and is shown in Figure 3-28. The

isotopes are not well separated. The systematic error from the downstream PID was estimated using narrow gates on the mass number and the *pidZ* gate, instead of the graphical cuts on Figure 3-24. The mass gate was set to be 2σ in width, which contained 68.2% of the total strength, so that the contamination from other isotopes was 5%. The estimated full-strength count was compared with the count of graphical cut and it was 10% more. The final count was taken as an average of the counts from these two methods of downstream PID. The final statistical error was an average of the statistical errors from these two methods. The systematic error due to the downstream PID was the standard deviation of the counts, and it was 5%. The total systematic error, including the elements in Table 3-8 was 24%. The results of fittings of Figure 3-27, the counts, and the integrated cross-sections of all partitions are listed in Table 3-9.

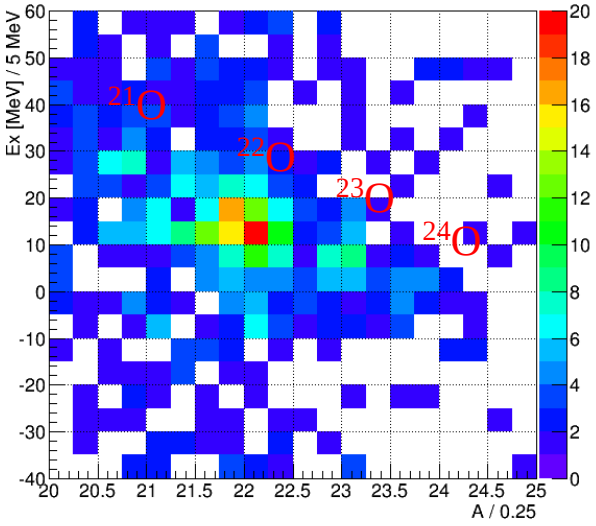

Figure 3-28 – Excitation energy versus oxygen mass number.
The plot is under the *Target* ∩ *pidZ* gate.

Table 3-9 – The results of the fitting, counts, and the integrated cross-sections from ^{25}F(p,2p) reaction. The error of the integrated cross-section included systematic error. The * means the fitting is not good, because the partition could contain two peaks.

Partition	E_x [MeV]	Width [MeV]	Count	σ_{exp} [μb]
(^{25}F, ^{24}O)	-0.8(1.0)	5.2(1.1)	36(8)	56(18)
(^{25}F, ^{23}O)	7.2(1.1)	6.3(0.8)	55(10)	86(26)
(^{25}F, ^{22}O)	12.8(0.7)	7.7(0.8)	176(19)	274(71)
(^{25}F, ^{21}O)	25.2(0.7)*	2.7(0.5)*	47(13)	73(27)

The momentum distributions of all partitions are shown in Figure 3-29, Figure 3-30, Figure 3-31, and Figure 3-32. The momentum distributions were also tested with null hypothesis of $aG_1(x) + bG_2(x)$, which is as same as section 3.9. The results are shown in the right plots of Figure 3-29, Figure 3-30, Figure 3-31, and Figure 3-32. The degree of freedom was 18. The 90% two-tailed confident interval is from 0.52 to 1.6. The error of the testing parameters a and b are the value with $\chi^2_{min} + 1$, or

$\chi^2_{min}/ndf + 0.06$. Note that the reduced chi-squared of the (^{25}F,^{23,21}O) partitions are out of the confident interval. This means the null hypothesis is rejected and the parameter is meaningless in this sense.

Table 3-10 – The value of minimum reduced chi-squared, a, and b.

Partition	χ^2/ndf	a	b	$\sigma_{exp}(1d_{5/2})$ [μb]	σ_{exp}(p-orbit) [μb]
(^{25}F, ^{24}O)	0.54	0.64 ± 0.10	0.00 ± 0.10	58 ± 18 ± 9	0 ± 0 ± 9
(^{25}F, ^{23}O)	2.3	0.40	0.00	86 ± 26	0 ± 0
(^{25}F, ^{22}O)	0.57	0.46 ± 0.10	0.34 ± 0.10	158 ± 41 ± 34	116 ± 30 ± 34
(^{25}F, ^{21}O)	2.2	0.0	0.5	0 ± 0	73 ± 27

The orbital angular momentum can be assigned using the momentum analysis and other experimental facts. The (^{25}F,^{24}O) partition must be from $1d_{5/2}$ orbit, because the ^{24}O has no bound excited state that the partition must only contain the ground state. The momentum analysis also agrees that the partition is originated from d-orbit. Since the result of the hypothesis testing is not meaningful for the (^{25}F,^{23,21}O) partitions, by a simple inspection on the peak position, the (^{25}F,^{23}O) partition was originated from d-orbit. Because of the large excitation energy, the (^{25}F,^{21}O) partition was most probability originated from the p-orbit. The mean excitation energy of the (^{25}F,^{22}O) partition is 12.8 MeV that it is agreed with the shall gap between the $1d_{5/2}$ and $1p_{1/2}$ orbits. This suggests the partition should be dominated by p-orbit.

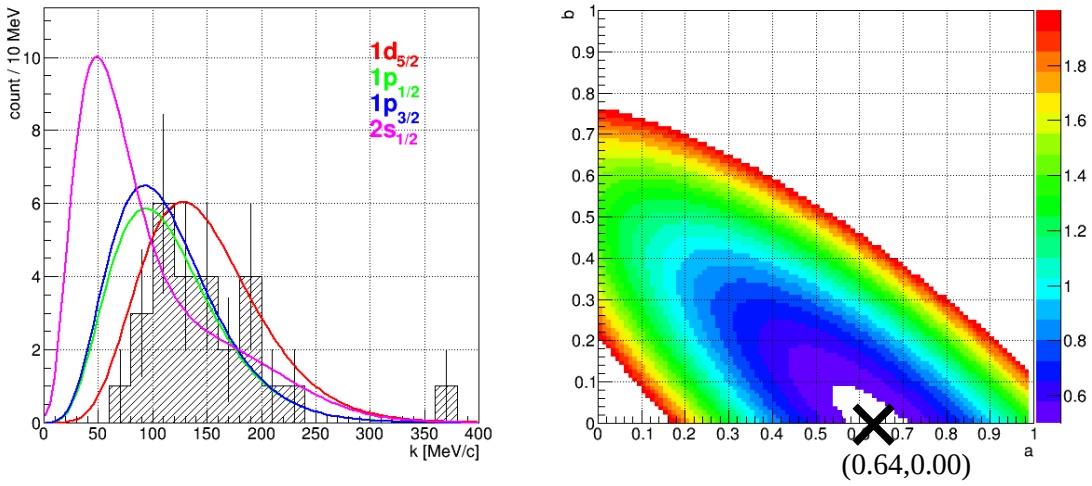

Figure 3-29 – Momentum distribution of residue for the (^{25}F, ^{24}O) partition.
The solid curves are calculated from code THREEDEE. The excitation energy of 0 MeV was used in the calculation. The cross marks the minimum reduced chi-squared.

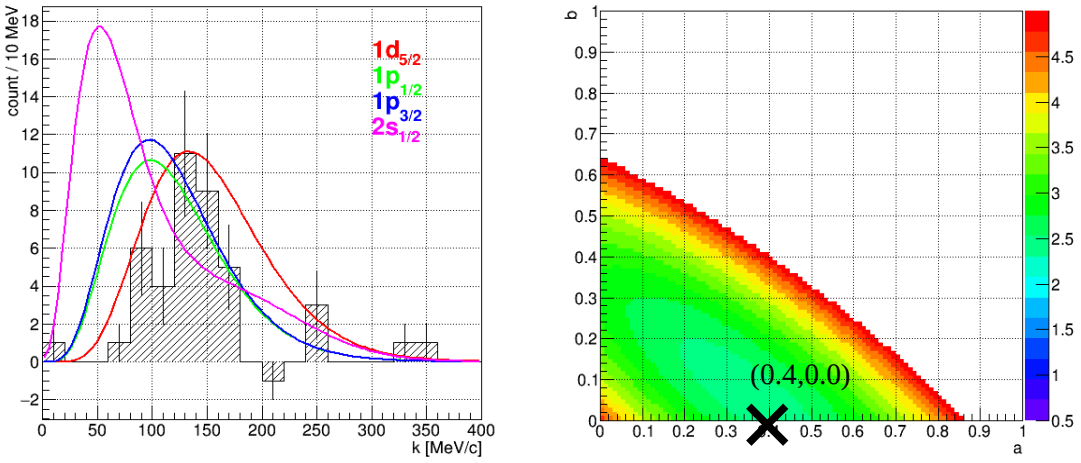

Figure 3-30 – Momentum distribution of residue for the (^{25}F, ^{23}O) partition.
The solid curves are calculated from code THREEDEE. The excitation energy of 15 MeV was used in the calculation. The cross marks the the minimum reduced chi-squared.

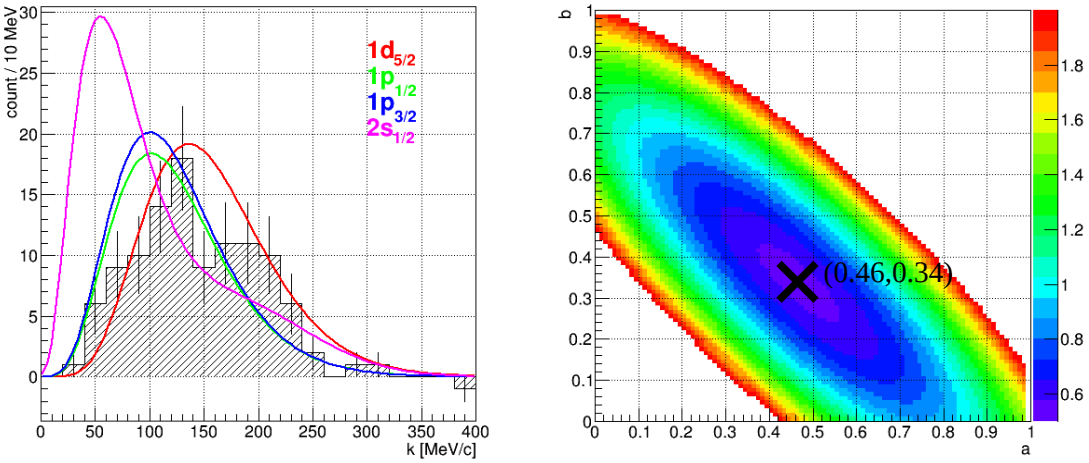

Figure 3-31 – Momentum distribution of residue for the (^{25}F, ^{22}O) partition.
The solid curves are calculated from code THREEDEE. The excitation energy of 13 MeV was used in the calculation. The cross marks the the minimum reduced chi-squared.

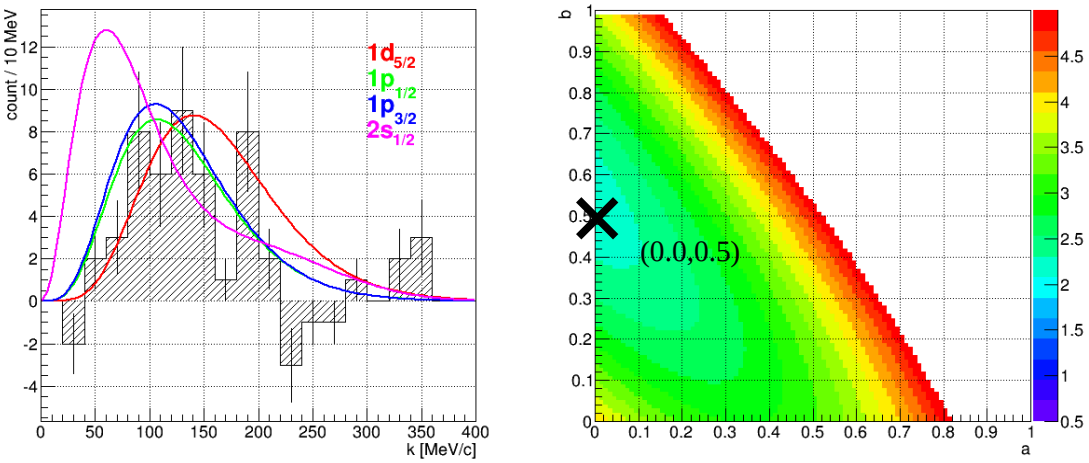

Figure 3-32 – Momentum distribution of residue for the (^{25}F, ^{21}O) partition.
The solid curves are calculated from code THREEDEE. The excitation energy of 25 MeV was used in the calculation. The cross marks the minimum reduced chi-squared.

3.11 Reliability of the Results

We verified the data analysis and the results in 6 aspects and concluded that the data analysis and the results are reliable.

1) The analysis method

   The same physical data (timings and positions) were analyzed using an independent analysis code and different gating conditions. The cross section of the ^{22}O(p,2p)^{21}N reaction (^{22}O came along with ^{23}F, Figure 3-1) was deduced and the result was 122 ± 26 μb. This value agreed with an independent analysis by S. Kawase [113]. The reliability of the analysis method has been confirmed.

2) The correctness of the excitation energy

   The calculation was crosschecked using the proton-proton elastic scattering (Appendix D.6). Also, the residue PID and the residue excitation energy are not related in the analysis, but still, the (^{22}O,^{21}N), (^{23}F,^{22}O) and (^{25}F,^{24}O) partitions are located on approximately 0 MeV. Moreover, the central values for most partitions are within the range of the neutron thresholds, except for the (^{25}F,^{23}O) and (^{25}F,^{21}O) partitions, these could be due to the uncertainty of the downstream PID and insufficient statistics. These indicate that the calculation of the excitation energy is accurate.

3) Missing strength caused by background estimation

   The carbon background was crosschecked using the target holder, which contained a lot of carbon atoms. Figure 3-33 shows the vertex(Z). The blue line is gated from the union of the *Common* gate, the *vertexXY* gate, the *tofS0DS1* gate, and the *pidZ* gate (see Table 3-2 for gates definition). And the red line is gated from the union of the *Common* gate, the negation of the *vertexXY* gate, the *tofS0DS1* gate, and the *pidZ* gate. The red line is scaled to cover the strength of the carbon target. The deduced counts using this scale were consistent with the pervious analysis within uncertainties.

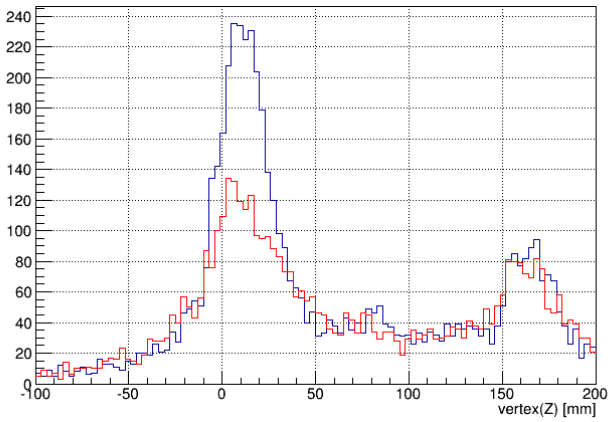

Figure 3-33 – The vertex(Z) plot of the *vertexXY* gate (blue) and !*vertexXY* gate (red). The *Common* ∩ *tofS0DS1* ∩ *pidZ* were included for both lines.

4) Contamination of downstream PID gate

The contamination from other isotopes was ruled out in the ^{23}F(p,2p). Figure 3-16 shows the correlation plot between the excitation energy and the oxygen mass number from the ^{23}F(p,2p) reaction. All loci are clearly separated. However, the downstream PID separation of the ^{25}F(p,2p) reaction was not clear and contamination may exist (Figure 3-28). The systematic error caused by the downstream PID was accounted using narrow gate on mass number and charge number, and it was 5%.

5) Missing strength caused by the Target gating

The *Target* gate was a union of the *vertexZ* gate, the *vertexXY* gate, and the *tofS0DS1* gate. We deduced the excitation-energy spectrum by varying the gate conditions of the *vertexZ* gate (|vertex(Z)|<60 mm) or using the negation of the *tofS0DS1* gate, and no strength was observed. The excitation-energy spectrum from a modified *vertexXY* gate (7 mm < r < 14 mm) is shown in Figure 3-34. The red, green, and blue histograms are form (^{23}F,^{22}O), (^{23}F,^{21}O), and (^{23}F,^{20}O) respectively. There is no strength for the (^{23}F,^{22}O) and (^{23}F,^{21}O) partitions, but the count of the (^{23}F,^{20}O) partition is 26 ± 13 count, which is within the uncertainty of the count from the original *vertexXY* gate (442 ± 32 count). Also, the modified *vertexXY* gate selected the events from the target holder. Those events are probably accidental events.

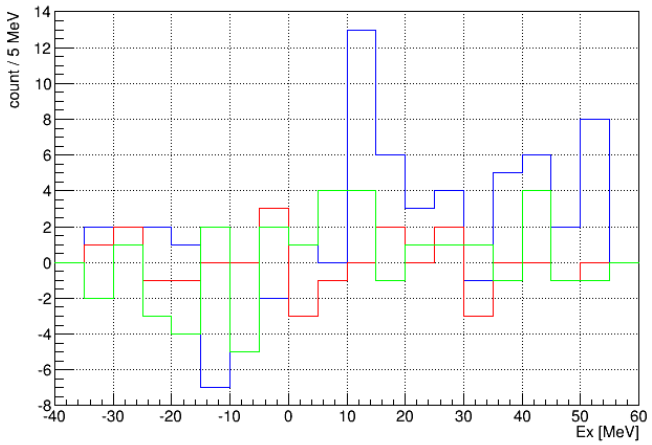

Figure 3-34 – The excitation energy of ^{22}O from the ^{23}F(p,2p) reaction with a modified *vertexXY* gate. See main text for detail explanation. The red, green, and blue histograms are for (^{23}F,^{22}O), (^{23}F,^{21}O), and (^{23}F,^{20}O) respectively.

6) Correctness of calculation elements of the cross section calculation

The calculation elements in Table 3-5 and Table 3-8 were cross checked and deduced independently by S. Kawase [113]. The values were consistent.

Chapter 4

Discussion

We discuss the experimental results and observations first. After that, the spectroscopic factors were extracted using the DWIA calculation. A unified nuclear structure of ^{23,25}F is proposed based on the results. The results and the underneath mechanism were then compared with the shell model calculation.

4.1 Results and Observations

We summarize the results of the ^{23}F(p,2p) and ^{25}F(p,2p) reactions in Table 4-1.

Table 4-1 – Results of the (p,2p) reactions from ^{23}F and ^{25}F.

Partition	E_x [MeV]	Width [MeV]	σ_{exp} [μb]	nL_j
^{23}F(p,2p)				
^{22}O	1.0 ± 0.8	6.0 ± 0.6	61 ± 14	$1d_{5/2}$
^{21}O	9.5 ± 0.4	7.9 ± 0.4	456 ± 67	d-orbit + p-orbit
^{20}O	18.0 ± 0.5	9.7 ± 0.5		
^{25}F(p,2p)				
^{24}O	-0.8 ± 1.0	5.2 ± 1.1	56 ± 18	$1d_{5/2}$
^{23}O	7.2 ± 1.1	6.3 ± 0.8	86 ± 26	$1d_{5/2}$
^{22}O	12.8 ± 0.7	7.7 ± 0.8	142 ± 31	
^{21}O	25.2 ± 0.7	2.7 ± 0.4	348 ± 82	d-orbit + p-orbit

There are several observations:

1) the mean excitation energies of the partitions (^{23}F,^{21}O) and (^{25}F,^{22}O) agreed with the shell gap between $1d_{5/2}$ orbit and $1p_{1/2}$ orbit,
2) the width of the (^{25}F,^{24}O) partition was the smallest,
3) the integrated cross-section of the (^{23}F,^{22}O) and (^{25}F,^{24}O) partitions were similar,
4) the total integrated cross-sections of ^{23}F (517 ± 68 μb) and ^{25}F (490 ± 82 μb) were similar,
5) the strength of the $1d_{5/2}$ proton of ^{25}F was fragmented, and
6) the observed strength of the $1d_{5/2}$ proton of ^{23}F was two times smaller than that of ^{25}F.

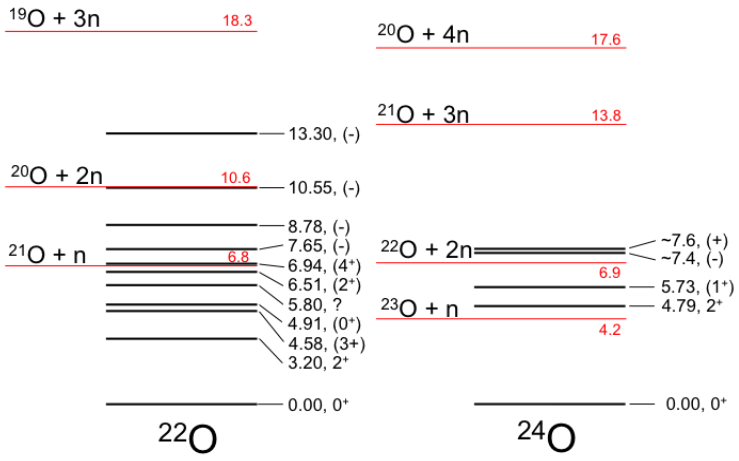

Figure 4-1 – Known excited states and neutron thresholds of ^{22}O and ^{24}O.

The observation 1) indicates that a peak from the $1p_{1/2}$ orbit dominates the partitions. The observation 2) can be understood by the fact that there is no bound excited state of ^{24}O (Figure 4-1), therefore, the (^{25}F,^{24}O) partition only contains 1 peak and the width of that partition is the resolution of excitation energy. The others partitions could contain many peaks that made the width larger. Since the nuclear potentials of ^{23}F and ^{25}F should be more or less similar, the integrated cross section of these two nuclei should be also similar. This explained the observation 3) and 4). The observation 5) and 6) will be discussed in the next two sub-sections.

There are three other issues. First, a $(\pi 1d_{5/2})^{1}(\pi 1p)^{-1}$ particle-hole state was formed in the residue ^{22}O (^{24}O) when a p-orbit proton of ^{23}F (^{25}F) was knocked out. The particle and hole can couple into 2 states with spin-parity of 2^- and 3^- from a $1p_{1/2}$ hole, or 4 states with spin-parity of 1^-, 2^-, 3^- and 4^- from a $1p_{3/2}$ hole. However, those fragmentations cannot be observed in the energy spectra due to the insufficient resolution.

Second, no significant signal was observed from neither the 1s- nor the 2s-orbits. However, the existence of those orbits cannot be ruled out absolutely. The missing s-orbit peaks could be due to the insufficient energy resolution and the lack of statistics. The large absorption in the nuclear interior caused by the imaginary potential and the insufficient residue PID of light oxygen isotopes may also be the reasons for the missing 1s-orbit.

Third, from Figure 1-32, one of the scattered protons would pass through the residual nucleus and could interact with it, so that the residual nucleus would be excited. However, the possibility of multi-step process should be very small in quasi-free knockout experiment. T. Noro showed that the cross sections of the multi-step process in quasi-free ^{12}C(e,e´p)^{11}B and ^{12}C(p,2p)^{11}B reactions were only 1% of the total cross section [114].

4.1.1 Fragmentation of the Strength of the $1d_{5/2}$ State of ^{25}F

The (^{25}F,^{24}O) partition is originated from the knockout of the $1d_{5/2}$ proton, because there is only one bound state of ^{24}O below neutron threshold. The momentum distribution of the (^{25}F,^{23}O) partition did not show any significant s-orbit signal but d-orbit signal (Figure 3-30). The positive parity of the known excited states (Figure 4-1) between 1-neutron and 2-neutron threshold also indicates the partition should be originated only from the sd-shell, unless there are some undiscovered states of negative parity. Because the $2s_{1/2}$ orbit is in the middle of the $1d_{5/2}$ and $1d_{3/2}$ orbits, and there is no significant s-orbit strength, it is not likely the configuration mixing happens in the $1d_{5/2}$ and $1d_{3/2}$ orbits but skips the $2s_{1/2}$ orbit. Therefore, that partition should be most probably originated from the knockout of the $1d_{5/2}$ proton. Thus, the strength of the $1d_{5/2}$ proton of ^{25}F was fragmented. The fragmentation in ^{25}F indicates the $1d_{5/2}$ proton changes the neutron-shell structure.

4.1.2 Strength of the $1d_{5/2}$ Proton of ^{23}F

The integrated cross sections were similar between ^{23}F and ^{25}F [observation 3) and 4)]. This suggests the knockout cross-sections of the $1d_{5/2}$ proton should be also similar between ^{23}F and ^{25}F. But the observed knockout cross-sections of the $1d_{5/2}$ proton up to 6.8 MeV of ^{23}F (61 ± 14 μb) and ^{25}F (142 ± 31 μb) were very different. The momentum distribution of the (^{23}F,^{21}O) partition (Figure 3-21) indicates some strengths from the $1d_{5/2}$ orbit. These evidences suggest that there were some missing strengths form the $1d_{5/2}$ proton above the neutron threshold. The missing strength was buried under the strong peaks of the p-orbit proton, because the strength of the p-orbit proton should be approximately 6 times more than that of the $1d_{5/2}$ proton, because there are 6 p-orbit protons and 1 d-orbit proton The missing strength indicates that the strength of the $1d_{5/2}$ proton of ^{23}F was also fragmented, similar in the case of ^{25}F. Besides, the missing strength also suggests some undiscovered positive parity states above neutron threshold.

4.1.3 Deformation effects

Mean field calculations suggested that ^{23}F nucleus is deformed with quadruple deformation parameter $\beta_2 = -0.2$ [115] [116] [117], while ^{16}O, ^{22}O, ^{24}O, and ^{25}F nuclei are spherical. Figure 4-2 shows the first 2^+ excitation energy (or E(2) transition energy) of oxygen of even neutron number [40]. The excitation energy is an indicator for nuclear deformation [77]. The figure supports that ^{16}O and ^{24}O are spherical because of the double magicity, and ^{22}O should be close to spherical. The deformation of ^{23}F from mean field calculation suggests many wavefunctions of excited ^{22}O is required to form the deformed wavefunction of ^{23}F, and then the spectroscopic factors of the $1d_{5/2}$ proton spreads to many excited states of ^{22}O.

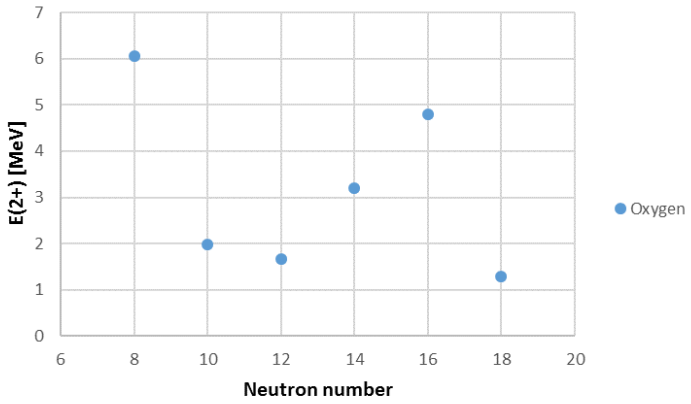

Figure 4-2 – The first 2^+ excitation energy of even-neutron oxygen isotopes.

A theoretical study on the cross section of a (p,2p) reaction of slightly deformed nuclei showed that the cross section increased (decreased) for oblate (prolate) deformed nuclei, because of the focusing effect [94]. A (d,p) reaction on the deformed nucleus ^{182}W ($\beta_2 = 0.25$) showed that the theoretical cross section based on spherical potential is too small [118] [119]. However, these two studies cannot help to explain our experimental results. More studies are needed to clarify the issue.

4.1.4 The Observability of the Fragmentation

The fragmentation of the strength of the $1d_{5/2}$ proton in both ^{23}F and ^{25}F were observed indirectly or directly. The first excited state of ^{24}O is above neutron threshold. This allows the fragmentation of the strength of the $1d_{5/2}$ proton of ^{25}F to be observed using neutron thresholds. There could be fragmentations in the case of ^{23}F, but the excited states of ^{22}O are low-lying that the experimental energy resolution is insufficient to separate them. The width of the (^{23}F,^{22}O) partition was larger than that of the (^{25}F,^{24}O) partition indicates there were multiple peaks inside that partition (Table 4-1).

4.2 Experimental Spectroscopic Factors

The experimental spectroscopic factor was deduced by comparing the experimental cross section and theoretical cross section (Section 1.1.2.3). The theoretical cross section was calculated using the DWIA method (Section 1.2.4). The spectroscopic factor was set to be unity in the calculation. A 3-dimensional kinematics calculation with the detector acceptance was performed. The incident energy of the proton and the experimental separation energy [equation (3.7.5)] were used. The Dirac-Cooper global potential was used to calculate the scattering optical potential (section 1.2.4.2). The bound state wavefunction was controlled by the reduced radius ($R/A^{1/3}$) and diffuseness parameter of the potential well of the fluorine isotopes. The potential depth was calculated by the code to reproduce the separation energy. The dependence of the DWIA cross-section on the reduced radius and diffuseness parameters is shown

in Figure 4-3. The DWIA cross-section is sensitive to the reduced radius (27 μb per 0.1 fm) and less sensitive to the diffuseness parameters (10 μb per 0.1 fm). A little inconsistence between the Dirac-Cooper global potential and the nuclear potential well may introduce error in the DWIA cross-section. The reduced radius of the imaginary vector and scalar potentials of the Dirac-Cooper global potential are 1.15 fm. The current reduced radius of the nuclear potential is 1.27 fm. That could result maximum 20% error.

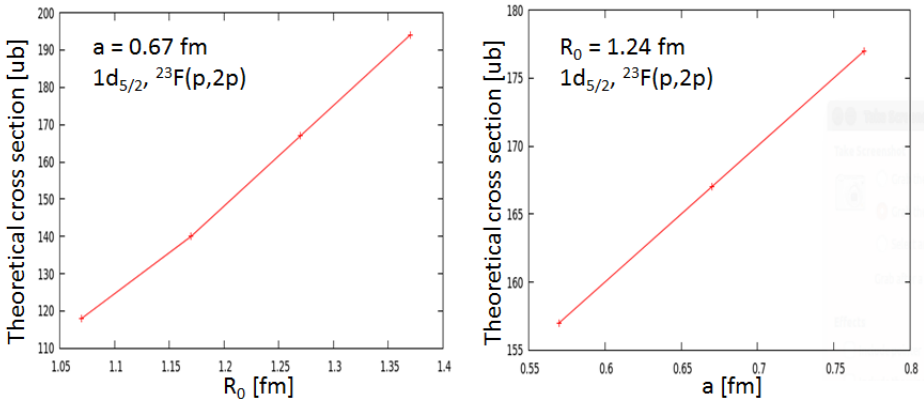

Figure 4-3 – The theoretical cross-section calculated by Dirac-Cooper global potential with different radius and diffuseness parameter of the bound state wavefunction.

The DWIA cross-section against excitation energy of ^{22}O is shown in Figure 4-4. The DWIA cross-section decreases when the excitation energy increases, because the radial integral of a deeper bound state is smaller [equation (1.2.11)], and the flux of incident proton losses inside of the nucleus due to the imaginary potential so that the chance for the incident proton interacts with a deeper bound state becomes small.

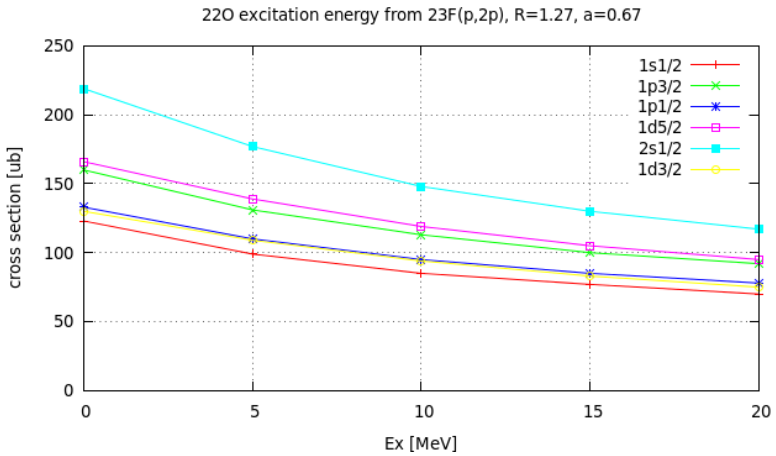

Figure 4-4 – The DWIA cross-section against excitation energy of ^{22}O from the ^{23}F(p,2p) reaction.

The DWIA cross-section of each partition was taken at the experimental mean energy and an error was taken into account due to the width of the partition. The spectroscopic factors of the ^{23}F(p,2p) and ^{25}F(p,2p) reactions are listed in Table 4-2 and Table 4-3 respectively. The orbit assignments were

discussed in Chapter 3. Since the $1p_{1/2}$ and $1p_{3/2}$ orbits cannot be distinguished, the orbits were grouped and called as the p-orbit. The peak position of the p-orbit was taken as the cross-section weighted mean. The uncertainty and the width of the p-orbit were using error propagation without weighting. The DWIA cross-section was taken as the cross-section weighted mean of the $1p_{1/2}$ and $1p_{3/2}$ orbits.

Table 4-2 – Cross sections and spectroscopic factors from the ^{23}F(p,2p) reaction.

Partition	E_x [MeV]	Width [MeV]	σ_{exp} [μb]	E_x (DWIA)	L (DWIA)	σ_{DWIA} [μb]	S_{exp}
(^{23}F,^{22}O)	1.0(8)	6.0(6)	61(14)	0	$1d_{5/2}$	166(28)	0.37(10)
(^{23}F,^{21,20}O)	14.0(6)	12.5(6)	456(67)	15	p-orbit	93(25)	4.9(1.5)

Table 4-3 – Cross sections and spectroscopic factors from the ^{25}F(p,2p) reaction.

Partition	E_x [MeV]	Width [MeV]	σ_{exp} [μb]	E_x (DWIA)	L (DWIA)	σ_{DWIA} [μb]	S_{exp}
(^{25}F,^{24}O)	-0.8(1.0)	5.2(1.3)	53(18)	0	$1d_{5/2}$	149(24)	0.38(14)
(^{25}F,^{23}O)	7.2(1.1)	6.3(0.8)	86(26)	5	$1d_{5/2}$	125(26)	0.69(25)
(^{25}F,^{22,21}O)	15.4(1.3)	9.2(1.3)	347(76)	16	p-orbit	80(24)	4.4(1.6)

The sum of the spectroscopic factors up to 6.8 MeV (neutron threshold) of the $1d_{5/2}$ proton of ^{23}F was only 0.37 ± 0.10. The value was quite small when comparing to the shell limit of 1. This indicates the change of neutron-shell structure. However, there were some missing strengths located in the (^{23}F,^{21,20}O) partitions as we explained on section 4.1.2, and the total sum of the spectroscopic factors should be larger. The sum of the spectroscopic factors up to 18 MeV of the p-orbit was 4.9 ± 1.5. The shell limit for the p-orbit was 6, so the fraction of occupancy was 0.82 ± 0.25. Note that the p-orbit included some strength from $1d_{5/2}$ orbit. The spectroscopic factor should be treated as an upper limit of the p-orbit.

The spectroscopic factor of the (^{25}F,^{24}O) partition was 0.38 ± 0.14 and it was much smaller than unity. This again indicates the change of neutron-shell structure. The sum of the spectroscopic factors of the (^{25}F,^{23}O) partition was 0.69 ± 0.25. Because both (^{25}F,^{24}O) and (^{25}F,^{23}O) partitions were originated from the $1d_{5/2}$ proton. Therefore, the sum of the spectroscopic factors of the $1d_{5/2}$ proton was 1.06 ± 0.28. The sum of the spectroscopic factors of the p-orbit was 4.4 ± 1.6 and the fraction of occupancy was 0.72 ± 0.27.

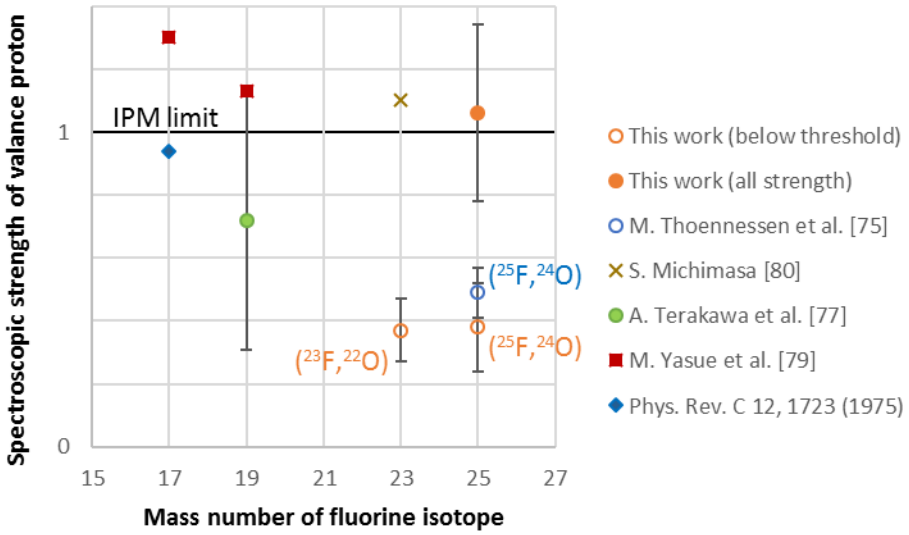

Figure 4-5 – The spectroscopic strength of the valence proton of the ground state of even-neutron fluorine isotopes [75] [77] [79] [80].
The solid dots represent full strength of the valance proton. The hollow dots represent partial strength of the valance proton. The cross is the result from S. Michimasa [80].

The results is compared with past results and shown in Figure 4-5. The spectroscopic factors of the (^{23}F,^{22}O) and (^{25}F,^{24}O) partitions are plotted as hollow orange dots. Our result was consistent with the result obtained by M. Thoennessen *et al.* [75]. They used a ^{12}C(^{25}F,^{24}O) reaction at 50.4*A* MeV and the spectroscopic factor of (^{25}F,^{24}O) was 0.5 ± 0.1.

The sum of the spectroscopic factors of the $1d_{5/2}$ proton of ^{25}F was 1.0 ± 0.3 and is plotted as an orange solid dot in Figure 4-5. The total spectroscopic strength was consistent with that of ^{17,19}F. The figure shows that the $1d_{5/2}$ proton is in a "single-particle orbit" but the strength of the $1d_{5/2}$ proton of ^{25}F was fragmented. The result from S. Michimasa *et al.* on ^{23}F using ^{4}He(^{22}O,^{23}F) at 35*A* MeV is also plotted as a brown cross. The spectroscopic factor of the $1d_{5/2}$ proton of ^{23}F was reported to be 1.1 [80]. Since the result was obtained by subtracting all excited states from γ-spectroscopy, and the experimental setup was not sensitive to the ground state, therefore a large uncertainty is expected.

4.2.1 Wavefunction of ^{25}F

From the experimental results, the wavefunction of ^{25}F could be expressed as a linear combination of the couplings of the wavefunction of the $1d_{5/2}$ proton and the wavefunction of ^{24}O core [equation (1.1.19)]. The ^{24}O core can be in the ground state and the excited states. The spectroscopic factor for the ^{24}O ground state was 0.38, and that for the first few excited states was 0.69. The wavefunction of ^{25}F is then written as

$$|^{25}\mathrm{F}\rangle_{\frac{5}{2}} \approx \sqrt{0.38}\left[\left|\pi 1d_{\frac{5}{2}}\right\rangle |^{24}\mathrm{O}\rangle\right]_{\frac{5}{2}} + \sqrt{0.69}\left\{\left[\left|\pi 1d_{\frac{5}{2}}\right\rangle |^{24}\mathrm{O}^{1}\rangle\right]_{\frac{5}{2}} + \left[\left|\pi 1d_{\frac{5}{2}}\right\rangle |^{24}\mathrm{O}^{2}\rangle\right]_{\frac{5}{2}} + \cdots\right\} + \cdots, \quad (4.1)$$

where the coupling of the $1d_{5/2}$ proton with the ground state of ^{24}O is weak and the coupling with excited states of ^{24}O is strong (the relative strength is important in here). This coupling is unusual when considering that the $1d_{5/2}$ proton is a valence nucleon of a nucleus that is on top of a double magic ^{24}O nucleus. For example, the $1p_{1/2}$ proton in ^{16}O [120], the $1d_{5/2}$ neutron in ^{17}O [64], the $1p_{1/2}$ proton of ^{18}O [92], and the $1d_{3/2}$ proton of ^{40}Ca [56], are all strongly coupled with the ground state of the residues and weakly coupled (or not coupled) to the excited states of the residues. Also, the spectroscopic factors of the valance proton of similar nuclei ^{49}Sc and ^{209}Bi are close to unity that the valance proton is strongly coupled with the ground state of the double magic core [21] [22].

4.2.2 Occupation Number

For the $1d_{5/2}$ proton of ^{25}F, the sum of the spectroscopic factors up to 6.8 MeV (2-neutrons threshold) was 1.06 ± 0.28. In principle, the occupation number is the sum of the spectroscopic factors for all energy. Therefore, the occupation number for the $1d_{5/2}$ proton was at least 1.06 ± 0.28, thus, the sd-shell proton mainly locates in the $1d_{5/2}$ orbit. This picture agrees with the "single-particle picture".

The p-orbit of ^{23}F or ^{25}F is at least 10 MeV below Fermi surface. Since the spectroscopic factors were summed up to ~20 MeV, the sum of the spectroscopic factors of the p-orbit should be close to the occupation number. The fractions of occupancy equaled 0.82 ± 0.25 and 0.72 ± 0.27 for ^{23}F and ^{25}F respectively. These values agree with the case of ^{208}Pb (Figure 4-6). Similar fractions of occupancy that below Fermi surface were also observed for ^{16}O, ^{40}Ca, ^{48}Ca, and ^{90}Zr [24]. The reduction of the occupation number below Fermi-surface is due to short-range correlation [38]. Our result indicates that the short-range correlation in neutron rich ^{23,25}F nuclei is similar to that of stable nuclei for the protons far below the Fermi surface.

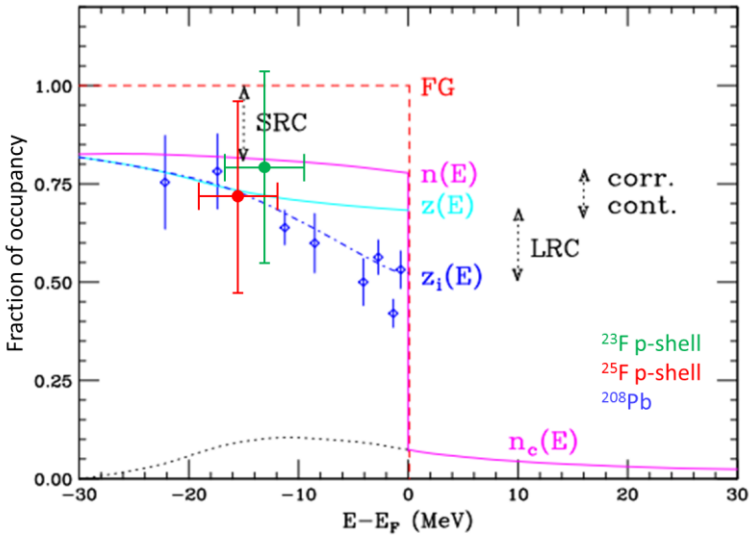

Figure 4-6 – Fraction of occupancy of the p-orbit of ^{23}F and ^{25}F.
See section 1.1.2.4, Figure 1-8.

4.3 A Unified Picture of the sd-shell of ^{23,25}F

The experimental results show that the $1d_{5/2}$ proton of ^{25}F is in a single-particle orbit but the spectroscopic strength of that proton was fragmented. This implies that the neutron-shell structure is changed by the proton. Since ^{23}F shows similar knockout cross-section and fragmentation, we could expect the wave functions of neutron-rich fluorine isotopes ^{23}F and ^{25}F are similar. The wavefunction can be expressed as

$$|\,^{A}\mathrm{F}\rangle = |\pi\rangle \otimes \left(\beta_0 |^{A-1}\mathrm{O}_{\mathrm{g.s.}}\rangle + \sum \beta_i |^{A-1}\mathrm{O}^{\mathrm{i}}\rangle\right), \tag{4.2}$$

where β_0 is the square-roots of the spectroscopic factor, $|\pi\rangle$ is the wavefunction of the $1d_{5/2}$ proton, $|^{A-1}\mathrm{O}_{\mathrm{g.s.}}\rangle$ is the wavefunction of the oxygen core in ground state, $|^{A-1}\mathrm{O}^{\mathrm{i}}\rangle$ is the oxygen core in excited state, and the operator $\otimes$ represents antisymmetric operator, isospin coupling, and spin coupling. The proton wavefunction can be factorized out because it is a single-particle state.

This means that fluorine nucleus is not a simple system formed by adding a $1d_{5/2}$ proton on top of a free oxygen nucleus, because the proton changes the neutron shell structure. Large components of the neutron shell are formed using excited states of oxygen. This suggests that the configuration mixing in the neutron shell of fluorine is larger than that of oxygen, the spacing between $1d_{5/2}$, $2s_{1/2}$ and $1d_{3/2}$ orbits of fluorine are smaller than that of oxygen, and the $N = 16$ magicity disappears.

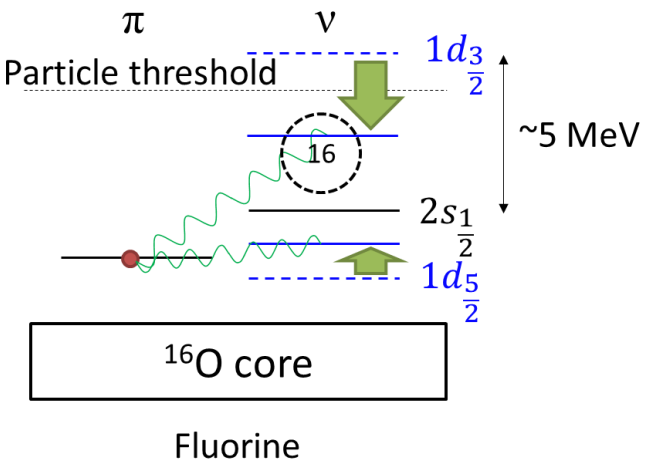

Figure 4-7 – The mechanism of the change of neutron shell structure by the $1d_{5/2}$ proton in fluorine. See main text for explanation.

Figure 4-7 shows a possible mechanism of the change of the neutron shell structure by the $1d_{5/2}$ proton in fluorine. The dashed lines are the energy levels of the d-orbit of oxygen. The red lines are the energy levels of the d-orbit of fluorine. The wavy lines are the proton-neutron interaction. Because the overlap between d-orbit and s-orbit is small and then the interaction is weak, we assumed that the $2s_{1/2}$ orbit is unaffected by the $1d_{5/2}$ proton. According to the mechanism of tensor force [20], the $1d_{5/2}$ proton lowers the $1d_{3/2}$ neutron orbit and drops below the neutron threshold. The proton also raises the $1d_{5/2}$ neutron orbit. The energy gap between $1d_{3/2}$ and $2s_{1/2}$ orbits in ^{24}O is ~5 MeV, this gap becomes smaller due to the proton-neutron tensor interaction. Because the energy states are closer, the neutron configuration mixing increases, and the $N = 16$ magicity disappeared. This is the Type-1 shell evolution driven by the tensor force [121].

4.4 Shell Model Calculation

In order to investigate the hypothesis of the Type-1 shell evolution, the shell structures of ^{23,25}F and ^{22,24}O were calculated using shell model calculation. As following section 1.1.5, the SFO interaction in the p-sd model space was used, Figure 4-8 (Figure 4-9) shows the result of the spectroscopic factors of various proton orbits from the ^{23}F(p,2p)^{22}O [^{25}F(p,2p)^{24}O] reaction. The calculated excitation energies roughly agree with the experiment values and support that p-orbit peaks dominate the (^{23}F,^{21,20}O) and (^{25}F,^{22,21}O) partitions. The bottom-left corner of the plots shows the percentage of d-orbit and p-orbit form the analysis of momentum distributions (section 3.9 and 3.10). Note that those values have roughly 30% uncertainty.

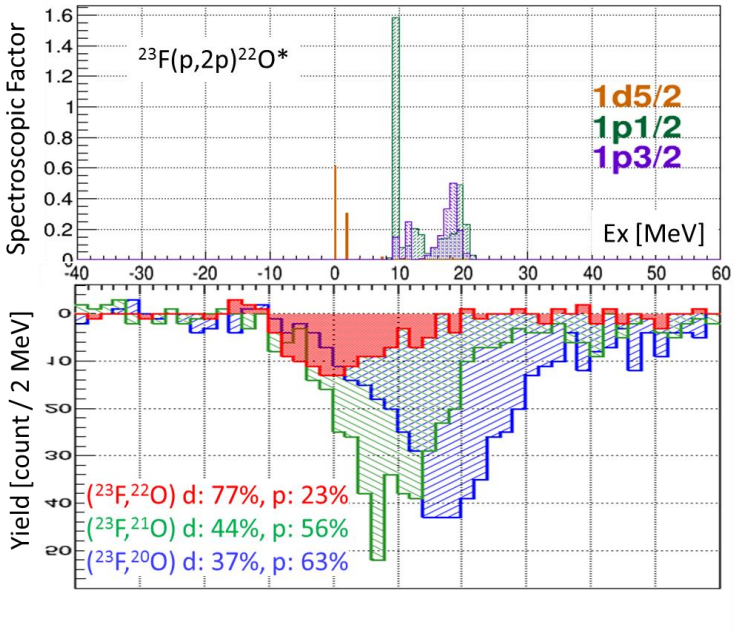

Figure 4-8 – The shell model calculation on the spectroscopic factors for the ^{23}F(p,2p) reaction. The top plot is the result of shell model calculation. The bottom plot is the experimental result. The bottom-left corner shows the precentages of d-orbit and p-orbit. see main text for detail.

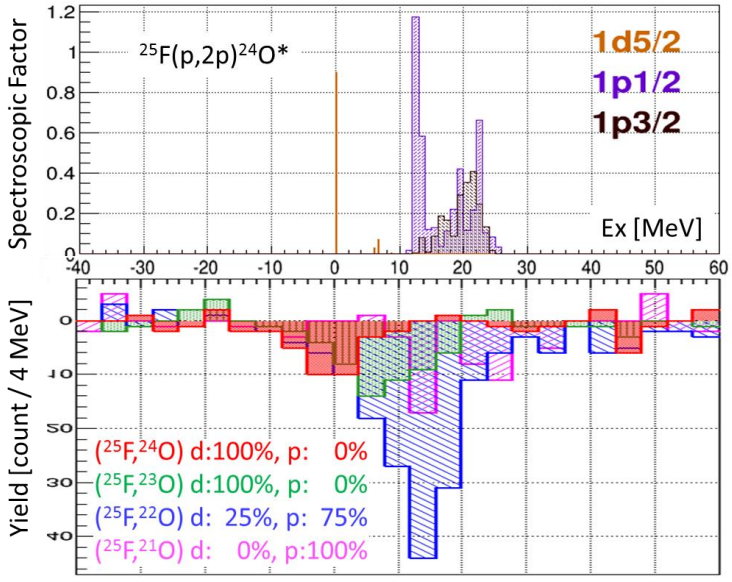

Figure 4-9 – The shell model calculation on the spectroscopic factors for the ^{25}F(p,2p) reaction. The top plot is the result of shell model calculation. The bottom plot is the experimental result. The bottom-left corner shows the precentages of d-orbit and p-orbit. see main text for detail.

The spectroscopic factors of the experimental results are compared with that of shell model calculation using different interactions in Table 4-4. The sums of the shell-model spectroscopic factors (using SFO interaction) of the $1d_{5/2}$ proton of ^{25}F is 1.0. The sum of the experimental spectroscopic factor of the $1d_{5/2}$ proton on ^{25}F was 1.06 ± 0.28. This agreed with the result of the shell model interaction. The strength of the $1d_{5/2}$ proton of ^{23}F should be also fragmented, we expect that the sum of the spectroscopic

factors is also similar to that of ^{25}F and agrees with shell model calculation. It is worthy to notice that the shell model calculation in section 1.1 supports the change of neutron structure due to the $1d_{5/2}$ proton.

Table 4-4 –Spectroscopic factors of experimental results and shell model calculations.

Partition	S_{exp}	S_{th}(SFO)	S_{th}(USDB)	S_{th}(SDPF-MU)
^{23}F(p,2p)				
^{22}O	0.37 ± 0.10	0.92	1.08	1.00
^{21,20}O	4.9 ± 1.5	5.21	-	-
^{25}F(p,2p)				
^{24}O	0.38 ± 0.14	0.9	1.01	0.95
^{23}O	0.69 ± 0.25	0.1	-	-
^{22,21}O	4.2 ± 1.6	6.139	-	-

The spectroscopic factors of shell model interactions have to be multiplied by a quenching factor of ~0.7 for normally bound nucleon. However, even including the quenching factor, the experimental spectroscopic factor of the (^{25}F,^{24}O) partition still disagrees with the theoretical value. Moreover, the present shell model interactions cannot reproduce the fragmentation. In ^{25}F, the SFO interaction shows some strengths of 0.1 form the knock-out of the $1d_{5/2}$ proton above the neutron threshold (Figure 4-9), but the strength is much smaller than the experimental value of ~0.7.

4.4.1 Deficit of the Shell Model Interactions

The discrepancy between the experimental and the shell model spectroscopic factors indicates there are missing components in the shell model interactions. Three possible causes will be discussed: missing of three-nucleon force, deformation effect of ^{23,25}F, and insufficient tensor force.

From Figure 1-13, the ground state binding energy of fluorine isotopes are reproduced with better agreement to the experimental value. It indicates the wavefunction of fluorine nucleus is more accurate when including three-nucleon force. However, since all shell model interactions are effectively fitted on experimental data, the three-nucleon force is implicitly included in the two-body matrix elements. One possibility is that, there are some components of the three-nucleon force may be not appeared in the fitting data. Considering the fluorine is the first isotopes that has a proton in the sd-shell and ^{23,25}F are close to the neutron dripline, there could be some missing components of the three-nucleon force which were not included in the fitting. Since the major component should be included in the shell model interaction, although missing some components of the three-nucleon force may be possible, it would not be the major factor for the discrepancy.

The ^{23,25}F nuclei could be deformed. As discussed in section 4.1.3, some mean field calcualtions suggest ^{23}F is slightly defromed. However, the shell model calculation should able to handle small deformation effect. Therefore, the deformation should not be the main reason for the discrepancy.

The strength of the tensor force near neutron dripline could be difference and stronger than that of stable nuclei. If the strength of the tensor force increased, the shell gap between the $1d_{5/2}$ and $1d_{3/2}$ neutron orbits could be smaller [20], and then the neutron configuration mixing would be stronger. In oder to explore this hypothesis and imitate an effect of a stronger tensor force, a toy model based on the USDB interaction was used. The original single particle energy of the $1d_{3/2}$ orbit was 2.117 MeV. This toy model keeps the single particle energy of the $1d_{3/2}$ state of ^{24}O, and lowers that of ^{25}F.

Figure 4-10 shows the result. The orange line is the spectroscopic factor of the ^{24}O ground state multiplied by a quenching factor of 0.7. The blue line is the sum of the spectroscopic fatcors of ^{24}O excited states up to 20 MeV. The single particle state has to be lowered by ~3.5 MeV to -1.5 MeV in order to be agreed with the experiemntal result. Note that the monopole-interaction energies bewteen the $1d_{5/2}$ proton and $1d_{3/2}$ neutron in the shell model interactions are roughlty -3.5 MeV (section 1.1.5) and the expeiemntal neutron separation energy of ^{26}F is 0.77 MeV. Although it is a toy model, the result suggests the tensor force should be stronger.

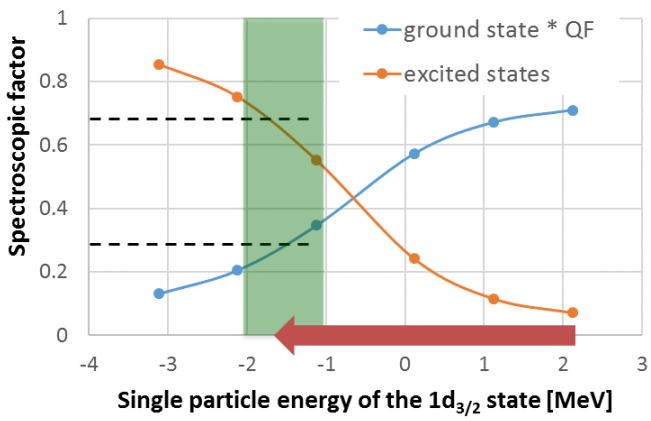

Figure 4-10 – The spectroscopic factors of the toy model on ^{25}F.
The two dashed lines indicates the experimental spectroscopic factors. The initial single-particle energy of the $1d_{3/2}$ neutron is 2.1 MeV. The ground-state spectroscopic factor of the ground state was multiplied by a quenching factor (QF).

The energy levels of ^{25}F using the toy model is shown in Figure 4-11 with experimental data and the result from the original USDB interaction. Since the single-particle energy of the $1d_{3/2}$ state of the neutron is lowered by 3.5 MeV to -1.5 MeV in the toy model, the state-mixing is stronger and the level density is also higher. The energy levels of the toy model suggests lowering the single-particle energy to imitate the tesnor force is a very crude appraoch. Since the toy model keeps the single-particle energy of ^{24}O, the energy levels of ^{24}O does not changed.

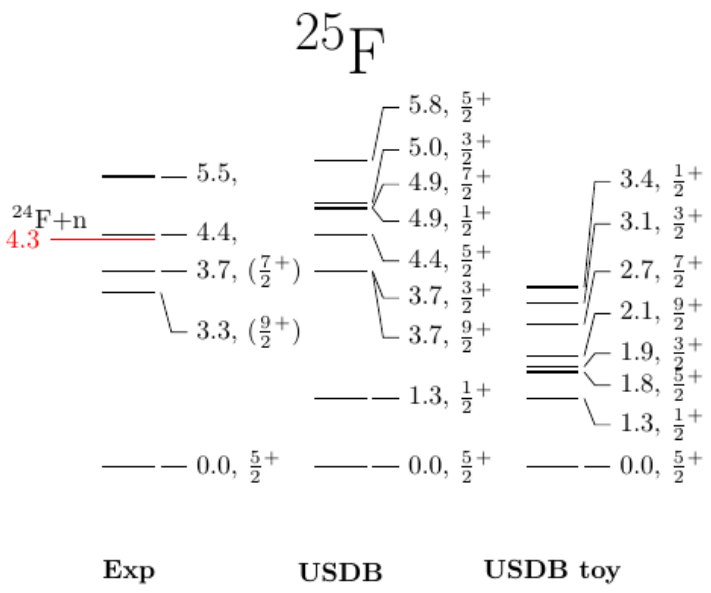

Figure 4-11 – The energy levels of ^{25}F from experiment, USDB interaction, and the modified USDB interaction (USDB toy).

4.4.2 Comment on Our Results and the Gade Plot

We have to emphasis that our results show that the reduction factors $R_s = S_{exp}/S_{th}$ accidentally agreed with the Gade plot (Figure 1-10). The author claimed that the plot was due to the correlation effect of the removed nucleon. However, there is no correlation effect in the $1d_{5/2}$ proton of ^{25}F, which is a single particle state, and the fragmentation is due to the change of the neutron shell. More fundamentally, the Gade plot relied on the accuracy of the shell model interactions, and our result indicates that the present shell model interactions are inaccurate. Therefore, the comparision between our results with the Gade plot is not valid.

4.5 Conclusion

We measured the integrated cross-section of the knocked-out deeply bound protons of ^{23}F and ^{25}F. The total integrated cross-sections, up to 20 MeV excitation energy, of (^{23}F,^{22}O) and (^{25}F,^{24}O) were similar. The spectroscopic factors were extracted using the DWIA calculation with the momentum analysis. The occupation numbers of the deeply bound $1d_{5/2}$ proton of ^{25}F was obtained and equaled 1.0 ± 0.3. Large fragmentations of the strength of the $1d_{5/2}$ proton of ^{23}F or ^{25}F were observed (indirectly in the case of ^{23}F). Since the $1d_{5/2}$ proton is a single-particle state, therefore, the fragmentation of the strength was caused by the change of neutron shell structure. The wavefunction of ^{25}F has large component of ^{24}O excited states indicates that the configuration mixing in the neutron shell is larger than that of oxygen. Larger configuration mixing indicates the spacing between $1d_{5/2}$, $2s_{1/2}$ and $1d_{3/2}$ orbits should be smaller than that of oxygen, and the $N = 16$ magicity disappears. The possible mechanism of the change of the

neutron shell by the $1d_{5/2}$ proton could be the tensor force that the $1d_{3/2}$ neutron orbit lowered while the $1d_{5/2}$ neutron orbit raised.

The spectroscopic strength of the $1d_{5/2}$ proton of ^{25}F and excitation energies of ^{23,25}F agreed with the shell model calculation. But the shell model interactions (SFO, USDB, and SDPF-MU) cannot produce the fragmentation of the strength. This indicates that the interactions are insufficient for the deeply bound nucleons near the neutron dripline. Using a toy model based on USDB interaction, the single particle energy of the $1d_{3/2}$ state has to be lowered by ~3.5 MeV to reproduce the fragmentation of the spectroscopic strength of ^{25}F. This suggests the strength of the tensor force should be stronger than present interactions.

Additional to the sd-shell, the occupation numbers of the p-orbit proton of ^{23,25}F, which is at least 10 MeV below the Fermi surface, were also deduced and equaled ~4.5 or ~75% of the IPM limit. This value was similar to that of ^{16}O, ^{40}Ca, ^{48}Ca, ^{90}Zr, and ^{208}Pb. It suggests that the short-range correlation in nuclear interior is same for neutron rich and stable nuclei.

Chapter 5

Summary

How the neutron sd-shell structure is changed by the $1d_{5/2}$ proton in neutron-rich ^{23,25}F nuclei? The change of neutron dripline from oxygen to fluorine suggests that the neutron-shell structure is difference between neutron-rich oxygen and fluorine because of the single $1d_{5/2}$ proton. For example, if the neutron-shell structure of fluorine is as same as that of oxygen, the spectroscopic factor of the $1d_{5/2}$ proton should be unity. Using proton removal spectroscopy and the fact that the $1d_{5/2}$ proton is in a single-particle orbit, we can study how the proton changes the neutron shell.

The quasi-free (p,2p) direct knockout reaction at medium energy is a clean and simple reaction to study the spectroscopic properties. The ^{23,25}F cocktail beams were produced by RIBF, RIKEN Nishina Center using the BigRIPS in-flight fragment separator and were transported to the SHARAQ spectrometer. The ^{23,25}F nuclei were ~285A MeV and bombarded on a proton crystal-target ($C_{10}H_8$). The (p,2p) knockout reaction was identified using coincident of the two scattered protons. The energies and the scattering angles of the protons were measured using plastic scintillators and multi-wire drift chambers that covered forward angle from $20°$ to $70°$. The reaction residues were identified using the SHARAQ spectrometer. The missing mass or the excitation energy was deduced using the four-momenta of the incident nuclei, the target proton, and the two scattered protons. The carbon background was estimated using a carbon target. The spectra of the excitation energy were partitioned using neutron thresholds of the residues.

The experimental integrated cross-sections were compared with the DWIA calculation after analysis of momentum distributions. The result shows that the spectroscopic factors of the ground state of the oxygen residue are too small. This indicates the neutron shell do change by the proton. Also, the fragmentation of the spectroscopic strength of the $1d_{5/2}$ proton was observed in ^{25}F (indirectly observed in ^{23}F). Using the fact that the $1d_{5/2}$ proton is in a single-particle state, which was also confirmed by this experiment that the occupation number of the $1d_{5/2}$ proton was 1.0 ± 0.3, the fragmentation implies that the wavefunction of ^{25}F could be expressed as $|^{25}\mathrm{F}\rangle \approx \sqrt{0.36}\left[|\pi\rangle|^{24}\mathrm{O}_{\mathrm{g.s.}}\rangle\right] + \sqrt{0.65}\left\{\left[|\pi\rangle|^{24}\mathrm{O}^{1}\rangle\right] + \left[|\pi\rangle|^{24}\mathrm{O}^{2}\rangle\right] + \cdots\right\} + \cdots$, where $|\pi\rangle$ is the wavefunction of $1d_{5/2}$ proton and $|^{24}\mathrm{O}^{i}\rangle$ is the wavefunction of the excited state of ^{24}O. The single $1d_{5/2}$ proton changes the neutron sd-shell structure significantly that ^{25}F has large component of excited ^{24}O. This result indicates that the configuration mixing in the neutron shell in ^{25}F is larger than that in ^{24}O. This is possible when the spacing between $1d_{5/2}$, $2s_{1/2}$ and $1d_{3/2}$ orbits in ^{25}F becomes smaller and the $N = 16$ magicity disappears. The experimental results

suggest a similar case should be in ^{23}F. The possible mechanism of the change of the neutron shell by the proton could be the tensor force that the energy of the $1d_{3/2}$ neutron orbit lowered while that of the $1d_{5/2}$ neutron orbit raised. The nuclear structures of the ^{25}F and ^{23}F demonstrated the Type-1 shell evolution, which driven by tensor force.

The experimental results were compared with the shell model calculations to explore the shell structure. The sum of the spectroscopic factors of the $1d_{5/2}$ proton of the experiment was agreed with that of the calculation. However, none of the present interactions (SFO, USDB, and SPDF-MU) can reproduce the fragmentation in the ^{25}F(p,2p) reaction. Using a toy model, the single particle energy of the $1d_{3/2}$ state of USDB interaction has to be lowered by ~3.5 MeV to reproduce the fragmentation of spectroscopic strengths of ^{25}F.

Additional to the sd-shell, the occupation numbers of the p-shell, which is at least 10 MeV below the Fermi surface, were obtained. The fractions of occupancy are ~0.75 for both ^{23}F and ^{25}F, which is similar to that of stable nuclei ^{16}O, ^{40}Ca, ^{48}Ca, ^{90}Zr, and ^{208}Pb. This suggests the short-range correlation is same for stable and unstable nuclei.

In conclusion, we aim to know how the neutron shell structure is changed by the $1d_{5/2}$ proton in ^{23,25}F. Using proton removal spectroscopy, the experimental results implied that the ^{25}F cannot be expressed as a simple system of a proton on top of the ground state of double magic ^{24}O that the $1d_{5/2}$ proton reduces the d-shell gap of the neutron shell, increases the neutron configuration mixing, and then the $N = 16$ magicity disappears. The change of the neutron shell by the $1d_{5/2}$ proton could be explained using Type-I shell evolution driven by tensor force. The discrepancy between the experimental results and the shell model interactions suggests that the strength of the tensor force should be stronger than present shell model interactions.

Appendix A

Miscellaneous Calculations

A.1 Kinematics of Knockout Reaction

In the reference frame of fluorine nucleus, the proton is coming at medium energy. After an orbital proton was knocked out, the residual oxygen nucleus is in an excited state. We assume that the knockout process does not change the nuclear structure but only leaving a hole based on the impulse approximation. If we notate the reaction as $T(F,O)12, F = O + k$ in the laboratory frame, we have five four-momenta. The conservation law in the laboratory frame is

$$\mathbb{P}_T + \mathbb{P}_F = \mathbb{P}_1 + \mathbb{P}_2 + \mathbb{P}_O, \qquad \mathbb{P}_k = \mathbb{P}_F - \mathbb{P}_O, \tag{A.1.1}$$

where $\mathbb{P}$ is four-momentum, the subscript T stands for the proton target, F stands for the fluorine nucleus, 1 stands for the knocked out proton, 2 stands for the scattered proton, O stands for the oxygen residue, and k stands for the orbital proton. The information of the incident proton, the fluorine, the scattered proton and the knocked out proton were detected in the experiment. The only missing information was the four-momentum of the oxygen residue.

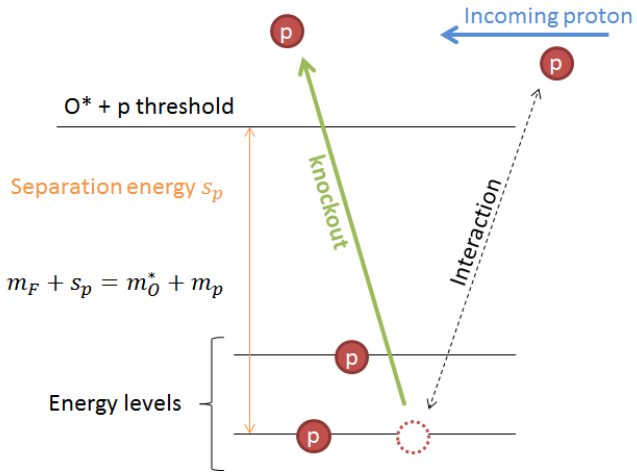

Figure A-1 – Illustration on the energy level of a knockout reaction and the definition of the separation energy

The mass of the excited residue m_O^* pluses the mass of proton m_p is equal to the mass of fluorine m_F and the experimental proton separation energy s_p

$$m_O^* + m_p = m_F + s_p, \tag{A.1.2}$$

or

$$s_p = m_O^* + m_p - m_F. \tag{A.1.3}$$

The energy part and the momentum part in the conservation law [see equation (A.1.1)] are

$$\begin{aligned} E_T + m_F &= E_1 + E_2 + E_O, \\ \overrightarrow{p_T} &= \overrightarrow{p_1} + \overrightarrow{p_2} + \vec{k}, \qquad \vec{k} = \overrightarrow{p_O} \end{aligned} \tag{A.1.4}$$

where E is the total energy, $\vec{p}$ and $\vec{k}$ are the momenta. The conservation laws can be rearranged as

$$\begin{aligned} E_T + (m_F - E_O) &= E_1 + E_2, \\ \overrightarrow{p_T} - \vec{k} &= \overrightarrow{p_1} + \overrightarrow{p_2}. \end{aligned} \tag{A.1.5}$$

Then, the four-momentum of the orbital proton (quasi-proton) can be defined as

$$\begin{aligned} \mathbb{P}_k &= \left(m_F - E_O, -\vec{k}\right), \\ E_O &= \sqrt{{m_O^*}^2 + k^2} = \sqrt{\left(m_F - m_p + s_p\right)^2 + k^2}. \end{aligned} \tag{A.1.6}$$

Thus the many-body scattering reduced to a 2 body proton-quasi-proton inelastic scattering, and the conservation law becomes

$$\mathbb{P}_T + \mathbb{P}_k = \mathbb{P}_1 + \mathbb{P}_2. \tag{A.1.7}$$

Changing into the center of momentum (CM) frame, by a center of momentum four-momentum

$$\mathbb{P}_c = (E_c, \overrightarrow{p_c}) = \frac{1}{2}(\mathbb{P}_T + \mathbb{P}_k). \tag{A.1.8}$$

The required boost of the Lorentz transform is

$$\vec{\beta} = -\frac{\overrightarrow{p_c}}{E_c} = -\frac{\overrightarrow{p_T} - \vec{k}}{E_T + m_F - E_O}. \tag{A.1.9}$$

In the CM frame

$$p_T' + p_k' = p_1' + p_2' = 0. \tag{A.1.10}$$

The energy part from the CM frame to the laboratory frame is

$$E_1 + E_2 = \gamma(E_1' + E_2') - \gamma\vec{\beta} \cdot (p_1' + p_2') = \gamma(E_1' + E_2'). \tag{A.1.11}$$

Define the total energy in the CM frame be

$$E = \frac{1}{\gamma}(E_1 + E_2) = \frac{1}{\gamma}\left(E_T + m_F - \sqrt{\left(m_F - m_p + S_{exp}\right)^2 + k^2}\right), \tag{A.1.12}$$

then

$$E_1' + E_2' = \sqrt{m_p^2 + {p_1'}^2} + \sqrt{m_p^2 + {p_2'}^2} = E. \tag{A.1.13}$$

The solution of the scattered momneutm in the CM frame can be found by solving equations (A.1.10) and (A.1.13). The solution is

$${p_1'}^2 = \frac{1}{2}\left(E^2 - 4m_p^2\right), \tag{A.1.14}$$

The four-momentum of $\mathbb{P}_1'$ and $\mathbb{P}_2'$ can be calculated with a suitable rotation by the scattering angles θ_{NN} and ϕ_{NN}. By an inverse Lorentz transform, the four-momentum in any reference frame can be calculated.

We can calculate the scattering angles of $\mathbb{P}_1$ and $\mathbb{P}_2$, given the s_p, $\vec{k}$, θ_{NN} and ϕ_{NN}, In experiment, we know $\mathbb{P}_T$, m_F, m_O and measure $\mathbb{P}_1$ and $\mathbb{P}_2$. The s_p is given by

$$\begin{aligned} s_p &= m_O^* + m_p - M_F \\ &= \sqrt{(E_T + m_F - E_1 - E_2)^2 - (\overrightarrow{p_T} - \overrightarrow{p_1} - \overrightarrow{p_2})^2} + m_p - m_F. \end{aligned} \tag{A.1.15}$$

The missing momentum is

$$\vec{k} = \overrightarrow{p_T} - \overrightarrow{p_1} - \overrightarrow{p_2}. \tag{A.1.16}$$

We are going to show a supplementary calculation for the energy of the knocked out proton. We notate the reaction as $A(a, cd)B, A = B + b$ in the nuclear frame, which is used in the code THREEDEE. We have five four-momenta and the conservation law in the nuclear frame is

$$\mathbb{P}_A + \mathbb{P}_a = \mathbb{P}_c + \mathbb{P}_d + \mathbb{P}_B, \qquad \mathbb{P}_b = \mathbb{P}_A - \mathbb{P}_B, \tag{A.1.17}$$

where A is fluorine nucleus, a is the incident proton, c and d are the scattered protons, B is the oxygen residue, and b is the orbital proton. The kinematics input of the code THREEDEE are the proton separation energy s_p, the incident proton kinetics energy T, the scattered proton kinetics energy T_c, the scattered proton angle θ_c, the knocked out proton angle θ_d, and the off-plane angle $\beta_d = \phi_d - \phi_c$. We can calculate the total energy of the scattered proton E_d, the magnitude of the momentum of the residual oxygen k, the polar angles of the oxygen θ_k and ϕ_k, the scattering angles in the rest frame of the center of momentum θ_{NN} and ϕ_{NN}. According to the energy-momentum conservation laws

$$m_F + T + m_p = m_p + T_c + E_d + E_O, \tag{A.1.18a}$$

$$p_T = p_c \cos(\theta_c) + p_d \cos(\theta_d) + k \cos(\theta_k), \tag{A.1.18b}$$

$$0 = p_c \sin(\theta_c) \cos(\phi_c) + p_d \sin(\theta_d) \cos(\phi_d) + k \sin(\theta_k) \cos(\phi_k), \tag{A.1.18c}$$

$$0 = p_c \sin(\theta_c) \sin(\phi_c) + p_d \sin(\theta_d) \sin(\phi_d) + k \sin(\theta_k) \sin(\phi_k), \tag{A.1.18d}$$

using equation (A.1.18c) and (A.1.18d), eliminate ϕ_k

$$k^2 \sin^2(\theta_k) = p_c^2 \sin^2(\theta_c) + p_d^2 \sin^2(\theta_d) + 2p_c p_d \sin(\theta_c) \sin(\theta_d) \cos(\beta_d), \tag{A.1.19}$$

combine equation (A.1.18b) and (A.1.19), eliminate θ_k

$$\begin{aligned} k^2 = p_T^2 + p_c^2 + p_d^2 - 2p_T p_c \cos(\theta_c) - 2p_d p_T \cos(\theta_d) \\ + 2p_c p_d (\cos(\theta_c) \cos(\theta_d) + \sin(\theta_c) \sin(\theta_d) \cos(\beta_d)). \end{aligned} \tag{A.1.20}$$

Square the equation (A.1.18a) after separated out E_O

$$E_O^2 = m_O^2 + k^2 = (m_F + T - T_c)^2 - 2E_d(m_F + T - T_c) + E_d^2, \tag{A.1.21}$$

Set $a = m_F + T - T_c$, $\Delta = \cos(\theta_c)\cos(\theta_d) + \sin(\theta_c)\sin(\theta_d)\cos(\beta_d)$, and substitute k with equation (A.1.20), and then replace $p_d = \sqrt{E_d^2 - m_p^2}$

$$m_O^2 + p_T^2 + p_c^2 - m_p^2 - 2p_T p_c \cos(\theta_c) + (2p_c\Delta - 2p_T\cos(\theta_d))\sqrt{E_d^2 - m_p^2} = a^2 - 2E_d a, \quad \text{(A.1.22)}$$

grouping the constant terms and set $b = m_O^2 + p_T^2 + p_c^2 - m_p^2 - 2p_T p_c \cos(\theta_c) - a^2$, and $c = 2p_c\Delta - 2p_T\cos(\theta_d)$

$$b - c\sqrt{E_d^2 - m_p^2} = -2E_d a, \quad \text{(A.1.23)}$$

after some manipulation

$$(4a^2 - c^2)E_d^2 + 4abE_d + b^2 + c^2 m_p^2 = 0. \quad \text{(A.1.24)}$$

There are two solutions of E_d, one corresponds to real p_d and the other one is complex p_d. After obtained E_d, the four-momenta $\mathbb{P}_d$ and $\mathbb{P}_B$ are known, we can easily deduce θ_k, ϕ_k, θ_{NN}, and ϕ_{NN}.

A.2 Time Resolution of Plastic Scintillators

A typical plastic scintillator equips 2 PMTs at the ends. We define the leading time of each PMT be t_1 and t_2 and assume the time reference has no uncertainly. The times recorded are

$$\begin{aligned} t_1 &= t_H + \frac{x}{\beta c} + t_{W1} + \tau_1 + \delta t_1 - T, \\ t_2 &= t_H + \frac{l - x}{\beta c} + t_{W2} + \tau_2 + \delta t_2 - T, \end{aligned} \quad \text{(A.2.2)}$$

where t_H is the real time of the scintillator is being hit, x is the distance between the hit position and the PMT, βc is the average speed of light in the scintillator and the light guide, t_W is the additional time caused by the walk effect, τ is the time offset, δt is the time uncertainty, and T is the reference time. The time-average and time-difference are defined as

$$\begin{aligned} \bar{t} &= \frac{t_1 + t_2}{2} = t_H + \frac{l}{2\beta c} + \frac{1}{2}(t_{W1} + t_{W2}) + \frac{1}{2}(\tau_1 + \tau_2) + \frac{1}{2}\delta t_1 + \frac{1}{2}\delta t_2 - T, \\ \Delta t &= t_1 - t_2 = \frac{x}{\beta c} + (t_{W1} - t_{W2}) + (\tau_1 - \tau_2) + \delta t_1 - \delta t_2. \end{aligned} \quad \text{(A.2.2)}$$

The uncertainly of time-difference is

$$\delta(\Delta t)^2 = \delta\left(\frac{x}{\beta c}\right)^2 + \delta(t_{W1} - t_{W2})^2 + \delta t_1^2 + \delta t_2^2. \quad \text{(A.2.3)}$$

In most cases, we can assume both time-uncertainly are the same or similar

$$\delta t_1 \sim \delta t_2 = \delta t. \quad \text{(A.2.4)}$$

With a further assumption that the walk effect is not serious, that is usually in case for large light output. Or the hit position is on the middle of the scintillator. Then, the uncertainly of the time-difference is simplified to

$$\delta(\Delta t)^2 = \delta\left(\frac{x}{\beta c}\right)^2 + \delta t_1^2 + \delta t_2^2. \tag{A.2.5}$$

And with the same assumptions and the hit-time t_H has no uncertainty, the uncertainly of the time-average is

$$\begin{aligned} \delta(\bar{t})^2 &= \frac{1}{4}(\delta t_1^2 + \delta t_2^2) = \frac{1}{4}\left(\delta(\Delta t)^2 - \delta\left(\frac{x}{\beta c}\right)^2\right), \\ \delta(\bar{t}) &= \frac{1}{2}\sqrt{\delta(\Delta t)^2 - \delta\left(\frac{x}{\beta c}\right)^2} \sim \frac{1}{2}\delta(\Delta t). \end{aligned} \tag{A.2.6}$$

If there is a drift chamber near the plastic scintillator, the hit-location can be known by the tracking result, and then a fixed position range can be selected. Assuming the events are within $\Delta x = 1$ mm and the speed of light in the plastic is 0.66c, the quantity $\delta\left(\frac{x}{\beta c}\right) = 5$ ps, which can be neglected.

A.3 Multiple Dimension Linear Regression

The ray tracking was done using the theory of multi-dimension linear regression. If the position of the trajectory is (X, Y, Z), and

$$\begin{aligned} X &= AZ + X_0 \\ Y &= BZ + Y_0 \end{aligned} \tag{A.3.1}$$

where A, B are the parameters related to the incident angle and X_0, Y_0 is the position at $Z = 0$. Hence, the position vector $\vec{r}$ can be parameterized by Z

$$\vec{r}(Z) = (X(Z), Y(Z), Z) = (X_0, Y_0, 0) + Z(A, B, 1) = \overrightarrow{r_0} + Z\vec{n}. \tag{A.3.1}$$

In theory of multi-dimension linear regression [109], the master equation is

$$P_i = H_{ij}\beta_j + \epsilon_i, \tag{A.3.2}$$

Where P_i is the dependent variable from the i-th measurement, β_j is the fitting parameter, H_{ij} is the independent variable that defines from the point of measurement, and ϵ_i is the error. In the case of 6-plane ray tracking for a 6 planes MWDC, the above set of equation reads as

$$\begin{pmatrix} X_1 \\ X_2 \\ U_1 \\ U_2 \\ V_1 \\ V_2 \end{pmatrix} = \begin{pmatrix} Z_1 & 1 & 0 & 0 \\ Z_2 & 1 & 0 & 0 \\ \cos\theta_U Z_3 & \cos\theta_U & \sin\theta_U Z_3 & \sin\theta_U \\ \cos\theta_U Z_4 & \cos\theta_U & \sin\theta_U Z_4 & \sin\theta_U \\ \cos\theta_V Z_5 & \cos\theta_V & \sin\theta_V Z_5 & \sin\theta_V \\ \cos\theta_V Z_5 & \cos\theta_V & \sin\theta_V Z_6 & \sin\theta_V \end{pmatrix} \begin{pmatrix} A \\ X_0 \\ B \\ Y_0 \end{pmatrix} + \begin{pmatrix} \epsilon_1 \\ \epsilon_2 \\ \epsilon_3 \\ \epsilon_4 \\ \epsilon_5 \\ \epsilon_6 \end{pmatrix}, \tag{A.3.3}$$

or in a matrix form

$$P = H \cdot \beta + \epsilon. \tag{A.3.4}$$

The degree of freedom is the number of rows subtracted by the number of parameters in β

$$DF = 6 - 4 = 2. \tag{A.3.5}$$

The unbiased best estimator of the ray vector β is $\hat{\beta}$, and this gives $\hat{P}$, the best estimator of P

$$\hat{P} = H \cdot \hat{\beta}. \tag{A.3.6}$$

The normal equation, which is as same as the equation deduced by least square method is

$$H^T \cdot H \cdot \hat{\beta} = H^T \cdot P. \tag{A.3.7}$$

Thus, the solution for the best estimator of β is

$$\hat{\beta} = (H^T \cdot H)^{-1} \cdot H^T \cdot P = G \cdot P. \tag{A.3.8}$$

The estimated respond can be calculated by equation (A.3.6)

$$\hat{P} = H \cdot G \cdot P. \tag{A.3.9}$$

The residue vector is defined as

$$e = P - \hat{P}. \tag{A.3.10}$$

The sum of square of residues is

$$SSR = e \cdot e^T = \sum \left(P_i - \hat{P}_i\right)^2. \tag{A.3.11}$$

The unbiased sample variance is

$$\sigma^2 = \frac{SSR}{DF}. \tag{A.3.12}$$

The variances of $\hat{\beta}$ and e are

$$\begin{aligned} Var(\hat{\beta}) &= (H^T \cdot H)^{-1}\sigma^2, \\ Var(e) &= (I - H \cdot G)\sigma^2. \end{aligned} \tag{A.3.13}$$

This algorithm can be extended to any-number-plane ray tracking as long as the inverse of $H^T \cdot H$ exist. We found that even in the case of 4-plane, this inverse exist, although the sample variance is undefined as the degree of freedom becomes zero. In this case, the linear regression becomes solving equation (A.3.2). When a weighting is needed. The master equations becomes

$$(W \cdot P) = (W \cdot H) \cdot \beta + (W \cdot \epsilon)\,, \tag{A.3.14}$$

where $W_{ij} = \delta_{ij} w_i$, w_i is the weighting factor.

The covariance matrix of $\hat{\beta}$ and e for 6-plane ray tracking in MWDC-L/R are,

$$Var(\hat{\beta}) = \begin{pmatrix} 0.799 & 0.018 & -0.775 & 0.073 \\ 0.018 & 8.123 \times 10^{-4} & -0.016 & 0.002 \\ -0.775 & -0.016 & 2.01 & -0.103 \\ 0.073 & 0.002 & -0.103 & 9.212 \times 10^{-3} \end{pmatrix} \sigma^2,$$

$$Var(e) = \begin{pmatrix} 0.35 & -0.42 & -0.12 & 0.17 & -0.02 & 0.07 \\ -0.42 & 0.60 & 0.05 & -0.16 & -0.17 & 0.06 \\ -0.12 & 0.05 & 0.16 & -0.12 & 0.25 & -0.21 \\ 0.17 & -0.16 & -0.12 & 0.11 & -0.13 & 0.12 \\ -0.02 & -0.17 & 0.25 & -0.13 & 0.49 & -0.37 \\ 0.07 & 0.06 & -0.21 & 0.12 & -0.37 & 0.29 \end{pmatrix} \sigma^2. \quad \text{(A.3.15)}$$

The covariance matrix of $\hat{\beta}$ and e for 7-plane ray tracking in DCX1, DCX2 are,

$$Var(\hat{\beta}) = \begin{pmatrix} 5.632 & 0.008 & 0.026 & 0.000 \\ 0.008 & 1.062 \times 10^{-5} & 0.000 & 0.000 \\ 0.026 & 0.000 & 17.753 & 0.024 \\ 0.000 & 0.000 & 0.024 & 3.387 \times 10^{-5} \end{pmatrix} \sigma^2$$

$$Var(e) = \begin{pmatrix} 0.53 & -0.4 & -0.29 & -0.01 & 0 & 0.01 & 0.03 \\ -0.40 & 0.3 & 0.22 & -0.01 & -0.01 & 0.01 & -0.01 \\ -0.29 & 0.22 & 0.17 & -0.04 & 0 & -0.01 & 0.03 \\ -0.01 & -0.01 & -0.04 & 0.55 & 0 & 0 & -0.5 \\ 0 & -0.01 & 0 & 0 & 0.52 & -0.5 & 0 \\ 0.01 & 0.01 & -0.01 & 0 & -0.5 & 0.48 & 0 \\ 0.03 & -0.01 & 0.03 & -0.5 & 0 & 0 & 0.45 \end{pmatrix} \sigma^2 \quad \text{(A.3.16)}$$

A.4 Scheme of code THREEDEE

The code THREEDEE uses the DWIA method to calculate the differential cross section of a knockout reaction. The flow chart of the code THREEDEE is shown in Figure A-2. The code first calculates the bound state radial wavefunction (BDSTS) from a predefined Woods-Saxon shape central potential, spin-orbit potential, and the Coulomb potentials, with user-input parameters. If the depth of the central potential is not specified, the code finds a consistence depth with the bound state wavefunction. Next, the code calculates the partial distorted wave (DSTWAV) from the Dirac phenomenological global potential with the central, the spin-orbit, and the Coulomb terms (EDAD, DP, COULPOT, and SCHEQ). The S-matrix of each partial wave is deduced by comparing with the Coulomb wavefunction. In additional, the Perey factor is also calculated from the Dirac phenomenological global potential (SCHEQ), and this enhanced asymmetry in the cross section by adding a damping effect on the distorted wavefunction (DAMP). If a potential table was used (GET_POTS_FROM_FILE), the Perey factor does not calculate, and no damping on the distorted wavefunction. The kinematics of the scattered particles then are calculated (PROLOG) and the corresponding partial distorted waves are also calculated with kinetic energy and Dirac phenomenological global potential of the residue. At this point, all radial parts

of the partial distorted waves are calculated. Each radial part of the distorted wave is combined with Winger D-matrix (WAVEB), which is the angular part, to form the complete wavefunction.

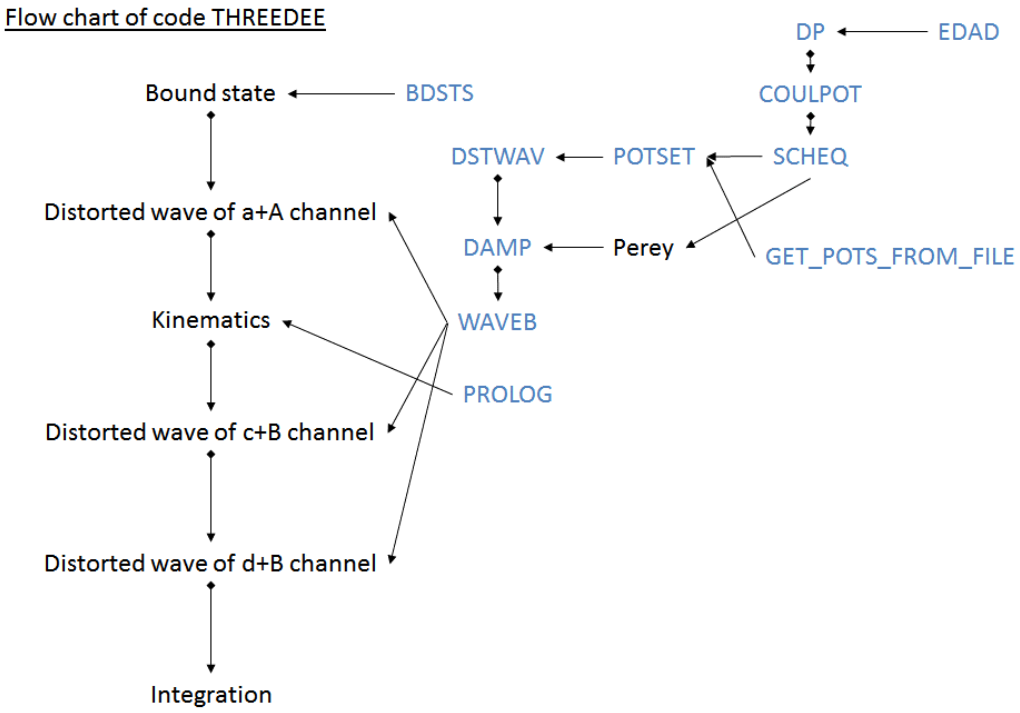

Figure A-2 – Flow chart of the code THREEDEE.
The blue texts are the name of subroutines.

The scattering amplitude $f(E_c, \Omega_c, \Omega_d)$ is calculated by Gaussian integration

$$f(E_c, \Omega_c, \Omega_d) = \int \chi_c^* \chi_d^* V_{ab} \chi_a \phi_b dr_a dr_b, \tag{A.4.1}$$

where χ are distorted wave for particle a, c, and d. The bound state wavefunction is ϕ_b. The scattering amplitude also depends on E_d, but E_c and E_d are correlated.

A.5 Multiple Scattering and Energy Acceptance

Because of the multiple scattering, the actual energy acceptance cannot be zero but a minimum value. We estimate the effect of multiple scattering using data from LISE++, which is from the code ATIMA [122]. We are aware the energy loss for low energy proton could be inaccurate. An energy loss calculation for low energy was calculated in the case of 10 MeV proton in 1-meter-air [123]. The energy loss was smaller by 3% than that of ATIMA. Therefore, the low energy effect should be insignificant. The multiple scattering produces energy loss dE, energy staggering δE (which is the fluctuation of energy loss), angular staggering $\delta\theta$, and lateral spread d. These qualities are illustrated in Figure A-3.

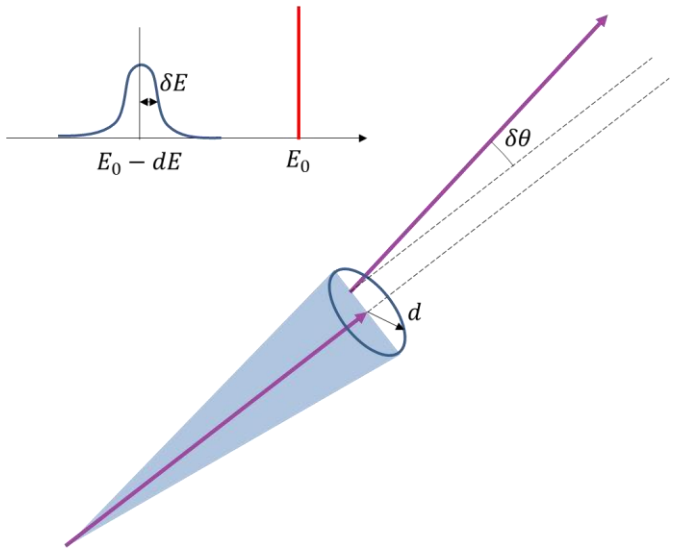

Figure A-3 – Meaning of energy loss *dE*, energy staggering *δE*, angular staggering *δθ*, and lateral spread *d*.

We use a simplified picture of the experimental setup as in Figure A-4. There is the target crystal, 72-mm N_2 gas, 128-μm Kapton film, then 38-mm vacuum, another 128-μm Kapton film, then at least 1-meter-thick air. We neglected the effect of the MWDC in front of the Tpla. We also did not include the boundary effect of the crystal.

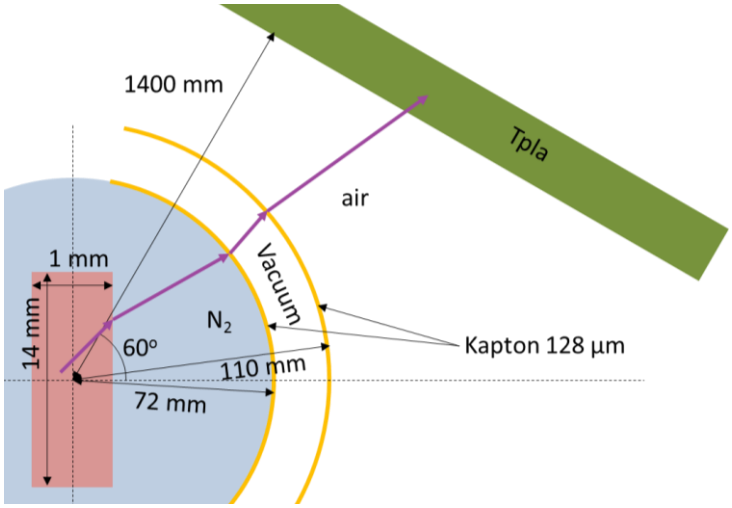

Figure A-4 – Illustration of the materials of the multiple scattering process.
The drawing is not in scale. The pink box is the crystal target. The blue circle is the N_2 gas. The yellow arcs are Kapton film. The rest is air. The purple arrows are the path of the proton that originates inside the target.

We denote a point on a boundary be $P = (r, k, E, t)$, where r is the position, $k = (\theta, \phi)$ is the unit vector of the direction that θ is the polar angle and ϕ is the azimuthal angle, E is the energy, t is the time elapsed. The process of calculating the effect of multiple scattering is shown in Figure A-5.

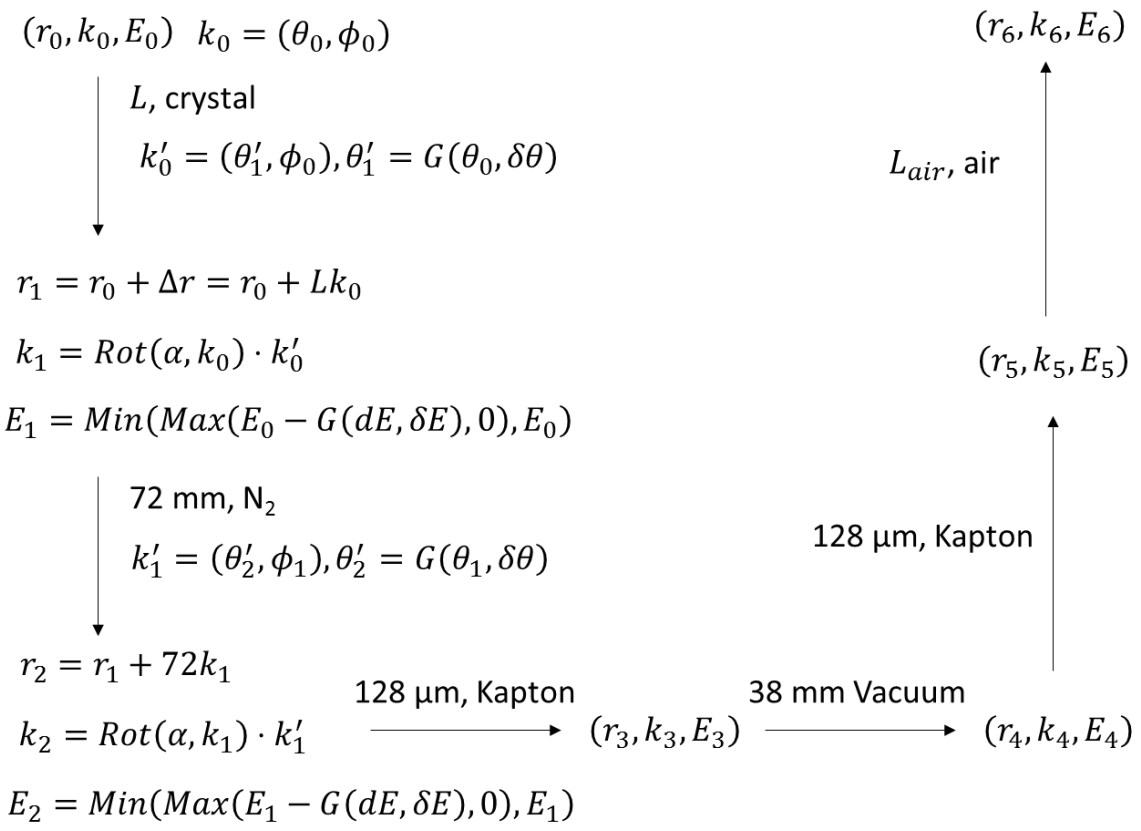

Figure A-5 -The flow chart of multiple scattering calculation.

At the beginning, an initial point $P_0 = (r_0, k_0, E_0, 0)$ was randomly generated uniformly inside the crystal. The direction and energy are also randomly generated. And the time elapsed is set to be 0. The travel path L inside the crystal can be calculated using the position and direction. Using the travel path and energy, the energy loss, energy staggering, angular staggering, and lateral spread was calculated. Since the lateral spread due to the crystal is only order of few µm, we neglected the lateral spread. The energy loss was randomly draw from a Gaussian distribution $G(dE, \delta E^2)$ of mean dE and variance δE^2. We limited the energy loss should be smaller than the original energy E_0 and larger than 0. The polar angle of a temporary direction vector was randomly draw from a Gaussian distribution of mean θ_0 and variance $\delta\theta^2$, while the azimuthal angle was kept the same. Then the new direction vector was calculated by randomly rotating the temporary direction vector around the old direction vector with a random angle α. The new position was calculated by offset the old position in the direction of the old direction vector by the length of the path. The time elapsed was calculated using the path length and mean energy $(E_0 + E_1)/2$. Thus, we have the new point P_1 on the boundary between the crystal and N_2 gas. We repeat the process that the lateral spread was very small and neglected. We added the lateral spread to the position after the air. The lateral spread vector is calculated using the cross product of the direction vector k_5 and z-axis (0,0,1), then rotating this vector around k_5 with a random angle, finally multiplied by the lateral spread which draw from a Gaussian distribution of mean 0 and variance d^2. i.e.,

$$\Delta r = r_5 + L_{air}k_5 + G(0, d)Rot(\alpha, k_5) \cdot (k_5 \times z),$$

$$L_{air} = \frac{1400 - r_5 \cdot n}{k_5 \cdot n},$$

where $n = (\pm \sin 60°, 0, \cos 60°)$ is the normal vector of the plane of plastic, 1400 is the minimum distance from target to plastic. In case the particle loss all energy or the energy is smaller than the stopping thickness, the position, direction, energy, and time elapsed were set to 0. The stooping thickness of the materials are shown in Figure A-6, Figure A-7, and Table A-1.

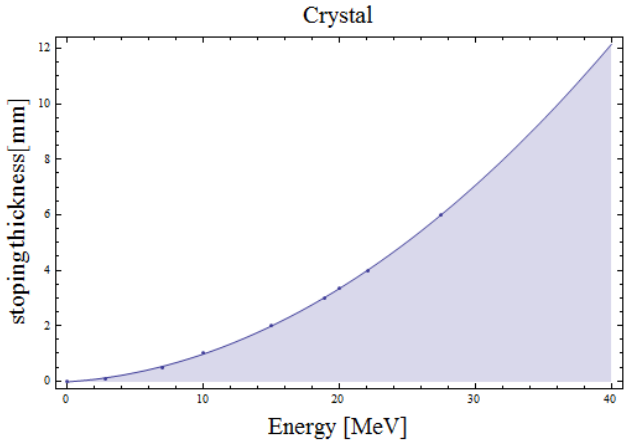

Figure A-6 - Stopping thickness in function of energy in crystal

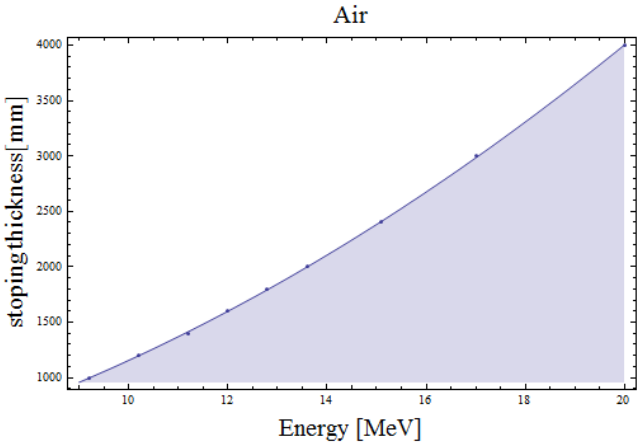

Figure A-7 - Stopping thickness in function of energy in Air

Table A-1 – The stopping thickness or energy of the materials.

Material	Stopping Thickness [mm] or Energy [MeV]
Crystal	$s_{cry}(E) = 0.00681E^2 + 0.032\,E - 0.02328$
N_2 (72 mm)	5.5 MeV
Kapton (128 μm)	3.3 MeV
Vacuum	0 MeV
Air	$s_{air}(E) = 7.89\,E^2 + 48.40\,E - 117.27$

To identify the minimum energy that can pass through N_2 gas, Kapton films, and air, we simulate random energy from (10, 30) MeV and angles of $\theta \in (15°, 70°)$ and $\phi \in (-20°, 20°)$. The result is shown in Figure A-8.

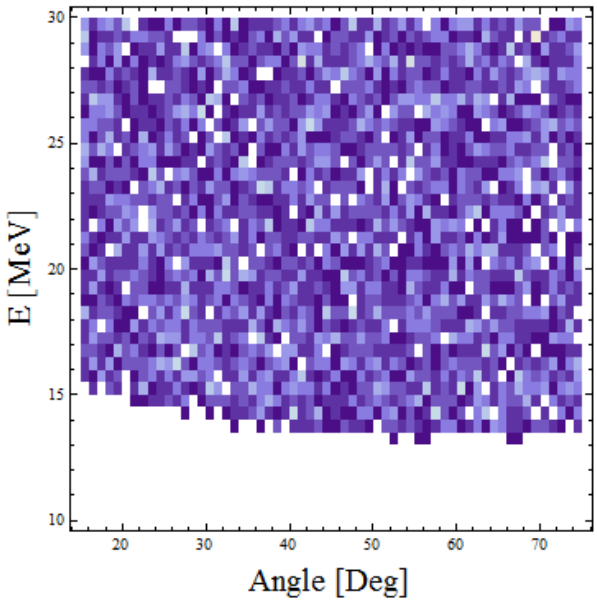

Figure A-8 – The effective kinematic acceptance due to multiple scattering of N_2 gas, Kapton films and air.

The result shows that the minimum energy that can pass through N2 gas, Kapton films, and air is 13 MeV. Therefore, the minimum energy of the original proton should be larger than 13 MeV, in order to reach to the detector.

Next, we simulate the full effect caused by all materials. The initial position was generated randomly inside the crystal, but the boundary of the crystal was not considered. The energy is generated randomly from (10, 30) MeV. The ray direction is randomly generated between $\theta \in (15°, 70°)$ and $\phi \in (-20°, 20°)$. The result shows in Figure A-9. The minimum energy that can be detected is around 14 MeV. Therefore, the minimum range of the effective energy acceptance is 14 MeV. Ideally, the energy range of the detection is very small, only limited by the time window. We assume the windows is ranging from 0 ns to 50 ns, which is corresponding to minimum energy of 4 MeV.

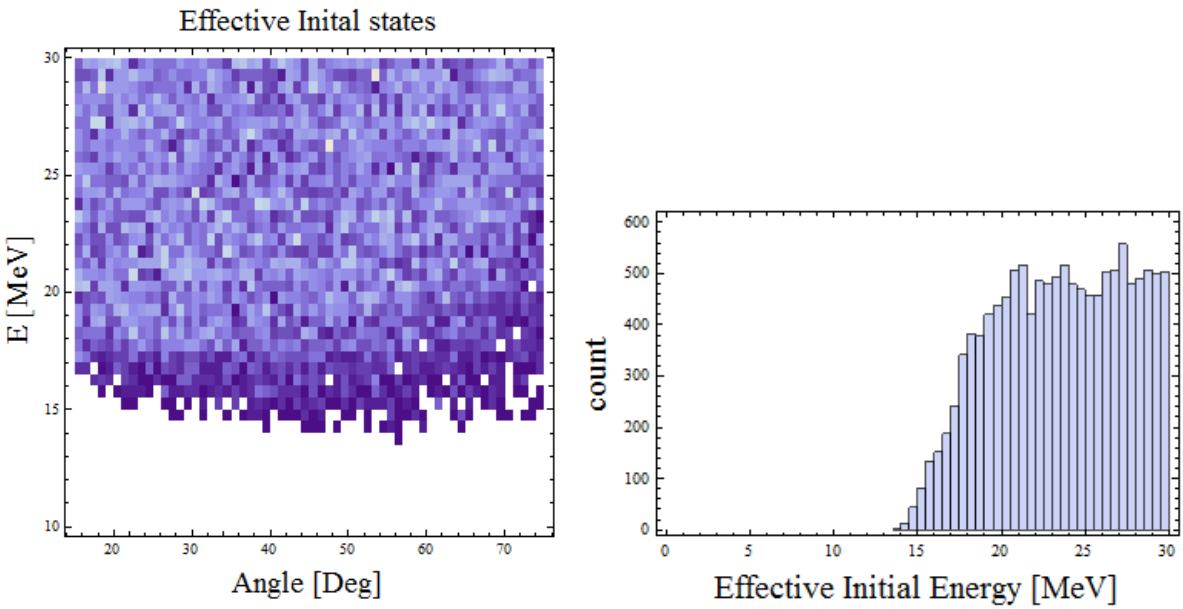

Figure A-9 – The distribution after multiple scattering.
The left plot is the initial distribution that being detected. The right plot is the distribution of initial energy.

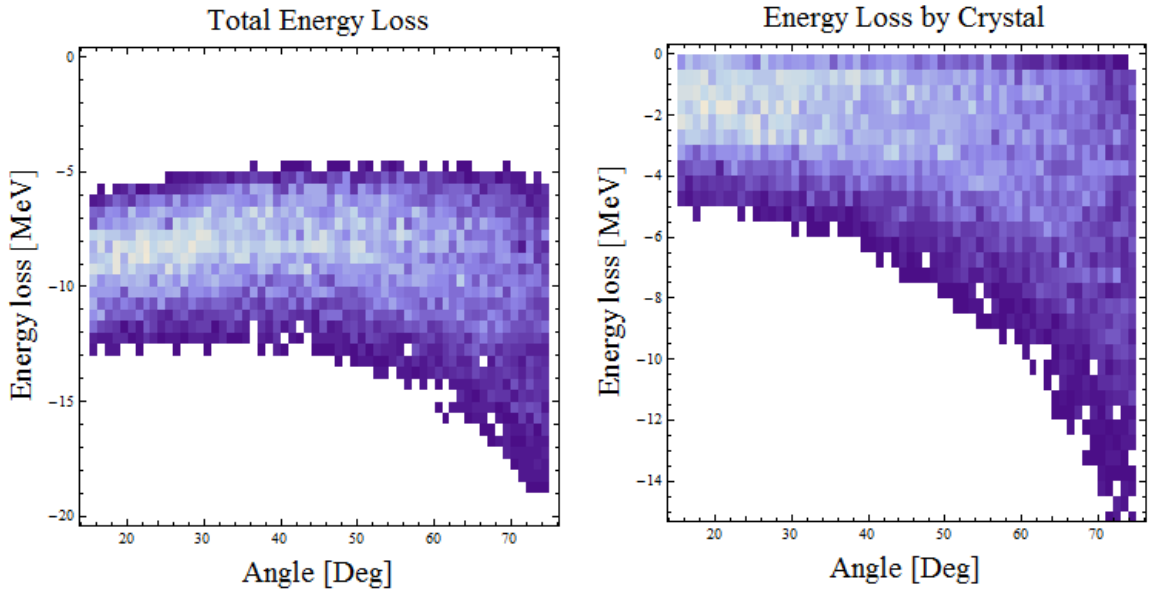

Figure A-10 – The energy loss due to multiple scattering.
The left plot is the total energy. The right plot is the energy lost in crystal.

A.6 Basic of Nuclear Magnetic Resonance (NMR)

The direction of the spin of a spin-polarized protons ensemble under a static magnetic field can be rotated by applying a transverse magnetic field (field strength is H_{NMR}). This is called NMR. According to Rabi precession theory, the Hamiltonian in the Laboratory frame is

$$H_L = \Omega_I I_z + \cos(\omega_{NMR} t)\, I_x, \tag{A.5.1}$$

and the Hamiltonian in the rotating frame is,

$$H_R = (\omega_{NMR} - \Omega_I) I_z + \Omega_R I_x, \tag{A.5.2}$$

where I_z and I_x are the z- and x- component of the spin angular momentum operator in the rotating frame. ω_{NMR} is the frequency of the transverse magnetic field, Ω_R is the transverse Larmor frequency, such that

$$\Omega_R = \gamma_I B_{NMR}, \tag{A.5.3}$$

where B_{NMR} is the magnetic field strength generated from the NMR coil, and γ_I is the gyromagnetic ratio. Ω_I is the Larmor frequency of proton under external magnetic field B, the relation with the magnetic field is

$$\Omega_I = \gamma_I B. \tag{A.5.4}$$

The gyromagnetic ratio of proton is $\gamma_I = 267.5\ \text{Mrad}\,\text{s}^{-1}\,\text{T}^{-1} = 41.577\ \text{MHz}\,\text{T}^{-1}$. In general, the $(\omega_{NMR} - \Omega_I)$ is not zero and creates an effective magnetic field (or the precession axis) on the x-z plane of the rotating frame. The precession axis in the rotation frame is

$$\begin{aligned} r &= |r|(\cos(\theta), 0, \sin(\theta)), \\ |r| &= \sqrt{(\omega_{NMR} - \Omega_I)^2 + \Omega_R^2} = \Omega_{eff}, \\ \tan(\theta) &= \frac{\omega_{NMR} - \omega_I}{\omega_R}. \end{aligned} \tag{A.5.5}$$

The magnitude of the magnetic field along the precession axis determines the angular frequency of the precession.

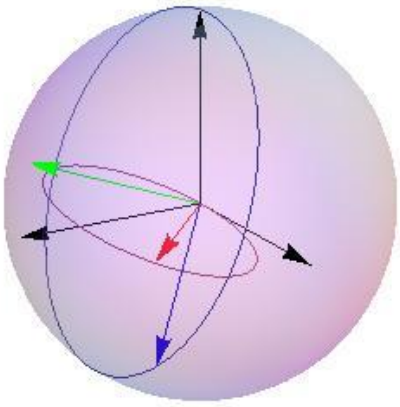

Figure A-11 – Illustration of the mechanism of the NMR.
The green arrow is the direction of the effective magnetic field or the precession axis, the blue arrow is the spin direction and the red arrow is the x-y plane projection of the spin. The blue circle is the locus by the tip of the spin and the red ellipse is the locus by the tip of the red arrow.

The locus of the tip of a normalized polarization vector v is rotating around the precession axis and form a cone (Figure A-11). The locus can be found by using the Euler angle

$$v = R_y(\theta)R_z(\alpha)R_y(-\theta)\hat{z} = \begin{pmatrix} \cos(\theta)\sin(\theta)\,(1-\cos(a)) \\ -\sin(\theta)\sin(\alpha) \\ \cos(\theta)^2 + \sin(\theta)^2\cos(\alpha) \end{pmatrix}, \tag{A.5.6}$$

where θ is the angle between the precession axis (direction of effective magnetic field) and the z-axis. α is the rotating angle of the polarization vector around the precession axis. The NMR coil only sensitive to the transverse component, thus, the magnitude of the NMR signal is

$$A = \sin(\theta)\sqrt{\cos^2(\theta)\,(1-\cos(\alpha))^2 + \sin^2(\alpha)}. \tag{A.5.7}$$

A.7 Fourier Transformation of the NMR Frequency Spectrum

This chapter explains the relationship between the NMR signal, or the FID (free induction decay) signal, and the frequency spectrum. The FID signal can contain different frequencies and can be written as a complex signal as

$$s(t) = \sum_n A_n e^{i2\pi f_n t + i\phi_n} e^{-t/T_n}, \tag{A.6.1}$$

where A_n is the amplitude of each frequency, f_n is the frequency, ϕ_n is the phase shift, and T_n is the decay time constant. The frequency spectrum can be obtained by Fourier transform on a finite time domain

$$S(f) = \int_a^{a+L} s(t)e^{-i2\pi ft}dt. \tag{A.6.2}$$

Since the integration is a linear operator, the Fourier spectrum is

$$\begin{aligned} S(f) &= \sum_n A_n \int_a^{a+L} e^{i2\pi f_n t + i\phi_n} e^{-t/T_n} e^{-i2\pi ft}dt\,, \\ S(f) &= \sum_n \frac{A_n e^{i\phi_n} e^{i2\pi(f_n - f)a} e^{-a/T_n}}{i2\pi(f_n - f) - 1/T_n}\left(e^{i2\pi(f_n-f)L} e^{-L/T_n} - 1\right). \end{aligned} \tag{A.6.3}$$

Let's assume the integration interval is much larger than the decay time and the integration start time is smaller than the decay time, so that $L \gg T_n \gg a$, then the result simplified to

$$\sum A_n e^{i\phi_n} e^{i2\pi(f_n - f)a} \tag{A.6.4}$$

$$= \sum_n \frac{A_n}{\frac{1}{T_n^2} + 4\pi^2(f_n - f)^2}\left(\frac{1}{T_n} + i2\pi(f_n - f)\right)e^{i(\phi_n + 2\pi(f_n - f)a)}.$$

The real part and imaginary part are

$$\begin{aligned} Re\big(S_n(f)\big) &= A_n \frac{\frac{1}{T_n}}{\frac{1}{T_n^2} + 4\pi^2(f_n - f)^2}\cos(\phi_n + 2\pi(f_n - f)a), \\ Im\big(S_n(f)\big) &= A_n \frac{2\pi(f_n - f)}{\frac{1}{T_n^2} + 4\pi^2(f_n - f)^2}\sin(\phi_n + 2\pi(f_n - f)a). \end{aligned} \tag{A.6.5}$$

The amplitude is

$$|S_n(f)| = A_n \frac{1}{\sqrt{\frac{1}{T_n^2} + 4\pi^2(f_n - f)^2}}. \tag{A.6.6}$$

By using the amplitude, the phase is gone and the result is simpler. The maximum and the FWHM (full-width half-maximum) of each peak are

$$\begin{aligned} |S(f_n)| &= A_n T_n, \\ \text{FWHM} &= \frac{\sqrt{3}}{\pi T_n}. \end{aligned} \tag{A.6.7}$$

Therefore, the FWHM is inversely proportional to the decay time constant. If we assume the cross terms of the Fourier Amplitude are small and can be neglected, which mean the frequency peaks are well separated, then we have

$$|S(f)| = \sum_n |S_n(f)| = \sum_n \frac{A_n}{\sqrt{\frac{1}{T_n^2} + 4\pi^2(f_n - f)^2}}. \tag{A.6.8}$$

A.8 Single Electron – Single Proton Continuous Wave Solid Effect

The solid effect is the heart of the dynamic nuclear polarization (DNP). It relies on the hyperfine coupling between an electron and a proton. In order to maximized the coupling, the Larmor frequencies of them have to be similar for resonance to occur, but the gyromagnetic ratios of electron (28025 $MHzT^{-1}$) and proton (42.577 $MHzT^{-1}$) are so different, about 660 times difference. Therefore, the DNP employed a traversed microwave to reduce the Larmor frequency of the electron in rotating frame, and then matching the Larmor frequency of the proton. The Hamiltonian between an electron, a proton, and the external magnetic fields is

$$
\begin{aligned}
H &= H_z + H_{SI} + H_{rf}, \\
H_z &= \Omega_S S_z + \Omega_I I_z, \\
H_{SI} &= A_0 \left(\vec{S} \cdot \vec{I} - 3\left(\vec{S} \cdot \hat{r}\right)\left(\vec{I} \cdot \hat{r}\right) \right), \\
H_{rf} &= 2\Omega_\mu \cos \omega t \, S_x = \Omega_\mu S_x \left(e^{i\omega t} + e^{-i\omega t} \right),
\end{aligned}
\tag{A.7.1}
$$

where, H is the total Hamiltonian, H_z is the Larmor term from the electron interacts with an external magnetic field, the Ω_S and Ω_I are the Larmor frequencies of the electron and the proton respectively, and the S_z and I_z are the electron and proton spin operators at z-axis. H_{SI} is the electron-proton spin-spin hyperfine coupling term, $A_0 = \left(\frac{\mu_0}{4\pi}\right)\gamma_e\gamma_p\frac{\hbar}{r^3}$ is the coupling strength, $\hat{r}$ the relative positon unit vector, and r is the relative distance. The coupling strength is about 3 MHz for 1 Å separation. H_{rf} is the electron spin affected by an external transverse microwave term, ω is the microwave frequency, Ω_μ is the electron Larmor frequency caused by the microwave, t is time, and S_x is the electron spin operator at x-direction because the microwave was applied from the y-axis and the magnetic field oscillating on the x-axis. The hyperfine coupling term can be expanded, without loss of generality, as

$$
H_{SI} = AS_zI_z + BS_zI_x, \qquad A = A_0(1 - 3\cos^2\theta_r), \qquad B = -\frac{3}{2}A_0 \sin 2\theta_r \tag{A.7.2}
$$

where θ_r is the polar angle of $\hat{r}$. The coefficients of terms related with S_x and S_y are zero, due to the electron polarization is only on the z-axis. The coefficients of the term related with I_y can be set to zero by rotating the coordinate system. The total Hamiltonian in the laboratory's frame is

$$
H = \Omega_S S_z + \Omega_I I_z + AS_zI_z + BS_zI_x + \Omega_\mu S_x\left(e^{i\omega t} + e^{-i\omega t}\right). \tag{A.7.3}
$$

In order to understand the effect of the microwave on the hyperfine term, we can change to the rotating frame created by the microwave. The rotating frame operator is

$$
U_R = e^{iS_z\omega t}, \tag{A.7.4}
$$

The rotating frame total Hamiltonian is

$$
H_R = U_R H U_R^{-1} - \omega S_z, \tag{A.7.5}
$$

After a change in rotation frame along with the oscillating frame, the high frequency terms are truncated. The total Hamiltonian becomes time independent

$$
H_R = (\Omega_S - \omega)S_z + \Omega_\mu S_x + \Omega_I I_z + AS_zI_z + BS_zI_x, \tag{A.7.6}
$$

The effective magnetic field direction is tilted on the x-z plane, the tilted operator is

$$
U_T = e^{i\theta S_y}, \qquad \tan\theta = \frac{\Omega_\mu}{\Omega_S + \omega}, \tag{A.7.7}
$$

Apply the tilted operator on S_z and S_x, we get

$$
\begin{aligned}
U_T S_z U_T^{-1} &= \cos\theta \, S_z - \sin\theta \, S_x, \\
U_T S_x U_T^{-1} &= \sin\theta \, S_z + \cos\theta \, S_x.
\end{aligned}
\tag{A.7.8}
$$

Then, we have the effective Larmor frequency on tilted rotating frame

$$(\Omega_S + \omega)S_z + \Omega_\mu S_x \to \Omega_{eff} S_z,$$
$$\Omega_{eff} = \sqrt{(\Omega_S + \omega)^2 + \Omega_\mu^2}. \tag{A.7.9}$$

The other terms in H_R transformed to

$$AS_zI_z + BS_zI_x \to A\cos\theta\, S_zI_z - A\sin\theta\, S_xI_z + B\cos\theta\, S_zI_x - B\sin\theta\, S_xI_x \tag{A.7.10}$$

Substitute

$$S_x = \frac{S_+ + S_-}{2}, \qquad I_x = \frac{I_+ + I_-}{2}. \tag{A.7.11}$$

And define

$$\begin{aligned} H_{SI}^T &= AS_zI_z + BS_zI_x \\ &= A\cos\theta\, S_zI_z - \frac{A}{2}\sin\theta\,(S_+ + S_-)I_z + \frac{B}{2}\cos\theta\, S_z(I_+ + I_-) \\ &- \frac{B}{4}\sin\theta\,(S_+I_- + S_-I_+) - \frac{B}{4}\sin\theta\,(S_+I_+ + S_-I_-) \end{aligned} \tag{A.7.12}$$

The rotated frame titled total Hamiltonian is

$$H_T = \Omega_{eff} S_z + \Omega_I I_z + H_{SI}^T. \tag{A.7.13}$$

The spin-flip operator $S_\pm I_\mp$ is contained titled rotated truncated hyper-fine Hamiltonian H_{IS}^T is the reason for spin transfer from the electron to the proton. In order to see the time evolution of the polarization, we have to go to interaction picture, by an operator [124]

$$U_H = e^{-i(\Omega_{eff}S_z + \Omega_I I_z)t} = e^{-i\Omega_{eff}S_z t} e^{-i\Omega_I I_z t}. \tag{A.7.14}$$

The time-dependence transform changes the Hamiltonian, so that

$$\frac{d}{dt}|\psi\rangle_H = -iV|\psi\rangle_H, \qquad V = U_H(H_{IS}^T)U_H^{-1}. \tag{A.7.15}$$

For spin-half particle

$$\begin{aligned} e^{-i\Omega_{eff}S_z t} &= \cos\left(\frac{\Omega_{eff}}{2}t\right)1 + 2i\sin\left(\frac{\Omega_{eff}}{2}t\right)S_z, \\ e^{-i\Omega_I I_z t} &= \cos\left(\frac{\Omega_I}{2}t\right)1 + 2i\sin\left(\frac{\Omega_I}{2}t\right)I_z, \end{aligned} \tag{A.7.16}$$

where 1 is identical matrix. And by the relation of angular momentum operator

$$[S_z, S_\pm] = \pm S_\pm, \qquad [I_z, I_\pm] = \pm I_\pm, \tag{A.7.17}$$

thus, we have

$$
\begin{aligned}
&U_H S_z I_z U_H^{-1} = S_z I_z, \\
&U_H S_z I_\pm U_H^{-1} = S_z I_\pm e^{\pm i\Omega_I t}, \\
&U_H S_\pm I_z U_H^{-1} = S_\pm I_z e^{\pm i\Omega_{eff} t}, \\
&U_H S_\pm I_\pm U_H^{-1} = S_\pm I_\pm e^{\pm i(\Omega_I + \Omega_{eff})t}, \\
&U_H S_\pm I_\mp U_H^{-1} = S_\pm I_\mp e^{\pm i(\Omega_{eff} - \Omega_I)t}.
\end{aligned}
\tag{A.7.18}
$$

We can see that each term is rotating in different frequencies in laboratory frame. In order to make $V = U_H(H_{IS}^T)U_H^{-1}$ be time independent, so that the density matrix ρ can be computed by

$$\rho(t) = e^{-iVt}\rho_0 e^{iVt}, \tag{A.7.19}$$

and the spin transfer term

$$-\frac{B}{4}\sin\theta\,(S_+I_- + S_-I_+), \tag{A.7.20}$$

survive and not truncated by high frequency, we can choose ω and Ω_μ, such that

$$\Omega_{eff} = \Omega_I \implies \sqrt{(\Omega_S + \omega)^2 + \Omega_\mu^2} = \Omega_I, \tag{A.7.21}$$

which is the Hartmann – Hahn condition. The terms $S_zI_\pm$, $S_\pm I_z$, and $S_\pm I_\pm$ truncated. And the final Hamiltonian is

$$V = A\cos\theta\, S_zI_z - \frac{B}{4}\sin\theta\,(S_+I_- + S_-I_+). \tag{A.7.22}$$

The polarization of the electron and the proton in the laboratory's rest frame are

$$P_e = \mathrm{Tr}(2S_z\rho), \qquad P_I = \mathrm{Tr}(2I_z\rho). \tag{A.7.23}$$

The operator ρ, S_z and I_z also have to be transformed as

$$
\begin{aligned}
S_z \to S_z \to{}& \cos\theta\, S_z - \sin\theta\, S_x \\
\to{}& \cos\theta\, S_z - \sin\theta\left(S_x\cos(\Omega_{eff}t) - S_y\sin(\Omega_{eff}t)\right) \\
\to{}& \cos\theta\, S_z,
\end{aligned}
\tag{A.7.24}
$$

$$I_z \to I_z \to I_z, \tag{A.7.25}$$

and for the special case, $\theta = \frac{\pi}{2}$, $S_z \to 0$. Thus, only the component of the electron polarization takes part in the spin transfer. The initial polarization $P_e = P_{e0}$ and $P_I = P_{I0}$ along z-axis, and no polarization along transverse axis, The transformation of density matrix in the basis $|m_s, m_I\rangle$, takes the form

$$\rho = \frac{1}{4}1 + \frac{P_{e0}}{2}S_z + \frac{P_{I0}}{2}I_z + P_{e0}P_{I0}S_zI_z. \tag{A.7.26}$$

Thus, after the transforms

$$\rho \to \frac{1}{4}1 + \frac{P_{e0}}{2}\cos\theta\, S_z + \frac{P_{I0}}{2}I_z + P_{e0}P_{I0}\cos\theta\, S_zI_z. \tag{A.7.27}$$

And the polarization are

$$
\begin{aligned}
P_e &= 2Tr(S_z\rho) \\
&= 2Tr\left(\cos\theta\, S_z \right. \\
&\left. \cdot\, e^{-iVt}\left(\frac{1}{4}1 + \frac{P_{e0}}{2}\cos\theta\, S_z + \frac{P_{I0}}{2} I_z + P_{e0}P_{I0}\cos\theta\, S_z I_z\right) e^{iVt}\right) \\
P_I &= 2Tr(S_z\rho) \\
&= 2Tr\left(I_z \right. \\
&\left. \cdot\, e^{-iVt}\left(\frac{1}{4}1 + \frac{P_{e0}}{2}\cos\theta\, S_z + \frac{P_{I0}}{2} I_z + P_{e0}P_{I0}\cos\theta\, S_z I_z\right) e^{iVt}\right)
\end{aligned}
\tag{A.7.28}
$$

Simplify, we get

$$
\begin{aligned}
P_e &= P_{e0}\cos^2\theta\cos^2\left(\frac{B}{4}\sin\theta\, t\right) + P_{I0}\cos\theta\sin^2\left(\frac{B}{4}\sin\theta\, t\right) \\
P_I &= P_{e0}\cos\theta\sin^2\left(\frac{B}{4}\sin\theta\, t\right) + P_{I0}\cos^2\left(\frac{B}{4}\sin\theta\, t\right)
\end{aligned}
\tag{A.7.29}
$$

The larger the θ, the smaller the usable electron polarization, however, the smaller the θ, the longer time for polarization transfer. And from the equation, the proton polarization is bound by

$$P_I(\max) = P_{e0}\cos\theta. \tag{A.7.30}$$

The solid effect for other experimental [125] is calculated in Figure A-12. The actually vale of A_0, θ_r and Ω_μ is unknown. The value was adjusted to reproduce the fact that the magnitude of the proton polarization was maximum for t~16 μs. Note that the truncation of equation (A.7.18) is not applicable for Ω_{eff} and Ω_I are small. This happens when the external magnetic field is weak and $\Omega_I = 42.58\ \mathrm{MHzT^{-1}}$ is small, which is the condition for this experiment. Because of the existence of the other terms in equation (A.7.18), the proton polarization reduced through other spin-flip channels.

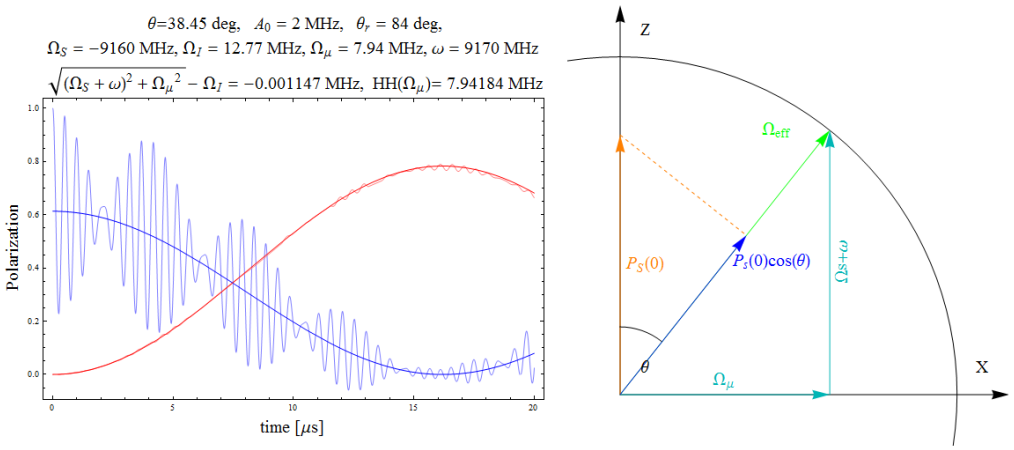

Figure A-12 – The solid effect with the experimental conditions in ref [125].
The blue and red curves are truncated electron and proton polarization respectively. The light blue and red curves are exact polarizations of the electron and the proton from equation respectively (A.7.3).

Appendix B
Theory on Proton Polarization

In this appendix, we are going to explain the principle and theory of the polarization method. A brief explanation is follow: The electron is excited from the ground state S_0 to higher energy states by laser irradiation. When the electrons relax from the higher energy states, part of them undergo inter-system-crossing to the first triplet state T_1 [126] [127]. Under a static magnetic field, the triplet state Zeeman levels are separated and created an effective electron polarization between any 2 states of the triplet state. The effective electron polarization can be transferred to the protons via the hyperfine interaction using a transverse microwave under the Hartmann-Hahn condition [128] [129]. The spin-polarization further diffuse to others protons via the dipole-dipole interaction [129].

B.1 Brief History on Spin-Polarized Proton Target

The development of the spin-polarized proton target for nuclear experiments has a long history. Early development was based on the thermal polarization (also called bull-force method) using Boltzmann distribution [108]. The target was operated under low temperature (few K) and high magnetic field (few T). Although the polarization can be as high as 70%, the high magnetic field deflects the path of charged particles. This makes the measurement and data analysis becomes difficult or even impossible.

On 1953, Overhauser proposed a method to polarize metal nuclei by transferring the polarization from spin-polarized conduction electrons [130]. The Overhauser's effect is based on the hyperfine interaction between the electron spin and the nuclear spin. In order for the polarization transfer, the electron and the nucleus gyromagnetic ratio should be similar. Later, Abragam and Goldman [129] extended Overhauser's idea to crystalline substance and called it as "solid effect". On 1962, Hartmann and Hahn developed a method that makes the gyromagnetic ratio of the nucleus and that of the electron be the same in a tilted rotating frame created by a microwave [128]. Because the polarization transfer is conducted in the rotating frame, it is also known as the dynamic nuclear polarization (DNP) (Appendix A.8). On 1985, Van Kesteren, Wenckebach, and Schmidt successfully produced "High, long-lasting, dynamic proton polarization" using the photo-excited triplet states of electrons in a pentacene doped crystal [131]. Since then, many people are working on to get a higher polarization using pentacene doped molecules [107] [132] [133] [134].

Throughout all the efforts mentioned above, the spin-polarized proton target, developed in Center of Nuclear Study, University of Tokyo, is a unique device that was designed for nuclear scattering experiments at high temperature (100K) and low magnetic field (0.064 T). We will explain the principle in this chapter and the operation of the target in the next chapter.

B.2 Materials

Pentacene is non-magnetic at the ground singlet state but paramagnetic in the excited triplet state [127] [132] [135]. The electron populations of the sub-state among the excited triplet state are different and that creates an effective polarization between any two sub-states. Therefore, it serves as a good polarization material as the nucleus-electron polarization/relaxation channel is closed at the ground state but opened at the excited states. However, a pure pentacene is a very sensitive to oxidation upon absorption of UV or visible light. Therefore, naphthalene ($C_{10}H_8$) doped with 0.05 mol% pentacene ($C_{22}H_{14}$) crystal was used [136]. The schematic chemical structures of pentacene and naphthalene are shown in Figure B-1. The properties of these chemicals are listed in Table B-1.

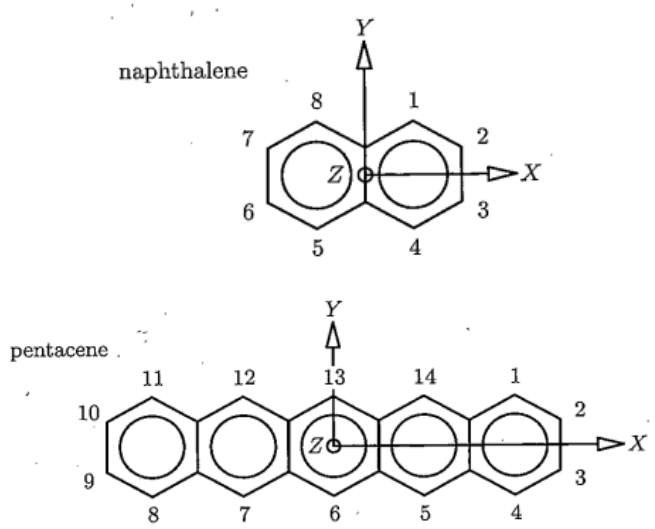

Figure B-1 – Diagrams of a naphthalene and a pentacene molecules [127].
The number indicated the hydrogen atoms and the arrows defined the molecular axis. The circle represents the π-bond.

Table B-1 – Physical Properties of Naphthalene and Pentacene in bulk.

	Naphthalene	Pentacene
Molar Mass [g mol^{-1}]	128.17	278.36
Density [g/cm^3]	1.14	1.3
Proton Density [mol/cm^3]	0.07116	0.05029
Carbon Density [mol/cm^3]	0.08895	0.07903
Melting point [K]	353	662
Sublimation point [K]	always	645
Crystal Structure	Monoclinic	Triclinic

B.3 Excitation of Pentacene to the Triplet State and Triplet State Polarization

The schematic energy levels of the pentacene in the naphthalene are shown in Figure B-2. The ground state is a singlet state (odd symmetry), which has no magnetic property because all electrons are coupled and total angular momentum is zero. The excited states from the ground state are all singlet state due to the conservation of symmetry. However, the fine-interaction (similar to the spin-orbital coupling) between the pentacene π-electrons can populate the triplet states (even symmetry). The transition from the singlet state to the triplet states is called inter-system crossing. Theory predicted that the transition rate is independent of temperature and external magnetic field. The triplet state is paramagnetic that the populations of each level are different [134]. This creates an effective polarization between any 2 levels. The paramagnetic property provided a channel to polarize the nucleus using the hyperfine-interaction between the π-electrons and the protons [127] [137] [138] [139].

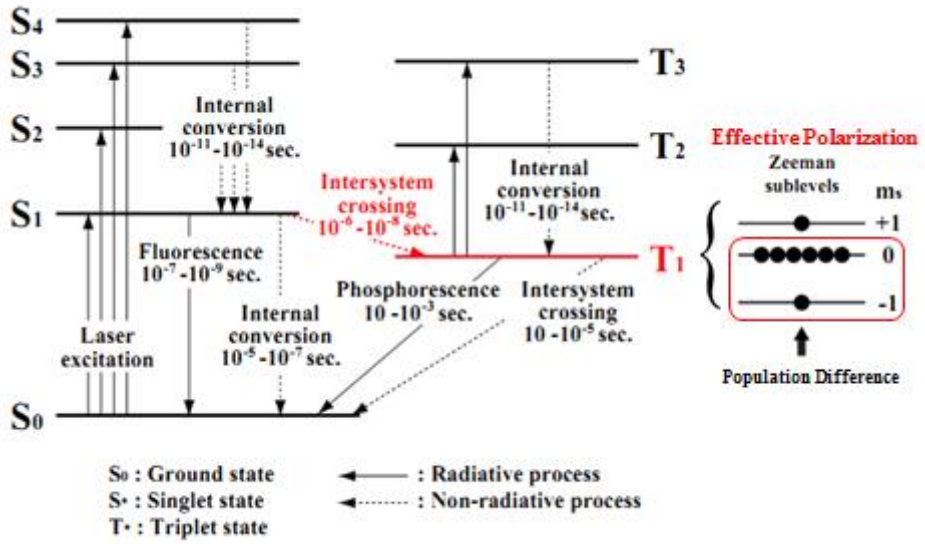

Figure B-2 – Pentacene energy levels scheme. Copy from Reference [140].

The electron triplet population can be described by a simple rate equation among the 5 states S_0, S_1, T_1^1, T_1^0 and T_1^{-1}. The rate equations can be written in a single matrix equation

$$\frac{d\vec{N}}{dt} = R \cdot \vec{N}, \tag{B.3.1}$$

where $\vec{N} = (N_{S_1}, N_1, N_0, N_{-1}, N_{S_0})$ is the population vector of the first excited singlet state, the 3 triplet states and the ground state. The rate matrix R takes the form

$$R = \begin{pmatrix} -A - W - (g_1 + g_0 + g_{-1}) & 0 & 0 & 0 & W \\ g_1 & -k_1 - \kappa_{10} & \kappa_{10} & 0 & 0 \\ g_0 & \kappa_{10} & -k_0 - \kappa_{10} - \kappa_{0(-1)} & \kappa_{0(-1)} & 0 \\ g_{-1} & 0 & \kappa_{0(-1)} & -k_{-1} - \kappa_{0(-1)} & 0 \\ A + W & k_1 & k_0 & k_{-1} & -W \end{pmatrix},$$

(B.3.2)

where A is the fluorescein rate, which is 23.5 ns or 43×10^6 s^{-1} for pentacene in p-terphenyl host [141] (we assumed the rate is not different significantly.), W is the induced rate by the laser. The coefficient g_i are the transition rates from S_1 state to T_1^i triplet states. The coefficient k_i are the rates from T_1^i to S_0, or the dark decay rate. The coefficient κ_{ij} is the phonon mixing rate between triplet states T_1^i and T_1^j. Since the rate matrix is time independent, the solution is

$$\vec{N}(t) = Exp(R\ t) \cdot \vec{N}(0). \tag{B.3.3}$$

B.4 Continuous Wave Solid Effect

The dynamic nuclear polarization involves 1 electron spin and many nuclear spin is called solid effect [129]. It required a microwave irradiation with frequency close to the electron spin resonance (ESR) frequency. If the ESR has to be induced by laser irradiation (the ESR frequency only resonances between triplet states, and the triplet states are excited by laser irradiation.), the solid effect also called microwave-induced optical nuclear polarization (MI-ONP).

The continuous wave solid effect is the basic principle of transferring the electron spin polarization to the nuclear spin. The detailed calculation can be found in Appendix A.8. The condition for polarization transfer is

$$\left(\Omega_S - \omega_\mu\right)^2 + \Omega_\mu^2 = \Omega_I^2, \tag{B.4.1}$$

which is called the Hartmann-Hahn condition [128]. The Ω_S is the ESR frequency of the electrons in the triple state, which depends on the external magnetic field. $\Omega_I = \gamma_I H$ is the Larmor frequency of the proton, γ_I is the proton gyromagnetic ratio, H is the strength of the external magnetic field. ω_μ is the microwave frequency, and Ω_μ is the Larmor frequency of the electrons, which is induced by the microwave wave magnetic component H_μ. The Hartmann-Hahn condition can be interpreted as the effective Larmor frequency $\left(\Omega_{eff}^2 = \left(\Omega_S - \omega_\mu\right)^2 + \Omega_\mu^2\right)$ of the electrons in the rotating frame is equal to the Larmor frequency of the nucleus in the laboratory's frame. (In fact, both Larmor frequencies should be in the rotating frame, but the Larmor frequency of the electron is much higher than that of the nucleus, then the effective Larmor frequency of nucleus in rotating frame is same as in the laboratory's frame. That is the reason for the name "microwave induced double nuclear resonance".) When this condition is fulfilled, the electron polarization can be transferred to the protons and polarize it. However, the usable electron polarization depends on the factor (Figure B-3)

$$\cos\theta = \frac{\Omega_S - \omega_\mu}{\sqrt{\left(\Omega_S - \omega_\mu\right)^2 + \Omega_\mu^2}} = \frac{\Omega_S - \omega_\mu}{\Omega_I}. \tag{B.4.2}$$

It is because the electron polarization is precessing around the effective magnetic field (Ω_{eff}). Therefore, if $\Omega_S = \omega_\mu$, there will be no polarization transfer even the condition is matched.

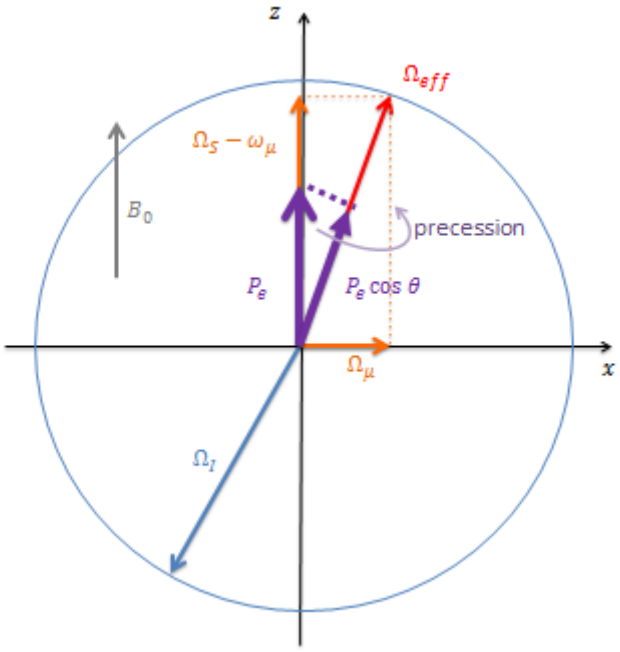

Figure B-3 – Pictorial presentation of the Hartmann-Hahn condition in rotating frame. See the main text for detailed explanation.

In Figure B-3, the circle radius is Ω_I, the z-axis is the direction of the laboratory's magnetic field and the x-axis is the rotating magnetic field direction viewed in the rotating frame. In the rotating frame, which is in phase with the microwave magnetic component, the electron polarization is rotating around the effective magnetic field direction with frequency Ω_{eff}. The electron interacts with the nucleus by hyperfine coupling, when the electron Larmor frequency (in rotating frame) is as same as the nuclear Larmor frequency, the polarization can be transferred back and forth by the operator

$$S_+ I_- + S_- I_+, \tag{B.4.3}$$

where S is the spin operator for electron and I is spin operator for the proton.

The ESR frequency of pentacene depends on the external magnetic field [127] [134]. The Hamiltonian for the electron triplet state is

$$H = R \cdot H_{ZFS} \cdot R^{-1} + \gamma_e B \frac{S_z}{\hbar}, \tag{B.4.4}$$

where γ_e is the gyromagnetic ratio of electron. B is the external magnetic field strength. R is the rotating operator that rotates the crystal frame to the Laboratory's frame. H_{ZFS} is the Zero Field Splitting Hamiltonian of the triplet state. It takes the form [127]

$$H_{ZFS} = D\left(S_z^2 - \frac{2}{3}\right) + E\left(S_x^2 - S_y^2\right) = \begin{pmatrix} \frac{D}{3} & 0 & E \\ 0 & -\frac{2D}{3} & 0 \\ E & 0 & \frac{D}{3} \end{pmatrix}, \tag{B.4.5}$$

where $D = 1381.5$ MHz and $E = -42.5$ MHz are the Zero Field Splitting parameters. The S_x, S_y, and S_z are spin 1 operator. If the crystal long axis (the X-axis in Figure B-1) is parallel with the external magnetic field, by using a suitable rotation operator

$$R = \frac{1}{2}\begin{pmatrix} 1 & -\sqrt{2} & 1 \\ \sqrt{2} & 0 & -\sqrt{2} \\ 1 & \sqrt{2} & 1 \end{pmatrix}, \tag{B.4.6}$$

and solving the eigenvalues. The Zeeman levels of the triplet state in the laboratory's frame are

$$\begin{aligned} \omega_+ &= -\frac{D - 3E}{6} + \frac{1}{2}\sqrt{(D+E)^2 + 4\,\gamma_e^2 H^2}, \\ \omega_0 &= \frac{D}{3} - E, \\ \omega_- &= -\frac{D - 3E}{6} - \frac{1}{2}\sqrt{(D+E)^2 + 4\,\gamma_e^2 H^2}. \end{aligned} \tag{B.4.7}$$

If we focus on the transition of $|m = 0\rangle$ state and $|m = -1\rangle$ state, the Ω_S is the difference between

$$\Omega_s = (\omega_0 - \omega_-). \tag{B.4.8}$$

The dependence of the Zeeman levels on magnetic field is plotted in Figure B-4.

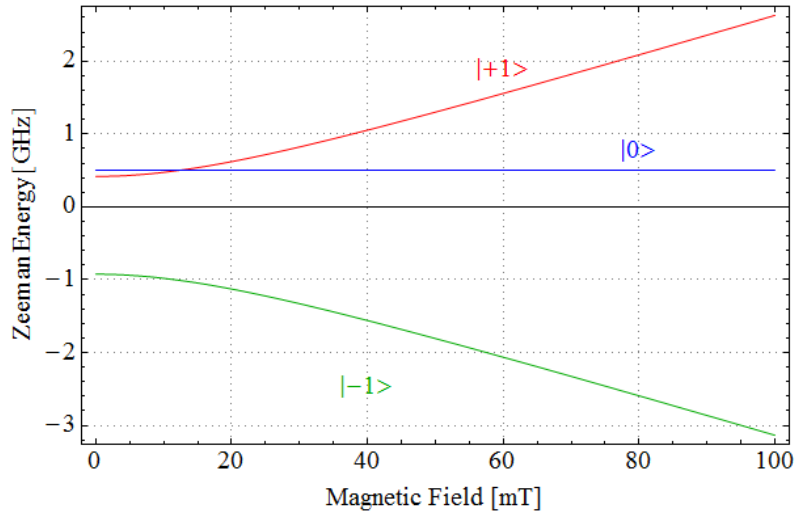

Figure B-4 – Zeeman Energy under the external magnetic field that parallel to the pentacene X-axis.

B.5 Adiabatic Field Sweep and Integrated Solid Effect

In order to coup with the magnetic field fluctuation due to the crystal internal magnetic environment and including more electrons take part in the polarization transfer, an adiabatic field sweep is applied. Together with a field sweep and solid effect, it is called integrated solid effect.

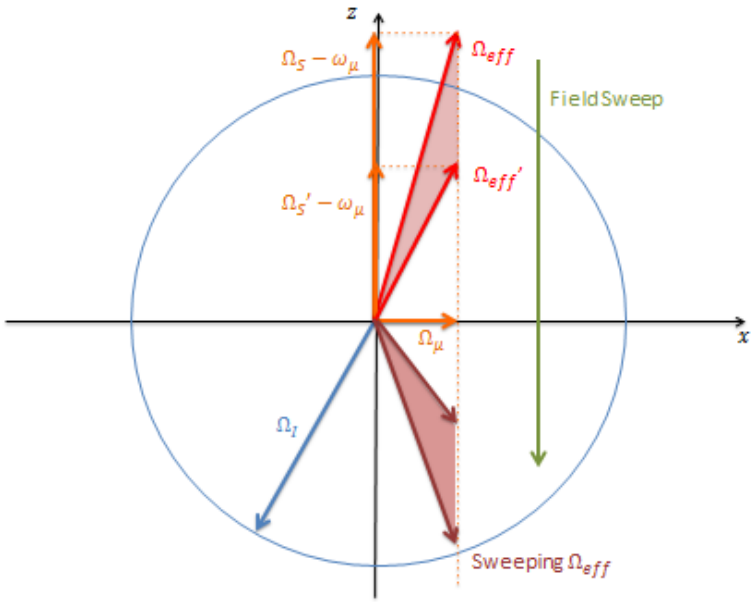

Figure B-5 – Field fluctuation and field sweep.
Notices that the Ω_I circle also splitted, but due to the small gyromagnetic ration, the splitting is very small and can be neglected.

The effect of magnetic field fluctuation is demonstrated in Figure B-5. The electron Larmor frequency depends on the total magnetic field. The total magnetic field is the sum of the external field and crystal field. The crystal field is created from the neighborhood electrons. The contribution of the crystal field is different for different electrons and created a distribution. This distribution is a shadow region between 2 effective Larmor frequencies in Figure B-5, which are created by highest and lowest total magnetic field. The gyromagnetic ratio of electron is about 600 times larger than that of the proton. Therefore, the electron is more sensitive to the field fluctuation and the proton Larmor frequency distribution can be neglected. The crystal field is ±3 mT, corresponding to ± 80 MHz at 64.4 mT, which is much larger than the proton Larmor frequency (2.74 MHz) at that external field. The adiabatic field sweep means that the change of the direction of the effective magnetic field is smaller than the Larmor frequency of electron

$$\left|\sqrt{\left((\omega_0 - \omega_-)H(t) - \omega_\mu\right)^2 + \Omega_\mu^2}\right| \gg \left|\frac{d\theta}{dt}\right|. \tag{B.5.1}$$

The variation magnetic field and the magnetic field are

$$\begin{aligned} &\Delta H(t) \ll H_0, \\ &H(t) = H_0 + \Delta H(t) \sim H_0. \end{aligned} \tag{B.5.2}$$

After calculations and approximation

$$\Omega_I^3 \gg \gamma_e \Omega_\mu \left| \frac{dH(t)}{dt} \right|, \tag{B.5.3}$$

when this condition is satisfied, the effective magnetic field $(\gamma_e H_{eff} = \Omega_{eff})$ will rotate slowly and the electron polarization will process around it and follow this direction. That makes more electrons under different effective magnetic field able to satisfy the Hartmann-Hahn condition and take part in the polarization transfer.

To see the essential of the adiabatic field sweep, we can imagine the opposite case that it is not adiabatic, say, we apply a positive and negative additional field. When positive additional field applied, the usable polarization is $P_e \cos\theta$, where P_e is the electron polarization in the z-axis. However, when the negative additional field applied, the usable polarization is $P_e \cos(\pi - \theta) = -P_e \cos\theta$, which transfer a "negative polarization" that reduce and even cancel the nuclear polarization. By using an adiabatic sweeping field, the electron polarization follows the effective magnetic field as the field rotates. Thus the usable polarization is always positive.

B.6 Polarization Diffusion

A spin-polarized proton in a pentacene molecule can react with other nuclear spin through the dipole-dipole interaction. It is similar to the hyperfine interaction. The Hamiltonian takes the form

$$H_{II} \propto \sum \vec{I^i} \cdot T^{ij} \cdot \vec{I^j}. \tag{B.6.1}$$

The T^{ij} is the dipole-dipole coupling tensor, which is inversely proportional to the distance. Since the distance between the protons in the pentacene is about several Angstroms. Therefore, the transition probability is much lesser then the polarization transfer.

Appendix C

Solid Spin-Polarized Proton Target

We explained the principle of the proton spin polarization in the previous appendix. A magnetic field, a laser, a microwave, and a sweeping magnetic field are required to polarize protons. A known-axes naphthalene crystal ($C_{10}H_8$) with radius of 7 mm was placed in the center of the magnet pole. The crystal was cool to -165ºC. A photo diode was used to detect the pulsed laser beam and sent a trigger signal to a wave-function generator. This trigger signal turns on a microwave and a sweeping magnetic field. The magnitude of the polarization was monitored by a NMR system. Figure C-1 is a photograph of the target system during the preparation of the experiment. A conceptual diagram of the target system is shown in Figure C-2. The structure of the pulses in one beam pulse is shown in Figure C-3. The parameters for the target system is shown in Table C-1.

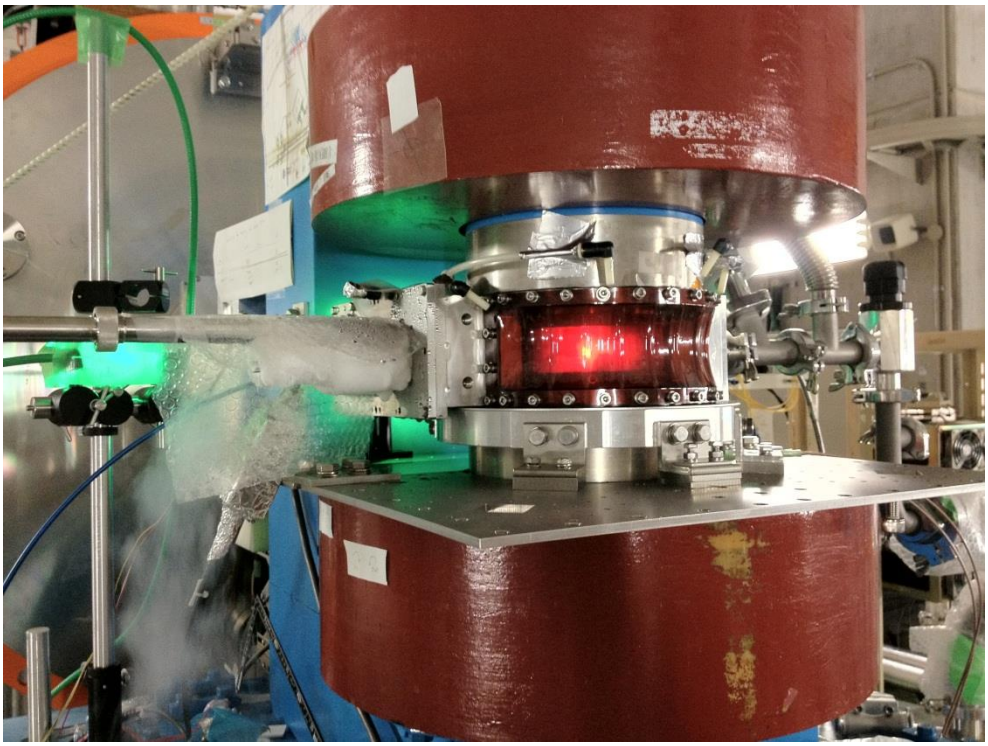

Figure C-1 – Photo of the target chamber and the magnet under operation.
The radioactive beam was coming from behind. The 2 red coils provide statics magnetic field. The chamber is placed in between. The electronic system of polarization is placed under the magnet (out of the photo). It was operated at -165ºC. The magnet coils are painted in dim red. The "red light" inside the chamber is the scattered light by the target crystal. The fog on the left side was due to the emission of cold nitrogen gas. The green light at the back side of the chamber was the ambience light from Argon laser beams.

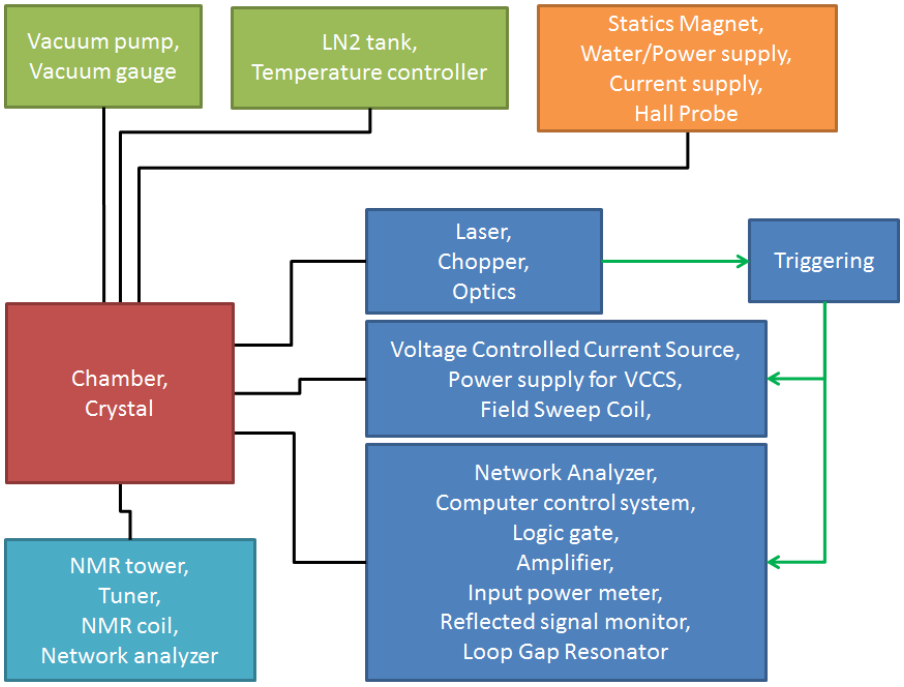

Figure C-2 – Conceptual overview of the target system.
The arrows represent the flow of controlling signal. The lines represent connections. The boxes with different colors represent different sub-systems.

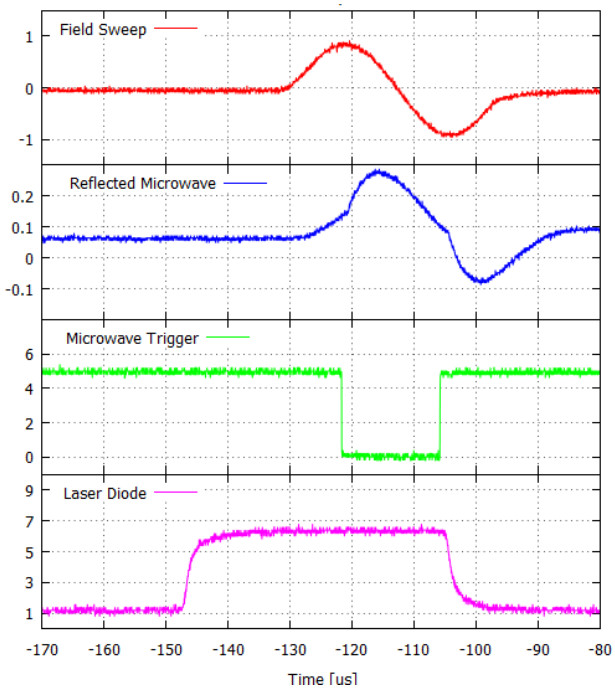

Figure C-3 – Pulses configuration for polarization during the experiment.

Table C-1 – Configuration of the polarization system.

Chamber Temperature	-160 ~ -170 °C	Laser 1 output power	10.8 ~ 11.0 W
Magnetic Field	64.2~65.8 mT	Laser 2 output power	12.1 ~ 12.3 W
Field sweep frequency	30 kHz	Repetition frequency	7kHz
Field sweep magnitude	2.4 mT	Repetition period	142.86 us
Field sweep Delay	16.1 us	Pulse width	41.6 ~ 50.2 us
Field sweep Phase	0° / 180°	Microwave frequency	2.677 ~ 2.709 GHz
Field sweep supply voltage	±40V	Microwave output power	3.4 W
Field sweep supply current	0.6A	Microwave Delay	10.5 us

C.1 Crystal and Crystal Preparation

A single crystal of naphthalene doped 0.05 mol% pentacene is a commercial product. It was cut into a 14 mm diameter and 1 mm thick sample for the experiment. The crystal has 3 molecular axes which named a, b and c. The geometry of the crystal was listed in Table C-2, and displayed in Figure C-4.

Table C-2 – Crystal properties of naphthalene

Number of molecules in a unit cell		2
	Cleavage plane	a-b plane
Lattice period	a	8.2 Å
	b	6.0 Å
	c	8.7 Å
Plane angle	α : a-b	90˚
	β : a-c	123˚
	γ : b-c	90˚

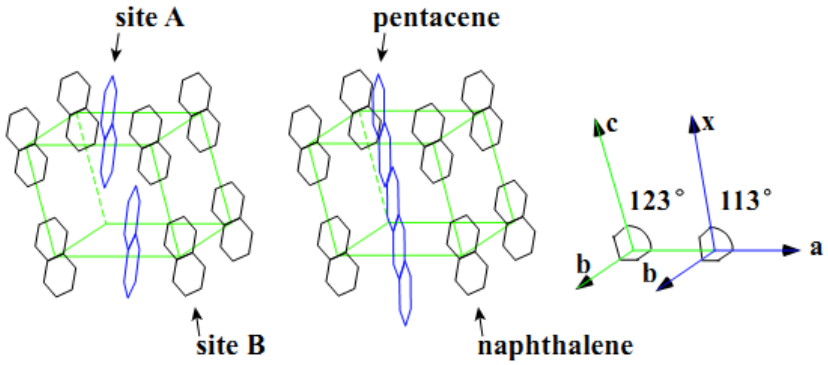

Figure C-4 – Crystal structure of the naphthalene and pentacene doping.
The pentacene replaced 2 naphthalene molecules. The picture is taken from Reference [140].

The a-b plane is the only cleavage plane. This property and the birefringence give us an easy method to identify the crystal axis. The crystal was cut little on the edge. Since the cleavage plane is easy to separate, it leaves parallel planes or lines on the cut surface. By removing a small portion of the crystal along the cleavage plane, the a-c plane can be identified by birefringence. The process is demonstrated in Figure C-5.

a. A roughly cut crystal. The surface is a-c plane.

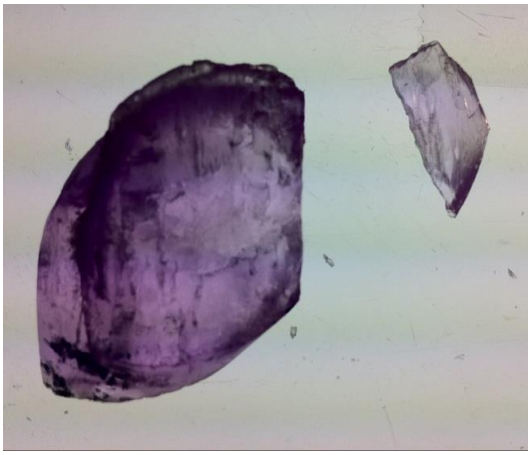

b. Cut a small piece along the a-b plane.

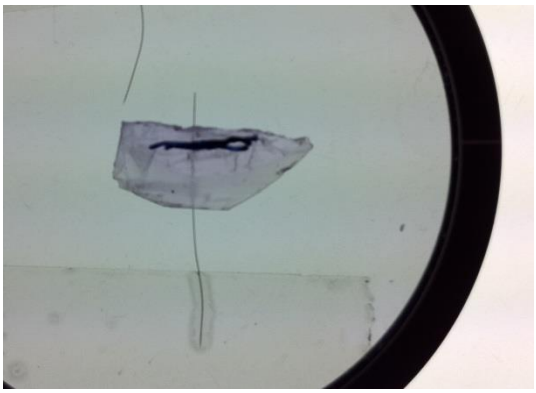

c. Under a polarizer on vertical direction, the hair under the crystal does not shift.

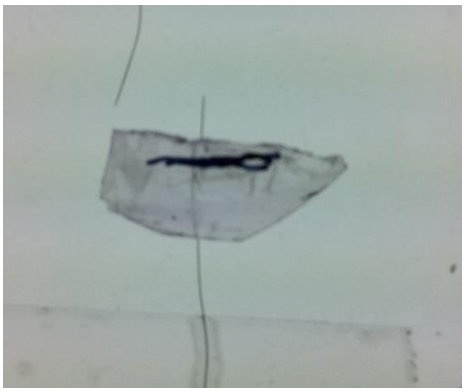

d. Under a polarizer on horizontal direction, the hair under the crystal was shift. The shift direction indicates the c-axis.

Figure C-5 – Demonstration of finding the crystal axis.

The axes-identified crystal was polished from several mm thick to 1mm. In order to make the crystal surface be clear and transparent, we used 4000 grits sand paper at finial polishing.

C.2 Static Magnet and Small Magnetic Field

The magnet produced a uniform 64.2mT ~ 65.8 mT statics magnetic field across 50 mm diameter from the center. Figure C-6 shows the magnetic field variation during beam time. We changed the magnetic field after the field sweep coil has been fixed on May 31st. The ESR frequency is linear at around 64mT (Figure B-4). It is related with the magnetic field by

$$\Omega_S = \frac{D}{2} - \frac{3}{2}E + \sqrt{\left(\frac{D+E}{2}\right)^2 + \gamma_e^2 B^2} \approx \frac{D}{2} - \frac{3}{2}E + \gamma_e B, \qquad \text{(C.2.1)}$$

Therefore, the change of the ESR frequency for 1 mT is 28 MHz. This does not affect the polarization as the NMR signal is almost the same (Figure C-24).

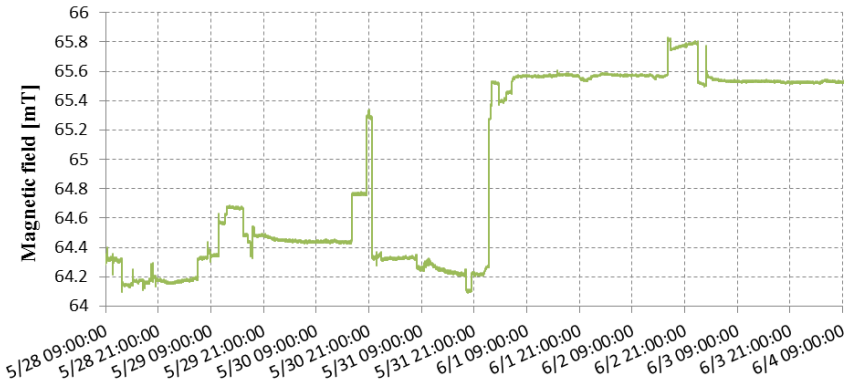

Figure C-6 – Magnetic field during experiment.

By using the NMR signal of a water sample (5 mm × 5 mm × 15 mm), we can determine the homogeneity of the magnetic field on the crystal. The FID (free induction decay) signal and the frequency spectrum of the water sample are shown in Figure C-7. The detail of the convertion can be found in Appendix A.7. The central peak of the frequency spectrum is caused by a vertical offset of the signal. The FWHM of the water peak is about 1 kHz. By knowing that the proton gyromagnetic ration is 42.577 MHz/T and the Larmor frequency of the proton is 2.75 MHz at 64.4 mT, the homogenous of the magnetic field around the water sample is less than 1 part in 2750, about 0.04%.

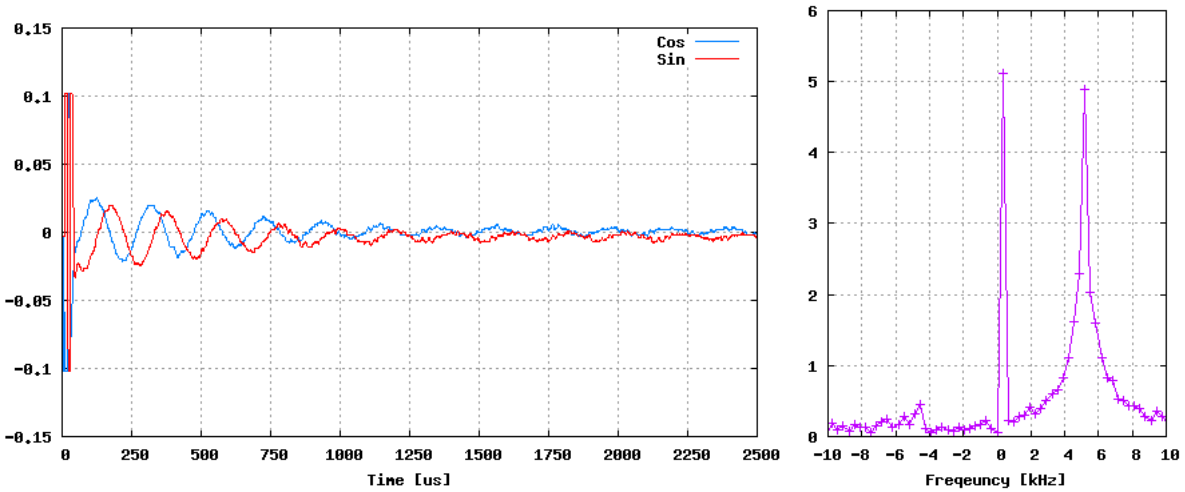

Figure C-7 – FID signal and freqeuncy spectrum of water sample.
The peak near 0 kHz is due to an vertical offset of the FID signal.

The magnetic field is measured using water nuclear magnetic resonance (NMR) and constantly monitored by a Hall probe (F. W. Bell, Hall generator model BH200). The sensitivity of 9.58 mV/kG

was provided from the factory. The working temperature is from -40°C to +100°C, the temperature dependence from 20°C to +80°C is 0.08%/ °C. The Hall probe connected to a mulitmeter (Keithley 2000 multimeter). Since the position of the Hall probe is not at the center of the magnet field, it was placed below the vacuum chamber, and then the magnetic field strength was different from the crystal position. This was calibrated using a water sample, which placed at the target position. The result is shown in Figure C-8. The sensitivity is 10.247 mV/kG, with error 0.06%. A larger sensitivity is expected, since the field strength should be larger at the Hall probe for a Helmholtz type coil.

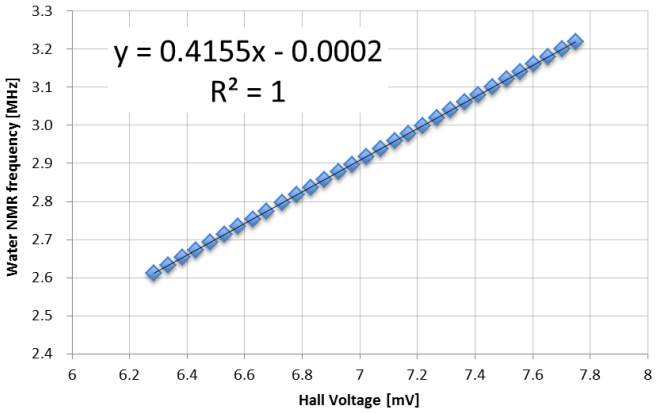

Figure C-8 – Measured Hall probe voltage against the water NMR frequency.

A small magnetic field is desired because the deflection of the scattered proton should be minimized. The diameter of the magnet core is 110mm, separated by 100mm. If we assumed a uniform magnetic field B covering an area of radius r, the Lorentz force of a proton with velocity $\beta = \frac{v}{c}$ is

$$\left|\vec{F}\right| = \left|q\ \vec{v} \times \vec{B}\right| = qc\beta B, \tag{C.2.2}$$

The deflection is defined as the angle between exiting angle and original angle. It is

$$\theta = 2\sin^{-1}\left(\frac{rqB}{2mv}\right) \sim \frac{rqB}{mc\beta}, \qquad for\ B \ll \frac{mc\beta}{rq}, \tag{C.2.3}$$

If the magnetic field is large and comparable to the value $\frac{mc\beta}{rq}$, the charge particle will be trapped inside the magnetic field. For our experiment condition, the scattered proton has β~0.2 to 0.6, r~0.1 m and $B = 70$ mT, the deflection is $\theta \leq 10$ mrad or 0.6 degree. For a slow proton ($\beta = 0.2$) the deflection on 1 m away is about 10 mm, which is half-cell of the MWDC-L and R.

C.3 Crystal axis and Magnetic Field Direction

The crystal X-axis (Figure B-1) should be parallel to the external field. If the crystal axis makes some angle with the field, the Zeeman states will not be a pure state but mixed.

C.4 Scattering Chamber

The scattering chamber need to fulfill 4 purposes: 1) provides a vacuum for beam transportation, 2) cools the crystal to 100K by liquid nitrogen, 3) allows scattered particles detection, and 4) contains target crystal and polarization components. Thus, the scattering chamber contains two chambers. A cooling chamber is inside a vacuum chamber. The vacuum chamber provides a thermal insulation. In order to let scattered particles passed through while maintaining the pressure. Kapton films of 128μm were used in both chambers.

The internal structure of the scattering chamber is drawn in Figure C-9. The crystal target is in transparent pink. The two green lines represent the light paths of the lasers beams. The yellow films are Kapton films of 128 μm each. The copper rings on the top and bottom of the crystal are the magnetic field sweep coil. The target holder was made of hydrogen-free plastic. Because of the complex structure of the target system, a large among of background events was expected.

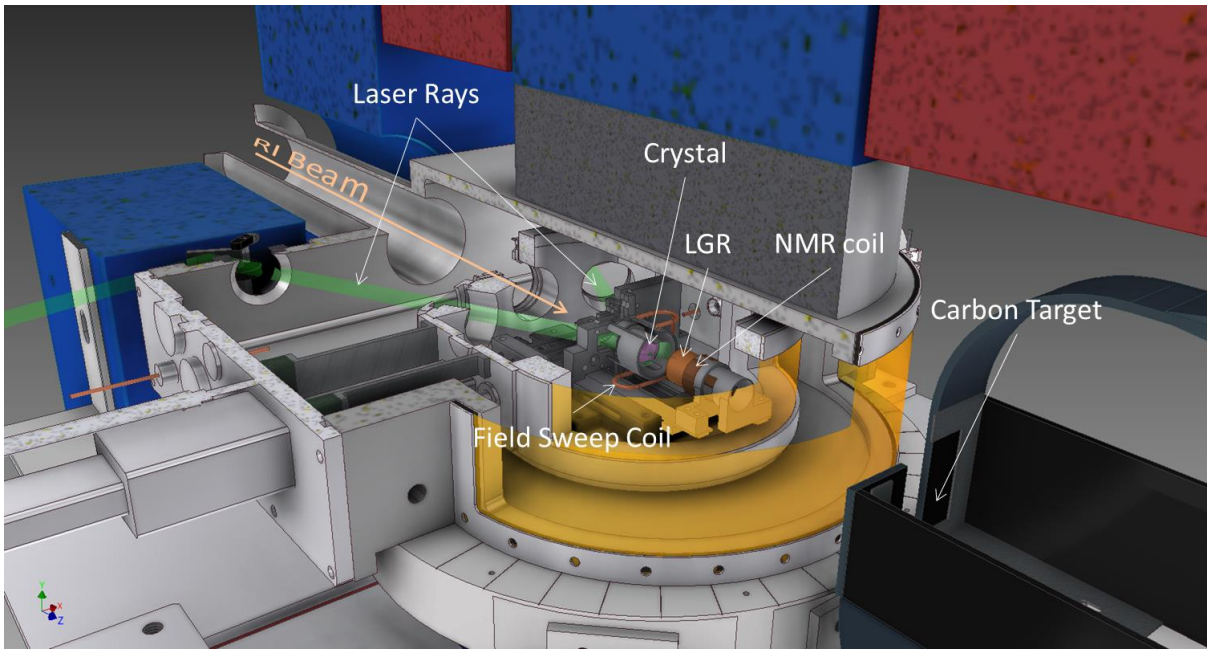

Figure C-9 – CAD drawing for the target system.
The vacuum chamber, cooling chamber, interior structure, crystal position and Laser beam path are shown. Electric cables are not included in this drawing.

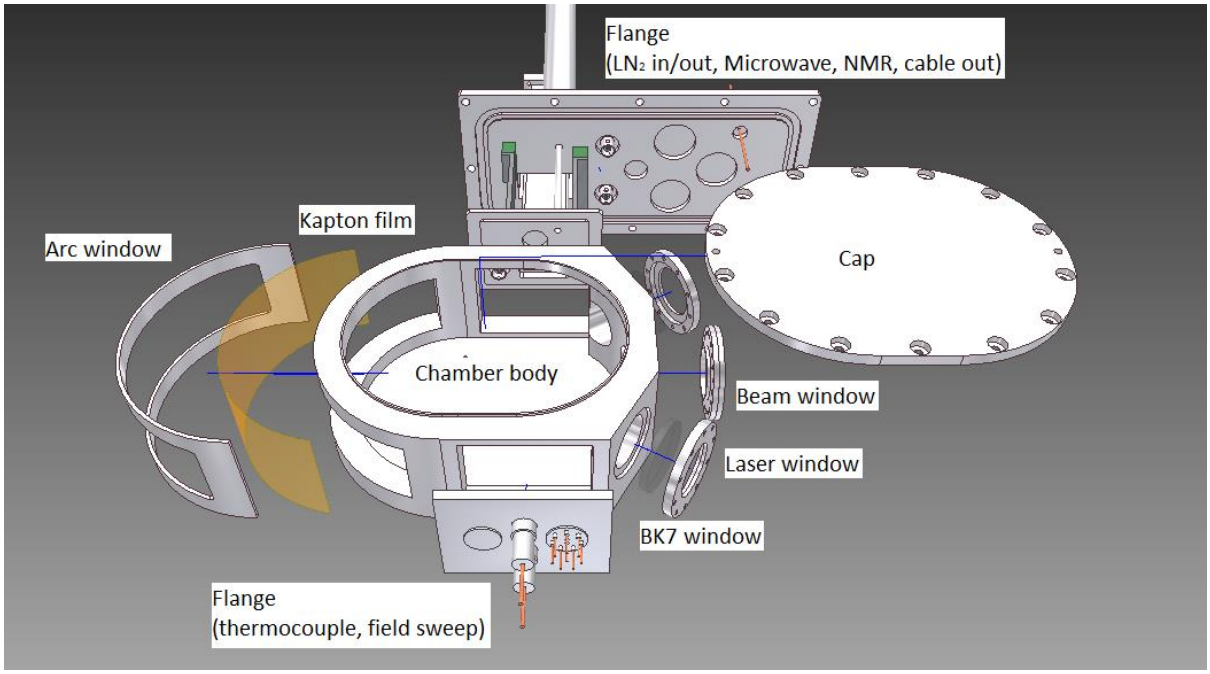

Figure C-10 – Assembly of the cooling chamber.

C.4.1 Vacuum

The vacuum provides two functions: 1) Connection with the beam pipe, and 2) thermal insulation. The pressure inside the vacuum chamber should be less then 10^{-2} mbar (1 mbar = 0.75 Torr = 100 Pa = 9.89×10^{-4} atm), which is medium to high vacuum [142], for getting temperature as low as -165 ^{o}C. A rotary vacuum pump from Alcatel model 2010SD was used for pumping. The pumping speed is 9.7 m^3/h, corresponding to 2.69 L/s. According to the factory, the ultimate total pressure at open gas ballast is 10^{-2} mbar. A molecular pump (Edwards PT640Z010 STP-iX455 Turbomolecular pump) was also used. Its pumping speed of N_2 and H_2 are 300 L/s. The principle ultimate pressure is 6.5×10^{-9} mbar. The pump starts to operate when chamber pressure is smaller than 0.1 mbar. The vacuum chamber is connected with an upstream MWDC for beam tracking. A schematic diagram for the vacuum system is shown Figure C-11. The final vacuum is 7×10^{-2} mbar.

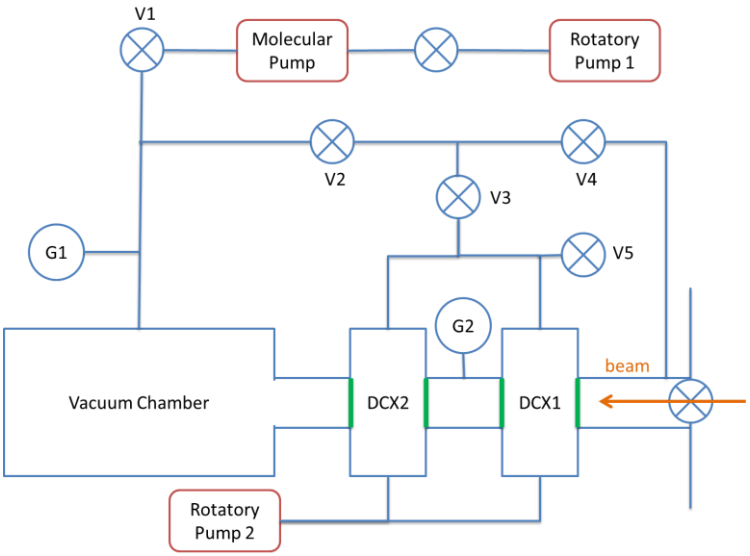

Figure C-11 – Schematic view of the vacuum system.
The green lines are Mylar foils.

The vacuum chamber is connected with an upstream drift chamber DCX2 for beam tracking on the target. The front end of the vacuum chamber is a 180° arc window. The area of the arc window is approximately 34000 mm^2 and perimeter is about 900 mm. Another leakage is from the cooling chamber. The cooling chamber is inside the vacuum chamber (Figure C-9). The cooling chamber has a lot of components, the arc windows, two laser widows, one beam window, and two flanges for cabling and inlet of nitrogen gas, that create possible leakage (Figure C-10). Since the cooling chamber was placed inside. It is difficult to find out the leakage. We had tested the cooling chamber by submerging it into bucket of ethanol and pumping nitrogen gas at around 1.5 atm. Some leakages were fixed.

The vacuum is 6×10^{-3} mbar with the vacuum chamber alone. The vacuum is 6.5×10^{-2} mbar after we installed the cooling chamber. The final vacuum at -165°C is 7×10^{-2} mbar.

C.4.2 LN_2 Cooling

The temperature was monitored and controlled by a temperature control unit (OMRON E5CN Basic-type Digital Temperature Controller). The temperature sensor was a Pt-100 resistance type thermometer, which was placed inside the chamber, just above the crystal holder. The temperature was control by the feed-back temperature and a heater coil inside a LN2 tank. The temperature variation during the beam time is shown in Figure C-12. The temperature went to room temperature from May 31st, 9 am, because we had to open the chamber and fix the field sweep coil. In most of the time, the temperature was ranging from -155°C to -170°C, around -165 ± 5°C.

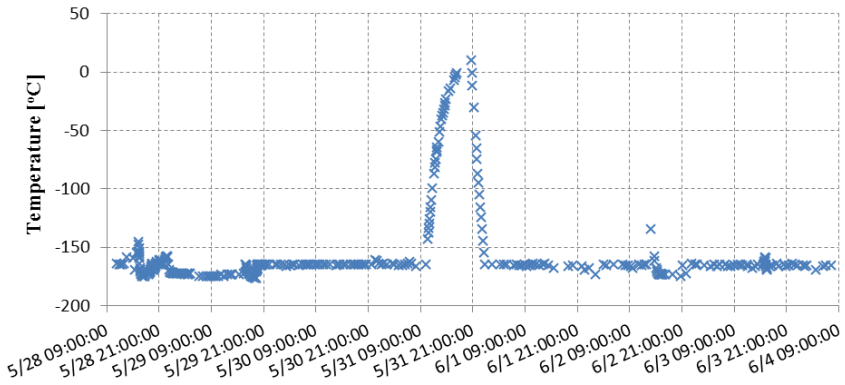

Figure C-12 – Temperature during experiment.

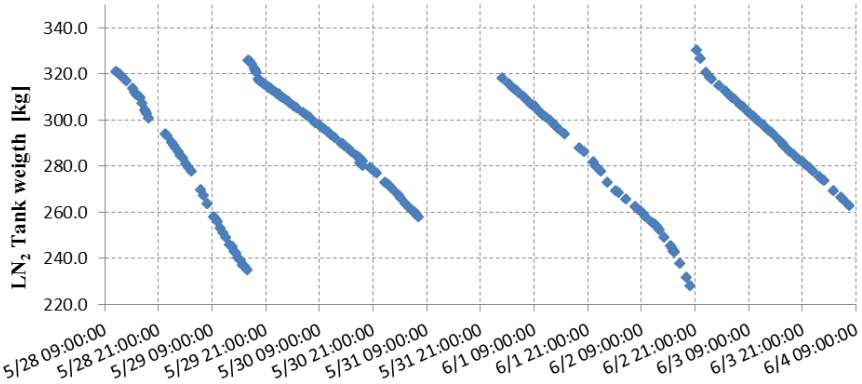

Figure C-13 – LN_2 consumption during experiment.

C.5 Optical System

The laser rays diagram is illustrated in Figure C-14. One of the rays turned left and the other turned right after the lasers. The rays focused by a f = 100 mm lenses. Both rays passed through a chopper to produce a laser pulse. The chopper was placed at the focal point at where the width of the beam was the narrowest. The laser pulse then passes through a f = 100 mm lenses to enlarge the beam back to its original width. It then entered an optical couplers and be transported by optical fibers. The lengths of the optical fibers are 100 meter each. A photograph of the chopper system is shown in Figure C-15.

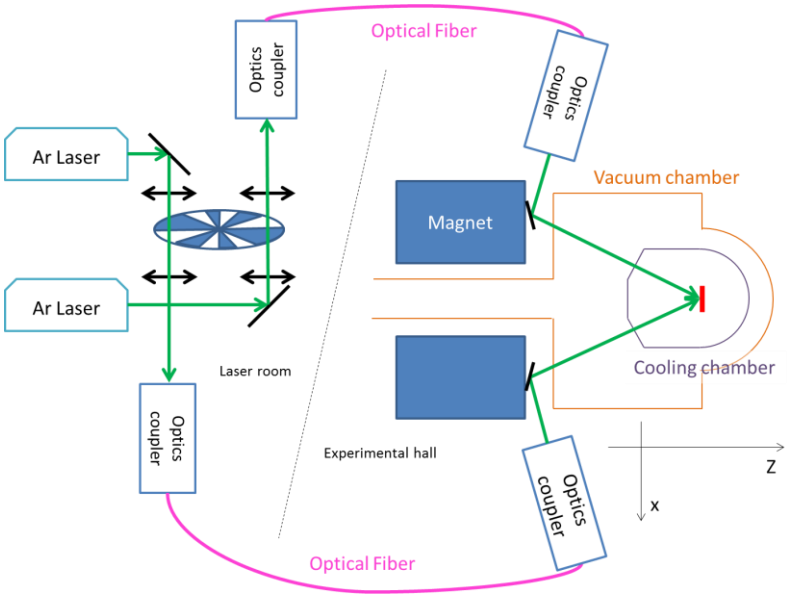

Figure C-14 – Schematic view of the laser system.
The Lasers and the target system were placed at different rooms.

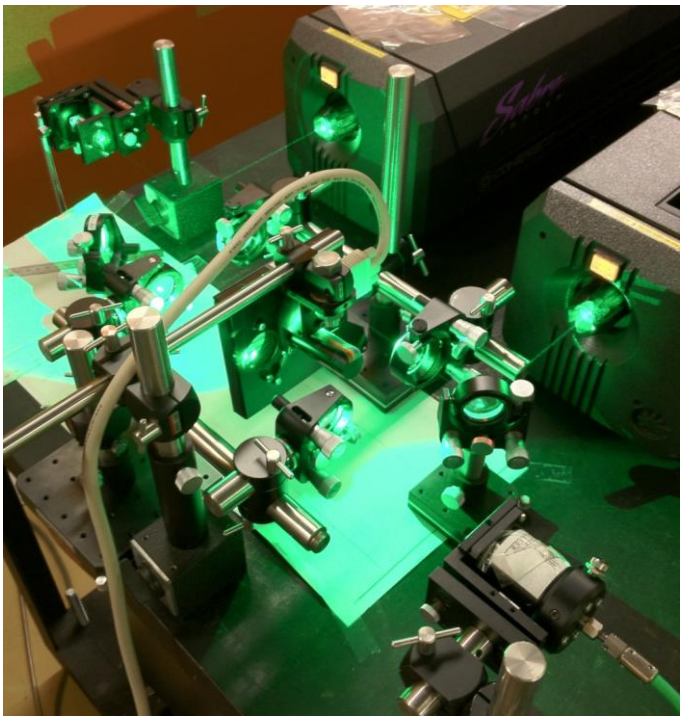

Figure C-15 – Photograph of the laser and the chopper system.
The 2 laser beams were reflected and pass through a chopper, and then entered optical couplers.

The optical fibers deliver the laser from the laser's room to the target, which installed along the beam line. We check that the beam profile after the fibers that the beam did not distorted and kept at TEM_{00} mode. The fiber's end was connected to another optical coupler. The beam divergence can be adjusted by the optical coupler and focused on the crystal. The laser spot on the target crystal is shown in Figure C-16.

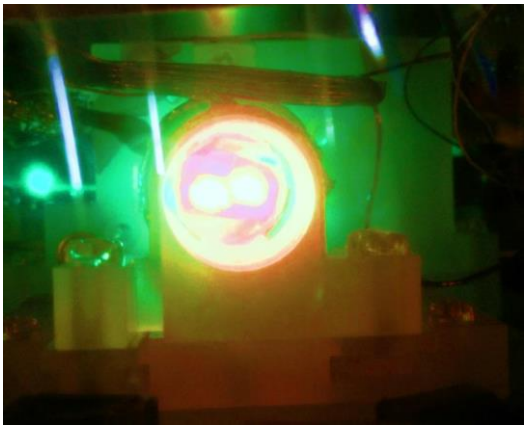

Figure C-16 – Laser spot on the target crystal on May 26th, before beam time.
This photo viewed from the forward angle, outside the chambers. The green spot on the left is the scattered laser light by the inner (cooling) chamber windows. The laser spot was enlarged and fine-tuned to cover as large area as possible.

The chopper was formed by two chopper disks of 40 slits and 50% duty each. The duty is the ratio between beam-on and pulse period. The frequency of the chopper was monitored and controlled by a chopper control unit from Scitec Instruments Ltd, Optical Chopper model 310CD. By overlapping the two chopper disks, we can adjust the duty. Let's the frequency be f, the pulse width of the chopped laser ray is t_p, the duty is α

$$f\alpha = t_p. \tag{C.5.1}$$

Two Argon Lasers, model Innova Sabre DBW25 from Coherent, Inc. were used at single-wavelength mode at 514.5 nm. These are a continuous wave (CW) laser, but we added an optical chopper to create laser pulse. According to the factory manual, at this wavelength, the beam divergence (full angle) is 0.35 mrad, beam waist at $1/e^2$ point is 2.1 mm, and the polarization is 100:1 vertical. The maximum power output at 514.5 nm is 10 W.

Two optical fibers are 100 m long each. One was model ST400E from Mitsubishi. Co., with diameter 400 μm, numerical aperture (NA)=0.2, transmission lost was 5 dB/km and maximum power was 2000 W for CW laser. Another one was 100 μm diameter with NA=0.2. We lost the manufacturer information for this fiber.

An optical coupler was used to feed the laser output into the fiber. A lens was used with matching the fiber diameter and NA. The formulas are

$$\frac{d}{2} > \frac{\theta}{2} f, \qquad NA > \frac{D}{2f}, \tag{C.5.2}$$

Combined them and get

$$\frac{d}{\theta} > f > \frac{D}{2\,NA}, \tag{C.5.3}$$

where d is fiber diameter, NA is the numerical aperture of the fiber, f is the focal length of the lens, θ is the full divergence of Laser and D is the diameter of Laser. Put the factory data of Laser and fiber, we have

$$\begin{aligned} 1143 > f > 5.25 \text{ mm}, \quad & \text{for } d = 400 \text{ µn} \\ 256 > f > 5.25 \text{ mm}, \quad & \text{for } d = 100 \text{ µn} \end{aligned} \tag{C.5.4}$$

We used a 65 mm lens for the 400 µm fiber and a 16.59 mm 10X objective for the 100 µm fiber as input optical coupler.

After passed through the fibers, we need another optical coupler to collimate the beam. The waist of the beam we needed is smaller than 8 mm and distance between the lenses to target crystal is around 600 mm. The calculation for this similar as above

$$\frac{w}{2} > NA\, f', \qquad \phi = \frac{d}{2f'} \tag{C.5.5}$$

where w is the beam waist, ϕ is the beam half divergence and f' is the focal length. Since we want to focus the beam at long optical path, the divergence has to be small. We used a 35mm lens for 400 µm fiber and a 16.59 mm 10X objective for the 100 µm fiber.

All mirrors and lenses are from Sigma Koki, Inc. Mirrors are designed to work at 500nm. Lenses have multi-layer anti-reflection coating and working at 549nm.

C.6 Microwave

The microwave was generated by a network analyzer (Rohde & Schwarz Vector Network Analyzer 1127.8500.60 ZVM). The whole circuit diagram is shown in Figure C-17. The output microwave was fed into a custom made computer control switch. The microwave then output to a circulator. The circulator passed the signal to a logic switch. This logic switch stopes the wave when there is no trigger signal. When the logic switch stops the signal, the signal is reflected back to the circulator. The circulator passed the reflection signal to a dummy load to protect the computer control switch and the Network Analyzer. After the logic switch, the microwave was amplified and went to a directional coupler. The directional coupler produced a coupling signal. The coupling signal was measured by a power meter. The microwave then went to another circulator. The circulator simply passed the microwave back to the computer control switch and then went to chamber. The circular acted as a circuit protector and provided a way to measure the reflected microwave. The reflected microwave was monitored by an oscilloscope (CRO). It is because the pulse shape is important for adjusting the position of the Loop-Gap-Resonator (LGR).

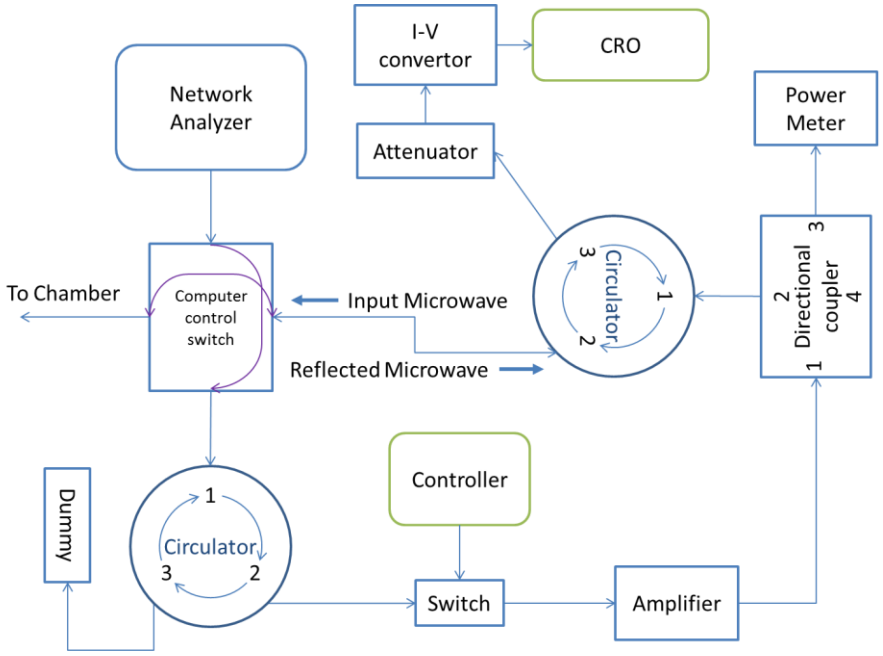

Figure C-17 – Circuit diagram of the microwave system

Inside the chamber, the microwave emits from an antenna coil. A LGR is surrounded the crystal. The microwave frequency should be matched with the resonance frequency of LGR to get maximum power transfer to the crystal.

C.7 Field Sweep

The high current is generated by a voltage controlled current source (VCCS) made from an Op-Amp (see Figure C-18). The Op-Amp was APEX microtechnology model PA05. It has maximum output current of 30 A, maximum input voltage difference of ± 20V, and maximum supply voltage of ± 100V. The output current is given by

$$I_{out} = -\frac{V_{in}}{R_s}\frac{R_f}{R_I}. \qquad \text{(C.7.1)}$$

The values of resistors R_I and R_f were the same in our setup. The value of resistor R_s was very small that we only use a copper wire as the resistor. The magnetic field was measured by a Hall probe from F. W. Bell model 5180 Gauss Meter.

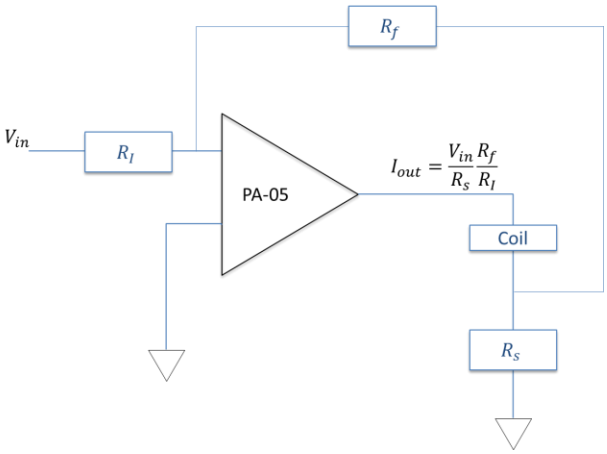

Figure C-18 – Effective circuit of the Voltage Controlled Current Source

The Helmholtz – like field sweep coil was custom made from a high current copper wire. The separation of the coil is fixed around 30mm by the chamber. The radius is limited to 15mm due to the crystal position. By a simple calculation $\left(B = \mu_0 nI \frac{r^2}{\left(r^2+\left(\frac{z}{2}\right)^2\right)^{\frac{3}{2}}} \right)$, the maximum magnetic field should be produced by coil of 20 mm radius, therefore, we have to use 15mm. We used a 7mm diameter copper wire with 12 turns on each coil (12 turns in upper coil, 12 turns in lower coil). The calculated magnetic field and field line is shown in Figure C-19. We can see the calculated field is almost uniform in the crystal area. We compressed it to be an elliptic coil to improve the uniformity. It is because the crystal was a thin disk with diameter of 14 mm and thickness of 1 mm. An elliptical coil can provide higher uniformity and field strength with same current. Due to the limited space of the interior, we compressed the coil into an elliptical shape with major axis 20mm and minor axis 10mm. A 8.4 A current is required to generate 2.4 mT.

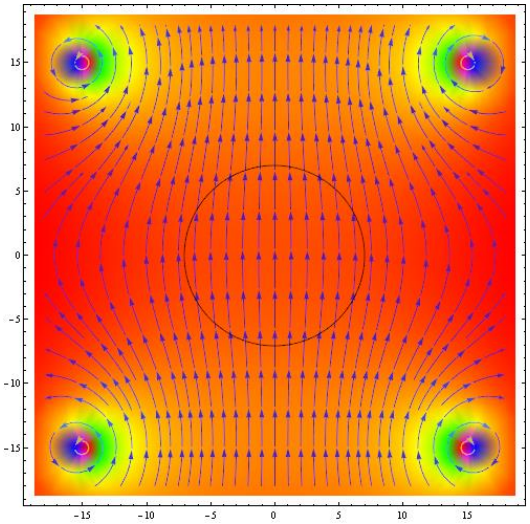

Figure C-19 – Calculated magnetic field line and strength of the field sweep coil (unit = 1mm). The Black circle is the size of crystal.

The field sweep was applied before the microwave by 9.9 us for it to rise. When the microwave was turned on, the field sweep is sweeping from maximum to minimum. The minimum is reached when the microwave is tuned off.

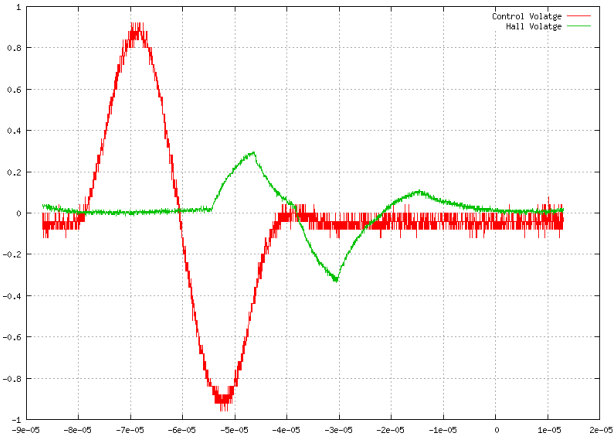

Figure C-20 – The magnetic field of field sweep coil.
The red line is the applied voltage. The green line is the measured magnetic field. The delay of the signals was caused by the cable length.

C.8 Polarization Measurement of NMR

The polarization was measured by two methods: Nuclear Magnetic Resonance (NMR) and proton-proton elastic scattering. These two methods then be compared and used to calibrate the NMR signal. The calibrated NMR signal can easily be used to monitor the polarization anytime. The measurement of the proton-proton elastic scattering will be discussed in Appendix D.

C.8.1 NMR

A spin undergoes precession along an external magnetic field. This is known as Larmor precession. When a traverse oscillating magnetic field applied at the Larmor precession frequency, the effective field is perpendicular to the spin direction in the rotating frame of the spin, and the precession is along this effective field. A well-controlled pulsed traverse oscillating field with definite time interval can rotate the spin by 90º in the laboratory's frame. After the pulse, the spin keeps precessing along the external magnetic field and undergoes Free Induction Decay (FID). The decay is caused by the tendency that the spin will eventually align with the magnetic field direction by interacting with other spins. The proton polarization can be measured by detecting the FID signal. This technique is called nuclear magnetic resonance (NMR). A brief calculation is on Appendix A.6. A detail explanation can be found on [143].

A PROT Series Wideband Fourier Transform NMR Spectrometer from Thamway Co., Ltd was used. It is an all-in-one NMR tower which provided all NMR components, from frequency generator, gate generator, mixer, preamplifier, amplifier, and computer. A typical NMR circuit is shown at Figure C-21.

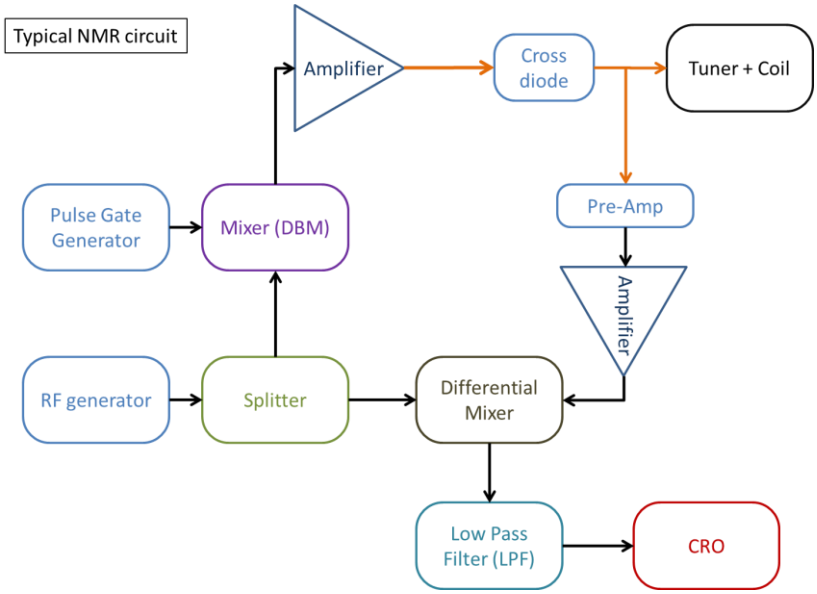

Figure C-21 – Typical NMR circuit and circuit elements.

We made a NMR coil and matching its impedance with a tuner. The NMR coil was 16 mm diameter with 33 turns, made by copper wire of 0.5 mm diameter. The tuner circuit is shown in Figure C-22. It contained two capacitors, one in parallel (shunt) and the other was in series. The parallel capacitor had 200 pF. The tuner and coil were connected by a cable with unknown capacitance and resistance. According to the transmission line theory, the total impedance of the coil, the cable between coil and tuner, and the tuner (Z_L) should be equal to the transmission line impedance (Z_0) , so that no reflection wave and power can fully transmitted into the coil. The reflectance is

$$\Gamma = \frac{Z_L - Z_0}{Z_L + Z_0}. \tag{C.8.1}$$

The input impedance (the impedance "sees" by the source) is related to a lossless transmission line by

$$Z_{in} = Z_0 \frac{1 + \Gamma\, e^{-2\kappa L}}{1 - \Gamma e^{-2\kappa L}} = Z_0 \frac{Z_L + iZ_0 \tan(\kappa L)}{Z_0 + iZ_L \tan(\kappa L)}, \tag{C.8.2}$$

where κ is the wave number of the transmission wave inside the cable, in which the refractive index or the speed of light is difference from free space. For the BNC cable we used, the velocity factor is 0.66. A BNC cable with length L should be fulfilled the condition

$$\kappa L = 2\pi n + \frac{\pi}{2}, \tag{C.8.3}$$

or the quarter wave-length matching. Under this matching, the input impedance is

$$Z_{in} = \frac{Z_0^2}{Z_L}. \qquad \text{(C.8.4)}$$

When the impedance matching $Z_0 = Z_L$ or $\Gamma = 0$, the source only "see" the transmission line impedance regardless the length. Usually, electric device is set and designed that the input impedance is 50 Ω. Although the impedance matching condition alone can give $Z_{in} = Z_0 = 50\,\Omega$, the prefect matching, i.e. $Z_0 = Z_L$, usually hard to achieve, especially the tuner is easily affected by environmental EM field.

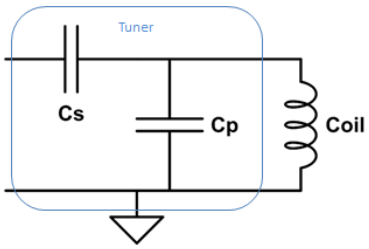

Figure C-22 – Tuner and coil circuits.

The impedance matching condition was achieved with a network analyzer (Advantest R3754B Network Analyzer). The network analyzer generated a sweeping frequency signal and measures the reflection lost and the device impedance. We adjust the capacitors (in the tuner) so that the impedance is 50 Ω at the working frequency (in our case is 2.832 MHz).

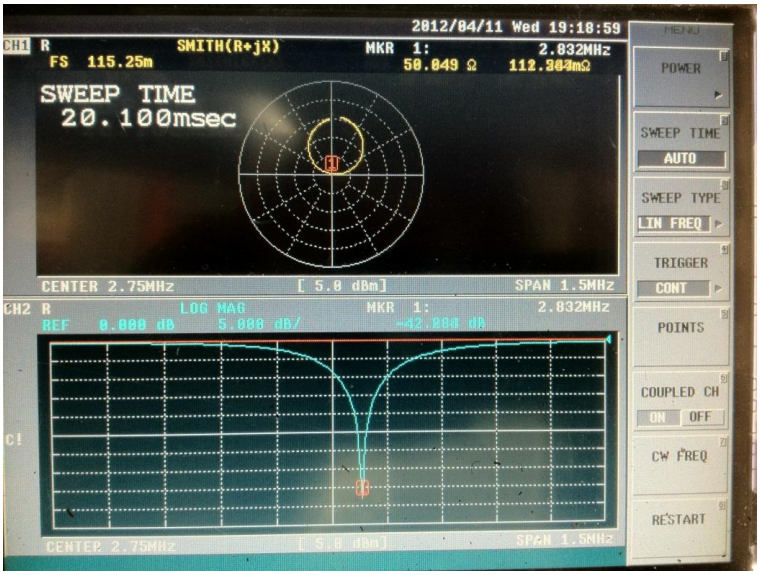

Figure C-23 – A screen captured from network analyzer.
The upper screen is the smith chat, and lower screen is the reflection loss.

After matched the impedance and found the NMR frequency, there are 3 parameters (The magnetic field, the NMR pulse width t_{NMR}, and power of the NMR pulse) have to be adjusted. The standard procedure is using high power pulse and short NMR pulse. It is because a high power pulse makes the rotation axis in rotating frame closer to the rotating x-axis. A 90° pulse (or $\pi/2$ pulse) satisfies the condition

$$t_{NMR}\Omega_{eff} = \frac{\pi}{2}, \tag{C.8.5}$$

where Ω_{eff} is the effective Larmor frequency of the proton spin. By changing the magnetic field, we can pick-up the water NMR signal. We can further calibrate the Hall probe by the water NMR signal (Figure C-8).

The power of the NMR pulse was adjusted by the "Level" of the NMR system. The actual power output is roughly proportional to the Level. We don't have a detail relationship. Therefore, we have to search different settings. The 90º pulse gives maximum FID signal. This is a very good starting point. After found the 90º pulse, we can also found that 180º pulse (polarization inversion) and a smaller pulse.

The 90º pulse can be confirmed by a second pulse after the transverse relaxation time. The transverse relaxation time (perpendicular to the static magnetic field) is short, about 100 μs. If it was a 90º pulse, all spins had rotated by 90º, precesses on the x-y plane. After the transverse relaxation time, the transverse polarization is gone but the longitudinal polarization does not build-up yet. The polarization is zero at that time. If a second 90º pulse is applied, the FID signal should be zero. The FID signal of 1st and 2nd pulse is changing with the Level. When the FID signal of the 2nd pulse meets zero again, this is the 90º pulse. The settings of the NMR system is shown in Table C-3.

Table C-3 – NMR settings.

NMR frequency	2.785 MHz
Pulse width	2 μs
Level for 180 degrees pulse	600
Level for 90 degrees pulse	550
Level for 4~5 degrees pulse	400
Gain	20 dB

C.8.2 FID signal

The FID signal displayed on the CRO was recorded and calculated to give the "FID area" by root-mean-square of the FID amplitude at all data points

$$\sqrt{\sum_{i}^{N}(s_i)^2 + (c_i)^2} = \text{FID area}. \tag{C.8.6}$$

The FID area is a numerical integration of the FID signal. This is directly proportional to the magnetization of the crystal. The induced electric field in the coil is, by integral form of Faraday equation

$$\mathcal{E}_2 = -\frac{\partial}{\partial t}\int \overrightarrow{B_1}\cdot\widehat{n_2}\, d^2x_2, \tag{C.8.7}$$

where the subscript 1 for the crystal, subscript 2 for the NMR coil. Included the geometry factor from the $\overrightarrow{B_1}$ field generated by the crystal and the finite length of the coil, with the help of Stoke's theorem, we have

$$\mathcal{E}_2 = -\frac{\mu_0}{4\pi}\frac{\partial}{\partial t}\oint\oint\frac{\vec{M}(\overrightarrow{r_1})\times\widehat{n_1}}{|\overrightarrow{r_2}-\overrightarrow{r_1}|}d^2x_1\cdot d\overrightarrow{l_2}, \tag{C.8.8}$$

Or in short form

$$\mathcal{E}_2 = -F\frac{d}{dt}\vec{M}, \tag{C.8.9}$$

where F is the filling factor between magnetized sample 1 and coil 2. It is related to the mutual inductance. The FID signal is proportional to the e.m.f. in the coil times the gain of the NMR system. Thus, the integration gives us the magnitude of the magnetization and the spin polarization.

C.8.3 Polarization Inversion

The traditional method to reverse the polarization is by destroying the polarization and start building-up in opposite direction. However, this method requires long time as the build-up rate is usually 7 to 15 hours. In order to quickly inverse the polarization, we apply a 180º NMR pulse to the system and changing the field sweep direction. Recalling the Figure B-5, if the field sweep direction reversed, although the effective electron polarization will not be reversed, the proton polarization is building up in opposite direction, which is the same direction with the 180 degree rotated proton magnetization.

The 180º pulse can be verified again by 2nd pulse. If the 1st pulse and 2nd pulse also give small signal, the corresponding Level is 180º pulse (see Figure C-24). However, the 180º pulse is not easy to achieve. It is because the proton Larmor frequency broadening. That makes different spins rotate at different frequencies. When the leading spin made 180º rotation, the trail spin is still far away from 180 degrees caused by the Larmor frequency differences. This broadening reduced the total magnetization and polarization. The best polarization inversion is about 60% (Figure C-24).

C.8.4 Results of NMR Measurement

During experiment, we measured the polarization by NMR every 2 hours. We applied a weak NMR pulse, corresponding to about 4º ~ 5º of rotation of the magnetization, to make minimum influence on polarization while able to detect NMR signal. The weak pulse was found by multiple pulses. The FID signal was measured for every 10 pulses, and total 100 pulses were measured. The corresponding 90º pulse signal was 12.75 times bigger. The FID signal during the experiment is shown in Figure C-24. Different beams were shadowed with different colors. The magnitude of polarization for FID area equal 150 is 30% (see Appendix D.5).

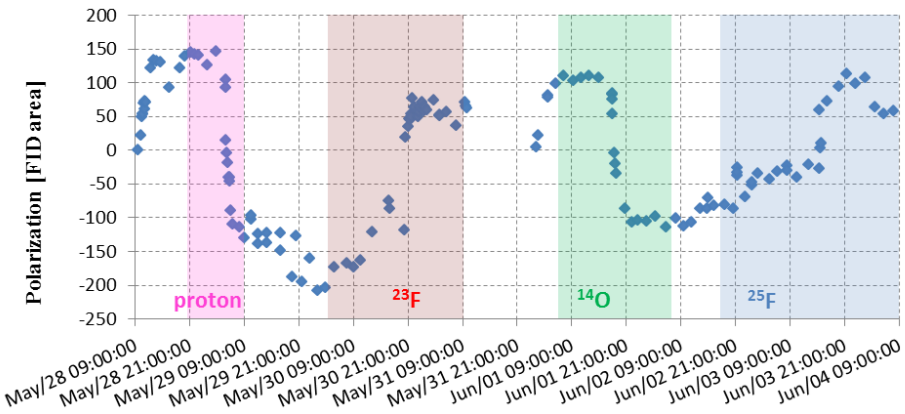

Figure C-24 – Polarization during experiment.
The proton runs were shaded with pink color, the ^{23}F runs were shaded with red color, the ^{14}O runs were shaded with green color, and the ^{25}F runs were shaded with blue color.

C.9 Analyzing Power

The analyzing power of each partition can be deduced from the left-right asymmetry of the differential cross section. The yield Y of the knockout reaction is

$$Y_{L/R}^{\uparrow/\downarrow}(\Delta\theta_{L/R}) = \alpha_{L/R} Y_0 \left(1 + s_{L/R}^{\uparrow/\downarrow} A_y P^{\uparrow/\downarrow}\right), \qquad s_{L/R}^{\uparrow/\downarrow} = \begin{cases} +1, & L^{\uparrow}, R^{\downarrow} \\ -1, & L^{\downarrow}, R^{\uparrow}, \end{cases} \tag{3.13.1}$$

where $Y(\Delta\theta)$ is the yield in the sector of scattering angle $\Delta\theta$, Y_0 is the average non-polarized yield, A_y is the average analyzing power in the sector, P is the average magnitude of the spin polarization of the proton target. The subscripts L, R represent left and right and the superscripts $\uparrow, \downarrow$ represent spin-up and spin-down of the target. $\alpha_{L/R}$ is the systematic asymmetry factor. Spin-up and spin-down runs were performed to cancel the systematic bias. The laboratory scattering angle was divided into 5 sectors from 20° to 70°. The systematic asymmetry was cancelled by using a combined yield

$$Y_L = \sqrt{Y_L^{\uparrow} Y_R^{\downarrow}}, \qquad Y_R = \sqrt{Y_R^{\uparrow} Y_L^{\downarrow}}, \tag{3.13.2}$$

and the asymmetry ϵ is

$$\epsilon = A_y P = \frac{Y_L - Y_R}{Y_L + Y_R}. \tag{3.13.3}$$

The statistical uncertainty of the asymmetry is

$$\delta\epsilon = \frac{2\sqrt{Y_L^2 \delta Y_R^2 + Y_R^2 \delta Y_L^2}}{(Y_L + Y_R)^2}. \tag{3.13.4}$$

The uncertainty of the analyzing power is

$$\delta A_y = A_y \sqrt{\left(\frac{\delta\epsilon}{\epsilon}\right)^2 + \left(\frac{\delta P}{P}\right)^2}. \tag{3.13.5}$$

The magnitude of the proton polarization was 0.30 ± 0.07, which was deduced from the proton runs (see Appendix D.5 for polarization measurement). The magnitudes of the polarization for the ^{23}F runs were more or less the same, while the magnitudes for the ^{25}F runs were reduced, according to the NMR measurement (Figure C-24).

Ideally, the analyzing power should be calculated in a narrow range of residue's momentum. i.e., the momentum distribution in Figure 3-20 should be sectored, and then deduced the analyzing power by left-right asymmetry of the differential cross section in each momentum sector. However, because of small statistics, we were unable to do so. The theoretical analyzing power was calculated by the DWIA method (Section 1.2.4). In order to have a consistent comparison, the theoretical cross section for the left or the right detector was plotted into a histogram, and the theoretical analyzing power was calculated using equation (3.13.2) to (3.13.5). Note that the theoretical analyzing powers had a similar trend, because the residues' momentum was integrated. These results agree with Figure 1-31 and the momentum distributions of Figure 3-20, Figure 3-21, and Figure 3-22. In Figure 1-31, the analyzing powers for all orbits (except the $2s_{1/2}$) have the same sign from 100 MeV to 200 MeV.

The results of analyzing power for each peak from the ^{23}F(p,2p) reaction are shown in Figure C-25, Figure C-26, and Figure C-27. The data point in angle sector 60° to 70° was omitted as there was no yield. The error of the yield $Y_L^{\uparrow}, Y_R^{\uparrow}, Y_L^{\downarrow}$, and $Y_R^{\downarrow}$ included the error of carbon background. When the yield is smaller than 3, the error of 1.15, 1.30, and 2.00 were used for yield of 0, 1, and 2 respectively because of Poisson distribution. Because of small statistics, the analyzing powers suffered large uncertainty. Therefore, it provides no help to distinguish the total angular momentum.

Table C-4 – Table of yield for ^{23}F(p,2p).

θ [deg]	$Y_L^{\uparrow}$	$Y_R^{\uparrow}$	$Y_L^{\downarrow}$	$Y_R^{\downarrow}$	Y_L	δY_L	Y_R	δY_R	A_y	δA_y	DWIA
(^{23}F,^{22}O) partition											
25	22	17	3	4	9.38	2.89	7.14	2.68	0.452	0.801	-0.33
35	28	26	10	8	14.97	3.74	16.12	3.87	-0.124	0.578	-0.16
45	20	22	10	11	14.83	3.97	14.83	3.74	0.000	0.613	0.24
55	23	27	3	3	8.31	2.80	9.00	3.11	-0.134	0.804	0.25
(^{23}F,^{21}O) partition											
25	38	53	15	12	21.35	4.24	28.20	4.66	-0.460	0.436	-0.34
35	90	75	24	19	41.35	6.10	42.43	5.94	-0.043	0.339	-0.14
45	76	86	19	22	40.89	5.79	40.42	5.72	0.019	0.334	0.04
55	49	39	10	15	27.11	4.40	19.75	4.15	0.524	0.449	0.53
(^{23}F,^{20}O) partition											
25	49	44	11	8	19.80	4.92	22.00	4.66	-0.176	0.545	-0.39
35	98	80	19	20	44.27	6.52	38.99	6.10	0.212	0.360	-0.05
45	82	106	14	16	36.22	5.79	38.52	6.24	-0.103	0.380	0.10
55	27	26	8	7	13.75	3.46	14.42	3.81	-0.080	0.608	0.46

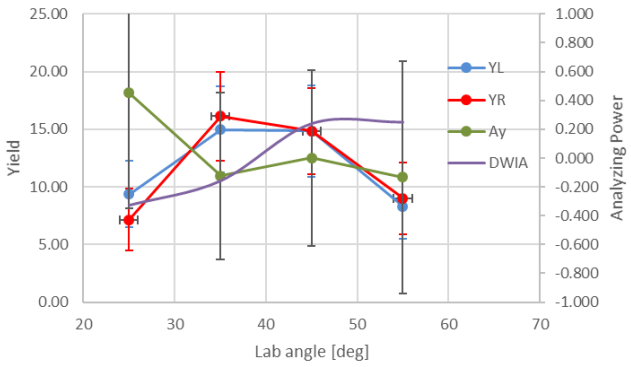

Figure C-25 – The combined yields of left and right detector, analyzing power, and theoretical analyzing power of $1d_{5/2}$ shell for (^{23}F,^{22}O) partition in Figure 3-17.

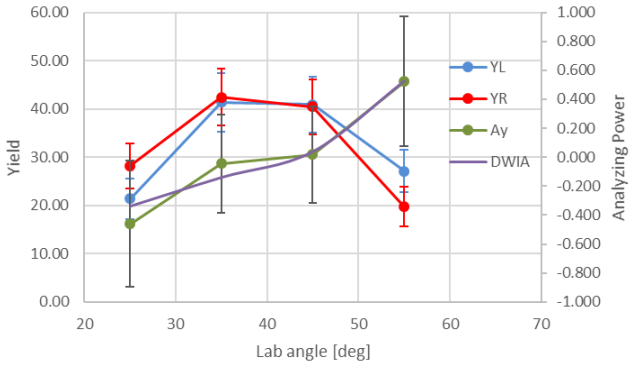

Figure C-26 – The combined yields of left and right detector, analyzing power, and theoretical analyzing power of $1p_{1/2}$ shell for (^{23}F,^{21}O) partition in Figure 3-17.

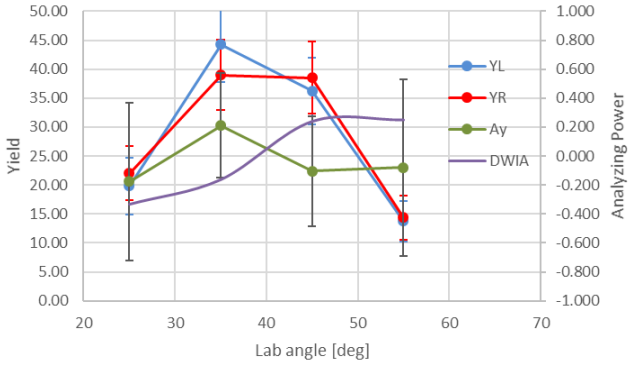

Figure C-27 – The combined yields of left and right detector, analyzing power, and theoretical analyzing power of $1p_{3/2}$ shell for (^{23}F,^{20}O) partition in Figure 3-17.

Table C-5 – Table of yield for ^{25}F(p,2p).

θ [deg]	$Y_L^{\uparrow}$	$Y_R^{\uparrow}$	$Y_L^{\downarrow}$	$Y_R^{\downarrow}$	Y_L	δY_L	Y_R	δY_R	A_y	δA_y	DWIA
(^{25}F,^{24}O) partition											
25	0	2	1	1	0.00	1.51	1.41	1.44	-3.333	7.141	-0.36
35	6	1	0	2	3.46	2.41	0.00	1.80	3.333	3.556	-0.01
45	5	7	4	2	3.16	1.98	5.29	1.94	-0.840	1.149	0.09
55	0	7	1	1	0.00	1.44	2.65	1.97	-3.333	3.720	0.39
(^{25}F,^{23}O) partition											
25	5	2	1	3	3.87	2.04	1.41	1.85	1.550	1.878	-0.4
35	10	10	14	15	12.25	2.63	11.83	2.86	0.057	0.539	0.02
45	12	16	13	12	12.00	2.86	14.42	2.87	-0.306	0.518	0.09
55	3	2	3	1	1.73	1.48	2.45	1.85	-0.572	1.846	0.47
(^{25}F,^{22}O) partition											
25	10	20	14	15	12.25	3.28	16.73	3.74	-0.516	0.580	-0.4
35	26	28	37	36	30.59	4.53	32.19	4.72	-0.085	0.347	0.02
45	28	27	26	26	26.98	4.58	26.50	4.33	0.030	0.393	0.09
55	15	5	13	14	14.49	3.20	8.06	2.74	0.950	0.659	0.47
(^{25}F,^{21}O) partition											
25	1	2	3	11	3.32	2.74	2.45	2.33	0.501	2.055	-0.4
35	17	8	9	13	14.87	3.39	8.49	3.20	0.911	0.712	0.02
45	5	14	13	4	4.47	3.04	13.49	3.43	-1.674	0.983	0.09
55	1	0	5	2	1.41	1.76	0.00	1.90	3.333	8.972	0.47

Some absolute values of A_y are larger than 1. This is because either Y_L or Y_R is zero that the asymmetry is 1 and the polarization of the target is 30%.

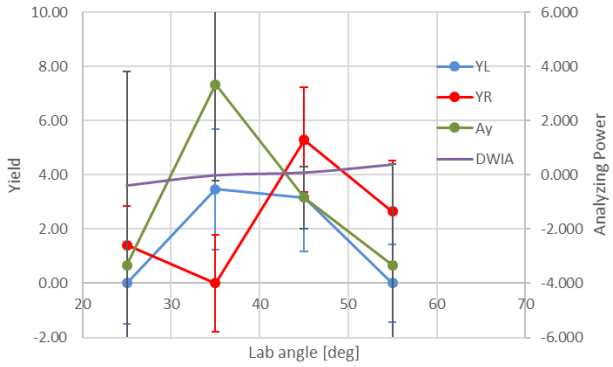

Figure C-28 – The combined yields of left and right detector, analyzing power, and theoretical analyzing power of 1p$_{3/2}$ shell for (^{25}F,^{24}O) partition in Figure 3-27.
Note that the range of analyzing power is from -6 to 6.

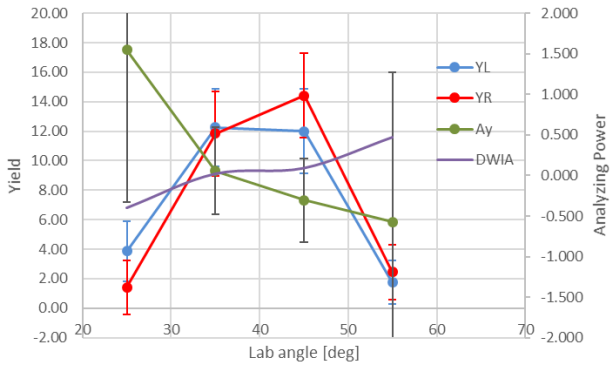

Figure C-29 – The combined yields of left and right detector, analyzing power, and theoretical analyzing power of $1p_{3/2}$ shell for (^{25}F,^{23}O) partition in Figure 3-27.
Note that the range of analyzing power is from -2 to 2.

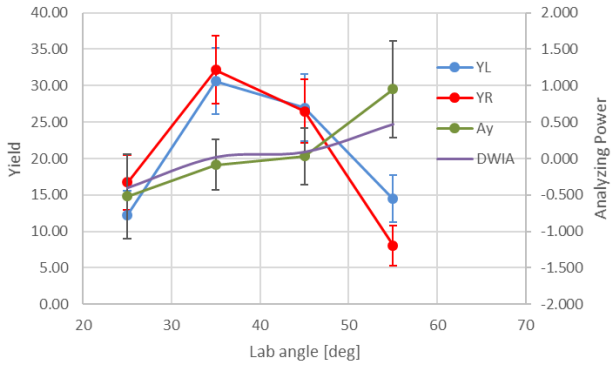

Figure C-30 – The combined yields of left and right detector, analyzing power, and theoretical analyzing power of $1p_{3/2}$ shell for (^{25}F,^{22}O) partition in Figure 3-27.
Note that the range of analyzing power is from -2 to 2.

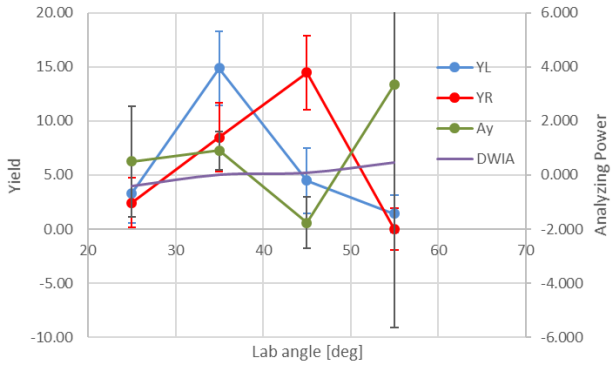

Figure C-31 – The combined yields of left and right detector, analyzing power, and theoretical analyzing power of $1p_{3/2}$ shell for (^{25}F,^{21}O) partition in Figure 3-27.
Note that the range of analyzing power is from -6 to 6.

Appendix D
Analysis and Results of Proton Elastic Scattering

The proton-proton elastic scattering was used to measure the absolute magnitude of the polarization of the proton target. Besides, it provides calibration data for major detectors in the experiment. This section will explain the polarization measurement and the calibration results.

D.1 Calculating Formula of Magnitude of Polarization

The absolute magnitude of the proton polarization can be found by the proton-proton elastic scattering. The differential cross section of $p(\vec{p},p)p$ elastic scattering is [88]

$$\frac{d\sigma}{d\Omega} = \left(\frac{d\sigma}{d\Omega}\right)_0 \left(1 + A_y(\theta)\hat{n}\cdot\vec{P}\right), \tag{D.1.1}$$

where $\left(\frac{d\sigma}{d\Omega}\right)_0$ is the differential cross section for the non-polarized proton-proton elastic scattering, $A_y(\theta)$ is the analyzing power which is angle dependence, $\vec{P}$ is the polarization vector of the target and $\hat{n} = \widehat{k_\iota} \times \widehat{k_f}$ is a normal unit vector of the scattering plane. The angles θ, ϕ are following the usual definition. The inner product $\hat{n}\cdot\vec{P}$ usually denoted as P_y.

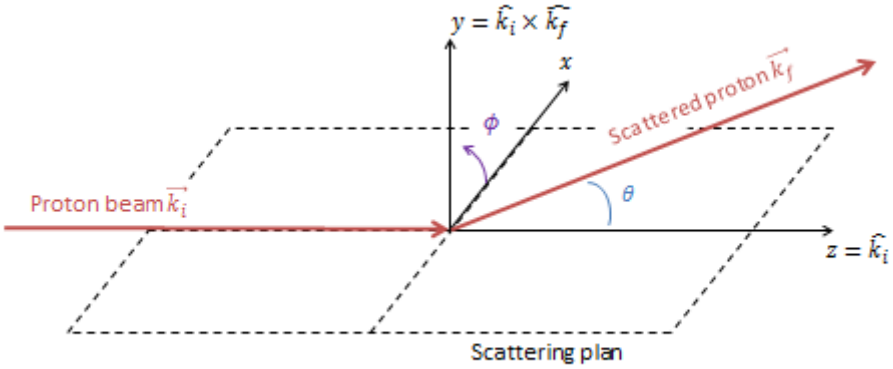

Figure D-1 – The coordinate system for a proton-proton elastic scattering.

The yield Y (number of true events detected) is proportion to the counting time ΔT, the number of particle of the beam N_B, the number of protons per unit area in the target N_T, the detector efficiency ϵ, the DAQ system life time α, the detector acceptance $\Delta\Omega$, and differential cross section

$$Y(\theta,\phi) = \Delta T N_B N_T \epsilon\, \alpha \int_{\theta_1}^{\theta_2} \frac{d\sigma}{d\Omega} \sin\theta\, d\theta d\phi. \tag{D.1.2}$$

To get the magnitude of the polarization of the target, we can place 2 detectors at $\phi = 0$ and $\phi = \pi$,

$$\begin{aligned} Y_L &= Y(\theta, \phi = 0) \\ &= \Delta T\, N_B N_T \epsilon\, \alpha \int_{\theta_1}^{\theta_2} \int_{\phi(\theta_1)}^{\phi(\theta_2)} \left(\frac{d\sigma}{d\Omega}\right)_0 \left(1 + A_y(\theta) P_y\right) \sin\theta\, d\theta\, d\phi, \\ Y_R &= Y(\theta, \phi = \pi) \\ &= \Delta T N_B N_T \epsilon\, \alpha \int_{\theta_1}^{\theta_2} \int_{\phi(\theta_1)}^{\phi(\theta_2)} \left(\frac{d\sigma}{d\Omega}\right)_0 \left(1 - A_y(\theta) P_y\right) \sin\theta\, d\theta\, d\phi. \end{aligned} \tag{D.1.3}$$

Because $A_y(\theta)$is independence of angle ϕ [88]. Thus

$$A_y(\theta) P_y = \frac{Y_L - Y_R}{Y_L + Y_R}. \tag{D.1.4}$$

The error of the asymmetry

$$A_y \Delta P_y = \frac{2}{(Y_L + Y_R)^2} \sqrt{Y_L^2 \Delta Y_R^2 + Y_R^2 \Delta Y_L^2}. \tag{D.1.5}$$

The detectors set up is shown in Figure 2-14. The geometry of acceptance is shown in Figure D-2. In the left plot, the beam is coming from the left, outside of the box. The crystal is a dark purple disk (enlarged 10 times for illustration). The scattered protons are presented by the 2 black arrows. The blue lines are the outlines of the MWDC's acceptance area on an imaginary sphere (green). The red outlines are the projection of the MWDC's windows on the sphere. The black outlines are the projection of the acceptance area on the crystal's plane. The ϕ dependence on θ is plotted in the right figure.

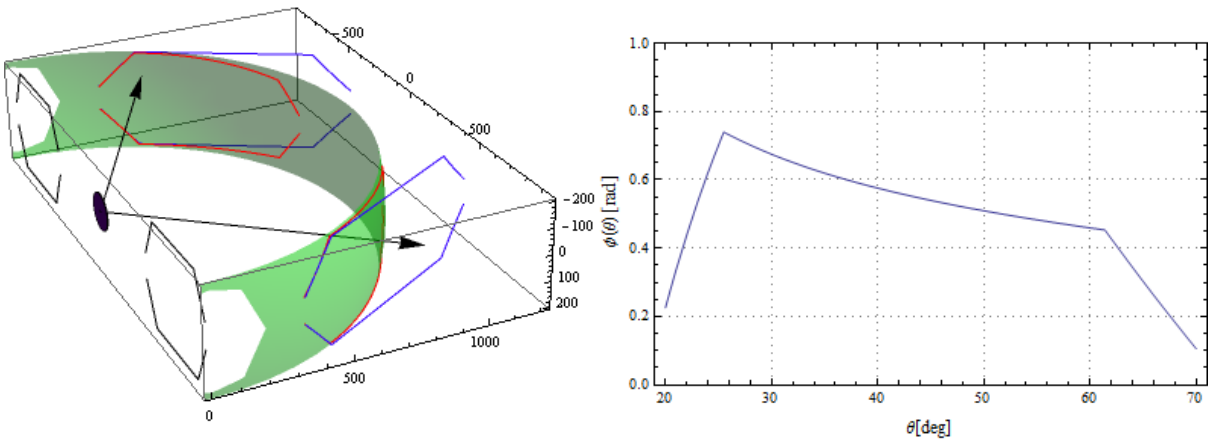

Figure D-2 – Geometry of the MWDC acceptance (Left).
Angular distribution of azimuthal open angle (Right). See text for explanation.

D.2 Conditions of Elastic Scattering

A proton beam at 260 MeV was bombarded on the spin-polarized solid target made of mainly naphthalene ($C_{10}H_8$), which was surrounded by hydrogen-free plastic (PCTFE, polychlorotrifluoroethylene, $[CF_2\text{-}CFCl]_n$) holder. The data was recorded whenever both Tpla-L and Tpla-R were fired (the ppcoin trigger, see Section 2.4.1). The number of the beam proton and the DAQ live time are shown in Table D-1.

Table D-1 – Scalar data for scattering runs

	Count (scattering runs)	
	Spin-up	Spin-down
FH9 plastic	1,254,720,099	874,817,768
Request	374,914	259,190
Accepted	287,755	199,918
DAQ live time	76.75%	77.13%

Although the target crystal and the surrounding material contain carbon atom, the proton-proton elastic scattering has a distinguish fingerprint on the opening angle for identification. The opening angle is almost 90º, while the proton-carbon elastic scattering has much larger opening angle. Moreover, the recoiled carbon cannot acquire enough energy to pass through two 128-μm Kapton films on the chamber's windows. Therefore, the proton-carbon elastic scattering events cannot be detected, as the trigger was set that both Tplas were fired. However, the proton-carbon inelastic scattering, especially the ^{12}C(p,2p) events can create a proton-pair that can be recorded. This gave a broad background signal.

The proton-proton elastic scattering opening angle is calculated and shown in Figure D-3. The opening angle in the laboratory frame $\Delta\theta_{Lab} = \theta_1 + \theta_2$ is not 90º and not a delta peak because of the relativistic effect. The scattering angle in the rest frame of the center of momentum θ_{NN} is limited from 40 º to 140 º due to the detector acceptance. The opening angle has a peak at 86.5 º after convolution with a Gaussian function with 0.3º uncertainties.

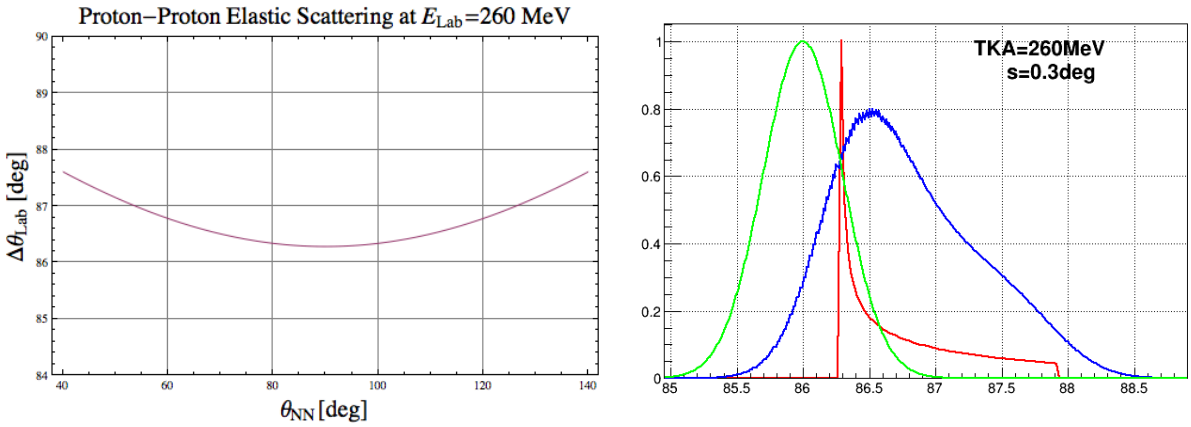

Figure D-3 – Proton-proton elastic scattering.
Left: Opening angle in the Laboratory's frame $\Delta\theta_{Lab}$ against scattering angle in the c.m. frame θ_{NN}.
Right: The red curve is the $\Delta\theta_{Lab}$ distribution. Green curve is Gaussian distribution with sigma 0.3 deg. Blue curve is the convolution of the red curve by the green curve.

The experimental data of the $\Delta\theta_{Lab}$ is shown in Figure D-4. It shows a peak on a broad background. Although the peak is located on 86 º instead of 86.5 º, it must be the proton-proton elastic scattering peak. The reason for the shift could be a fine misalignment of the experimental setup. The effect of the magnetic deflection was included in the calculation that it could not be the main contribution to the shift. The opening angle was gated by different opening angle sections (40 º – 60 º, 60 º – 80 º, 80 º – 100 º, 100 º – 120 º and 120 º – 140 º).

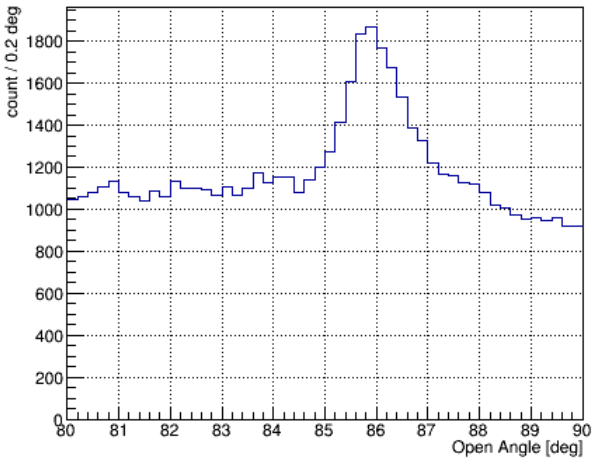

Figure D-4 – Experimental data of opening angle.

The spin polarization was monitored by the NMR method during experiment (Appendix C.8.1). Figure D-5 shows the NMR amplitude (in term of the integrated area of the free induction decay) during the PPES runs. The red shaded area represents the recorded scattering data of the spin-up runs, and the blue shaded area represents the recorded scattering data of the spin-down runs. The NMR measurements took place between runs. The average amplitude of the spin-up runs was 147 a.u. and that of spin-down runs was -115 a.u.. The amplitude of spin-down is approximately 78% of that of spin-up. The total recorded duration of spin-down runs is also shorter than that of spin-up runs.

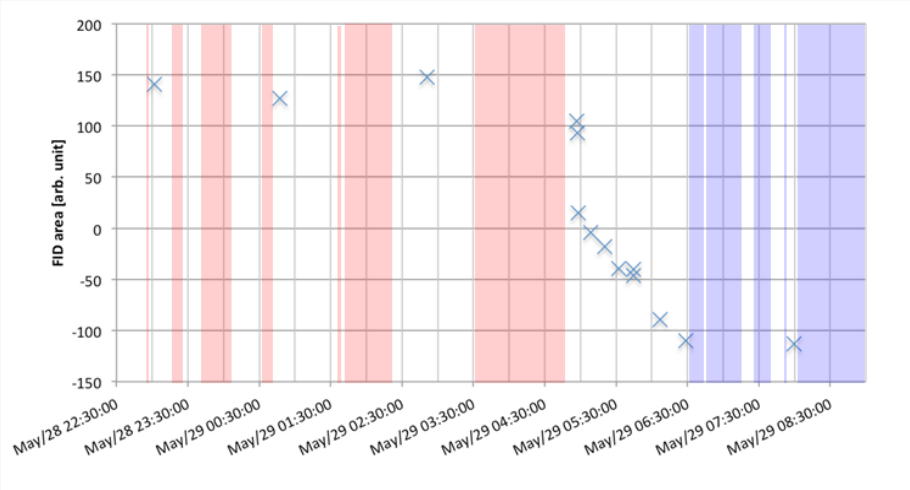

Figure D-5 – NMR signals during the PPES runs.
See main text for detail explanation.

D.3 Background Elimination

There are 3 independent qualities, spherical angles (θ, ϕ) and the separation energy s_p. The proton-proton elastic scattering events have a well-defined opening angle $\Delta\theta_{Lab} = \theta_1 + \theta_2$ and it must be coplanar $\Delta\phi = \phi_1 - \phi_2 = 180°$. The separation energy is not helpful in this case because a lot of background events came from the carbon scattering, which occurred in both the target crystal and the surrounding material. Another quality, Z_{beam} was constructed by the ray tracking result from the MWDCs

$$Z_{beam} = \frac{A\, z_0 - X}{A \cos 60° - \sin 60°}, \tag{D.3.1}$$

where X, A are the ray parameters, z_0 is the perpendicular distance from crystal to the MWDC, and 60° is the MWDC tilted angle (Figure 2-14). The Z_{beam} is the z-position on the Y-Z plane, which is an approximated reaction vertex. A weighted Z_{beam} was calculated from both MWDC-L and MWDC-R. Figure D-6 shows the result of the weighted Z_{Beam}. The meaning of the Z_{Beam} is similar to vertex(Z) (Section 3.3). The peak at 0 mm is from the target and the target holder. The peak at 50 mm is from the NMR coil. The peak at 170 mm is from the carbon target.

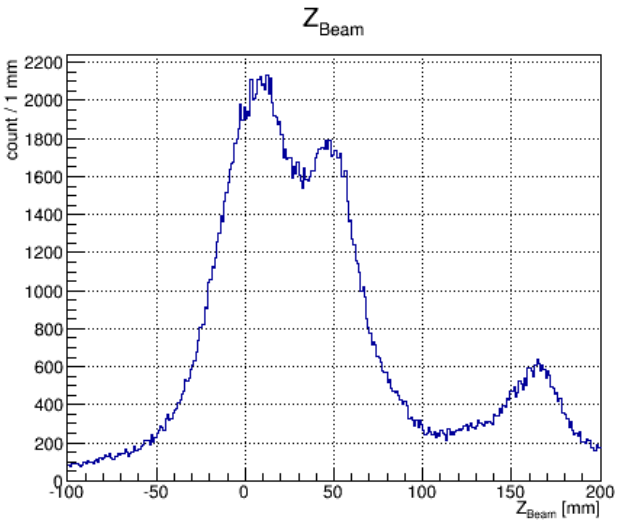

Figure D-6 – Plot of weighted Z_{Beam}.
See main text for detail explanation.

The coplanar angle $\Delta\phi$ is shown in Figure D-7. There are 2 closely packed peaks. The main peak is around 0°, and the second peak is around -10°.

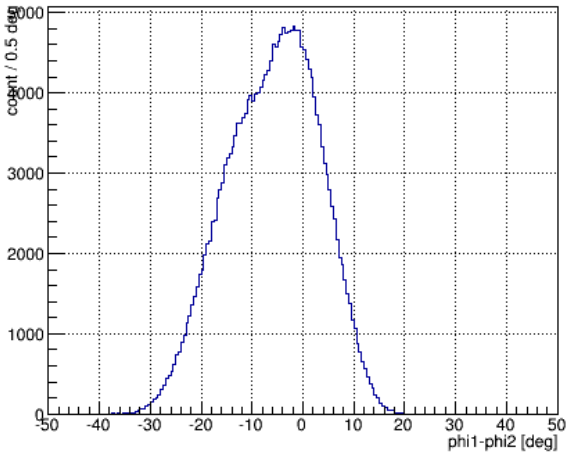

Figure D-7 – Coplanar angle $\Delta\phi$, 2 peaks are closely located.

We can see that, it is hard to define a suitable gate on $\Delta\phi$ and Z_{Beam} but $\Delta\theta$. Thus, an opening angle central gate (84° to 89°) and side gate (81.5° to 84° or 89° to 91.5°) were used as the signal and the background gate respectively. The central gate selected the proton-proton elastic scattering events and background events. The side gate selected background events.

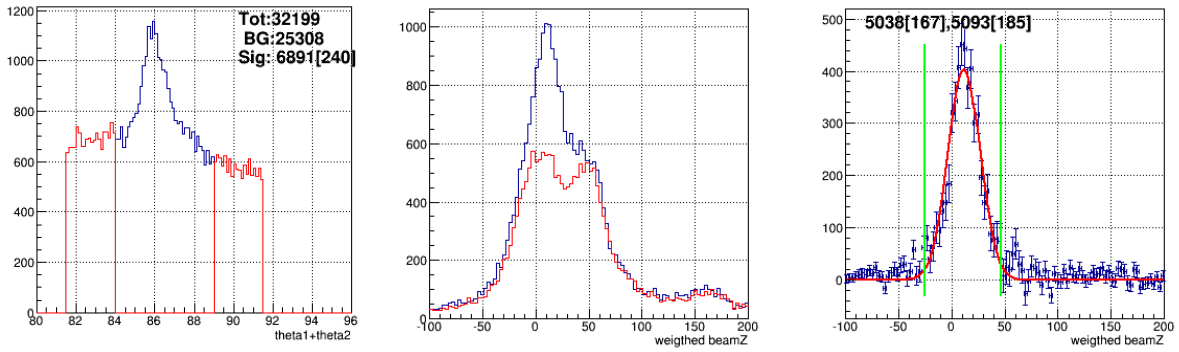

Figure D-8 – Gates and result on Z_{Beam}.
(Left) The central and the side gate of the opening angle. (Middle) the gate on Z_{Beam}. (Right) the Subtracted histogram of Z_{Beam}.

The results of the gating are shown in Figure D-8. The left plot is the $\Delta\theta$ gates, the blue line is the central gate and the red line is the side gate. The middle plot is the Z_{Beam} under $\Delta\theta$ gates with corresponding color. The right plot is the subtraction. The subtraction was fit by a Gaussian. The count range is between the two green lines. The side gate gives fairly good background estimation.

D.4 Summary of Gates

The gates are listed in Table D-2.

Table D-2 – List of gates in proton-proton elastic scattering analysis.

Gate Name	Content
Central gate	Opening angle from 84° to 89°
Side gate	Opening angle from 81.5° to 84° or from 89° to 91.5°
Z_{Beam}	Weighted Z_{Beam} from -40 mm to 60 mm
OpenPhi	$\lvert\Delta\phi - 180°\rvert < 7.5°$

D.5 Polarization Measurement

The scattering angle in the rest frame of the center of momentum θ_{NN} is divided into 5 sectors (40° – 60°, 60° – 80°, 80° – 100°, 100° – 120° and 120° – 140°). The central and side gates of the opening angle are applied. The yield is counted from the Z_{Beam} as same as Figure D-8. The result is shown in Table D-3. The error is shown in the bracket besides of the yield. The total yield is 5032.

Table D-3 – Yields of the proton-proton elastic scattering.

	$Y_L^{\uparrow}$	$Y_R^{\uparrow}$	$Y_L^{\downarrow}$	$Y_R^{\downarrow}$
40° – 60°	235(31)	309(40)	201(27)	183(28)
60° – 80°	713(63)	767(63)	509(53)	422(52)
80° – 100°	1149(80)	1098(81)	635(67)	600(66)
100° – 120°	766(64)	733(64)	387(52)	496(54)
120° – 140°	270(33)	227(30)	167(27)	197(26)
Total	3133(129)	3134(131)	1899(107)	1898(107)

In order to cancel the systematic asymmetry, spin-up and spin-down runs were measured. The yield

$$Y_{L/R}^{\uparrow/\downarrow}(\Delta\theta_{NN}) = \alpha_{L/R} L^{\uparrow/\downarrow} \epsilon\sigma \left(1 + s_{L/R}^{\uparrow/\downarrow} A_y P^{\uparrow/\downarrow}\right),$$
$$L^{\uparrow/\downarrow} = N_T \sum_i \left(N_B^{\uparrow/\downarrow}\right)_i \lambda_i, \qquad s_{L/R}^{\uparrow/\downarrow} = \begin{cases} +1, & L^{\uparrow}, R^{\downarrow} \\ -1, & L^{\downarrow}, R^{\uparrow}, \end{cases} \tag{D.5.1}$$

where $Y(\Delta\theta_{NN})$ is the yield in the sector of θ_{NN}, L is the luminosity, N_T is the number of protons in target, N_B is the number of protons in beam that on the target, λ is the DAQ live time, ϵ is the detection efficiency, σ is the integrated cross section of no polarization, A_y is the mean analyzing power, P is the mean magnitude of the spin polarization of the proton target. The subscripts L, R represent left and right side and the superscripts $\uparrow, \downarrow$ represent spin-up and spin-down. $\alpha_{L/R}$ is the systematic asymmetry factor and the proportional background factor.

If we assume the polarization of spin-up and spin-down are the same and assumed the background is a fraction of signal. A combined yield can eliminate the asymmetry factor α, it is

$$Y_L = \sqrt{Y_L^{\uparrow} Y_R^{\downarrow}}, \qquad Y_R = \sqrt{Y_R^{\uparrow} Y_L^{\downarrow}}, \tag{D.5.2}$$

The result is shown in Figure D-9. The asymmetry is calculated by

$$asym = A_y P = \frac{Y_L - Y_R}{Y_L + Y_R}, \tag{D.5.3}$$

The mean analyzing power is obtained from CNS database. The polarization is calculated for each sector and a weighted mean is used. The resulting spin polarization is -30.5% ± 7.3%.

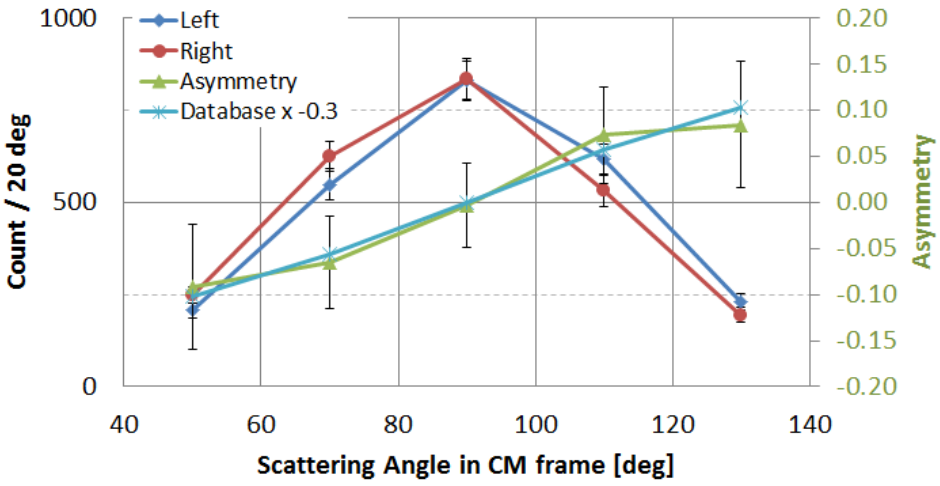

Figure D-9 – Yield and asymmetry of the proton-proton elastic scattering.

The magnitude of the spin polarization of spin-up and that of spin-down are different from the NMR measurement (Figure D-5). In order to eliminate the asymmetry, spin-up and spin-down on one-side is used. Assuming the $P^{\uparrow} = kP^{\downarrow} = P$, the asymmetry

$$A_y P = \frac{Y_L^{\uparrow} L^{\downarrow} - Y_L^{\downarrow} L^{\uparrow}}{Y_L^{\uparrow} L^{\downarrow} k + Y_L^{\downarrow} L^{\uparrow}}, \qquad A_y P = \frac{Y_R^{\downarrow} L^{\uparrow} - Y_R^{\uparrow} L^{\downarrow}}{Y_R^{\downarrow} L^{\uparrow} + Y_R^{\uparrow} L^{\downarrow} k}, \tag{D.5.4}$$

The weighted average of the polarization is -31.8% ± 12.7% for spin-up and 24.8% ± 9.9% for spin-down.

D.6 Integrated Cross Section

The number of particles in the beam and the DAQ live time can be obtained from the scalar data. However, the beam is not 100% overlap with the target. The beam profile is shown in the left plot of Figure D-10. The black circle is the crystal that the hit-ratio is about 32.8%. Because the DCX1X2 are turned off during the scattering runs, the target-hit-ratio

$$\text{Target} - \text{Hit} - \text{Ratio} = \frac{\#\text{on crystal}}{\#\text{proton}} = \frac{\#\text{tracked on crystal}}{\#\text{tracked}}. \tag{D.6.1}$$

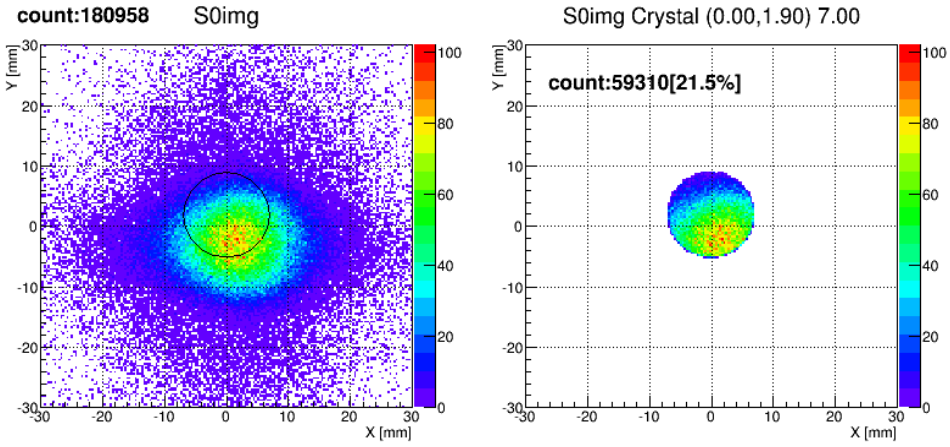

Figure D-10 – Beam profile and Hit ratio from the optics runs.

The target thickness is 1 mm. The molar mass of naphthalene is 128.17 $gmol^{-1}$. The density of the crystal is 1.14 gcm^{-3}. Each molecule has 8 protons. The number of protons on the crystal is

$$N_T = \frac{1.14}{128.17} \times 8 \times 0.1 \times N_A = 4.285 \times 10^{21}\ \text{cm}^{-2}. \tag{D.6.2}$$

The MWDCs combined detection efficiency is 75.9%. This efficiency is a combined efficiency of both MWDC-L and MWDC-R. Individual detection efficiency constrains two parts: tracking efficiency and fire efficiency. The fired efficiency is deduced from number of fired planes and fit by binomial distribution. The tracking efficiency is deduced from the number of tracked events over the number of events that at least one plane was fired. The product of these two efficiencies is the ratio of number of tracked particle over number of particles pass through.

Table D-4 – MWDC efficiency in the proton runs.

	MWDC-L	MWDC-R
Tracking efficiency	96.2%	88.0%
Fired efficiency	96.1%	93.4%
Detection efficiency	92.4%	82.2%
Combined efficiency	75.9%	

The experimental cross section is

$$\sigma_{exp} = \frac{Y^{\uparrow} + Y^{\downarrow}}{0.328\, N_T\, (\sum_i (N_B)_i \lambda_i)\, 0.759} = 2.72 \times 10^{-27}\text{cm}^{-2} = 2.70\ \text{mb} \pm 0.27\ \text{mb} \quad \text{(D.6.2)}$$

The uncertainty mainly came from the target thickness. The target was polished by hand that the thickness uncertainly might be almost 10%.

To compare with the theoretical cross section, the cross section and analyzing power of 260 MeV in the laboratory's frame is shown in Figure D-11 [100]. The integrated cross section

$$\sigma_{th} = \int_{20^\circ}^{70^\circ} \left(\frac{d\sigma}{d\Omega}\right)_{Lab} \sin\theta_{Lab}\, \phi(\theta_{Lab}) d\theta_{Lab} = 2.51\ \text{mb}, \quad \text{(D.6.3)}$$

where the azimuthal acceptance ϕ, of the MWDC depends on θ_{Lab}. The experimental cross section is more than the theoretical cross section. This may be due to under-estimated background.

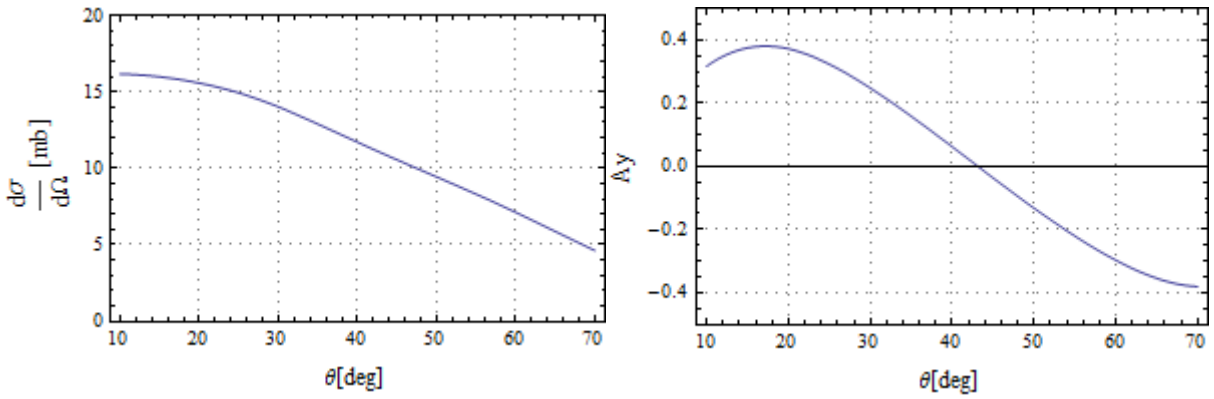

Figure D-11 – Differential cross section and analyzing power in Laboratory's reference frame [100].

D.7 Angular Resolution

The opening angle around $|\theta_{NN} - 90°| < 5°$ is almost a delta distribution with width $0.0141°$ (Figure D-3). The $85° < \theta_{NN} < 95°$ gate was applied on the $\Delta\theta$. The $|\Delta\phi - 180°| < 7.5°$ gate was also applied. The result shows in Figure D-12. The blue line on the left is the $\Delta\theta$ with $80° < \theta_{NN} < 90°$ gate and $|\Delta\phi - 180°| < 7.5°$ gate. The red line was applied $85° < \theta_{NN} < 95°$ gate and $|\Delta\phi -$

$180°| > 7.5°$ gate. The right plot is the subtraction and fitted by a Gaussian. The sigma of the fit is 0.5° = 8.7 mrad. If we assume the angular resolutions from MWDC-L and R are the same

$$\sigma(\theta_1) \approx \sigma(\theta_2) \approx 6 \text{ mrad.} \tag{D.7.1}$$

The resolutions of the tracking parameter X of the MWDC-L and MWDC-R are approximately 0.1 mm. Considering the minimum distance from MWDCs to the target crystal is 1 meter, the contribution of the angular resolution from the MWDC tracking uncertainty can be neglected. The angular uncertainty could be due to multiple scattering from target to detector, which is about 1.2 to 1.4 meter with nitrogen gas, Kapton films and air in between.

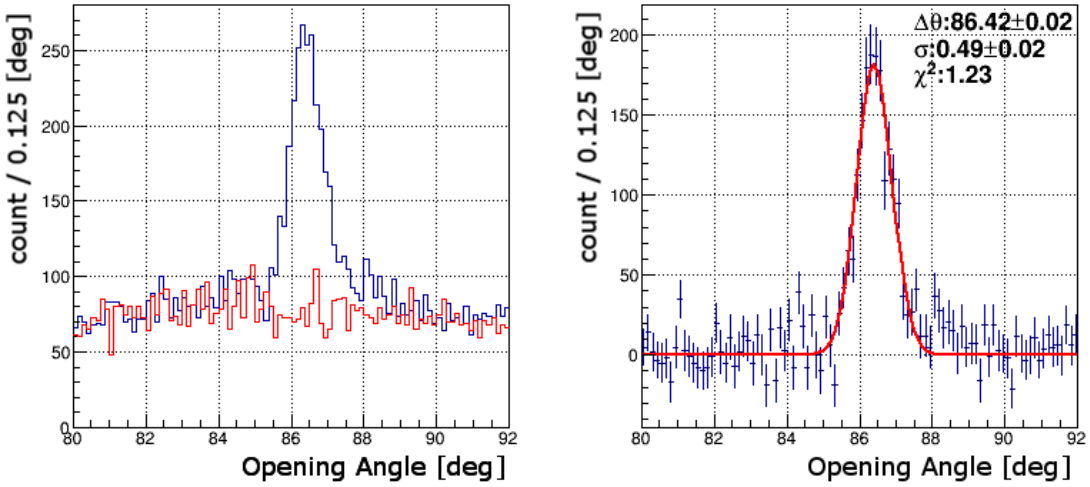

Figure D-12 – Resolution of opening angle.
(Left) The distribution of opening angle near θ_{NN} = 90 (see main text). The blue line is signal. The red line is estimated background. (Right) The background subtracted signal with Gaussian fitting.

D.8 Separation Energy Resolution

The separation energy s_p of proton-proton elastic scattering is calculated using the formula

$$s_p = (1-\gamma)m_p - \gamma(T_1 + T_2) + \gamma\beta(p_1 \cos\theta_1 + p_2 \cos\theta_2) \tag{D.8.1}$$

where γ and β are the Lorentz factor of incident particle, m_p is the mass of proton, T is the kinetic energy and p is the momentum. Thus, the resolution of separation energy depends on the time resolution and the angular resolution. The result of opening angle gate ($85° < \theta_{NN} < 95°$ and $|\Delta\phi - 180°| < 7.5°$) applied on spectrum of s_p is shown in Figure D-13. The blue line on the left plot is with the gate $85° < \theta_{NN} < 95°$ and $|\Delta\phi - 180°| < 7.5°$. The red line is with the gate $85° < \theta_{NN} < 95°$ and $|\Delta\phi - 180°| > 7.5°$. The right plot is the subtraction and fit with two Gaussians. The uncertainty of the larger peak is approximately 3 MeV.

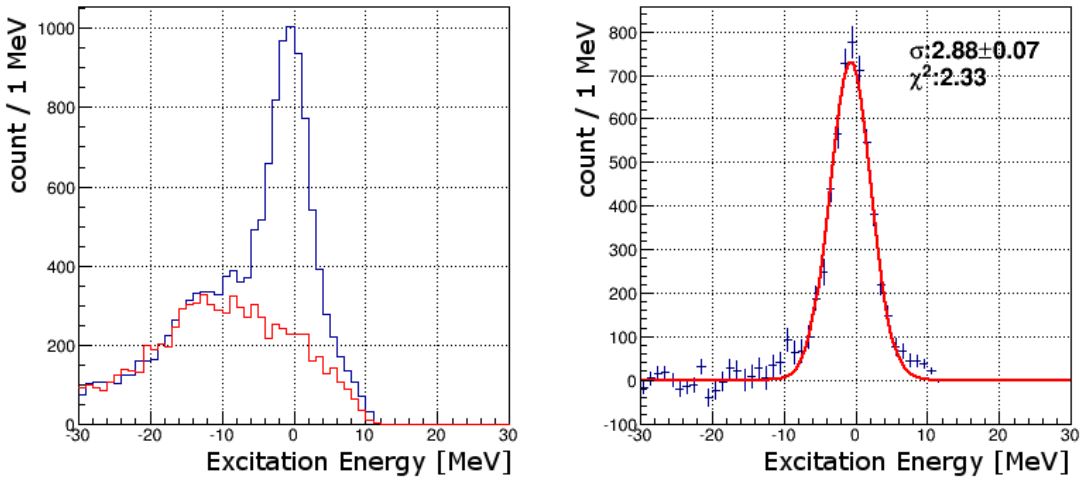

Figure D-13 – Spectra of excitation energy of the proton-proton elastic scattering.
(Left) The distribution of excitation energy with gates (see main text). The blue line is signal. The red line is estimated background. (Right) The background subtracted signal with Gaussian fitting.

Reference

[1] Vijay R. Pandharipande, Ingo Sick, Peter K. A. deWitt Huberts, "Idenpendent particle motion and correlations in fermion system," *Reviews of Modern Physics,* vol. 69, p. 981, 1997.

[2] N. A. Smirnova, B. Allly, K. Heyde, F. Nowacki, and K. Sieja, "Shell evolution and nuclear forces," *Physics Letter B,* vol. 686, pp. 109-113, 2010.

[3] Takaharu Otsuka, Rintaro Fujimoto, Yutaka Utsuno, B. Alex Brown, Michio Honma, and Takahiro Mizusaki, "Magic Numbers in Exotic Nuclei and Spin-Isospin Properties of the NN Interaction," *Physical Review Letters,* vol. 87, no. 8, pp. 082502-1, 20 August 2001.

[4] Rituparna Kanungo, "A new view of nuclear shells," *Physica Scripta,* vol. T152, p. 014002, 2013.

[5] Isao Tanihata, "Neutron halo nuclei," *Journal of Physics G: Nuclear and Particle Physics,* vol. 22, p. 157, 1996.

[6] H. Iwasakia et al., "Low-lying intruder 1− state in 12Be and the melting of the N=8 shell closure," *Physics Letters B,* vol. 491, no. 1-2, pp. 8-14, 2000.

[7] H. Simon et al., "Direct Experimental Evidence for Strong Admixture of Different Parity States in 11Li," *Physical Review Letters,* vol. 83, p. 496, 1999.

[8] D. Guillemaud-Mueller, C. Detraz, M. Langevin, F. Naulin, M. de Saint-Simon, C. Thibault, F. Touchard, M. Epherre, "β-Decay schemes of very neutron-rich sodium isotopes and their descendants," *Nuclear Physics A,* vol. 426, no. 1, pp. 37-76, 1984.

[9] T. Motobayashi, , Y. Ikeda, K. Ieki, M. Inoue, N. Iwasa, T. Kikuchi, M. Kurokawa, S. Moriya, S. Ogawa, H. Murakami, S. Shimoura, Y. Yanagisawa, T. Nakamura, Y. Watanabe, M. Ishihara, T. Teranishi, H. Okuno, R.F. Casten, "Large deformation of the very neutron-rich nucleus 32Mg from intermediate-energy Coulomb excitation," *Physics Letters B,* vol. 346, no. 1-2, pp. 9-14, 1995.

[10] E. K. Warburton, J. A. becker, B. A. Brown, "Mass systematics for A=29-44 nuclei: The deformed A~32 region," *Physical Review C,* vol. 41, no. 3, 1990.

[11] M. H. Storm, A. Watt and R. R. Whitehead, "Crossing of single-particle energy levels resulting from neutron excrss in the sd shell," *J. Physi. G: Nucl. Phys,* vol. 9, pp. L165-L168, 1983.

[12] Yutaka Utsuno, Takaharu Otsuka, Takahiro Mizusaki, and Michio Honma, "Extreme location of F drip line and disappearance of the N=20 magic structure," *PHYSICAL REVIEW C,* vol. 64, p. 011301, 2001.

[13] C. Nociforo et al., "Shell Closure N = 16 in 24O," *AIP Conf. Proc.,* vol. 1165, p. 90, 2009.

[14] A. Ozawa,T. Kobayashi,T. Suzuki,K. Yoshida and I. Tanihata, "New Magic Number, N=16, near the Neutron Drip Line," *PHYSICAL REVIEW LETTERS,* vol. 84, no. 24, 2000.

[15] Robert V. F. Janssens, "Unexpected doubly magic nucleus," *Nature,* vol. 459, p. 1069, 2009.

[16] Takaharu Otsuka, "Exotic nuclei and nuclear forces," *Physica Scripta,* vol. 2013, no. T152, p. 014007, 2013.

[17] B. Alex Brown, "The nuclear shell model towards the drip lines," *Progress in Particle and Nuclear Physics,* vol. 47, no. 2, pp. 517-599, 12 July 2001.

[18] Takaharu Otsuka, Toshio Suzuki, Jason D. Holt, Achim Schwenk and Yoshinori Akaishi, "Three-Body Forces and the Limit of Oxygen Isotopes," *Physical Review Letters,* vol. 105, p. 032501, 2010.

[19] T. Baumann, A. Spyrou, and M. Thoennessen, "Nuclear structure experiments along the neutron drip line," *Rep. Prog. Phys.,* vol. 75, p. 036301, 2012.

[20] Takaharu Otsuka, Toshio Suzuki, Rintaro Fujimoto, Hubert Grawe, Yoshinori Akaishi, "Evolution of Nuclear Shell due to the Tensor Force," *Physical Review Letters,* vol. 95, p. 232502, 2005.

[21] J.R. Erskine, A. Marinov, and J. P. Schiffer, "Eenergy levels in 49Sc from 48Ca(3He,d)49Sc and other reactions proceeding from 48Ca," *Physical Review,* vol. 142, p. 633, 1966.

[22] B. Berthier et al., "One-nucleon transfer reactions to discrete levels induced by a 793 MeV 16O beam on a 208Pb target," *Physics Letter B,* vol. 182, p. 15, 1986.

[23] Gerhard Jacob and Th. A. J. Maris, "Quasi-Free Scattering and Nuclear Structure. II.," *Review of Modern Physics,* vol. 45, no. 1, pp. 6-20, 1973.

[24] L. Lapikas, "Quasi-Elastic Electron Scattering off Nuclei," *Nuclear Physics A,* vol. 553, p. 297, 1993.

[25] G. R. Satchler, Introduction to Nuclear Reactions, 2nd Edition ed., New York: Ocford University Press, 1990.

[26] P. G. hansen and J. A. Tostevin, "Direct Reactions with Exotic Nuclei," *Annu. Rev. Nucl. Part. Sci.,* vol. 53, pp. 219-261, 2003.

[27] Maria G. Mayer, "On Close Shells in Nuclei," *Phys. Rev.,* vol. 74, p. 235, 1948.

[28] Maria Goeppert Mayer, "Nuclear Configurations in the Spin-Orbit Coupling Model. I. Empirical Evidence," *Physical Review,* vol. 78, no. 1, pp. 16-21, 1950.

[29] J. Heghes, K.J. Le Couteur, "Spin Orbit Coupling in the Nuclear Shell Model," *Proc. Phys. Soc A,* vol. 63, p. 1219, 1950.

[30] Kazuhiko Ando, Hiroharu Bando, "Single-Particle Spin-Orbit Splittings in Nuclei," *Progree of Theoretical Physics,* vol. 66, no. 1, 1981.

[31] S. C. Pieper, V. R. pandharipande, "Origins of Spin-Orbit Splitting in 15N," *Physical Review Letters,* vol. 70, no. 17, p. 2541, 1993.

[32] R. Machleidt, D. R. Entem, "Chiral effective field theory and nuclear forces," *arXiv [nucl-th],* 2011.

[33] Kenneth S. Krane , Introductory Nuclear Physics, 2nd ed., John Wiley & Sons, Inc., 1988.

[34] Donald K. Harriss and Frank Rioux, "A simple Hartree SCF calculation on a one-dimensional model of the He atom," *J. Chem. Educ.,* vol. 57, no. 7, p. 491, 1980.

[35] Richard F. Casten, Nuclear Structure from a Simple Perspective, Oxford Science Publication, 2000.

[36] B. Alex Brown, "New Skyrme interaction for normal and exotic nuclei," *Physical Review C,* vol. 58, no. 1, 1998.

[37] G. A. Lalazissis, J. König, and P. Ring, "New parametrization for the Lagrangian density of relativistic mean field theory," *Phsyical Review C,* vol. 55, no. 540, 1997.

[38] B. Alex Brown, "Lecture Notes in Nuclear Structure Physics," Michigan State University, 2011.

[39] A. Bohr and B.R. Mottelson, Nuclear Structure Volume 1: Single-Particle Motion, World Scientific, 1998.

[40] "National Nuclear Data Center," [Online]. Available: http://www.nndc.bnl.gov/.

[41] A. Ozawa, T. Suzuki, I. Tanihata, "Nuclear size and related topic," *Nuclear Physics A,* vol. 693, pp. 32-62, 2001.

[42] E. Caurier, G. Martinez-Pinedo, F. Nowacki, A. Poves, A. P. Zuker, "The shell model as a unified view of nuclear structure," *Reviews of Modern Physics,* vol. 77, p. 427, 2005.

[43] Norman K. Glendenning, Direct Nuclear Reactions, World Scientific, 2004.

[44] N. K. Glendenning, "IX.E one- and Two- Nucleon Transfer Reaction," in *Nuclear Spectroscopy and Reactions Part D,* New York, Academic Press, Inc, 1975, p. 319.

[45] B. K. Jennings, "Non-observability of Spectroscopic Factors," *arXiv:1102.3721 [nucl-th],* 2011.

[46] Michel Baranger, "A definition of the single-nucleon potential," *Nuclear Physics,* vol. A149, pp. 225-240, 1970.

[47] Alfredo Poves, "Shell model and spectroscopic factors," Madrid, Spain.

[48] C. Barbieri, "Role of Long-Range Correlations in the Quenching of Spectroscopic Factors," *Phsyical Review Letters,* vol. 103, p. 202502, 2009.

[49] I. Sick, *Quasi-free knockout reaction,* QFS workshop at ECT, Trento, 2008.

[50] N. S. Chant and P. G. Roos, "Distorted-wave impulse-approximation calculations for quasifree cluster knockout reactions," *Physical Review C,* vol. 15, no. 1, p. 59, 1976.

[51] Geoffrey F. Chew, Gian Carlo Wick, "The Impulse Approximation," *Physics Review,* vol. 85, pp. 636-642, 1952.

[52] M. Radici, S. Boffi, Steven C. Pieper, V.R. Pandharipande, "Many-body effects in 16O(e,e'p)," *Physical Review C,* vol. 50, no. 6, p. 3010, 1994.

[53] A. Gade et.al., "Reduction of spectroscopic strength:Weakly-bound and strongly-bound single-particle states studied using one-nucleon knockout reactions," *Physical Review C,* vol. 77, p. 044306, 2008.

[54] C. Barbieri, W.H. Dickhoff, "Spectroscopic factors in 16O and Nucleon Asymmetry," *International Journal of Modern Physics A,* vol. 24, no. 11, 2009.

[55] C. J. Oliver, P. D. Forsyth, J. L. Hutton, G. Kaye, "Spectroscopic factors derived from 16O(d,n)17F measurement," *Nuclear Phsyics A,* vol. 127, no. 3, 1969.

[56] Y. Yasuda et la., "Spectroscopic factors and strength distributions for the deeply bound orbitals in 40Ca obtained from the (p,2 p) reaction at 392MeV," *Phsyical Review C,* vol. 81, p. 044315, 2010.

[57] J. M. Udías, P. Sarriguren, E. Moya de Guerra, E. Garrido, and J. A. Caballero, "Spectroscopic factors in Ca40 and Pb208 from (e,e'p): Fully relativistic analysis," *Phsyical Review C,* vol. 48, p. 2731, 1993.

[58] G. J. Kramer, H. P. Blokb, L. Lapikás, "A consistent analysis of (e,e'p) and (d,3He)," *Nuclear Physics A,* vol. 679, pp. 267-286, 2001.

[59] J. A. Tostevin and A. Gade, "Systematics of intermediate-energy single-nucleon removal cross sections," *Physica Review C,* vol. 90, p. 057602, 2014.

[60] Jenny Lee, M. B. Tsang, W.G. Lynch, "Neutron scpectroscopic factors from transfer reactions," *Physical Review C,* vol. 75, p. 064320, 2007.

[61] Jenny Lee et al., "Neutron-Proton Asymmetry Dependence of Spectroscopic Factors in Ar Isotopes," *Physical Review Letters,* vol. 104, p. 112701, 2010.

[62] Ø. Jensen, G. Hagen, M. Hjorth-Jensen, B. Alex Brown, and A. Gade, "Quenching of Spectroscopic Factors for Proton Removal in Oxygen Isotopes," *Physical Review Letters,* vol. 107, p. 032501, 2011.

[63] N. K. Timodeyuk, "New Insight into the Observation of Spectroscopic Strength Reduction in Atomic Nuclei: Implication for the Physical Meaning of Spectroscopic Factors," *Phsyical Review Letters,* vol. 103, p. 242501, 2009.

[64] G. B. Crinean, G. M. Hudson, L. W. J. Wild, B. M. Spicer, "Proton reactions with 17O: (II). The 17O(p, d)16O reaction," *Nuclear Physics A,* vol. 244, no. 1, pp. 77-92, 1975.

[65] S. Burzynski†, M. Baumgartner, H.P. Gubler, J. Jourdan, H.O. Meyer, G.R. Plattner, H.W. Roser, I. Sick, K.-H. Möbius, "Accurate determination of the 17O-16O + n coupling constant and spectroscopic factor," *Nuclear Physics A,* vol. 399, no. 1, pp. 230-240, 1983.

[66] Satoshi Sakaguchi, PhD Thesis, University of Tokyo, 2008.

[67] G. A. Lalazissis, D. Vretenar, W. Poschl, P. Ring, "Reduction of the spin-orbit potential in light drip-line nuclei," *Physics Letters B,* vol. 418, pp. 7-12, 1998.

[68] I. Hamamotoa, S.V. Lukyanova, X.Z. Zhanga, "Kinetic energy and spin-orbit splitting in nuclei near neutron drip line," *Nuclear Physics A,* vol. 683, no. 1-4, pp. 255-256, 2011.

[69] A. Cipollone, C. Barbieri, and P. Navrátil, "Isotopic Chains Around Oxygen from Evolved Chiral Two- and Three-Nucleon Interactions," *Physical Review Letters,* vol. 111, p. 062501, 2013.

[70] V. Somà, C. Barbieri, A. Cipollone, T. Duguet, and P. Navrátil, "Three-nucleon forces in exotic open-shell isotopes," *EPJ Web of Conferences,* vol. 66, p. 02005, 2014.

[71] H. Sakurai et al., "Evidence for particle stability of 31F and particle instability of 25N and 28O," *Phsyics Letter B,* vol. 448, pp. 180-184, 1999.

[72] "Atomic Mass Adjustment," 16 Nov 2012. [Online]. Available: http://amdc.impcas.ac.cn/evaluation/data2012/data/mass.mas12.

[73] H. Tsubota, N. Kawamura, S. Oikawa, "Photoproton cross section for 19F," *Journal of the physical society of Japan,* vol. 38, no. 2, p. 299, 1975.

[74] M. D. High, J.F. Bedi, D. W. Devins, P. Shapiro, P. A. Deutchman, "The 19F(p, 2p)180 reaction," *Physics Letters B,* vol. 41, no. 5, p. 588, 1972.

[75] M. Thoennessen, T. Baumann, B. A. Brown, J. Enders, N. Frank, P. G. Hansen, P. Heckman, B. A. Luther, J. Seitz, A. Stolz and E. Tryggestad, "Single proton knock-out reactions from 24,25,26F," *Physical Review C,* vol. 68, p. 044318, 2003.

[76] Samuel Wong, Introductory Nuclear Physics, 2 ed., Germany: Wiley-VCH Verlag GmbH & Co. KGaA, 2004.

[77] A. Terakawa et al., "Proton single-particle strength in 19F measured via the 18O(d,n) reaction," *Physical Review C,* vol. 66, p. 064313, 2002.

[78] C. Schmidt and H. H. Duhm, "The 18O(3He,d)19F reaction at E3He = 16 MeV," *Nuclear Physics A,* vol. 155, pp. 644-658, 1970.

[79] M. Yasue et al., "Spectroscopic study of oxygen and fluorine isotopes with (α,3He) and (α,t) reaction on 16,17,18O," *Physical Review C,* vol. 46, no. 4, p. 1242, 1992.

[80] S. Michimasa, Proton shell structure in nuetron-rich nucleus 23F (PhD. Thesis), 2006.

[81] C. S. Sumithrarachchi, D. J. Morrissey,B. A. Brown,A. D. Davies,D. A. Davies, M. Fancina, E. Kwan, P. F. Mantica, M. Portillo, Y. Shimbara, J. Stoker and R. R. Weerasiri, "Structure of 23F via β decay of 23O," *Physical Review C,* no. 75, p. 024305, 2007.

[82] S. Michimasa, S. Shimoura, H. Iwasaki, M. Tamaki, S. Ota, N. Aoi, H. Baba, N. Iwasa, S. Kanno, S. Kubono, K. Kurita, M. Kurokawa, T. Minemura, T. Motobayashi, M. Notani, H.J. Ong, A. Saito, H. Sakurai, E. Takeshita, S. Takeuchi, Y. Yashida, "Proton single-particle states in the neutron-rich 23F nucleus," vol. 638, no. 2-3, 2006.

[83] B. A. Brown and W. A. Richter, "New "USD" Hamiltonians for the sd shell," *Physical Review C,* vol. 74, p. 034315, 2006.

[84] Zs. Vajta et al., "Excited states in the neutron-rich nucleus 25F," *Physical Reveiw C,* no. 89, p. 054323, 2014.

[85] B. A. Brown, A. Etchegoyen, N. S. Godwin, W. D. M. Rae, W. A. Richter, W. E. Ormand, E.K. Warburton, J.S. Winfield, L. Zhao and C.H. Zimmerman, "MSU-NSCL report number 1289".

[86] Toshio Suzuki, Rintaro Fujimoto, Takaharu Otsuka, "Gamow-Teller transitions and magnetic properties of nuclei and shell evolution," *Physical Review C,* vol. 67, p. 044302, 2003.

[87] Y. Utsuno et al., "Shape transitions in exotic Si and S isotopes and tensor-force-driven Jahn-Teller effect," *Physical Review C,* vol. 86, p. 051301, 2012.

[88] J. R. Taylor, Scattering Theory, New York: Dover Publication, Inc., 2000.

[89] M. Leuschner, J. R. Calarco, and F. W. Hersman, E. Jans, G. J. Kramer, L. Lapikas, G. van der Steenhoven, and P. K. A. de Witt Huberts, H. P. Blok and N. Kalantar-Nayestanaki, J. Friedrich, "Quasielastic proton knockout from 16O," *Physical Review C,* vol. 49, no. 2, p. 955, 1994.

[90] A. A. Cowley, J. J. Lawrie, G. C. Hillhouse, D. M. Whittal, S. V. Fortsch, J. V. Pilcher, F. D. Smit, P. G. Roos, "Quasifree knockout in 16O(p, 2p)15N at an incident energy of 151Mev," *Physical Review C,* vol. 44, no. 1, p. 329, 1991.

[91] T. Noro et al., "A study of nucleon properties in nuclei through (p, 2p) reactions," *Nuclear Physics A,* vol. 629, p. 324, 1998.

[92] Shoichiro Kawase, "Master Thesis," University of Tokyo, 2010.

[93] G. Mairle, G.J. Wagner, "The decrease of ground-state correlations from 12C to 14C," *Nuclear Physics A,* vol. 253, pp. 253-262, 1975.

[94] P. A. Deutchman and J. G. Old, "The (p, 2p) reaction for slightly deformed nuclei," *Nuclear Physics,* vol. A283, pp. 289-306, 1977.

[95] P. Kitching, C.A. Miller, W.C. Olsen, D.A. Hutcheon, W.J. McDonald, and A.W. Stetz, "Quasi-Free Scattering of Polarized Proton," *Nuclear Physics A,* vol. 340, pp. 423-444, 1980.

[96] G. Jacob, Th. A. J. Maris, C. Schneider, M.R. Teodoro, "Quasi-free scattering with poalrized proton," *Nuclear physics A,* vol. 257, pp. 517-532, 1976.

[97] E. D. Cooper, S. Hama and B. C. Clark, "Global Dirac phenomenology for proton-nucleus elastic scattering," *Physical Review C,* vol. 47, no. 1, p. 297, 1993.

[98] Gerald G. Ohlsen, "Polarization transfer and spin correlation experiments in nuclear physics," *Rep. Prog. Phys.,* vol. 35, p. 717, 1972.

[99] Gerhard Jacob, Th. A. J. Maris, C. Schneider, and M. R. Teodoro, "Quasi-free scattering with polarized protons," *Nuclear Physics A,* vol. 257, pp. 517-532, 1976.

[100] "CNS Data Analysis Center," [Online]. Available: http://gwdac.phys.gwu.edu/.

[101] Carlos A. Bertulani, Pawel Danielewicz, Introduction to nuclear reactions, Bristal and Philadelphia: Institute of physics publishing, 2004.

[102] Toshiyuki Kubo, "In-flight RI beam separator BigRIPS at RIKEN and elsewhere in Japan," *Nuclear Instruments and Methods in Physics Research B,* vol. 204, pp. 97-113, 2003.

[103] T. Uesaka, S. Shimoura, H. Sakai, G.P.A. Berg, K. Nakanishi, Y. Sasamoto, A. Saito, S. Michimasa, T. Kawabata, T. Kubo, "The high resolution SHARAQ spectrometer," *Nuclear Instruments and Methods in Physics Research B,* vol. 266, pp. 4218-4222, 2008.

[104] H. Kumagaia, A. Ozawaa, N. Fukudab, K. Sümmererc, I. Tanihataa, "Delay-line PPAC for high-energy light ions," *Nuclear Instruments and Methods in Physics Research Section A,* vol. 470, no. 3, pp. 562-570, 2001.

[105] H. Miya et al., "Development of low-pressure multi-wire drift chambers for high-resolution spectroscopy with radioactive isotope beams," *Nuclear Instruments and Methods in Physics Research Section B,* vol. 317, no. B, pp. 701-704, 2013.

[106] H. Okamuraa, S. Ishida, N. Sakamoto, H. Otsu, T. Uesaka, T. Wakasa, Y. Satou, H. Sakai, T. Niizeki, H. Ohnuma, T. Ichihara, "Detector system of the first focal-plane of the spectrometer SMART at RIKEN," *Nuclear Instruments and Methods in Physics Research Section A,* vol. 406, no. 1, pp. 78-88, 1998.

[107] A. Obertelli, T. Uesaka, "Hydrogen targets for exotic-nuclei studies developed over the past 10 years," *The European Physical Journal A,* vol. 47, p. 105, 2011.

[108] Tomohiro Uesaka, Hideyuki Sakai, Akihiro Yoshimi, Koichiro Asahi, Polarized Source and Targets, World Scientific, 2007.

[109] John Fox, Applied Regression Analysis, Linear Models, and Related Methods, Sage Publications, Inc, 1997.

[110] T. L. Tang, et al., "Analysis of proton-proton elastic scattering in SHARAQ04 experiment," *CNS Annual report 2013,* p. 11, 2015.

[111] T. L. Tang, et al., "The polarized proton target in SHARAQ04 experiment.," *RIKEN Accel. Prog. Rep.*, vol. 46, p. 162, 2012.

[112] T. L. Tang, et al., "Polarized proton target in SHARAQ04 experiment," *CNS annual report 2012*, p. 59, 2013.

[113] S Kawase, *PhD Thesis*, 2016.

[114] T. Noro, *QFS studies at RCNP*, QFS workshop at ECT, Trento, 2008.

[115] G. A. Lalazissis, D. Vretenar, P. Ring, "Relativistic Hartree-Bogoliubov description of deformed light nuclei," *The European Physical Journal A*, vol. 22, no. 1, pp. 37-45, 2004.

[116] Mahesh K. Sharma, R.N. Panda, Manoj K. Sharma, S.K. Patra, "Nuclear structure study of some bubble nuclei in the light mass region using mean field formalism," *Chinese Physics C*, vol. 39, no. 6, p. 064102, 2015.

[117] P. Moller, J.R. Nix, W.D. Myers, W.J. Swiatecki, "Nuclear Ground-State Masses and Deformations," *Atomic Data and Nuclear Data Tables*, vol. 59, no. 2, pp. 185-381, 1995.

[118] R. H. Siemssen and J. R. Erskine, "W182(d,p)W183 Reaction at 7.5 and 12 MeV: An Investigation of the Stripping Process on a Deformed Heavy Nucleus," *Physical Review*, vol. 146, p. 911, 1966.

[119] R. H. Siemssen and J. R. Erskine, "Absolute spectroscopic factors for (d,p) reactions on heavy deformed nuclei," *Physical Review Letters*, vol. 19, no. 2, p. 90, 1967.

[120] W. J. McDonald, R. N. Macdonald, W. C. Olsen, R. Dymarz, F. KHanna, L. Antonuk, J. M. Cameron, P. Kitching, G.C. Neilson, and D. M. Sheppard, "Quasi-free nucleon scattering on 16O," *Nuclear Physics A*, vol. 456, pp. 577-598, 1986.

[121] T. Otsuka and Y. Tsunoda, "The role of shell evolution in shape coexistence," *J. Phys. G: Nucl. Part. Phys.*, vol. 43, p. 024009, 2016.

[122] "ATIMA," [Online]. Available: https://web-docs.gsi.de/~weick/atima/.

[123] J. F. Ziegler and J. M. Manoyan, "The stopping of ions in compounds," *Nuclear Instruments and Methods in Physics Research B*, vol. 35, pp. 215-228, 1988.

[124] J.J. Sakurai, Modern Quantum Mechanics, Addison-Wesley, 1994.

[125] T. L. Tang, A. Shiubusawa, T. Kawahara, T. Wakui, T. Uesaka, "Dynamic nuclear polarization on para-terphenyl at room temperature," *CNS annual report 2011*, p. 78, 2012.

[126] A. B. Zahlan, The Triple State, Cambridge University Press, 1967.

[127] T. Wenckebach, "Dynamic Nuclear Polarization using Photexcited Triplet States," (electronic material), Burgh-Haamsted, Netherlands, 2008.

[128] S.R. Hartmann, E.L. Hahn, "Nuclear Double Resonance in the Rotating Frame," *Physical Review*, vol. 128, p. 2042, 1962.

[129] A. Abragam, M. Goldman, "Principle of Dynamic Nuclear Polarization," *Rep. Prog. Phys.,* vol. 41, p. 397, 1978.

[130] A. W. Overhauser, "Polarization of Nuclei in Metals," *Physical Review,* vol. 92, p. 411, 1953.

[131] H. W. van Kesteren, W. Th. Wenckebach, J. Schmidt, "Production of High, Long-Lasting, Dynamic Proton Polarization by Way of Photoexcited Triplet States," *Physical Review Letters,* vol. 55, no. 15, pp. 1642-1644, 1985.

[132] Kazuyuki Takeda, K. Takegoshi, Takehiko Terao, "Dynamic nuclear polarization by photoexcited-triplet electron spin in polycrystalline sample," *Chemical Physics Letters,* vol. 345, pp. 166-170, 2001.

[133] Kazuyuki Takeda, K. Takegoshi, Takehiko Terao, "Dynamic Nuclear Polarization by Electron Spins in the Photoexcited Triplet State: I. Attainment of Proton Polarization of 0.7 at 105 K in Naphthalene," *J. Phys. Soc. Jpn.,* vol. 73, pp. 2313-2318, 2004.

[134] K. Takeda, "Studies on dynamic nuclear polarization using photo-excited triplet electron spins," in *42th NMR Conference,* 2003.

[135] A. Brillante, D.P. Craig, "Host and guest emission in pentacene-anthracene mixed crystals," *J. Chem. Soc., Faraday Trans. 2,* pp. 1457-172, 1975.

[136] A. Henstra, T.S. Lin, J. Schmidt, T. Wenckebach, "High dynamic nuclear polarization at room temperature," *Chemical Physics Letters,* vol. 165, no. 1, pp. 6-10, 1990.

[137] V. Weis, R.G. Griffin, "Electron-nuclear cross polarization," *Solid State Nuclear Magnetic Resonance,* vol. 29, pp. 66-78, 2006.

[138] Kan-Nian Hu, Galia T. Debelouchina, Albert A. Smith, Robert G. Griffin, "Quantum mechanical theory of dynamic nuclear polarization in solid dielectrics," *Journal of Chemical Physics,* vol. 134, p. 125105, 2011.

[139] W.T. Wenckebach, "The Solid Effect," *Applied Magnetic Resonance,* vol. 34, pp. 227-235, 2008.

[140] S. Sakaguchi, PhD Thesis, Tokyo University, 2008.

[141] J.B.W. Morsink, T.J. Aartsma, D.A. Wiersma, "Photon-echo relaxation measurements with two dye-lasers application to pentacene-h14 and -d14 in p-terphenyl-h crystals at 1.5 K," *Chemical Physics Letters,* vol. 49, no. 1, pp. 34-38, 1977.

[142] J. F. O'Hanlon, A User's Guide to Vacuum Technology.

[143] Malcolm H. Levitt, Spin Dynamics, : John Wiley & Sons, Ltd., 2001.

~~~~~ End of Thesis ~~~~~
~~~~~